



Structure-Property Relationship:  
Polystyrene Model Systems and The Molecular  
Impact on Physical Foaming

Zur Erlangung des akademischen Grades eines

DOKTORS DER NATURWISSENSCHAFTEN  
(Dr. rer. nat.)

von der KIT-Fakultät für Chemie und Biowissenschaften  
des Karlsruher Instituts für Technologie (KIT)

genehmigte

DISSERTATION

von

M.Sc. Marie-Christin Helena Röpert

Erster Gutachter: Prof. Dr. Manfred Wilhelm

Zweiter Gutachter: Prof. Dr. Patrick Théato

Tag der mündlichen Prüfung: 13. Februar 2023



## DECLARATION

Hiermit erkläre ich, Marie-Christin Helena Röpert, dass ich die vorliegende Doktorarbeit selbstständig im Rahmen der Betreuung durch Prof. Dr. Manfred Wilhelm verfasst und keine anderen als die von mir angegebenen Quellen und Hilfsmittel benutzt, die wörtlich oder inhaltlich übernommene Stellen als solche kenntlich gemacht und die Satzung des Karlsruher Instituts für Technologie (KIT) zur Sicherung guter wissenschaftlicher Praxis in der gültigen Fassung beachtet habe.

Karlsruhe, den 09.01.2023

---

Marie-Christin Röpert



## ABSTRACT

Polymer foams are composed of statistically dispersed gas-containing cells in a polymer matrix and have distinct physical, mechanical, and thermal properties compared to non-cellular materials. The application areas are diverse, including, e.g., thermal insulation or lightweight constructions. Because of their interdisciplinary and multiple application possibilities, they have attracted increasing attention from both academia and industry. The cell morphology of polymeric foams is dictated primarily by the interaction between technical process parameters and the inherent molecular characteristics of the polymer melt. Few studies have addressed the influence of molecular characteristics, while the vast majority focus on foaming techniques and process conditions. However, these studies are often based on industrial samples with an unknown topology or semi-crystalline polymers, which hinders the ability to distinguish co-occurring effects. To overcome this challenge, the dissertation investigates the impact of intrinsic molecular polymer properties on three main stages of the physical foaming process, namely cell nucleation, growth, and stabilization. For this purpose, living anionic polymerization is used to synthesize well-defined amorphous homo- and block copolymers with defined molecular characteristics, including molecular weight, block order, and branching. Furthermore, this dissertation intends to expand the understanding of the intriguing relationship between intrinsic molecular parameters, melt rheological properties, and macroscopic cellular morphology. The investigated polymer models enabled the production of foams with volume expansion ratios between  $VER = 1.5$  and  $16.0$ , average cell sizes of  $D = 0.39$  and  $17.21 \mu\text{m}$ , and cell densities of  $N = 5.53 \times 10^9$  and  $2.07 \times 10^{13} \text{ cell cm}^{-3}$ , foamed with  $\text{scCO}_2$  at a pressure of  $p = 500 \text{ bar}$ , depressurization rate of  $dp/dt \approx 200 \text{ bar s}^{-1}$ , and temperatures ranging between  $T_f = 60 - 150 \text{ }^\circ\text{C}$ . Thereby, the following relationships prove to be particularly significant: (I) Heterogeneous nucleation was enhanced by self-assembled block copolymers with heterogeneous chain mobility or blowing agent. Heterogeneous nucleation led to increased  $N$  and decreased  $D$  values down to the nanometric range for spherical microdomains, which display the highest proportion of interfaces. (II) Branched polymers with variable topologies enhanced the polymers' melt strength and foam expansion by reducing the melts' shear viscosity and improving stretchability. An optimized structure-property relationship was identified to maximize  $VER$  and  $D$  by minimizing cell coalescence. For this purpose, the relationship between molecular topology, linear and non-linear rheological properties, and cellular morphology was investigated. (III) Polymers with varying molecular dynamics enabled controlling the vitrification of the polymer. Under similar foaming conditions, higher glass transition temperatures  $T_g$  ultimately resulted in smaller  $D$ . The comprehensive study of the influence of distinct and independently investigated parameters, such as morphology, topology, and molecular dynamics, can guide the design of polymeric foams with intended cell morphologies.



## ZUSAMMENFASSUNG

Polymerschäume bestehen aus statistisch verteilten gashaltigen Zellen in einer Polymermatrix und weisen im Vergleich zu nicht-zellulären Materialien unterschiedliche physikalische, mechanische und thermische Eigenschaften auf. Die Anwendungsbereiche sind vielfältig und umfassen z. B. Wärmedämmungen oder Leichtbaukonstruktionen. Aufgrund ihrer Interdisziplinarität und vielfältigen Anwendungsmöglichkeiten haben sie sowohl in der Wissenschaft als auch in der Industrie zunehmend an Bedeutung gewonnen. Ihre Zellmorphologie wird in erster Linie durch die Wechselwirkungen zwischen technischen Prozessparametern und inhärenten molekularen Eigenschaften der Polymerschmelze bestimmt. Nur wenige Studien haben sich mit dem Einfluss der molekularen Eigenschaften befasst, da sich die überwiegende Mehrheit auf Schäumungstechniken und Prozessbedingungen bezieht. Diese Studien basieren zudem häufig auf industriell gefertigten Polymeren mit unbekannter Topologie oder teilkristallinen Polymeren, was die Differenzierung von simultan auftretenden Effekten erschwert. Um diese Herausforderung zu analysieren, zielt die Dissertation darauf ab, den Einfluss intrinsischer molekularer Polymereigenschaften auf die drei Phasen des physikalischen Schäumens zu untersuchen: Zellnukleierung, Wachstum und Stabilisierung. Die essenziellen, amorphen Homo- und Blockcopolymere mit definierten molekularen Eigenschaften einschließlich Molekulargewicht, Blockordnung und Verzweigungen werden mittels lebender anionischer Polymerisation synthetisiert. Darüber hinaus sollen die erzielten Ergebnisse das Verständnis der Beziehung zwischen intrinsischen molekularen Parametern und makroskopischer zellulärer Morphologie erweitern. Die untersuchten Polymermodelle ermöglichten die Herstellung von Schäumen mit Volumenausdehnungsverhältnissen zwischen  $VER = 1.5 - 16.0$ , mittleren Zellgrößen von  $D = 0.39 - 17.21 \mu\text{m}$  und Zelldichten von  $N = 5.53 \times 10^9 - 2.07 \times 10^{13} \text{ Zellen cm}^{-3}$ , geschäumt mit  $\text{scCO}_2$  bei einem Druck von  $p = 500 \text{ bar}$ , einer Druckentspannungsrate von  $dp/dt \approx 200 \text{ bar s}^{-1}$  und Temperaturen im Bereich von  $T_f = 60 - 150 \text{ }^\circ\text{C}$ . Dabei erwiesen sich die folgenden Zusammenhänge als besonders bedeutsam: (I) Die heterogene Keimbildung wurde durch phasenseparierte Blockcopolymere mit heterogener Kettenbeweglichkeit oder Treibmittellöslichkeit unterstützt. Heterogene Nukleierung führte zu erhöhten  $N$ - und  $D$ -Werten bis in den Nanometerbereich, unter Ausbildung sphärischer Microdomänen, die den höchsten Anteil an Grenzflächen aufweisen. (II) Verzweigte Polymere mit variabler Topologie verbesserten die Schmelzfestigkeit der Polymere und damit die Schaumexpansion, indem sie die Scherviskosität reduzierten und die Dehnbarkeit steigerten. Durch die Untersuchung des Zusammenhangs zwischen molekularer Topologie, linearen und nicht-linearen rheologischen Eigenschaften und zellulärer Morphologie wurde eine optimierte Struktur-Eigenschafts-Beziehung zur Maximierung von  $VER$  und  $D$  durch Minimierung der Zellkoaleszenz ermittelt.

(III) Polymere mit unterschiedlicher molekularer Dynamik, ermöglichten die Steuerung der Verglasung des Polymers. Bei gleichen Schäumungsbedingungen führte eine erhöhte Glasübergangstemperatur  $T_g$  letztlich zu kleineren  $D$ . Die umfassende Untersuchung des Einflusses verschiedener und unabhängig voneinander untersuchter Parameter wie Morphologie, Topologie und molekulare Dynamik kann die Entwicklung von Polymerschäumen mit gewünschten Zellmorphologien unterstützen.



## ACKNOWLEDGMENTS

Firstly, my enduring gratitude is dedicated to my academic supervisor, Prof. Dr. Manfred Wilhelm, for his constant guidance, valuable support, and encouragement throughout this dissertation. Especially, I am grateful for his enthusiasm, immense knowledge, constructive criticism, and intellectual stimulation related to my topic. I immeasurably appreciate Dr. Valerian Hirschberg and Dr. Lorenz Faust for their enthusiastic assistance, insightful inputs, and continuous support at every stage of the research.

I am genuinely grateful to have had the pleasure of working with Prof. Dr. Chul B. Park (Microcellular Plastics Manufacturing Laboratory, University of Toronto, Canada) and his employee Dr. Andrew Anstey, gaining new insights into polymer characteristics, especially their foaming behavior. Both deserved my sincere gratitude and appreciation. In this regard, I give special thanks to the Karlsruhe House of Young Scientists for funding my research visit at the University of Toronto.

My sincere thanks to Max G. Schußmann, Anika Goecke, and Leonardo Rocha Dias for their incredible effort in the laboratory during their theses and Ingrid Zeller for her assistance regarding SEM imaging. I also gratefully acknowledge the provision of nucleation particles by Prof. Dr. Claus Feldmann (Institute of Inorganic Chemistry, KIT) and his employee Mark Rutschmann. Prof. Patrick Théato (Institute for Chemical Technology and Polymer Chemistry, KIT) is especially thanked for co-examining the dissertation and his employee Dr. Stefan Frech is thanked for providing TGA measurements. Heartfelt thanks to Maxi Hoffmann for our continuous exchange of ideas and fruitful discussions. Lastly, I owe a huge thanks to all members of the Polymeric Materials group for creating such an incredible working environment and team spirit.



# CONTENTS

PART I INTRODUCTION AND FUNDAMENTALS .....	1
1 OUTLINE AND OBJECTIVES.....	3
2 POLYMER FOAMS .....	7
2.1 CLASSIFICATION, APPLICATION, AND FOAMING METHODS.....	7
2.2 STAGES OF THE ONE-BATCH PHYSICAL FOAMING PROCESS....	9
3 RHEOLOGY OF POLYMER MELTS.....	19
3.1 SHEAR RHEOLOGY.....	19
3.2 ELONGATIONAL RHEOLOGY .....	26
3.3 POLYMER DYNAMICS AND MOLECULAR CONSTITUTIVE EQUATIONS .....	30
4 LIVING ANIONIC POLYMERIZATION.....	33
4.1 FUNDAMENTALS .....	33
4.2 BLOCK COPOLYMERS .....	38
4.3 POLYMER TOPOLOGY .....	40
PART II RESULTS AND DISCUSSION.....	43
5 CELL NUCLEATION.....	45
5.1 SUITABILITY OF PHASE BOUNDARIES AS NUCLEATION CENTERS .....	47
5.2 HETEROGENEOUS GAS SOLUBILITY VS. CHAIN MOBILITY .....	57
5.3 INTRINSIC AND EXTRINSIC HETEROGENEOUS NUCLEATION..	61
6 CELL GROWTH.....	65
6.1 THE POM-POM TOPOLOGY.....	67
6.2 THREADING POLYSTYRENE STARS ALONG A CHAIN.....	87
7 CELL STABILIZATION.....	97
8 CONCLUSION AND OUTLOOK.....	103
PART III APPENDIX.....	109
9 REFERENCES.....	133



---

PART I

INTRODUCTION AND FUNDAMENTALS



---

## 1 OUTLINE AND OBJECTIVES

The increased focus on sustainability combined with the increasing use of plastic products has created a demand for materials with even lower densities while yet maintaining sufficient mechanical solid or insulation properties to save energy and, ultimately, raw materials, e.g., in lightweight constructions, aircraft, and automotive parts, or thermal insulations.<sup>1-8</sup> These requirements are often met with porous structures, such as polymer-based foams.

Polymeric foams are complex systems with a vast number of adjustable properties, i.e., lightweight and good thermal insulation; thus, they have drawn increasing interest in both academia and industry.<sup>1-8</sup> Their diversity is based on their unique physical, mechanical, and thermal properties, arising mainly from their versatile cell structure. One of the most common techniques for producing porous polymer foams is the physical batch foaming with supercritical carbon dioxide (scCO<sub>2</sub>) as a blowing agent. The foaming process can be divided into three key stages: cell nucleation, growth, and stabilization. Within these stages, the following physical properties exert a particular influence on the resulting cellular morphology: solubility, diffusivity, interfacial tension, shear viscosity, elongational melt strength, and the related molecular dynamics. The complexity increases even more when the dependency of these parameters on temperature, pressure, and CO<sub>2</sub>-concentration is considered. Therefore, studies to understand the fundamental molecular principles governing the physical foaming process are necessary to design cellular morphology and facilitate product control.

However, despite numerous studies, the correlation of influencing molecular variables on the final foam morphology and properties has not been fully elucidated yet. There is a need for fundamental studies of the influence of intrinsic molecular polymer properties on cellular morphology, as most studies in the literature refer only to foaming techniques and process conditions. Nevertheless, a few studies address the influence of polymer molecular properties.<sup>9-14</sup> However, they are often based on industrial samples with unknown topology or do not separate correlated effects of topology and crystallinity. Therefore, tailor-made amorphous polymers are essential to study the structure-property relationship from the molecular to the macroscopic level. While this can only be realized using a highly controllable synthesis route, such as living anionic polymerization (LAP). Living anionic polymerization is a technique that allows a high control over molecular properties such as molecular weight, narrow molecular weight distribution (dispersity), and polymer topology, thus studying their specific influence on the resulting cellular structure.

This dissertation aims to investigate the structure-property relationship of three key intrinsic molecular polymer properties on the cellular structure based on well-defined, self-synthesized polystyrene (PS) model systems, with emphasis on the following aspects:

1. Morphology (Nucleation): Phase separating block copolymers exhibit intrinsic nucleation superior to homopolymers. By synthesizing systematically varied block copolymers, the effect of heterogeneity in blowing agent solubility, the limitation of chain mobility, and the benefit of phase boundaries are studied. Additionally, a comparison of intrinsically and extrinsically promoted heterogeneous nucleation is drawn.
2. Branching (Expansion): Polymer topology determines the shear and elongational rheological properties of the polymer melt, and thus, the expansion process. By systematically varying the topology, the influence of rheological properties such as shear viscosity, elongational viscosity, and strain hardening behavior are investigated and correlated with the foam expansion.
3. Molecular dynamics (Stabilization): Foam stabilization is determined by the polymer mobility and the type and proportion of the blowing agent. Specially synthesized homopolymers with a different glass transition temperature  $T_g$  but identical blowing agent solubility are used to separate different influencing parameters.

The results obtained within this dissertation will allow the tailoring of cell morphology by adjusting the intrinsic molecular polymer properties, thus, significantly simplifying the application-specific adaptation of the manufacturing process.

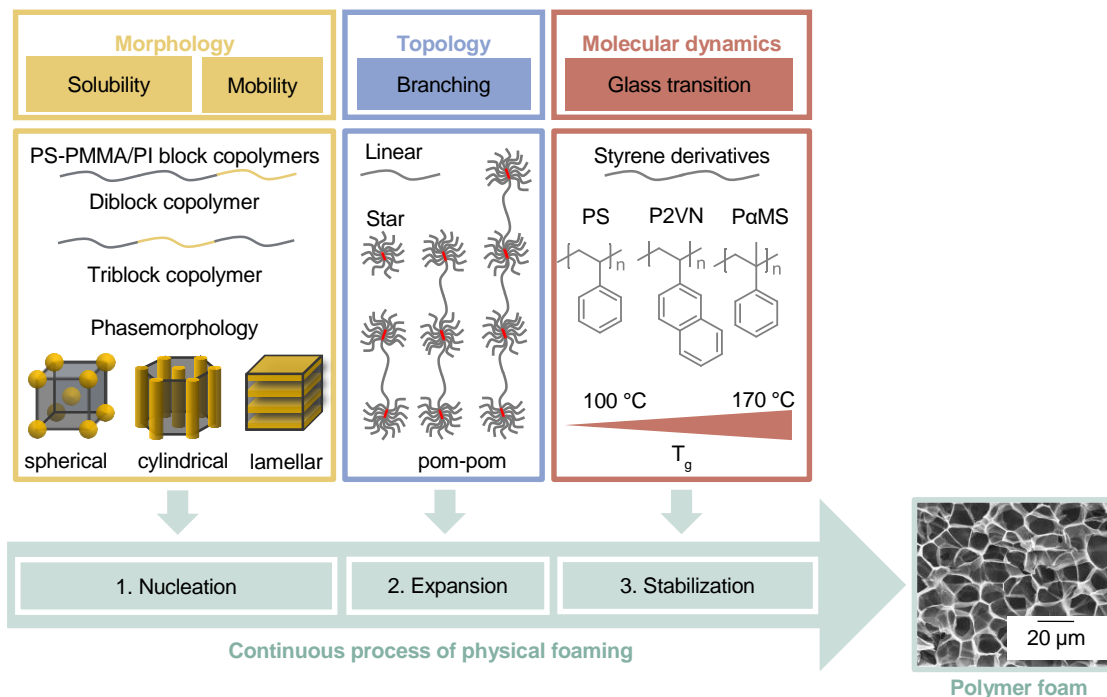


Figure 1.1. Dissertation outline: Investigation of the three stages of physical polymer foaming: (1) nucleation, (2) expansion, and (3) stabilization using well-defined, tailor-made polymer model systems synthesized by living anionic polymerization.



---

The outline of the dissertation is as follows:

Chapter 2 reviews the current data on polymer foams and introduces their fundamentals, including classification and historical perspectives on the research. Particular attention is paid to physical batch foaming and its underlying stages: cell nucleation, growth, and stabilization, while addressing influencing parameters such as process conditions and polymer properties.

Chapter 3 introduces linear shear and nonlinear elongational rheology of polymer melts. Fundamental rheological principles covering small-amplitude oscillatory shear and uniaxial elongation measurements will be discussed. Moreover, constitutive models like Doi-Edwards, molecular stress function (MSF), and pom-pom model will be explained.

Chapter 4 summarizes the general concept of the living anionic polymerization of homo- and block copolymers. In particular, the assumptions and kinetics of initiation, propagation, termination, and side reactions will be presented. Essential molecular parameters used throughout this dissertation will be introduced, such as molecular weight, dispersity, block copolymers, and topology.

Chapter 5 discusses the effect of present phase boundaries within the polymer matrix on cell nucleation. Particular attention is devoted to the morphology of self-assembled block copolymers with either different chain mobility or CO<sub>2</sub>-solubility, and the associated influence on cell density. The intrinsic nucleation in phase separated block copolymers is compared with extrinsically enhanced nucleation-based on the addition of SiO<sub>2</sub>-particles.

Chapter 6 explores the influence of defined polymer topology on the cell growth stage. Topological parameters and underlying melt rheological behavior will be discussed, especially zero-shear viscosity and strain hardening. This chapter concludes with the correlation of polymer topology, melt rheological properties, and resulting cell morphology of corresponding foams. Predominantly the impact on volume expansion, average cell size, and cell wall thickness will be demonstrated.

Chapter 7 elucidates the use of polymers with different molecular dynamics to manipulate foam stabilization by controlling the vitrification of the polymer matrix.



---

## 2 POLYMER FOAMS

Polymer foams are one of the most prominent representative solid cellular materials, with a global market share of about 123 billion USD in 2021.<sup>15</sup> The major market segments are divided into three sectors: First, the building and construction business with ~30 vol%, second, the automotive industry with ~20 vol%, and third, the packaging business with ~15 vol%. The residual 35 vol% is divided into furniture and bedding, rail, wind marine, and others. Polyurethane (PU) foams account for over 50 vol% of matrix materials established on the foam market. Polystyrene (PS) foams are the second largest segment with around 32 vol% (expanded polystyrene EPS and extruded polystyrene XPS), followed by polyolefin (PO), phenolic and polyvinyl chloride (PVC) foams.<sup>15</sup>

The chapter introduces polymers foams, their applications, and foaming methods. Essential structural and morphological criteria specifying the properties of polymer foams are summarized. Particular emphasis is put on the physical foaming procedure with supercritical carbon dioxide as a foaming agent. The underlying physical principles of the three foaming stages, i.e., cell nucleation, cell growth, and cell stabilization, will be discussed.

### 2.1 CLASSIFICATION, APPLICATION, AND FOAMING METHODS

Polymer foams are two-phase systems of distributed gas bubbles in a cellular polymer matrix. In 1981, Martini et al.<sup>16–18</sup> first developed the microcellular foaming of amorphous polymers with a physical blowing agent, like supercritical carbon dioxide (scCO<sub>2</sub>) or nitrogen (N<sub>2</sub>). Based on his findings, two main production routes have emerged: batch and continuous extrusion foaming. While Martini<sup>16</sup>, Waldman<sup>19</sup>, and Colton<sup>20</sup> performed initial work on batch foaming, Baldwin<sup>21</sup> and Park<sup>22</sup> established continuous extrusion foaming preliminary. Nowadays, both methods have become commercially relevant and are still of utmost importance for academics and industry due to the challenging foamability control but interdisciplinary nature and numerous application possibilities of polymer foams.

The basic description of the polymer framework structure originated in the pioneering work of William Thomson in 1887.<sup>23</sup> He postulated that the polygonal cell morphology of all kinds of foams is disorganized, composed of vertices, edges, and faces, and the cells distribute in size. He hypothesized a tetrakaidekahedron structure with six cut corners and eight hexagonal and six square surfaces that are slightly curved, resulting in 14 adjacent cells, that maximizes volume while minimizing the surface area.<sup>23</sup> Only more than a century later, in 1994, a foam structure with a lower surface area of 0.3 % was proposed by Weaire and Phelan.<sup>24</sup> The framework comprised a regular arrangement of deformed dodecahedrons and irregular tetradecahedrons with an average of 13.5 adjacent cells.<sup>25</sup>

Meanwhile, structural analyses revealed that foams are based on 55 – 65 % pentagonal, 20 % hexagonal, and 10 – 24 % quadratic faces, which is regarded as the best approximation of foam architecture to date. For instance, whereas soap bubbles have, on average, 14 neighboring cells, polyurethane (PU) based cells are surrounded mainly by 13 cells.<sup>7</sup> Both postulated foam structures are visualized in Figure 2.1.

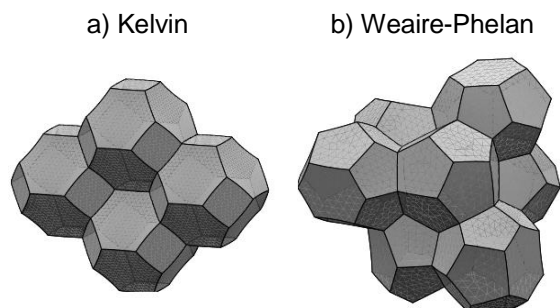


Figure 2.1. a) Tetrakaidekahedron structure of four cells of the Kelvin foam, resulting in a total of 14 neighboring cells. b) Eight cells, distorted dodecahedrons, and irregular tetradecahedrons form the Weaire-Phelan foam. This fundamental unit, on average, 13.5 neighboring cells, lowers the surface by 0.3 % (adapted and modified from literature<sup>26</sup>).

The techniques used to produce polymer-based foams have also evolved. They include numerous variants of discontinuous, semi-continuous, or continuous chemical, and physical foaming besides using templates or phase separation.<sup>1–6,27–34</sup> An excellent method for physically foaming with a blowing agent, e.g., supercritical carbon dioxide ( $\text{scCO}_2$ ), is the one-batch process in an autoclave, mainly used in research for modeling the foaming behavior of, e.g., amorphous polymers such as PS. For instance, the cellular morphology of a neat polymer foamed in a one-batch physical foaming process is often adjusted by the foaming conditions, such as the saturation pressure, temperature, and depressurization rate. While higher pressures typically led to smaller cells and a narrower cell size distribution, higher temperatures provided larger cells with broader distributions.<sup>35</sup> Increasing the depressurization rate leads to forming smaller cells and results in higher foam densities.<sup>36,37</sup> The underlying physical justifications are explained in Chapter 2.2.

Depending on the application, the foam properties' requirements differ. Essential parameters for describing the foam properties are the basic foam structure (open- or closed-pored) and their cellular morphology. The cell structure of open-cell foams is interconnected to their adjacent cells, which leads to a high material porosity, permeability to gases or liquids, and, depending on the matrix, high flexibility. They are typically used as membranes, sponges, or cushions/mattresses. In contrast, the cells in closed-cell foams are separated from their neighbors by a thin, surrounding cell wall. Their main properties provide high dimensional stability and good mechanical and thermal insulation properties while maintaining a low material density, making them ideal candidates for lightweight constructions and insulations. Figure 2.2 displays open-cell (a) and closed-cell foam (b).

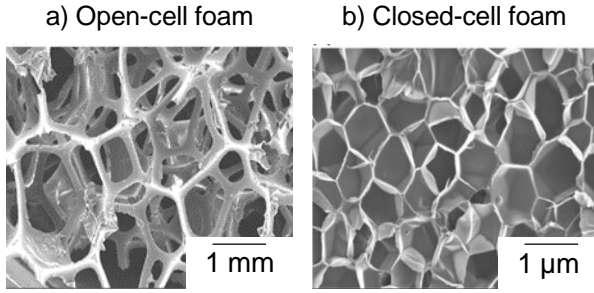


Figure 2.2. Examples of the two basic foam structures: Open- (a) and closed-cell foam (b). Open-cell foams can be found in membranes, sponged, or cushions/mattresses. Closed-cell foams are used for lightweight constructions or insulations (adapted and updated from literature<sup>34</sup>).

The cell morphology is typically characterized by four different parameters: the volume expansion ratio  $VER$ , the foam density  $\rho_f$ , the average inner cell size  $D$  without the thickness of the cell walls  $d$ , and the cell density  $N$ . According to these criteria, foams can be divided into subclasses, summarized in Table 2.1. In the 1980s, the first investigations on microcellular foams revealed that foams with more delicate cellular structures exhibit superior properties.<sup>16</sup> For instance, higher impact strength, toughness, stiffness-to-weight ratio, or fatigue life can be achieved with decreasing cell size, and thus, increasing cell density. The properties can be even more tuned by using a nanocellular cell morphology, which has excellent heat insulators properties due to a diffusive phenomenon, the so-called Knudsen-effect.<sup>34,38,39</sup> The Knudsen-effect refers to a more frequent collision of gas molecules with cell walls than other gas molecules and occurs if the cell sizes are only around the mean free path of gas molecules of approximately 70 nm.

Table 2.1. Characteristics of different foam types according to their cell morphology.<sup>2</sup>

Cell morphology	$D$ [ $\mu\text{m}$ ]	$N$ [ $\text{cell cm}^{-3}$ ]	Description	$\rho_f$ [ $\text{g cm}^{-3}$ ]	$VER$
Macrocellular	$> 300$	$< 10^6$	Very low-density	$< 0.025$	$> 40$
Fine cellular	$10 - 300$	$10^6 - 10^9$	Low-density	$0.1 - 0.025$	$10 - 40$
Microcellular	$0.1 - 10$	$10^9 - 10^{12}$	Medium-density	$0.25 - 0.1$	$4 - 10$
Nanocellular	$< 0.1$	$> 10^{13}$	High-density	$> 0.25$	$< 4$

The foaming method, the selected process parameters, and the intrinsic molecular polymer properties, i.e., their molecular structure, composition, and dynamics, influence the cell morphology. Consequently, carefully selecting their parameters determines the achievable performance of foams. The parameters and their influence will be revisited and explained in Chapter 2.2, introducing the stages of the physical foaming process.

## 2.2 STAGES OF THE ONE-BATCH PHYSICAL FOAMING PROCESS

The one-batch physical foaming process consists of four main stages: polymers' saturation with a blowing agent, cell nucleation, growth, and stabilization, as shown in Figure 2.3. Within the physical foaming process, the polymers are first placed in an autoclave and then saturated with the blowing agent under defined conditions, i.e., temperature, pressure, and duration time, to achieve a single-phase polymer/gas solution.

The polymers' saturation and sorption with the blowing agent occur at supercritical conditions as the solubility increases enormously, improving the homogenization of the polymer/gas mixture and the overall uptake.<sup>5</sup> For instance, the critical point of carbon dioxide is at a critical temperature of  $T_c = 31.1$  °C and a critical pressure of  $p_c = 73.8$  bar.<sup>40</sup> Supercritical carbon dioxide, also established in industrial processes, is particularly suitable as an inert, non-toxic, non-flammable, reusable, and environmentally friendly blowing agent compared to the discredited ozone-destroying fluorochlorinated hydrocarbons.<sup>41</sup> Furthermore, it can diffuse thoroughly into most polymers due to its low surface tension<sup>42</sup>, even though most polymers show a rather poor solubility under readily achievable conditions, except fluoropolymer and polysiloxane<sup>43</sup>.

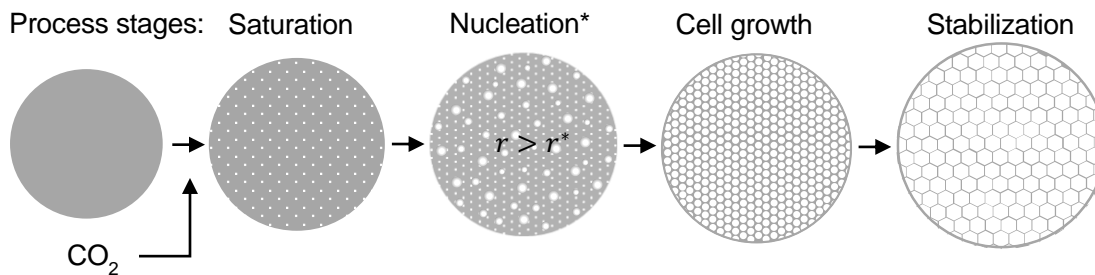


Figure 2.3. Scheme of the physical foaming process with its four stages, i.e., saturation, nucleation, growth, and stabilization. \*To illustrate the process, the CO<sub>2</sub>-cells are shown oversized concerning the polymer matrix in the nucleation stage.

During the saturation stage, CO<sub>2</sub> plasticizes the polymer by reducing the polymer-polymer interactions. Therefore, the glass transition temperature  $T_g$  decreases to the effective glass transition temperature  $T_{g,eff}$  with increasing CO<sub>2</sub>-content in the polymer melt.<sup>44-46</sup> The plasticization of several polymers, including poly(lactic acid) (PLA)<sup>47,48</sup>, poly(methyl methacrylate) (PMMA)<sup>49</sup>, isotactic polypropylene (*i*-PP)<sup>50</sup>, polycarbonate (PC)<sup>51</sup>, low-density polyethylene (LDPE)<sup>50</sup>, poly(ethylene terephthalate) (PET)<sup>52</sup>, polyvinyl chloride (PVC)<sup>52</sup>, polyisoprene (PI)<sup>53</sup> and polystyrene (PS)<sup>54</sup> have been reported.<sup>55</sup> For instance, the solubility of scCO<sub>2</sub> in PS at 180 bar and 125 °C – 145 °C is 9 g CO<sub>2</sub>/100 g PS, accompanying by a reduction of 55 °C in  $T_g$  from 100 °C to approximately 45 °C.<sup>53,56-58</sup> In the nucleation stage, the phase separation is triggered by inducing thermodynamic instabilities, e.g., via a subsequently abrupt pressure drop. The CO<sub>2</sub> begins to phase separate from the polymer, and thermodynamic fluctuations lead to the formation of gas clusters, i.e., cells. A concentration gradient of CO<sub>2</sub> drives cell growth by diffusion to the generated nuclei. Depending on whether their size exceeds or falls below the so-called critical radius  $r^*$ , these newly generated cells can either expand or decay at the microscopic level.<sup>59,60</sup> The critical radius represents the minimum size a cell has to overcome to grow spontaneously, resulting in a thermodynamically stable cell that does not collapse until the foam stabilizes.<sup>3,61</sup>

The critical radius  $r^*$  is defined as

$$r^* = \frac{2\gamma_{lg}}{p_{\text{cell}} - p_{\text{atm}}} = \frac{2\gamma_{lg}}{\Delta p}, \quad (2.1)$$

where  $\gamma_{lg}$  is the interfacial tension at the polymer/gas interface,  $p_{\text{cell}}$  is the hypothetical pressure inside the nucleated cell, and  $p_{\text{atm}}$  is the atmospheric pressure.

For instance,  $r^*$  is approximately 3 nm for  $\Delta p = 180$  bar and  $\gamma_{lg} = 27 \times 10^{-3}$  N m<sup>-1</sup> for PS-CO<sub>2</sub><sup>62</sup>. A spherical cell with  $r^* = 3$  nm contains only about 300 CO<sub>2</sub> molecules at 180 bar and a temperature between 125 °C – 145 °C.<sup>32</sup> After the nucleation of cells, the residual dissolved gas will either participate in further nucleation or diffuse into previously nucleated cells, resulting in a competition between cell nucleation and cell growth. The cells continue to expand and due to the phase separation of CO<sub>2</sub> and the polymer matrix  $T_{g,\text{eff}}$  of the polymer increases to  $T_g$ . As a consequence of the CO<sub>2</sub>-loss, the viscosity of the polymer increases rapidly, the cell walls vitrify, and the internal cell pressure is no longer sufficient for a further expansion of the cells. Hence, the mechanical stabilization of the foam occurs and the formed cellular structure reaches the thermodynamic equilibrium.<sup>3-6</sup> This effect can be enhanced by the onset of the cooling effect of the blowing agent expansion (Joule-Thomson-effect<sup>63</sup>) or external cooling. For amorphous polymers, the foam is significantly stabilized by reaching  $T_g$ . Consequently, the choice of polymer and the corresponding thermal properties can influence the occurrence of mechanical stabilization. Additionally, this means that foaming is only possible within a temperature range between  $T_{g,\text{eff}}$  and an upper-limit temperature  $T_{\text{max}}$ . In contrast,  $T_{\text{max}}$  reflects the temperature at which CO<sub>2</sub>-loss dominates by diffusion out of the polymer matrix, resulting in an imminent foam collapse. Between these limits, the cell density passes through a maximum due to two competing processes: first, cell nucleation and growth, and second, diffusion of CO<sub>2</sub> from the plasticized polymer matrix.<sup>64</sup> Due to this, the formation of smaller cells in a polymer with a higher  $T_g$  and therefore, higher  $T_{g,\text{eff}}$  is favored as long as both materials exhibit similar CO<sub>2</sub>-concentrations.<sup>65,66</sup> Another advantage of a higher  $T_g$  (or difference between room temperature and  $T_g$ ) is that the faster foam stabilization reduces cell coalescence, thus, maintaining higher nucleation densities.<sup>65,66</sup> Therefore, the molecular dynamics of a polymer, such as the  $T_g$ , represents an important parameter in controlling the foamability of polymers. The individual interrelationships are discussed in the following sections.

**SATURATION.** The polymer matrix consists of polymer chains with a random conformation. The random conformation creates free volume within the matrix into which molecules such as the blowing agent can diffuse. Achieving a homogeneous polymer/gas mixture is crucial to obtain foams with a uniform cell structure and desirable mechanical properties. Optimizing the processing parameters based on the diffusivity and solubility limit of the blowing agent in the polymer matrix can support the dissolution.

Solubility depends mainly on the type of polymer and gas, i.e., their affinity and interaction, as well as the ambient conditions, and is crucial regarding the physical foaming of thermoplastics.<sup>1,3-6,33,67</sup> A simple approach to quantify the solubility in first approximation provides Henry's law<sup>33,68</sup>, which expresses a linear dependence of the saturation concentration  $c$  (cm<sup>3</sup>/g) of the absorbate with increasing hydrostatic pressure  $p$  (Pa) in ideal systems,

$$c = K_H p, \quad (2.2)$$

with  $K_H$  as Henry's constant in (cm<sup>3</sup>[STP] g<sup>-1</sup> Pa<sup>-1</sup>). An Arrhenius approach describes the temperature dependence yielding to

$$K_H = K_{H,0} \exp\left(-\frac{\Delta H_L}{RT}\right), \quad (2.3)$$

where  $K_{H,0}$  (cm<sup>3</sup>[STP] g<sup>-1</sup> Pa<sup>-1</sup>) is the solubility coefficient constant,  $\Delta H_L$  (J) to the solution enthalpy,  $R$  (J K<sup>-1</sup>) to the universal gas constant, and  $T$  (K) to the temperature. Since the solution enthalpy of most polymer/gas combinations is negative, solubility decreases with increasing temperature, such as the solubility of CO<sub>2</sub> in PS. However, the solubility of nitrogen N<sub>2</sub> in PS increases with increasing temperature.<sup>33</sup> In general, the solubility rather increases concave (PS/CO<sub>2</sub>) or decreases convex (PS/N<sub>2</sub>) as the temperature rises, as shown in Figure 2.4.

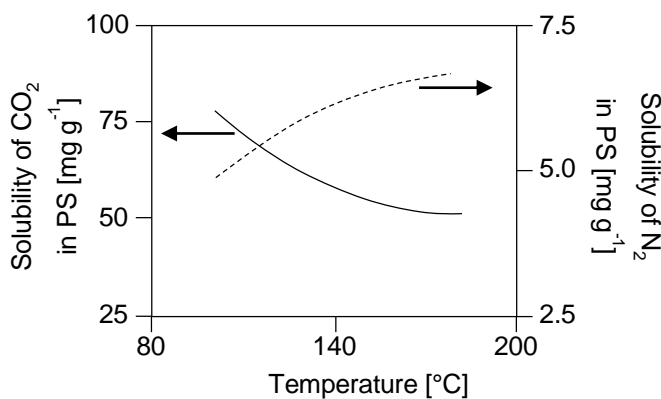


Figure 2.4. Comparison of the temperature-dependent solubility of carbon dioxide CO<sub>2</sub> and nitrogen N<sub>2</sub> in PS at a saturation pressure of about 120 bar. Adapted from literature.<sup>33</sup>

The CO<sub>2</sub>-affinity of PS is approximately one order of magnitude higher than N<sub>2</sub>-affinity. As a higher concentration of blowing agent results in a higher foam expansion and supports cell nucleation, CO<sub>2</sub> is typically preferred as a blowing agent.<sup>1,3-6,33</sup> With an increasing concentration of blowing agent, the  $T_g$  of the polymer matrix is reduced as the dissolved CO<sub>2</sub> molecules reduce the polymer-polymer interactions, thus acting as a plasticizer. At first approximation,  $T_g$  decreases linearly with increasing uptake of blowing agent.<sup>1,33,58,69</sup> Consequently, the viscosity of the polymer/gas mixture is reduced with an increasing amount of blowing agent.<sup>69</sup> To ensure maximum gas uptake, saturation should occur at the lowest possible  $T$  at a maximized pressure.



The sorption kinetic of the blowing agent inside the polymer matrix is subject to Fick's law, describing a diffusive mechanism. Both are affected by the polymers' rubbery or glassy state, crosslinks, crystallinity, plasticizers, or fillers. In the presence of crystallites or fillers, gas solubility diminishes and diffusive transport occurs solely in the amorphous fractions, as both act like a barrier.

While solubility describes the maximum quantity of gas that may dissolve in a polymer matrix, the sorption kinetics and diffusivity determine the time required for complete dissolution. Fick's law<sup>70,71</sup> describes the diffusive mechanism by

$$J = -D \frac{d\varphi}{dx}, \quad (2.4)$$

where  $J$  is the diffusion flux,  $D$  is the diffusion coefficient or diffusivity,  $\varphi$  is the concentration for ideal mixtures, and  $x$  is the position. It should be noted that  $D$  is also temperature-dependent and its rate decreases with decreasing  $T$  given by an Arrhenius approach

$$D = D_0 \exp\left(-\frac{\Delta E_D}{RT}\right), \quad (2.5)$$

where  $D_0$  ( $\text{cm}^2 \text{s}^{-1}$ ) is the maximum diffusion coefficient constant at infinite temperature and  $\Delta E_D$  (J) is the diffusion activation energy if  $T > T_g$ .<sup>70,71</sup>

According to Henry's<sup>68</sup> and Fick's law<sup>70,71</sup>, a compromise must be found between maximum gas absorption within an acceptable time frame. Influencing factors for blowing agent uptake include, for instance, the polymer melt dynamics (rubbery or glassy state), crosslinking, crystallinity, or the presence of additives, like fillers or additional plasticizers. As the diffusion only occurs in the amorphous phases, additives and crystallites prolong the diffusion process and, therefore, the saturation process until a homogenous polymer/gas mixture is obtained.<sup>1,3-6,33</sup> However, they can be beneficial for cell nucleation.

**CELL NUCLEATION.** Inducing a non-gradual thermodynamic instability in the saturated polymer/gas mixture causes cell nucleation. The most common physical ways to induce instabilities in a saturated system are a rapid temperature increase, a sudden pressure drop, or severe shearing. Consequently, the equilibrated mixture in the supersaturated stage is transferred into a metastable phase between the binodal and spinodal, tending to form a stable two-phase system consisting of a gaseous phase surrounded by the polymer matrix. This phenomenon is known as cell nucleation, a kinetic phenomenon fundamentally represented by the classical nucleation theory (CNT) and its subsequent revisions.<sup>4,61,72-76</sup>

The CNT was initially developed for liquid/gas systems to describe the minimum energy needed to overcome the free energy barrier for cell nucleation. The free energy  $\Delta G$  is defined as the sum of the volume fraction of the cells  $V_{\text{cell}}$  as a function of the pressure difference  $\Delta p$ , and the cell surface  $A_{\text{cell}}$  considering its surface energy  $\gamma_{\text{lg}}$

$$\Delta G = -V_{\text{cell}}\Delta p + A_{\text{cell}}\gamma_{\text{lg}}. \quad (2.6)$$

Presuming the phase separation forms a spherical cellular structure, as it minimizes  $\Delta G$ , and thus, supports the formation of cells, Equation (2.6) can be transformed to

$$\Delta G = -\frac{4}{3}\pi r^3 \Delta p + 4\pi r^2 \gamma_{\text{lg}}. \quad (2.7)$$

Differentiating Equation (2.7) with regard to  $r$  yields the critical radius  $r^*$ , according to Equation (2.1) and the Gibbs free energy for the nucleation of a critical nucleus.

The CNT distinguishes between two mechanisms: Homogeneous and heterogeneous nucleation.<sup>4,61,72-75</sup> Within homogeneous nucleation, cell formation occurs spontaneously and randomly without additives or other interfaces within the polymer. In heterogeneous nucleation, nucleation agents are added selectively and nucleation occurs at the phase boundary between two phases, e.g., nucleation agent and polymer melt. Two types of nucleation agents can be used: Inorganic particles or organic phases such as nanostructured polymers. The presence of nucleation agents lowers the surface tension, and thus, the Gibbs free energy barrier, which has to be overcome to form stable cells, as represented in Figure 2.5.

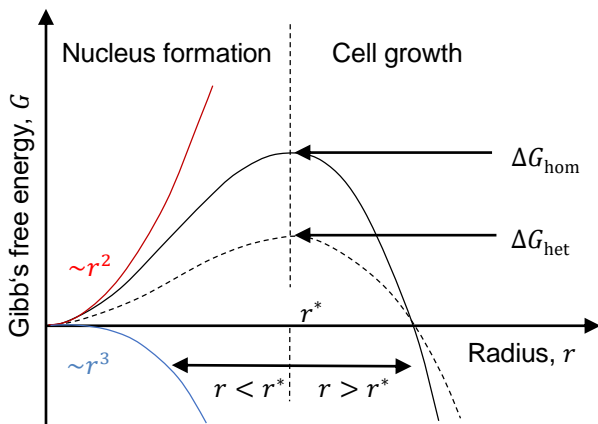


Figure 2.5. Dependency of cell nucleation and growth to Gibb's free energy barrier of homogeneous and heterogeneous nucleation ( $G_{\text{hom}}$ ,  $G_{\text{het}}$ ). By overcoming the corresponding free energy, stable cells with the radius  $r$  are formed, which continue to growth via  $\text{CO}_2$ -diffusion. Cells with  $r < r^*$  collapse and the  $\text{CO}_2$  lead to further growth of cells that have already exceeded  $r^*$ . The red line describes the surface term and the blue line is the volume term.

If the Gibb's free energy barrier of the homogeneous or heterogeneous nucleation ( $G_{\text{hom}}$ ,  $G_{\text{het}}$ ) is not overcome and  $r < r^*$ , the  $\text{CO}_2$  within the cells re-dissolve, thus, the formed cell will collapse. Thereby  $G_{\text{hom}}$  and  $G_{\text{het}}$  are given by

$$\Delta G_{\text{hom}} = \frac{16\pi\gamma_{\text{lg}}^3}{3\Delta p^2}, \quad (2.8)$$

$$\Delta G_{\text{het}} = \frac{16\pi\gamma_{\text{lg}}^3}{3\Delta p^2} F(\theta, \beta), \quad (2.9)$$

$$F(\theta, \beta) = \frac{1}{4} \left[ 2 - 2 \sin(\theta - \beta) + \frac{\cos(\theta) \cos^2(\theta - \beta)}{\sin(\beta)} \right], \quad (2.10)$$

where  $F(\theta, \beta)$  is a geometrical factor that relates to the nucleating agents' surface geometry,  $p_{\text{sys}}$  is the average system pressure,  $\Delta p_{\text{local}}$  is the local pressure variation,  $\theta$  is the contact angle of the polymer/additive/gas interface between  $0^\circ < \theta < 180^\circ$ , and  $\beta$  is the semi-conical angle cavities between  $0^\circ$  and  $90^\circ$ .

The principle of the contact angle is visualized in Figure 2.6.

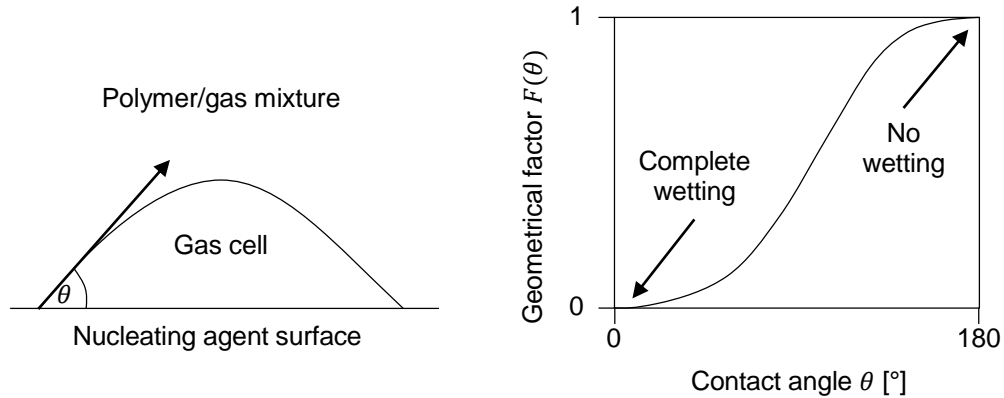


Figure 2.6. Heterogeneous nucleation occurs at the surface of a nucleating agent.

The contact angle depends on the interfacial energies within the polymer/gas mixture and is quantitatively described by Young's equation

$$\cos(\theta) = \frac{\gamma_s - \gamma_{sl}}{\gamma_l}, \quad (2.11)$$

where  $\gamma_s$  and  $\gamma_l$  are the surface energies of the solid nucleation agent and the liquid phase, respectively, and  $\gamma_{sl}$  the interfacial energy between both.<sup>77</sup> The homogeneous and heterogeneous nucleation rates  $J_{\text{hom}}$  and  $J_{\text{het}}$  are expressed as by

$$J_{\text{hom}} = N \sqrt{\frac{2\gamma_{lg}}{\pi m'}} \exp\left(-\frac{\Delta G_{\text{hom}}^*}{k_b T}\right), \quad J_{\text{het}} = N^{\frac{2}{3}} Q \sqrt{\frac{2\gamma_{lg}}{\pi m'}} \exp\left(-\frac{\Delta G_{\text{het}}^*}{k_b T}\right), \quad (2.12, 2.13)$$

where  $N$  is the number of gas molecules per unit volume polymer, also known as cell density,  $Q$  is the ratio of the surface area of a heterogeneously nucleated cell to that of a spherical cell with the same radius of curvature,  $m'$  is the mass of gas molecules, and  $k_b$  as Boltzmann constant.

**CELL GROWTH.** Once cells are nucleated and have reached the critical value, they continue to grow until they are either stabilized, e.g., by reaching  $T_g$  of the amorphous polymer matrix or ruptured by overstretching.<sup>1,3-6,33</sup> The cell growth depends on the pressure difference between the developing cell and the foaming autoclave, which drops exponentially to the atmospheric pressure due to the initiated depressurization. Moreover, the diffusion of the blowing agent molecules creates a concentration gradient within the polymer matrix and the blowing agents' plasticizing effect decreases. Simultaneously, the occurring Joule-Thomson-effect<sup>63</sup> drastically reduces the temperature. The occurring temperature loss can be calculated according to the Joule-Thomson coefficient<sup>78,79</sup>  $\mu$  with

$$\mu = \left(\frac{dT}{dp}\right)_h. \quad (2.14)$$

Therefore, the growing process has many variables influencing the polymers' rheological response to the deformation induced by expansion which strongly depends on the temperature and the plasticization of the polymer melt.

Effort has been dedicated to simulating cell growth. Theoretical models have progressed from a single cell surrounded by fluid with an infinite quantity of blowing agent available for its expansion to a cell model, where the melt is divided into equal and constant mass unit cells.<sup>80-83</sup> A comparison between the estimated values and the empirically observed cell growth rate confirmed the conclusion of the initial approximation.<sup>84,85</sup> For instance, using a high-speed camera allowed to study and pursue the nucleation and cell growth during a one-batch physical foaming experiment of PS with CO<sub>2</sub>. By comparing the experimental growth profiles to their simulation, they discovered that the cell model accurately predicted the behavior of cell growth.<sup>85</sup> Notably, the boundary condition of the cell model is that it is only valid during the initial stage of cell growth under isothermal conditions, where the Joule-Thomson-effect<sup>63</sup> is still negligible.

During cell growth, the polymer melt experiences deformation through biaxial elongation.<sup>59,60,86</sup> Initially, shear and elongational deformations dominate cell growth within the linear viscoelastic regime. As expansion increases and the cell wall thickness decreases accordingly, the upcoming deformations occur within the non-linear viscoelastic regime. Hence, non-linear biaxial elongational viscosity controls cell growth until the cell dimensions affect the neighbor cells' growth. At this stage, forces in shear and elongational melt flow simultaneously affect the deformations. Therefore, the dynamics of cell growth (biaxial deformation) are related to the pressure difference and melt rheological properties of the polymer/gas mixture. Consequently, the investigation of the polymer melts' viscosity (shear flow) and strain hardening behavior (uniaxial deformation, elongational flow) is of particular interest as soon as the foaming potential of polymers is concerned. According to the practicability and high reproducibility of uniaxial elongation experiments, the resulting data can be related to the foaming behavior as a prospective rheological fingerprint for the foamability of polymers. The relationship between biaxial and uniaxial deformation is introduced in Chapter 3.2.

**CELL STABILIZATION.** From cell growth to stabilization, the viscosity of the matrix continuously increases due to the phase separation of the polymer/gas mixture and the simultaneous changing thermal conditions decreasing the sample temperature. The upcoming internal cooling based on the gas expansion, i.e., Joule-Thomson-effect<sup>63</sup>, or an additional external cooling amplifies the viscosity increase. Foams based on amorphous polymers stabilize by reaching  $T_g$ , as the internal cell pressure is no longer sufficient for further cell expansion by deformation of the polymer cell walls; the polymer chains vitrify.<sup>1,3-6,33</sup>

If the cell growth surpasses the maximum tensile stress of the polymer, the cell walls rupture, decreasing the resulting cell density and increasing open-cell content. However, cell wall stability can be supported using strain hardening polymers as matrices or additives. As soon as the strain hardening phenomenon sets in, the elongational viscosity increases. Therefore, the  $\text{CO}_2$ -concentration within the polymer and its elongational viscosity impact the cell stabilization, as outlined in Figure 2.7.

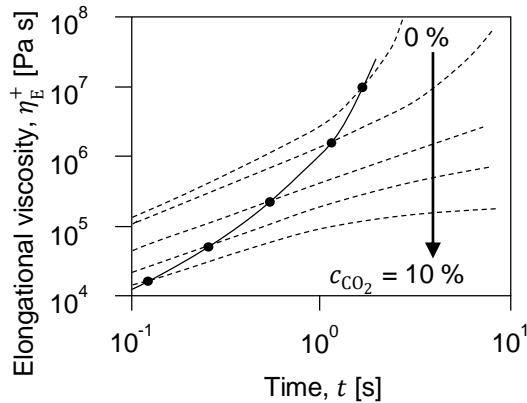


Figure 2.7. Illustration of the continuous increase of the elongational viscosity  $\eta_E^+$  of a PS melt due to the time-dependent loss of the blowing agent  $\text{CO}_2$ . The solid line represents the superposition effect of  $\text{CO}_2$ -loss, i.e., phase separation and onset of strain hardening as a function of time  $t$ . Adapted from literature.<sup>33</sup>

The gas's strong plasticization within the polymer has to be considered while addressing the glass transitional behavior. In a first approximation, the  $T_g$  decreases linearly with gas solubility.<sup>33,69</sup> However, several models exist to determine the  $T_g$ -reduction as a function of blowing agent solubility and the associated plasticization. For instance, the Chow equation<sup>58</sup> rather accurately describes the  $T_g$  as a function of carbon dioxide weight fraction in simple polymers. Further examples are the Cha-Yoon model<sup>87</sup> and the Condo-Sanchez model<sup>49</sup>. For further details, the reader is referred to the established literature.<sup>58,87,49</sup>



---

### 3 RHEOLOGY OF POLYMER MELTS

Rheology is a semi-quantitative tool in polymer science and engineering that permits the investigation of the structure-property relationship, and thus, the correlation of the macroscopic viscoelastic material response with the molecular chain dynamics under applied stress. To correlate and improve material properties, it is essential to comprehend the effect of molecular structure, such as chemical composition or topological parameters, on deformation behavior.<sup>88</sup> This chapter provides an overview of basic rheological concepts of melt flow. The fundamentals of polymer melts' shear and elongational flow, the underlying physical principles, and the essential consecutive equations are explained.

#### 3.1 SHEAR RHEOLOGY

Rheological measurements are performed to investigate and evaluate materials' deformation and flow behavior under applied forces.<sup>88-90</sup> The general properties vary from ideally viscous liquids to viscoelastic materials and ideally elastic solids. The viscoelastic properties range from fluids that exhibit elastic behavior under rapid deformation to solids that are deformable or flowable on long-time scales or under a sufficiently high applied force. The following basic rheological principles and models are introduced using a simple shear experiment of a polymer melt in a linear direction of motion, as outlined in Figure 3.1. Here, the upper plate with an area  $A$  is moved with a constantly applied shear force  $F$  over a distance  $s$ .

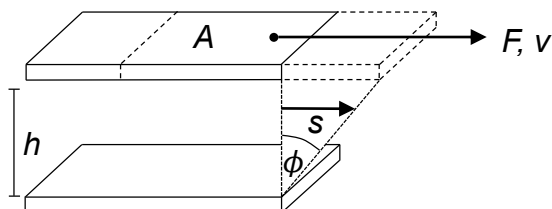


Figure 3.1. Graphical illustration of a simple shear experiment in a linear direction of motion. A material, e.g., a polymer melt, is placed between two parallel plates and deformed.<sup>91,92</sup>

The resulting shear stress  $\sigma$  can be expressed by

$$\sigma = \frac{F}{A}. \quad (3.1)$$

The deformation  $s$  normalized to the height  $h$  yields the shear strain  $\gamma$ , where, ideally, the same  $\gamma$  occurs within the whole material and independent of the plate distance  $h$  with

$$\gamma = \frac{s}{h}. \quad (3.2)$$

The velocity  $v$  of the sheared samples is dependent on  $h$ , yielding to the shear rate  $\dot{\gamma}$ , which can be described as constant  $v$  normalized to  $h$  by

$$\dot{\gamma} = \frac{1}{h} \frac{ds}{dt} = \frac{dv}{dt} = \frac{v}{h}. \quad (3.3)$$

Most common experiments to characterize the linear behavior of molten polymers, like its relaxation, are based on oscillatory shear and creep instead of the introduced linear movement. Consequently, the following section discusses the phenomenological models of oscillatory strain-stress response, i.e., Hooke's and Newton's laws.<sup>88–92</sup>

**ELASTICITY.** Hooke's law<sup>88–92</sup> describes ideal elastic deformation using a one-dimensional spring model, which states that the force  $F$  is proportional to the deformation  $x$ , as represented in Figure 3.2. Here, the material stress response  $\sigma$  is proportional to the shear deformation  $\gamma$  and can be expressed as

$$\sigma = G \gamma, \quad (3.4)$$

where  $G$  is the relaxation modulus, a material characteristic proportionality constant.

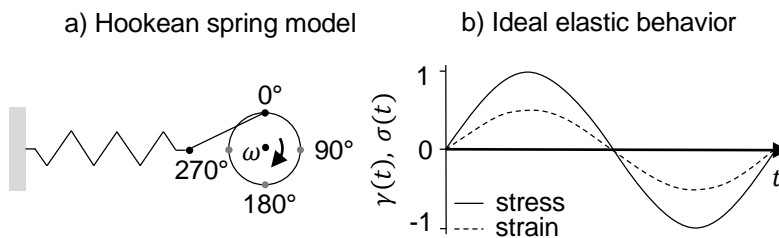


Figure 3.2. Schematic representation of the Hookean spring model (a) for ideal elastic solids, where the periodic excitation and response are in the same phase with a phase difference of  $\Delta\delta = 0^\circ$  (b).<sup>92</sup>

The sinusoidal deformation is performed over time  $t$  and with a maximum deformation amplitude  $\gamma_0$ , leading to

$$\gamma(t) = \gamma_0 \sin(\omega_1 t), \quad (3.5)$$

with  $\omega_1$  as the excitation frequency. The time-dependent stress  $\sigma(t)$  in phase with the deformation can be expressed by inserting Equation (3.5) in Equation (3.4), yielding to

$$\sigma(t) = G\gamma_0 \sin(\omega_1 t). \quad (3.6)$$

If  $\sigma(t)$  and  $\gamma(t)$  are sinusoidal and in phase, i.e.,  $\delta = 0^\circ$ , then  $G = \sigma(t)/\gamma(t) = \text{const.}$ , which represents ideal elastic deformation.

**VISCOSITY.** Newton's law<sup>88–92</sup> describes the ideal viscous matter by a linear dashpot model, where the force is proportional to the displacement. A plate is immersed in a Newtonian fluid to dissipate the upcoming energy and convert the viscous friction into heat, as introduced in Figure 3.3.

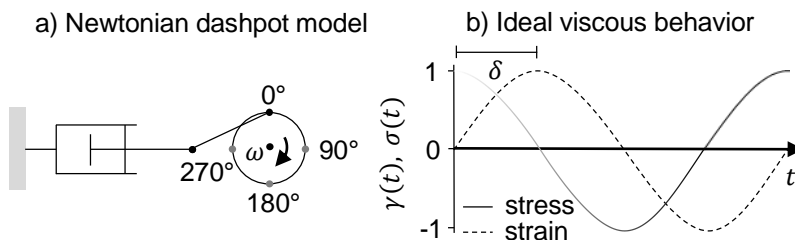


Figure 3.3. Schematic representation of the Newtonian dashpot model (a) for ideal viscous solids, where the periodic excitation and response exhibit a phase shift of  $\delta = 90^\circ$  (b).<sup>92</sup>



The proportionality of  $\sigma$  to the shear rate  $\dot{\gamma}$  is usually temperature dependent and as soon as the temperature is constant, the shear viscosity  $\eta$  becomes a material-specific property for low shear rates with

$$\sigma = \eta \dot{\gamma}, \quad (3.7)$$

while  $\dot{\gamma}$  (see Equation (3.3)) is given by the first derivative of the time-dependent deformation in oscillatory motion with

$$\dot{\gamma}(t) = \frac{d\gamma}{dt} = \gamma_0 \omega_1 \cos(\omega_1 t). \quad (3.8)$$

Combining  $\dot{\gamma}$  with Newton's law yields to the time-dependent shear stress  $\sigma(t)$  with

$$\sigma(t) = \eta \gamma_0 \omega_1 \cos(\omega_1 t + \delta) = \eta \gamma_0 \omega_1 \sin(\omega_1 t + 90^\circ), \quad (3.9)$$

if the sinusoidal deformation  $\sigma(t)$  has a  $90^\circ$  phase shift relative to  $\gamma$ .

**VISCOELASTICITY.** Ideal behavior, both elastic and viscous, is obtained only for a few materials and under limited shear conditions, as most materials, e.g., polymers, simultaneously display elastic and viscous responses. i.e., viscoelastic behavior or viscoelasticity.<sup>88–92</sup> Generally, viscoelasticity can be represented by either a parallel or a serial arrangement of the spring (Hookean) and dashpot (Newtonian) model and is accordingly known as the Kelvin-Voigt model or the Maxwell model, respectively, as outlined in Figure 3.4.

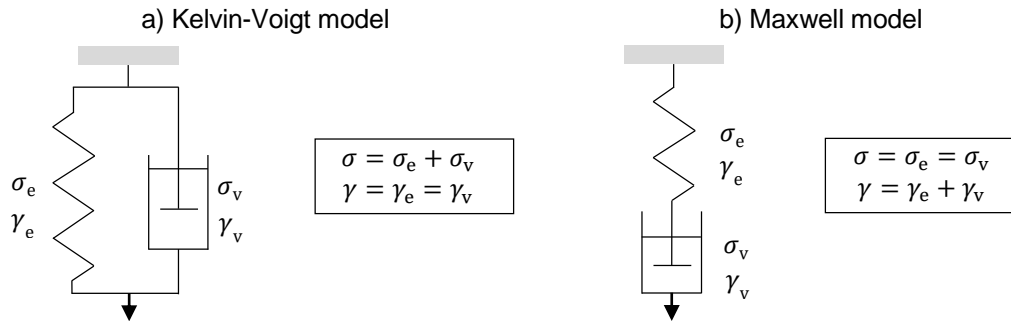


Figure 3.4. Schematic representation of viscoelastic response by combining Hooke's and Newton's law, i.e., spring and dashpot model, in a parallel or serial alignment. (a) Kelvin-Voigt model for elastic solids with low viscous part and (b) Maxwell model for viscous fluids with low elastic part.<sup>89</sup>

The Kelvin-Voigt model elucidates an elastic solid with a low viscous part by a parallel aligned spring and dashpot. Thereby, the spring describes the polymers' total relaxation after displacement in tension or shear, whereas the dashpot describes a time delay based on energy dissipation due to viscous friction. The overall stress  $\sigma$  is composed of the elastic stress of the spring  $\sigma_e$  and the viscous stress resulting from the dashpot  $\sigma_v$  with

$$\sigma = \sigma_e + \sigma_v. \quad (3.10)$$

The parallel arrangement results in the same  $\gamma$  and  $\dot{\gamma}$  for the elastic and viscous parts, so

$$\gamma = \gamma_e = \gamma_v \text{ and } \dot{\gamma} = \dot{\gamma}_e = \dot{\gamma}_v. \quad (3.11, 3.12)$$

Furthermore,  $\sigma$  may be described using Hooke's and Newtonian's law, leading to the following differential equation:

$$\sigma = \sigma_e + \sigma_v = G\gamma_e + \eta\dot{\gamma}_v = G\gamma + \eta\dot{\gamma}. \quad (3.13)$$

In contrast, the Maxwell model is applied to materials composed of a mainly viscous part with a low elastic proportion. The materials undergo plastic deformation under strain and can be described by a serial arrangement of a dashpot and a spring. It is valid for mono-disperse polymer melts at high temperatures, i.e., low frequencies. For instance, polymer melts behave like viscoelastic liquids at low shear rates. In the Maxwell model,  $\sigma$  is equally distributed over both the dashpot and the spring as

$$\sigma = \sigma_e = \sigma_v. \quad (3.14)$$

Thus,  $\gamma$  and  $\dot{\gamma}$  are composed of the sum of  $\gamma_e$  and  $\gamma_v$  or  $\dot{\gamma}_e$  and  $\dot{\gamma}_v$ , respectively, so

$$\gamma = \gamma_e + \gamma_v \text{ and } \dot{\gamma} = \dot{\gamma}_e + \dot{\gamma}_v. \quad (3.15, 3.16)$$

Inserting Hooke's and Newton's law in Equation (3.16) results in the following Maxwell's differential equation with

$$\dot{\gamma} = \dot{\gamma}_e + \dot{\gamma}_v = \frac{\sigma_v}{\eta} + \frac{\dot{\sigma}_e}{G} = \frac{\sigma}{\eta} + \frac{\dot{\sigma}}{G}. \quad (3.17)$$

However, with its single exponential stress relaxation, the Maxwell model only insufficiently describes the response of non-ideal materials like polymer melts. Disperse Polymers are governed by different molecular relaxation modes, leading to a more complex viscoelastic response within a broad spectrum of frequencies. Adjusting the Maxwell model by a theoretically infinite number of parallelly-connected Maxwell elements leads to the multi-mode Maxwell model.<sup>89</sup> The multi-mode Maxwell model is mathematically expressed by

$$G(t) = \sum_{i=1}^N g_i \exp\left(-\frac{t}{\tau_i}\right), \quad (3.18)$$

with  $N$  (discrete) exponential stress relaxations (number of Maxwell elements),  $g_i$  as partial moduli and  $\tau_i$  as relaxation time. Applying the relationship to linear viscoelastic constitutive equations, which will be introduced in the following section,  $g_i$  and  $\tau_i$  can be fitted to the oscillatory shear data resulting in the discrete relaxation spectrum<sup>93</sup> of the storage  $G'$  and loss modulus  $G''$  as follows:

$$G'(\omega) = \sum_{i=1}^N \frac{g_i(\omega\tau_i)^2}{1 + (\omega\tau_i)^2}, \quad (3.19)$$

$$G''(\omega) = \sum_{i=1}^N \frac{g_i(\omega\tau_i)}{1 + (\omega\tau_i)^2}. \quad (3.20)$$

LINEAR VISCOELASTIC BEHAVIOR. Small-amplitude oscillatory shear measurements are widely used to investigate the flow and deformation behavior of polymer melts. It enables to determine the linear viscoelastic properties, such as storage  $G'$  and loss modulus  $G''$ , describing the elastic and dissipating deformation energy, respectively. Moreover, the linear viscoelastic properties of the molten polymers are highly dependent on their chemical composition and molecular structure.<sup>88–92</sup> Furthermore, SAOS measurements can be used to study the relaxation behavior of the materials and provide molecular information like the mass average  $M_w$ , the entanglement molecular weight  $M_e$  and the dispersity  $\mathfrak{D}$ . The following sections will address and introduce the molecular parameters in detail.

In practice, oscillatory shear is a technique typically utilized to examine the viscoelastic properties of a molten polymer. These experiments yield  $G'$  and  $G''$  as a function of  $\omega$  and algorithms exist to convert the data into the relaxation modulus and corresponding relaxation spectrum. Time-temperature superposition (TTS) is occasionally exploited to extend the frequency range, enabling the determination of the relaxation spectrum.<sup>88–94</sup> The TTS principle will be discussed later in this chapter. In oscillatory shear experiments, samples undergo homogeneous deformation under sinusoidal shear strain or shear stress. In a controlled strain experiment, one induces a strain that resembles a sine wave described by

$$\gamma = \gamma_0 \sin(\omega t). \quad (3.21)$$

If the strain amplitude  $\gamma_0$  is small enough for the response to be linear, the resulting stress is sinusoidal and may be described by the stress amplitude  $\sigma_0$  and the phase shift  $\delta$ , usually known as the loss angle:

$$\sigma(t) = \sigma_0 \sin(\omega t + \delta). \quad (3.22)$$

As it is the case for any linear system in the frequency domain, the oscillatory shear test findings can be expressed in terms of a frequency-dependent amplitude ratio  $G_d \equiv \sigma_0/\gamma_0$  and phase shift  $\delta$ . While the function  $\delta(\omega)$  is occasionally used to describe the linear behavior of a melt, dynamic test results are often expressed as follows

$$\sigma(t) = \gamma_0 [G'(\omega) \sin(\omega t) + G''(\omega) \cos(\omega t)], \quad (3.23)$$

also known as the linear viscoelastic equation (LVE).

The quotient ratio of the viscous  $G''$  and elastic proportion  $G'$  represents the dissipation factor  $\tan(\delta)$ , where  $0^\circ \leq \delta \leq 90^\circ$ , as  $\tan(\delta)$  of polymeric melts with viscoelastic behavior ranges between ideal elastic ( $\tan(\delta) = 0$ ) and ideal viscous ( $\tan(\delta) = \infty$ ),

$$\tan(\delta) = \frac{G''}{G'}. \quad (3.24)$$

For high  $a_T \omega$  or long  $\tau$ , the storage modulus predominates. Within this regime, the polymer chains relieve the shear stress too slowly, and hence, follow the shear strain deformation without phase shift, resulting in an elastic behavior close to ideal.

By lowering  $\omega$  or shortening  $\tau$  due to an increase of  $T$  and the accompanying acceleration of the temperature-dependent relaxation dynamics, the viscous behavior becomes dominant. Consequently,  $G''$  has a higher contribution. A proportionality of  $G' \propto \omega^2$  and  $G'' \propto \omega^1$  may be found within this range. More details will be explained in the course of this chapter.

A principle widely used to extend the relaxation spectrum and examine the materials' viscoelasticity over a wide range of frequencies is called time-temperature superposition (TTS). Due to the same temperature dependence, the TTS principle states that the viscoelastic properties generated at different temperatures are equivalent to those generated over a broad time or frequency scale. Hence, every motion on a molecular or segmental level is subject to the same temperature-based influence. For instance, in dynamic testing, frequency sweep data collected under different temperature steps can be horizontally shifted along the x-axis, which is the frequency. After the selection of a reference temperature  $T_{\text{ref}}$ , the low-temperature data is shifted to high frequencies and vice versa, resulting in a master curve, as shown in Figure 3.5.

The underlying time-temperature dependency is given by the Williams-Landel-Ferry (WLF) equation<sup>95</sup>, as follows:

$$\log(a_T) = -\frac{C_1(T - T_{\text{ref}})}{C_2 + T - T_{\text{ref}}}, \quad (3.25)$$

with the horizontal shifting factor  $a_T$  and the empirical parameters  $C_1$  and  $C_2$ , where  $C_1 = 17.44$  and  $C_2 = 51.6$  K are typical values if  $T_{\text{ref}} = T_g$ . The vertical shift factor  $b_T$  compensates minor vertical differences by using the temperature-dependent polymer density  $\rho_p$  and is given by

$$b_T = \frac{T_0 \rho_0}{T \rho_p}. \quad (3.26)$$

According to the resulting master curve, specific polymer parameters such as  $M_e$  and the characteristic relaxation time  $\tau$  of polymer chain segments can be obtained. These parameters, the general molecular weight dependence and the plateau modulus are described in the following section by explaining the zones of the master curve, as shown in Figure 3.5.

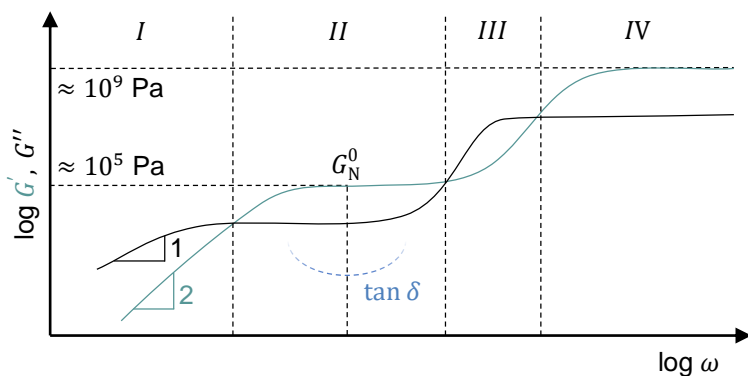


Figure 3.5. Frequency dependence of the shear moduli  $G'$  (green) and  $G''$  (black) of a linear monodisperse homopolymer melt and the four zones of the resulting master curve: (I) viscoelastic regime, (II) rubber plateau, (III) transition zone, and (IV) glass region.

Zone I represent the terminal regime, where  $G''(\omega) > G'(\omega)$ . The materials exhibit typical flow behavior with  $G' \propto \omega^2$  and  $G'' \propto \omega^1$  at low frequencies and can be described using the Maxwell model. As the frequency increases, the system is less and less able to dissipate the deformation energy by viscous flow. Instead, the system stores the energy, resulting in a sharper increase of  $G'$  compared to  $G''$  until the moduli intersect for the first time. The frequency-dependent moduli calculated by the Maxwell model are shown in Figure 3.6.

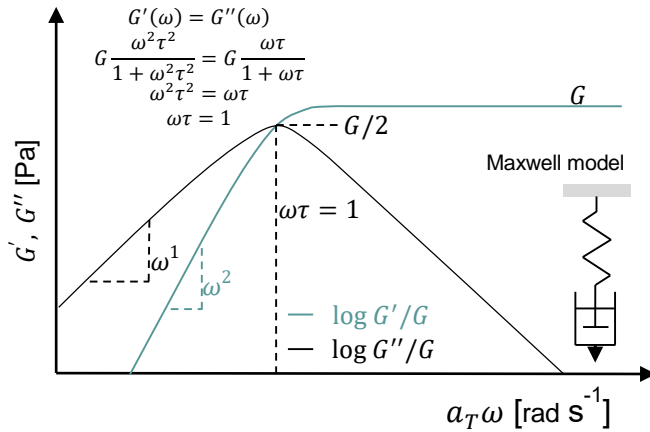


Figure 3.6. Frequency-dependent moduli calculated by the Maxwell model. On the left side of the cross over  $G' \propto \omega^2$  and  $G'' \propto \omega^1$ . The cross over indicates the longest relaxation time  $\tau_l$ .

Moreover, in the terminal regime, the viscosity of the polymer is shear rate independent, resulting in a Newtonian plateau. The corresponding viscosity is also designated as zero-shear viscosity  $\eta_0$  and can be determined according to the Cox-Merz rule<sup>96</sup>. The empirical relations proposed by Cox and Merz relate the frequency dependence of the dynamic complex viscosity to the shear-rate dependence of the steady state viscosity as follows:

$$|\eta_{(\omega)}^*| = \eta_{\dot{\gamma}=\omega}, \text{ so } \eta_0 = \lim_{\dot{\gamma} \rightarrow 0} \eta(\dot{\gamma}) = \lim_{\omega \rightarrow 0} |\eta_{(\omega)}^*|. \quad (3.27)$$

The  $\eta_0$  depends strongly on the molecular weight and follows characteristic scaling laws, summarized in Table 3.1.

Table 3.1. Scaling laws for the molecular weight dependence of the zero-shear viscosity  $\eta_0$  and related relaxation modes of a polymer with a weight average molecular weight of  $M_w$ .<sup>89,97</sup>

Molecular weight dependence	Scaling law	Dominant relaxation
$M_w < M_c$	$\eta_0 \propto M_w$	Rouse motion
$M_c < M_w < M_r$	$\eta_0 \propto M_w^{3.4}$	Reptation, Contour Length Fluctuation, Convective Constraint Release
$M_r < M_w$	$\eta_0 \propto M_w^3$	Pure reptation

$M_c$  as the critical molecular weight,  $M_c \approx 3M_e$ , and  $M_r$  with  $M_r \approx 15M_c$  for PS;  $M_{e,PS} \approx 16.8 \text{ kg mol}^{-1}$ .

The first cross over can be explained by the relaxation time using the reptation model, which states that a single polymer chain diffuses along its tube contour length. The overall time a polymer chain needs to diffuse once along its contour length is called the longest relaxation time  $\tau_l$ .

Hence,  $\tau_1$  can be estimated by the inverse of the frequency of the first cross over

$$\tau_1 = \frac{1}{\omega_1}. \quad (3.28)$$

In zone II, the storage modulus  $G'$  exhibits a plateau over a wide range of frequencies  $\omega$  called the rubber plateau. The deformation frequency is already too high to ensure complete relaxation of the overall polymer. Therefore, the entanglements of the polymer chains act like physical branching points. Only the chain segments between these physical branching points are relatively accessible for motion and capable of dissipating incoming energy, as elucidated by the theory of rubber elasticity. While the range of the rubber plateau depends on the molecular weight of the polymer, the plateau modulus  $G_N^0$  is proportional to the entanglement density of the polymer melt, and thus, a polymer-specific value. Therefore,  $G_N^0$  can be used to calculate the molecular weight between two physical entanglements, yielding the entanglement molecular weight  $M_e$ <sup>89</sup> by

$$M_e = \frac{4 \rho_p RT}{5 G_N^0}. \quad (3.29)$$

The prefactor derived from the consideration that 1/5 of the initial stress is already relaxed by fast Rouse motions.<sup>98,99</sup> With increasing  $M_e$ , the length between the entanglements within the polymer chain increases, and thus,  $M_e$  indicates the molecular stiffness of the polymer chains. The minimum number of entanglements needed to incorporate sufficient mechanical properties into a polymer is called the critical molecular weight  $M_c$ , which is typically three times  $M_e$ . If  $M_w < M_c$ , no rubber plateau occurs.

With increasing frequencies,  $G'(\omega)$  and  $G''(\omega)$  intersects a second time and both moduli rise relatively sharply over a short frequency range. In subsequent zone III, chain segment mobility decreases. The transition from rubber-elastic (transition zone) to glass occurs.

After the last crossing point of  $G'(\omega)$  and  $G''(\omega)$ , the moduli reach the glass zone (zone VI), where the polymer behaves like a classical solid: constant  $G'(\omega)$  and  $G''(\omega)$  values, indicating an almost purely elastic behavior. No viscous behavior occurs since the thermal energy is no longer sufficient to move entire chains against the Van-der-Waals binding energy between the individual polymer chains. The deformation energy is, therefore, elastically stored in small, local displacements of chain parts.

### 3.2 ELONGATIONAL RHEOLOGY

Non-linear behavior in elongational deformation provides structural information about polymers not revealed by linear shear data. It is particularly important in commercial polymer processing, like extrusion, injection, film blowing, or foaming. Therefore, comprehension of linear rheological parameters like zero-shear viscosity and non-linear rheological parameters such as elongational melt strength are essential.

While  $\eta_0$  can be determined by linear oscillatory shear measurements, the elongational melt strength can be investigated during non-linear elongation experiments. The principle of an uniaxial elongation experiment is that both ends of a sample with length  $L$  are attached to rotating drums. The sample is uniformly deformed along the axis  $x$  with a certain elongation rate, i.e., Hencky strain rate  $\dot{\varepsilon}_H$  (Equation (3.33)), and a constant velocity  $v_x$ ,

$$v_x = x\dot{\varepsilon}_H. \quad (3.30)$$

Consequently, the sample center remains stationary, but the sample ends distance increases continuously from  $L_0$  to  $L$ , i.e.,

$$v_{\text{end}} = \dot{\varepsilon}_H \frac{L}{2}, \quad \frac{dx}{dt} = \dot{\varepsilon}_H x, \quad (3.31, 3.32)$$

resulting in uniaxial deformation of the sample, as outlined in Figure 3.7.

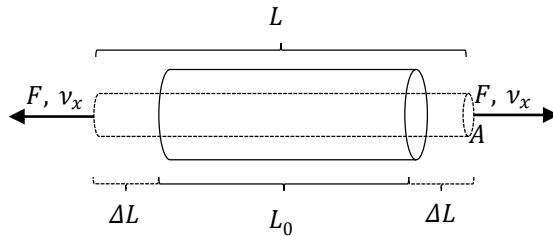


Figure 3.7. Transient elongation experiment of a cylindrical sample. The sample is uniformly deformed in  $x$  direction by  $2 \times \Delta L$  with a constant force  $F$  applied to both sample ends.<sup>90</sup>

The Integration of the overall length range, i.e.,  $2\Delta L$ , leads to the following relationship

$$\dot{\varepsilon}_H t = \varepsilon_H = \int_{L_0}^L \frac{1}{x} dx = \ln\left(\frac{L}{L_0}\right) \Leftrightarrow L = L_0 \exp(\dot{\varepsilon}_H t), \quad (3.33)$$

with  $\varepsilon_H$  as Hencky strain. Elongations of several hundred percent can arise during typical melt processing techniques, like the foaming of polymers, leading to  $\varepsilon_H \approx 2 - 3$ . However, only if the velocity increases exponentially, a constant  $\dot{\varepsilon}_H$  can be attained, as described by

$$v_{\text{end}} = \frac{1}{2} \dot{\varepsilon}_H L_0 \exp(\dot{\varepsilon}_H t). \quad (3.34)$$

Though, an exponential increase in the specimen length is challenging regarding the elongation instrumentation. During elongation, the sample undergoes a bidirectional deformation with an axial stress  $\sigma_x$  and its surface is subjected to uniform normal stress in the radial plane  $\sigma_r$ . The resulting tensile stress or elongation stress  $\sigma_{\text{ext}}$  is defined by

$$\sigma_{\text{ext}} = \sigma_x - \sigma_r = \frac{F}{A(t)}. \quad (3.35)$$

As polymer melts are considered incompressible, the sample volume  $V$  with

$$V = \pi R_0^2 L_0, \quad (3.36)$$

is assumed to be constant over  $t$ , which results in

$$V = V_0 = A(t)L(t). \quad (3.37)$$

An exponential increase in the specimen length consequently leads to an exponential decrease in the cross-sectional area yielding to

$$A(t) = A_0 \exp(-\dot{\epsilon}_H t). \quad (3.38)$$

Applying Equation (3.38) to Equation (3.35),  $\sigma_{\text{ext}}$  can be expressed as

$$\sigma_{\text{ext}} = \sigma_x - \sigma_r = \frac{F \exp(\dot{\epsilon}_H t)}{A_0}, \quad (3.39)$$

while  $F$  is measured indirectly via the torque of the drum. In analogy to the shear viscosity, the transient elongational viscosity, i.e., tensile stress growth coefficient,  $\eta_E^+$  is defined by

$$\eta_E^+ = \frac{\sigma_{\text{ext}}(t, \dot{\epsilon}_H)}{\dot{\epsilon}_H}. \quad (3.40)$$

The relationship of the transient shear viscosity  $\eta_S^+$  and  $\eta_E^+$  for a viscoelastic material is defined as

$$\eta_E^+(t) = 3 \int_0^t G(t) dt = 3\eta_S^+, \quad (3.41)$$

at low  $\dot{\epsilon}_H$ , i.e., long times  $t$ , if a constant volume under uniaxial tension is maintained, i.e., Poisson's ratio of  $\mu = 0.5$ . The relationship  $\eta_E^+(t) = 3\eta_S^+$  is referred to as the Trouton ratio.<sup>100</sup> It is commonly utilized to normalize  $\eta_E^+$  data and evaluate the quality and dependability of the elongation experiment.

If the polymer undergoes strain softening,  $\eta_E^+$  decreases below the LVE prediction. Strain softening is frequently observed in linear or barely entangled polymers. In contrast, if  $\eta_E^+$  increases above the LVE predictions, the polymer experience strain hardening. The strain hardening phenomenon typically occurs in polymer melts based on long-chain branched (LCB) topologies; low-density polyethylene (LDPE) might be the most prominent and noteworthy example. Figure 3.8 presents the relationship of  $\eta_S^+$ ,  $\eta_E^+$ , strain softening and strain hardening behavior.

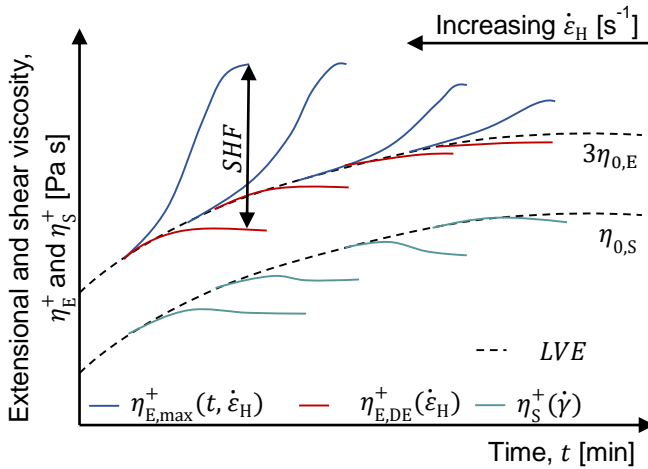


Figure 3.8. Transient shear viscosity  $\eta_S^+$  and elongational viscosity  $\eta_E^+$  of a viscoelastic polymer melt at different shear  $\dot{\gamma}$  and elongation Hencky strain rates  $\dot{\epsilon}_H$ . The strain hardening factor is quantified by the ratio of the maximum measured  $\eta_{E,\text{max}}^+(t, \dot{\epsilon}_H)$  (blue line) and the theoretical viscoelastic linear response predicted by the Doi-Edwards model  $\eta_{E,\text{DE}}^+(\dot{\epsilon}_H)$  (red line), which is introduced in Chapter 3.3.



The strain hardening factor  $SHF$  is a parameter to evaluate the elongation capability and is defined by the ratio of the maximum measured tensile stress growth coefficient  $\eta_{E,\max}^+(t, \dot{\epsilon}_H)$  to the theoretical viscoelastic linear response predicted using the Doi-Edwards (DE) model  $\eta_{E,DE}^+(\dot{\epsilon}_H)$ . The DE model will be explained in the following Chapter, 3.3.

$$SHF = \frac{\eta_{E,\max}^+(t, \dot{\epsilon}_H)}{\eta_{E,DE}^+(\dot{\epsilon}_H)}. \quad (3.42)$$

In elongation processes like foaming, the polymer melt underlies a biaxial deformation process as the foam expands. To stabilize and maintain an intact closed cell structure, strain hardening is necessary. The expandability of amorphous polymer foams can be enhanced by increasing melt strength through the incorporation of strain hardening in combination with a low viscosity of the polymer melt. Minimizing cell coalescence and rupture is achieved by increasing melt strength, which enables the cell walls to withstand greater stresses before rupturing.<sup>10</sup> Nonetheless, the stretching deformation of the polymer melt during foaming is rather biaxial than uniaxial. Notably, the relationship between uniaxial and biaxial deformation mechanisms depends on the material. For instance, it was found that the strain hardening behavior of linear PS is significantly lower when subject to biaxial deformation as compared to its uniaxial deformation. The relationship was determined through dynamic shear experiments utilizing the relaxation spectrum and the predictions derived from the Papanastasiou-Scriven-Macosko-Luo-Tanner (PSMLT) model<sup>101</sup>, initially designed for LDPE. Hence, the strain hardening phenomenon exhibits greater prominence in a uniaxial deformation direction as opposed to a biaxial one, owing to significant variations in the molecular alignment strength across the different types of deformation.<sup>102-104</sup> The simplified relationship for the viscoelastic linear response in uni- and biaxial elongation, such as the LVE envelope, is applicable:<sup>97</sup>

$$\eta_{E,bi}^+ = 2 \eta_{E,uni}^+, \quad (3.43)$$

$$\eta_{0,E,bi} = 2 \eta_{0,E,uni}^+ = 6 \eta_{0,S}^+, \quad (3.44)$$

where  $\eta_{E,bi}^+$  and  $\eta_{E,uni}^+$  are the biaxial and the uniaxial time-dependent elongational viscosity and  $\eta_{0,S}^+$  is the time-dependent shear viscosity, using the Cox-Merz rule and the Gleissle mirror relation. Furthermore, a qualitative correlation was discovered between the strain hardening behavior in uniaxial and biaxial flow by investigating linear and LCB-PP.<sup>10</sup> Due to the high reproducibility achievable with relatively simple and readily available equipment<sup>105,106</sup> and the given inherent complexity of the polymer foaming process as well as its underlying physical principle, elongation experiments in uniaxial deformation have been suggested for a correlation to the resulting foam morphology.<sup>10</sup> Therefore, uniaxial elongation measurements and the resulting  $SHF$  can be used to predict the foamability of a polymer melt, i.e., the capacity of the polymer foam to expand.

## 3.3 POLYMER DYNAMICS AND MOLECULAR CONSTITUTIVE EQUATIONS

Disclaimer. The theoretical explanation of this chapter has been published in *Macromolecules* (ACS).<sup>107</sup> Parts of this chapter were adapted with permission from Röpert, M.-C.; Schußmann, M. G.; Esfahani, M. K.; Wilhelm, M.; Hirschberg, V. Effect of Side Chain Length in Polystyrene POM-POMs on Melt Rheology and Solid Mechanical Fatigue. *Macromolecules* 2022. DOI: 10.1021/acs.macromol.2c00199. Copyright 2022 American Chemical Society. The publication was written by the author (Marie-Christin Röpert).

The so-called tube model is one of the first concepts to describe the dynamic-mechanical fundamentals in linear, entangled polymer systems from a molecular point of view.<sup>108–112</sup> The fundamental approach is based on the mobility of one single chain in a tube formed by the surrounding polymer chains. According to this model, the physically entangled neighbor polymer chains are considered static and non-mobile, and thus, the chains' movement is restricted to diffusion along the tube axis, i.e., reptation.<sup>109,113</sup>

DOI-EDWARDS MODEL. The Doi-Edwards (DE) model is based on the tube model<sup>114</sup>, predicting linear polymer melts' shear and elongational flow behavior. The DE time-dependent stress tensor  $\sigma(t)$  is given by

$$\boldsymbol{\sigma}(t) = \int_{-\infty}^t m(t-t') \mathbf{S}_{\text{DE}}^{\text{IA}}(t, t') dt' \quad (3.45)$$

The memory function  $m(t-t')$  is defined as follows:

$$m(t-t') = \frac{dG(t-t')}{dt'} \quad (3.46)$$

with  $G(t)$  as the relaxation modulus.<sup>115,116</sup> Integrating over a unit vector sphere allows the expression of the orientation tensor  $\mathbf{S}_{\text{DE}}^{\text{IA}}(t, t')$  by

$$\mathbf{S}_{\text{DE}}^{\text{IA}}(t, t') = 5 \left\langle \frac{\mathbf{u}'\mathbf{u}'}{u'^2} \right\rangle_0 \quad (3.47)$$

where  $\mathbf{u}'$  is the deformed unit vector and  $\langle \dots \rangle_0$  is defined as the average integral over the unit vector sphere with

$$\langle \dots \rangle_0 = \frac{1}{4\pi} \oint [\dots] \sin \theta_0 d\theta_0 d\varphi_0 \quad (3.48)$$

However, calculating the orientation tensor is mathematically time-consuming. Therefore, the Currie approximation<sup>117</sup> can be applied to calculate the orientation tensor<sup>118</sup> by

$$\mathbf{S}_{\text{DE}}^{\text{IA}}(t, t') = \left( \frac{1}{J-1} \right) \mathbf{B} - \left( \frac{1}{(J-1) \left( I_2 + \frac{13}{4} \right)^{0.5}} \right) \mathbf{C}, \quad \text{with } J = I_1 + 2 \left( I_2 + \frac{13}{4} \right)^{0.5} \quad (3.49)$$

where  $\mathbf{B}$  and  $\mathbf{C}$  are the Finger and Cauchy tensors, and  $I_1$  and  $I_2$  are the first and second invariants of the Finger tensor, respectively.

The DE model implies that the diameter of the polymer chains constraining tube remains unaffected and in its equilibrium state during deformation.<sup>114,119,120</sup> Hence, the strain hardening of branched polymers in elongational flow is underestimated, even though the backbones' stretching is predicted to be the phenomenon's origin. Several adjustments have been applied to the DE model to overcome the inadequacy and incorporate the stretching.

**MOLECULAR STRESS FUNCTION MODEL.** One modification of the DE model is the molecular stress function (MSF) model<sup>119,120</sup>, considering the decrease of the tube diameter due to chain stretching in elongational flow. For instance, in elongational deformation, the backbone segment of a branched polymer is stretched in flow direction and sidearms are compressed. The change of the tube diameter is included within the calculation of the DE stress tensor as molecular stress function  $f(t, t')$  leading to the MSF stress tensor:

$$\boldsymbol{\sigma}(t) = \int_{-\infty}^t m(t-t') f^2(t, t') \mathbf{S}_{\text{DE}}^{\text{IA}}(t, t') dt'. \quad (3.50)$$

Dividing the initial tube diameter  $a_0$  by the tube diameter at a specific time  $a(t, t')$ , yields  $f(t, t')$  of long-chain branched polymers<sup>120</sup>

$$f(t, t') = \frac{a_0}{a(t, t')}. \quad (3.51)$$

According to the energy balance equation,  $f(t, t')$  can be expressed as

$$\frac{df^2}{dt} = \dot{\epsilon} \frac{\beta f^2}{1 + \frac{\beta - 1}{f^4}} \left( S_{11} - S_{22} - \frac{(f^2 - 1)}{(f_{\text{max}}^2 - 1)} \sqrt{S_{11} + \frac{1}{2} S_{22}} \right), \quad (3.52)$$

where the nonlinear fitting parameters  $\beta$  and  $f_{\text{max}}$  reflect the slope and the steady state elongational viscosity, i.e., the maximum stretching, respectively. The energy balance equation assumes that  $f^2$  is proportional to the stored strain energy and relates  $\beta$  to the ratio of all polymer segments relative to the backbone ( $\beta \equiv \Phi_{\text{b}}^{-1}$ , while  $\Phi_{\text{b}}$  is the backbones' volume fraction). With  $\beta$  segments in the tube, one is the backbone and  $(\beta - 1)$  are sidearms.<sup>120,121</sup> Consequently,  $\beta = 1$  for a linear chain, but more sidearms result in increased  $\beta$  values.<sup>122</sup>

**POM-POM MODEL.** The pom-pom model has attracted substantial attention since it predicts strong shear thinning and extreme strain hardening in elongational flow.<sup>94,118,123,124</sup> A pom-pom molecule consists of a linear chain, also known as the backbone, connecting two identical star-shaped polymers, visualized in Chapter 6.1, Figure 6.1. It presumes that each backbone is entangled with other backbones. As the flow is significantly slower than the sidearms' relaxation time  $\tau_{\text{a}}$ , the molecular constitutive equation assumes that the sidearms are entirely relaxed ( $\dot{\epsilon} < 1/\tau_{\text{a}}$ ).

Therefore, only the backbone orientation and stretching contribute to the overall stress. In general, the pom-pom topology requires the definition of three time constants: the backbone orientation time  $\tau_b$ , the backbone stretch time  $\tau_s$ , and  $\tau_a$ , which can be calculated by

$$\tau_b[\xi(t)] = \frac{4}{\pi^2} Z_b^2 \Phi_b \tau_a[\xi(t)] q, \quad (3.53)$$

$$\tau_s = Z_b \tau_a(1) q, \quad (3.54)$$

$$\tau_a(\xi) = \tau_r \exp \left\{ \frac{15}{8} Z_a \left[ \xi^2 - (1 - \Phi_b) \frac{2\xi^3}{3} \right] \right\}, \quad (3.55)$$

where  $Z_b = M_{w,b}/M_e$ , and  $Z_a = M_{w,a}/M_e$  are the backbone and the sidearm entanglement number, respectively;  $\tau_r$  describes the reptation time.<sup>125</sup> The normalized contour coordinate along the sidearm  $\xi$  increases from zero to one for the branch tip to the branch point. The final expression for the stress tensor of the pom-pom model is given by

$$\boldsymbol{\sigma}(t) = G_N^0 \Phi_b \left( \Phi_b \lambda^2(t) + \frac{2q S_a(t)}{2q S_a(t) + Z_b} \right) \mathbf{S}(t), \quad \text{with} \quad \Phi_b = \frac{Z_b}{Z_b + 2q Z_a}, \quad (3.56)$$

where  $\Phi_b$  is the volume fraction of the backbone segment,  $S_a(t)$  is the part of the sidearms, which is pulled into the backbone tube (which here is assumed to be zero),  $q$  is the number of sidearms, and  $\lambda(t)$  is the time-dependent backbone stretch described by

$$\dot{\lambda} = \lambda \boldsymbol{\kappa} : \mathbf{S} - \frac{1}{\tau_s} (\lambda - 1) \quad \text{for } \lambda < q, \quad (3.57)$$

where  $\boldsymbol{\kappa}$  is the transpose of the velocity gradient tensor.

The thesis introduces more details about the dynamics of linear and branched polymers or their relaxation processes within the respective chapters. For further information, the reader is referred to cited literature within Chapter 3.

---

## 4 LIVING ANIONIC POLYMERIZATION

In 1920, Hermann Staudinger introduced the concept of large molecules, the so-called macromolecules.<sup>126,127</sup> He was awarded the Nobel prize in chemistry in 1953, as his findings built the fundamentals of polymer science we know today. A synthetic route to synthesize defined polymers is living anionic polymerization (LAP). First discovered by Szwarc et al.<sup>128</sup> in 1956, LAP is still a powerful and unique tool to highly control macromolecules with a high degree of molecular, structural, and compositional homogeneity.

This chapter is dedicated to the principles and assumptions of LAP, divided into initiation, chain propagation, termination, and the underlying kinetics. Relevant influencing parameters, e.g., suitable monomers and solvents, are introduced. Particular attention is paid to synthesizing block copolymers and polymers with different architectures, i.e., topologies, where high synthesis control is crucial.

### 4.1 FUNDAMENTALS

The first principle of a “living” polymerization was established by the pioneering work of Szwarc et al.<sup>128</sup> based on the anionic polymerization of styrene, utilizing a sodium naphthalene complex as initiator. The absence of any termination steps is the distinguishing characteristic of anionic polymerization. Still, the absence is only guaranteed if all impurities, such as traces of humidity, oxygen, carbon dioxide, and protic substances introduced with the used chemicals or reaction vessels, have been eliminated. Once the requirement is met, well-defined homo- and block copolymers with a linear or rather complex branched topology can be synthesized with extremely high molecular weights of up to  $M_w > 1,000 \text{ kg mol}^{-1}$  combined with a dispersity of  $\mathfrak{D} < 1.1$ . Furthermore, LAP enables a high control of the polymers’ architecture. However, in addition to the technical challenges for bulk production due to the high purity requirements and the intensive costs, the two monomers with the most industrial relevance, ethylene, and propylene, are incapable of undergoing anionic polymerization. Nevertheless, the polymerization method is industrially used to produce high-performance polymers with unique material properties based on characteristic molecular structures. Prominent examples of industrial relevance of the LAP are the synthesis of *cis*-1,4-polybutadiene and -isoprene for the production of tires or polyols serving as precursors for polyurethane production by ring-opening polymerization of cyclic epoxides.<sup>129,130</sup>

Suitable monomer classes are conjugated hydrocarbon monomers, electron-deficient polar monomers, and cyclic monomers. Examples of the monomer categories are vinylic monomers (a), ketones (b), aldehydes (c), isocyanides (d), epoxides (e), lactams (f), and lactones (g) are shown in Figure 4.1.<sup>131,132</sup>

The high basicity of the anionic chain ends restricts the choice of monomers, as monomers with polar substituents or a strong electrophilicity (halogens) would lead to the termination of the chain ends.<sup>131</sup> Nevertheless, the anionic polymerization of carbonyl-containing monomers is not impossible. For instance, acrylates can be polymerized anionically by reducing their reactivity towards a nucleophilic attack at the carbonyl group by, e.g., lowering the polymerization temperature, using bulky initiators, or adding ligands to stabilize the carbonyl group.<sup>133-135</sup>

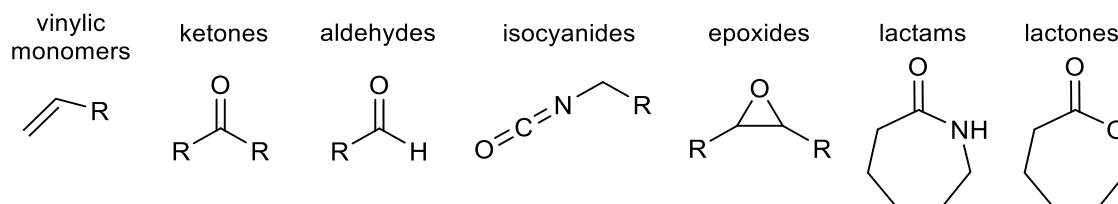


Figure 4.1. Examples of monomers suitable for living anionic polymerization.<sup>132</sup>

The anionic polymerization of vinyl monomers is highly dependent on the electron-withdrawing character of the substituents (-I/-M-effect). While the preference for polymerization rises as electronegativity decreases, as visualized in Figure 4.2. Additionally, substituents with a stabilization effect of the anionic functionality by charge delocalization along the growing chain favor the nucleophilic attack at the positively polarized  $\beta$ -carbon atom of the double bond.<sup>131,136</sup>

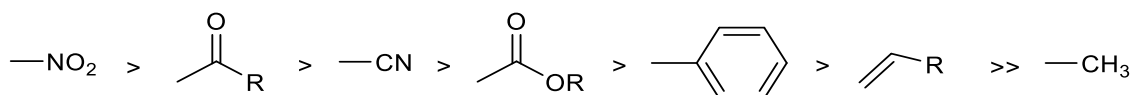
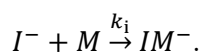


Figure 4.2. Impact of substituents (-R) on the reactivity of vinyl monomers according to a decreasing stabilization of the carbanions, i.e., -I/-M-effect.<sup>136</sup>

The LAP reaction mechanism generally consists of the following stages: initiation, chain propagation, and induced termination, all detailed in the following sections. Within these reaction steps, the polymerization kinetics depend on three key assumptions:<sup>136-138</sup>

1. Initiation is significantly faster than chain propagation ( $k_i \gg k_p$ ), while the initiation of all chains takes place instantly, simultaneously, and stoichiometrically.
2. All chains have the same propagation conditions; consequently, the chains' kinetics are equal.
3. No spontaneous chain transfer or termination reaction occurs; hence the number of propagation chains remains unchanged.

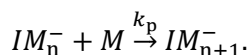
Independent of the initiator, the initiation can be described by a nucleophilic attack of a base  $I^-$  at the positively polarized functionality of the monomer  $M$ , forming a carbanion  $MI^-$  with a reaction constant of  $k_i$



Hence, the respective reaction law can be expressed as

$$v_i = -\frac{d[I^-]}{dt} = k_i[I^-][M] = k_i[I]_0[M], \quad (4.1)$$

where  $[I^-]$  and  $[I]_0$  are the concentration of the initiator, as the initiator is converted instantaneously and stoichiometrically, and  $[M]$  is the concentration of the monomer. Chain propagation takes place by adding monomers to the propagating anion with a reaction constant  $k_p$ , leading to



Under the assumption that no chain transfer or termination reactions occur, the overall concentration of the propagating anions  $[M^-]$  is equal to the initial concentration of the initiator  $[I]_0$ . Thus, the reaction law for propagation can be described by

$$v_p = -\frac{d[M]}{dt} = k_p[IM^-][M] = k_p[I]_0[M], \quad (4.2)$$

Moreover, the polymerization degree  $P_n$  can then be estimated at each reaction time by the concentration of incorporated monomers  $[M]_0 - [M]_t$  with

$$P_n(t) = \frac{[M]_0 - [M]_t}{[I]_0}. \quad (4.3)$$

Equation (4.3) can be simplified following a complete conversion of the monomer<sup>138</sup>, so  $[M]_t \rightarrow 0$  to

$$P_n = \frac{[M]_0}{[I]_0}. \quad (4.4)$$

Statistically, all initiated polymer chains have the same probability of chain propagation within the same reaction time. A Poisson distribution expresses the possibility of finding a polymer molecule with chain length  $n$ . The probability function  $P(n)$  is described by<sup>137</sup>

$$P(n) = \frac{(P_n - 1)^{n-1} \times \exp(1 - P_n)}{(n - 1)!}. \quad (4.5)$$

The probability function is based on Kolmogorov axioms (differential equations) which is recognized as a standard mathematical formalization of probability.<sup>139,140</sup> However, the molecular weight distribution (dispersity  $\mathfrak{D}$ ) is extraordinarily narrow and converges to  $\mathfrak{D} \rightarrow 1$  with increasing  $P_n$ , resulting in

$$\mathfrak{D} = \frac{M_w}{M_n} = 1 + \frac{P_n - 1}{P_n^2} \approx 1 + \frac{1}{P_n}, \quad (4.6)$$

with  $M_n$  as the number average molecular weight, and  $M_w$  as the weight average molecular weight, respectively.<sup>138</sup>

INITIATION. For initiation, (Lewis) bases like organometallics such as alkyl lithium or Grignard reagents, alkali metal amides, and alkoxides are typically used. According to the monomers' reactivity differences and to ensure a faster initiation compared to propagation, the initiators' reactivity needs to be aligned to the electronegative character of the substituent.<sup>131</sup> The initiators' reactivity is related to its nucleophilicity and basicity. Moreover, it depends on the kind and size of the counterion. Counterions having a small ionic radius remain close to the active anionic center, forming covalent bonds with a more partial nature, like lithium. Larger-radius cations have a higher distance to the active center, resulting in relatively free ion pairs, which is the case for, e.g., potassium.<sup>131</sup> The solvents' polarity influences the ion pairs' interaction, as shown in Figure 4.3. Nonpolar hydrocarbon solvents like cyclohexane or toluene favor aggregate formation, energetically disfavoring the separation of the ions due to a low dielectric constant. Polar solvents like tetrahydrofuran (THF) solvate the ion pair. The equilibrium shift towards free ion pairs increases reactivity and favors insertion of monomers. If nonpolar solvents are necessary, the complexation of the cations can be induced by adding crown ethers, enhancing the availability of the anion.<sup>141</sup>

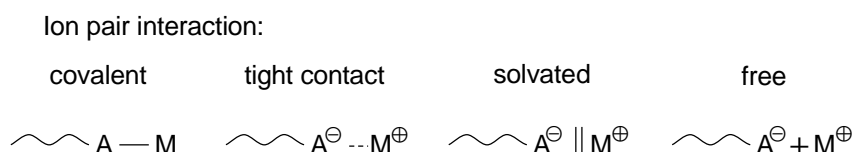


Figure 4.3. Character of ion pair interaction between polymer anions and metal counterions.

In 1956, Szwarc et al.<sup>128</sup> used sodium naphthalene as an initiator, leading to an aromatic anion radical. An aromatic anion radical enables a bifunctional chain growth of PS, as shown in Figure 4.4. The bifunctionality enables, e.g., ring closure, resulting in polymers having a ring topology.

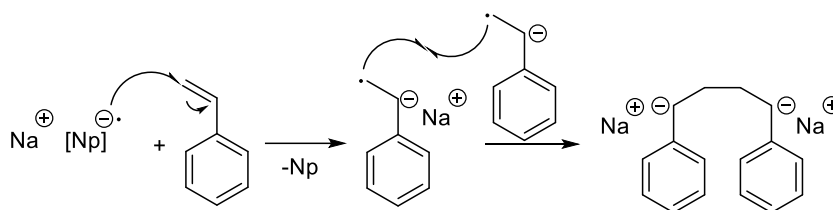


Figure 4.4. Initiation of styrene with sodium naphthalene (NaNp) by electron transfer.

However, the most common example to initiate economically significant monomers such as styrene, 1,3-butadiene, or isoprene is the addition of a strong nucleophilic Lewis base, like lithium organyls, see Figure 4.5.<sup>141</sup>

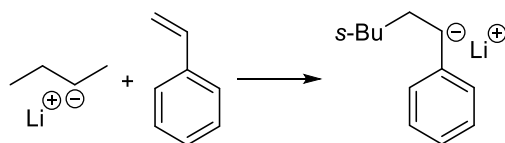


Figure 4.5. Initiation of styrene with *s*-butyl lithium (*s*-BuLi).



PROPAGATION. Chain growth proceeds at the same rate until all provided monomers are inserted. Consequently, the degree of polymerization increases linearly with monomer conversion. Due to the absence of spontaneous termination or chain transfer reactions, the chain ends maintain their reactivity, as shown in Figure 4.6.<sup>136-138</sup>

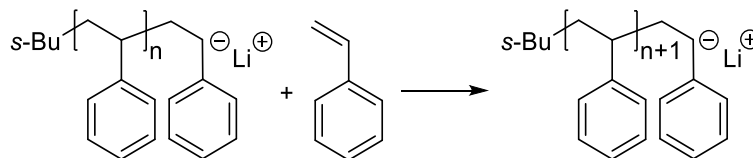


Figure 4.6. Chain propagation by monomer addition at the example of PS.

Assuming the relationship between the reactivity of the monomer and the chain end anion is sufficient, the polymerization can be continued by adding more purified monomer or a purified comonomer to the reaction mixture or terminated with protic substances like degassed methanol.

TERMINATION. Termination of the polymerization is typically induced by a proton transfer via a nucleophilic addition of protic reagents, such as methanol, as shown in Figure 4.7. During polymerization, residual moisture on labor equipment like glass apparatuses or air humidity, oxygen, or carbon dioxide can cause undesired chain end termination. For instance, if the propagating chains are terminated with  $O_2$ , an electron transfer from the anion to the  $O_2$  occurs, resulting in reactive radicals, which undergo recombination and form molecular chains with twice the molecular weight of the original polymer, see Figure 4.8 a). Disproportionation represents another possibility. Therefore, all termination agents have to be purified from protic reagents before adding to the reaction mixture to avoid the formation of by-products and the broadening of the resulting dispersity.

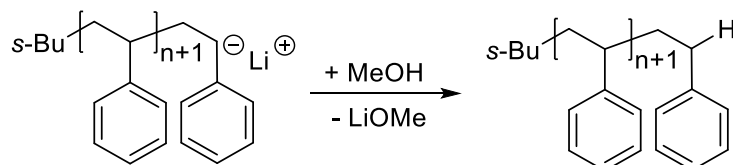


Figure 4.7. Induced termination of the living anionic PS chains by adding a protic substance such as methanol (MeOH).

However, the living chain ends can also be selectively functionalized by adding reagents such as carbon dioxide or epoxides as termination agents, see Figure 4.8 b) and c), respectively. While the reaction with carbon dioxide leads to the formation of a carboxylate, the ring-opening reaction of epoxides generates alcoholates.<sup>142-144</sup>

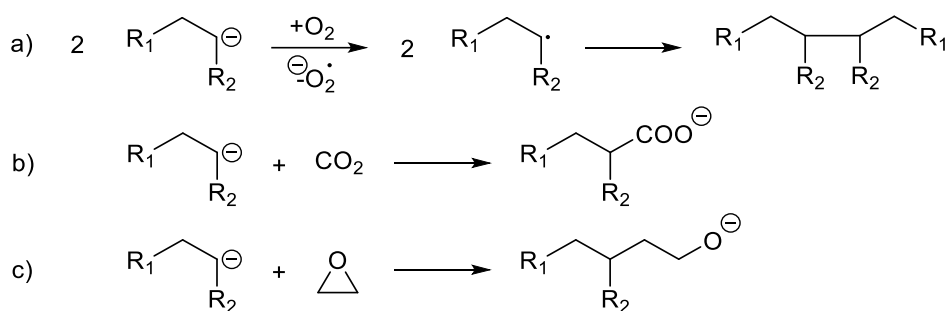


Figure 4.8. Examples of termination and functionalization of chain ends by reaction with oxygen via dimerization (a), carbon dioxide via nucleophilic addition (b), or ethylene oxide via ring-opening (c).

In summary, LAP is devoid of any spontaneous termination or chain transfer reactions under appropriate experimental conditions. Consequently, well-defined and low-disperse polymers can be synthesized with high control over their molecular architecture. For the synthesis of complex molecular architectures, numerous functional initiators and diverse linking agents with a variety of functionalities are available. Key restrictions are the stringent polymerization conditions mandatory to generate a living system and its adaptability to just a limited amount of monomers.<sup>131,145</sup>

## 4.2 BLOCK COPOLYMERS

The umbrella term “block copolymer” comprises various macromolecular structures composed of linear arrangements of at least two (A, B) chemically different and covalently bonded homopolymer-based blocks. Usually, incompatible copolymers form a vast array of well-defined self-assembled structures, which will be discussed in greater depth later in this chapter. For instance, block copolymers can be synthesized by controlled polymerizations, including LAP, atom transfer radical polymerization (ATRP), or reversible addition fragmentation chain transfer polymerization (RAFT).<sup>131,145</sup> Nonetheless, LAP has emerged as the most dependable and versatile approach to synthesize defined block copolymers, enabling a controlled molecular microstructure (e.g., cis, trans, etc.), including block order, comonomer content, molecular weight, and molecular weight dispersity. In contrast to radical polymerizations, LAP does not necessarily lead to unintended terminations of the chain ends, while ATRP and RAFT exhibit radical recombination and termination reactions.

The following three specifications<sup>145</sup> are the essential requirements for the synthesis of well-defined block copolymers:

1. The anion of the first monomer (A) must be the stronger nucleophile to initiate the polymerization of the second monomer (B).
2. The initiation rate of the polymerization of monomer B has to be higher than the propagation rate to ensure a narrow chain length distribution, i.e., low  $\mathcal{D}$ .
3. High purity of monomer B prevents partial termination and the corresponding decrease of living anions A.

Different architectures (linear vs. branched) and block arrangements (AB, ABA, ABC) can be realized through the adjustment of synthesis procedures and monomers.<sup>145,146</sup> Additionally, using nonpolar solvents such as cyclohexane lead typically to a high content of 1,4-*cis*-PI with around 95 %.<sup>147-149</sup> The possible microstructures of PI are shown in Figure 4.9.

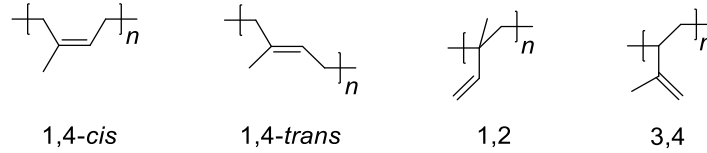


Figure 4.9. Microstructures of polyisoprene (PI).

Combining several polymers with different chemical, physical, and mechanical properties allows tailoring the resulting materials' overall properties.<sup>145,146</sup> By copolymerizing two or more homopolymer blocks with, e.g., different polarities, the polymers tend to phase separate. However, the generated covalent bond between the homopolymer blocks inhibits the block copolymer from macroscopic phase separation. Consequently, phase separation can only occur on a microscopic level, leading to the formation of so-called microdomains with a typical nanometer length scale of 10 – 100 nm, consisting predominantly of one kind of the used homopolymers.<sup>150</sup>

The phase separation is thermodynamically driven by the repulsion of unlike segmental contacts, which is related to the Gibbs free energy  $\Delta G$  of the polymer chains as

$$\Delta G = \Delta H - T\Delta s . \quad (4.7)$$

However,  $\Delta G$ , in turn, can be characterized by mean-field theories such as the Flory-Huggins theory. For a detailed description of the Flory-Huggins theory,<sup>151,152</sup> the underlying thermodynamic effects, enthalpy  $\Delta H$ , entropy  $\Delta s$ , and the theory of microphase separation in general, reference is made to the literature.<sup>67,150-157</sup> In summary:  $\Delta G$  depends on the following three parameters: the overall degree of polymerization  $P_n$ , the volume fraction  $f$  of each block, and the monomer-monomer interaction parameter, also known as Flory-Huggins parameter  $\chi$ .<sup>150,151</sup> The Flory-Huggins parameter normalizes the additional interaction energy to the thermal energy  $k_B T$ , see Equation (4.8).

Below the order-disorder-transition temperature  $T_{\text{ODT}}$ , phase separation occurs when the product  $P_n \chi$  surpasses a specific threshold value depending on the interacting monomers and the volume fraction of each block.<sup>158,159</sup> Assuming equal volume fractions of A and B, i.e.,  $f_A = f_B$ , the minimum  $P_n \chi$  values for phase separation are  $P_n \chi = 10$  and 18 for di- and symmetric triblock copolymers, respectively.<sup>160-162</sup> Entropic restrictions impede the phase separation of A and B blocks in symmetrical ABA triblock copolymers. Hence, phase separation occurs at higher  $P_n$  values compared to AB diblock copolymers.<sup>163</sup> In Figure 4.10 a), the calculated phase diagrams of polystyrene-block-polyisoprene (PS-*b*-PI) diblock and PS-*b*-PI-*b*-PS triblock copolymers as a function of the volume fraction and segregation strength are shown using a mean-field approach.<sup>164</sup>

Block copolymers often generate body-centered cubic BCC (spheres, **S**), hexagonal (cylinders, **C**), gyroid (**G**), or lamellar (**L**) microdomains to reduce the interfacial energy, as shown in Figure 4.10 b).

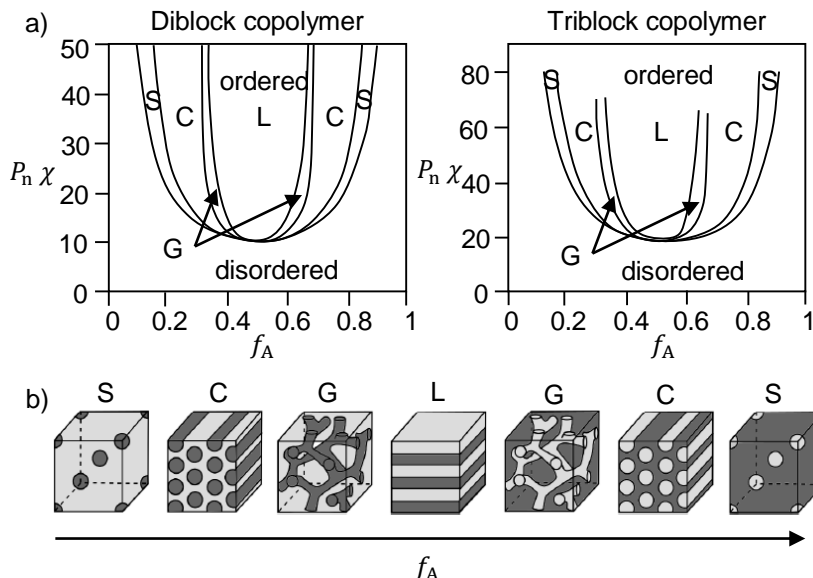


Figure 4.10. a) Phase diagram of PS-*b*-PI diblock<sup>165</sup> and PS-*b*-PI-*b*-PS triblock<sup>161</sup> copolymers with BCC (spheres, **S**), hexagonal (cylinders, **C**), gyroid (**G**), or lamellar (**L**) microphase morphologies. Adapted with permission from literature.<sup>162</sup> b) Schematic representation of the resulting morphologies at  $P_n \chi = 30$ ; dark zones correspond to the volume fraction of PS (A).

The temperature-dependent mixing parameter  $\chi$  for PS and PI can be calculated by<sup>166</sup>

$$\chi = \frac{(z-2)\Delta\epsilon}{k_B T} = A - \frac{B}{T} \approx -0.0419 + \frac{39}{T} \approx 0.089 \quad (4.8)$$

if  $T = 298$  K (rt). Therefore,  $P_n \approx 113$  is required for phase separation of a PS-*b*-PI diblock copolymer with  $f_{PS} = f_{PI} = 50$  vol%.

### 4.3 POLYMER TOPOLOGY

The molecular design and synthesis of branched polymers by LAP have achieved tremendous progress in the past quarter-century. Anionic polymerization based grafting techniques offer precise control over the backbones' and sidearms' molecular weight, branching spacing, number of branch points, and functionality. Due to these distinctive molecular features and the underlying rheological melt properties, i.e., low viscosity in combination with high melt strength, the resulting well-defined branched topologies have progressively attracted attention. Consequently, these materials may be utilized in numerous applications, ranging from thermoplastic elastomers to high-impact plastics, pressure-sensitive adhesives, additives, and, last but not least, foams.<sup>145</sup> The synthesis of branched model systems has developed to encompass further living and controlled polymerizations and hybrid methodologies.

Well-known examples are, for instance, ATRP, RAFT, ring-opening polymerization (ROP), ring-opening metathesis polymerization (ROMP), single electron transfer living radical polymerization (SET-LRP), and nitroxide-mediated polymerization (NMP).<sup>131,167,168</sup> However, controlled radical polymerizations are susceptible to termination reactions, e.g., radical recombination, that lead to increased dispersities, incomplete monomer conversions, and diminished grafting efficiencies.<sup>131,168</sup> Different approaches have been investigated to synthesize branched polymers based on a combination with LAP, focusing on three different grafting procedures: grafting-through, grafting-from, and grafting-onto methodology.<sup>131</sup>

The architecture of branched polymers can be simplified to the most straightforward topology: a star with three or four arms. Besides stars, numerous other polymer architectures exist, such as H-polymers, pom-poms, comb, and dendritic polymers, e.g., dendritic and barbwire structures or ring-shaped architectures, see Figure 4.11.

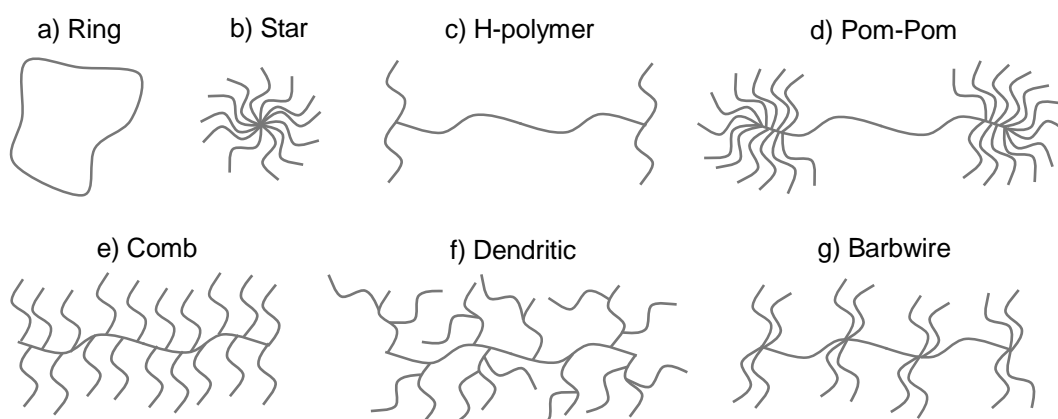


Figure 4.11. Examples of different polymer architectures including a) ring, b) star, c) H-polymer, d) pom-pom, e) comb, f) dendritic, and g) barbwire structures.

The following structural parameters can be used to describe the polymers' topology:

1. The weight average molecular weight of the backbone,  $M_{w,b}$ ;
2. The weight average molecular weight of the sidearms  $M_{w,a}$ ;
3. The number of the sidearms  $q$ , i.e., grafting density;
4. The sidearm generation, like combs or dendritic structures, with only one or up to five generations of sidearms, respectively.

Branched polymers exhibit different rheological behavior than linear ones, as the branching point changes the dynamics, e.g., relaxation behavior, and the sidearms can act as a plasticizer, reducing the overall shear viscosity of the polymer melt and simultaneously incorporating strain hardening in elongational flow. Combining these rheological melt properties makes branched polymers essential for investigating the structure-property relationship and comprehending the association between polymer topology, composition, and physical properties to adapt polymers for specific applications.<sup>131</sup>



---

PART II

RESULTS AND DISCUSSION





---

## 5 CELL NUCLEATION

Understanding the effects of phase boundaries within a polymer matrix on the nucleation state in the physical foaming process is essential for developing foams with the highest possible cell density. This chapter distinguishes between heterogeneous chain mobility and gas solubility based on phase separated di- and triblock copolymers with either higher chain mobility (PI-block in PS-*b*-PI) or higher blowing agent solubility (PMMA-block in PS-*b*-PMMA) and discusses their influence on the cellular morphology, particularly cell density and cell size. The obtained values indicate an improvement in cell nucleation based on spherical microdomains, accompanied by the highest proportion of interfaces between the two polymer phases, i.e., PS-*b*-PI. However, the low glass transition temperature within the PI-phase also facilitates cell coalescence at higher foaming temperatures or PI-concentrations. These limitations can be overcome using copolymers with a higher CO<sub>2</sub>-solubility in one polymer phase but similar glass transition temperatures, as in PS-*b*-PMMA, resulting in increased cell densities with an increasing PMMA-fraction. Please note, within this chapter, PI refers specifically to the 1,4-*cis* configuration of the PI.

Disclaimer. For the ensuing investigation, samples were used whose synthesis, molecular and morphological characterization have already been published by our group in *Macromolecules* (ACS).<sup>162</sup> A part of the knowledge gained about the phase morphology is essential for the correlation with the cellular morphology and, thus, was adapted with permission from Hirschberg, V.; Faust, L.; Rodrigue, D.; Wilhelm, M. Effect of Topology and Molecular Properties on the Rheology and Fatigue Behavior of Solid Polystyrene/Polyisoprene Di- and Triblock Copolymers. *Macromolecules* 2020, *53* (13), 5572–5587. DOI: 10.1021/acs.macromol.0c00632. Copyright 2022 American Chemical Society.

---

Cell nucleation during polymer foaming is one key factor in adjusting the resulting cellular morphology of the foams as it indirectly affects the cell size  $D$  and, consequently, the final foam properties. An often-desirable combination is a high cell density  $N$  with a small average cell size. An alternative strategy to improve the nucleation stage of the foaming process is to adjust the processing parameters. A typical combination represents low foaming temperatures  $T_f$ , dependent on the polymer matrix and high saturation pressures, e.g.,  $p > 300$  bar CO<sub>2</sub>.<sup>169–171</sup> The resulting increase in CO<sub>2</sub>-solubility and the higher pressure drop ensure a higher nucleation density. In contrast, lower  $T_f$  supports earlier fixation of the cellular morphology and minimizes the available time for cell growth. Regardless of the process conditions, three main approaches are distinguished that influence cell nucleation:

1. The addition of micron- or nano-sized nucleation particles to a polymer matrix,
2. The use of phase separating block copolymers and blends, or
3. The use of semi-crystalline polymers.

All three strategies have in common that they affect the cellular morphology by introducing structured heterogeneous phases, resulting in intrinsic nucleation superior to homopolymers. Due to the weak interaction and reduced surface tension, the energy barrier for cell formation is lowered at the emerging interfacial regions, energetically favoring nucleation. Consequently, the heterogeneous nucleation leads to the production of polymer foams with ever smaller  $D$  in combination with higher  $N$ , as introduced in Chapter 2.2.<sup>4,61,72–76</sup>

Silica-based nanoparticles are a low-cost, relatively easy-to-produce type of solid-state filler because they are controllable in size and adjustable at the surface, although their reported nucleation efficiency is typically very low with  $< 0.01$ .<sup>172–174</sup> The nucleation efficiency is defined as the ratio of cells obtained within  $1 \text{ cm}^3$  and the overall amount of added particle per  $\text{cm}^3$ . Other common nucleation particles, such as fibers, tubes, or clay, also suffer from low nucleation efficiencies.<sup>175,176</sup> Prior to foaming, a high amount of well-dispersed particles has to be added to the polymer matrix to produce a single foam cell.

Instead of nucleating particles, it is possible to incorporate a second polymer phase, i.e., using immiscible blends or self-assembled block copolymers. Typically, the magnitude of phase separation is in the order of  $1 - 10 \text{ }\mu\text{m}$  for blends, while the one of block copolymers is around  $20 - 50 \text{ nm}$ .<sup>28</sup> The formed phase boundaries promote nucleation by lowering the free energy that must be overcome to form a stable nucleus, as introduced in Chapter 2.2. A few known examples are blends consisting of high-density polyethylene (HDPE) with isotactic PP (*i*-PP)<sup>177</sup>, immiscible polyolefin blends<sup>178–181</sup>, PE with styrene-based polymers or copolymers and PE copolymers<sup>182</sup>, high-melt-strength polypropylene HMS-PP with PP-*b*-PE<sup>183</sup>, PMMA with poly(methyl methacrylate)-*b*-poly(butyl acrylate)-*b*-poly(methyl methacrylate) (MAM)<sup>171,184–186</sup>, PS with PVDF<sup>187</sup>, poly(ethylene glycol) (PEG)<sup>188</sup>, PMMA/exfoliated montmorillonite (MMT)<sup>189,190</sup>, acrylic homo- and copolymers<sup>191</sup>, or the addition of CO<sub>2</sub>-philic components such as fluoroalkyl, fluoroether, carbonyl and siloxane functional materials<sup>192–195</sup>, or various variations of poly(*p*-phenylene oxide) (PPE) and styrene-acrylonitrile resin (SAN) blends<sup>196</sup>. Moreover, the usage of copolymers based on PS and poly(dimethyl siloxane) (PDMS), ethylene-propylene copolymer (PEP), PMMA, polystyrene-*b*-polybutadiene-*b*-poly(methyl methacrylate) (SBM), or poly(perfluorooctylethyl methacrylate) (PFMA) is also a versatile approach<sup>184,197–199</sup>.

These studies demonstrated that several factors had been identified to be particularly crucial for foaming copolymers and polymer blends, such as the morphology and domain size, interfacial properties, and chemical nature of the used polymers, which affect the solubility and diffusivity of the specific blowing agent. For instance, incorporating a polymer phase that selectively dissolves a significant amount of the blowing agent supports the diffusivity of the blowing agent to the interfaces. Moreover, it introduces thermodynamic instabilities that aid nucleation.<sup>196</sup>

Nevertheless, controlling the foamability in terms of understanding the nucleation stage in the foaming process is still challenging due to the short period of a few milliseconds, where nucleation and phase transition happens.

### 5.1 SUITABILITY OF PHASE BOUNDARIES AS NUCLEATION CENTERS

Linear block copolymers can be distinguished by their molecular structure, i.e., block order, comonomer content, molecular weight, and dispersity, while each parameter impacts the microdomain morphology. Phase separation in blends, di- and triblock copolymers results in different phase morphologies and microdomain sizes.<sup>157</sup> Figure 5.1 illustrates the morphologies of the microdomains with their corresponding periodicity or repeating unit  $L_0$ , crystallographic vector of the unit cell  $B_0$ , and domain size  $d_0$  using PS- and PI-based di- and triblock copolymers with a PI-content of  $\phi_{PI} = 10$  mol%, 20 mol%, and 40 mol%.

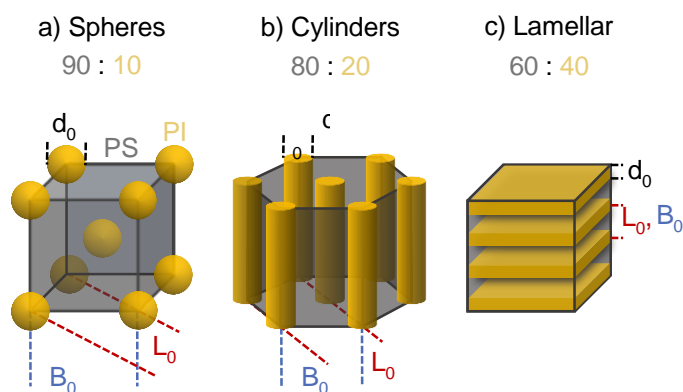


Figure 5.1. Three-dimensional representation of ideal spheres (a), cylinders (b), and lamellar (c) microdomain morphology. Furthermore, the diameter  $d_0$  of the dispersed phase, the periodicity  $L_0$  and the crystallographic vector of the unit cell  $B_0$  are labeled.

Typical  $L_0$  values for AB di- and ABA triblock copolymers vary from 5 – 100 nm.<sup>150,161</sup> Furthermore, the distance between two PI microdomains, denoted by  $B_0$ , and their diameter  $d_0$  are proportional to  $L_0$ , which will be discussed more in detail throughout this chapter. The resulting difference in microdomain sizes and morphologies, e.g., spherical (S), cylindrical (C), and lamellar (L) domains, is ideal for investigating the suitability of phase boundaries as nucleation centers and understanding the influence of polymer properties on the foaming process and especially the nucleation stage.

**SEQUENTIAL LIVING ANIONIC POLYMERIZATION.** Symmetrical, phase separating block copolymers based on PS and PI were synthesized by sequential anionic polymerization in cyclohexane, as demonstrated for a PS-*b*-PI-*b*-PS (SIS) triblock copolymer in Figure 5.2 a). The living anionic polymerization allows tailoring the block order, comonomer content, molecular weight, dispersity, and microdomain morphology.

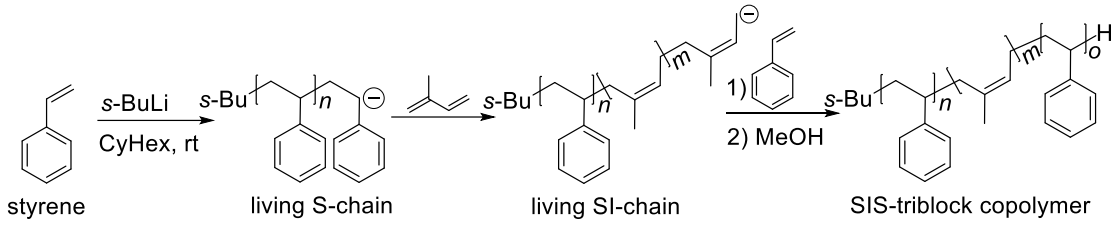


Figure 5.2. Sequential living anionic polymerization of styrene and isoprene to a PS-*b*-PI-*b*-PS (SIS) triblock copolymer. The monomers are added reverse order to synthesize the ISI triblock sequence. Diblock copolymers are obtained by terminating the anions after polymerization of the second block.

As introduced in Chapter 4.2, the block copolymer phase separates, forming microdomains with a spherical, cylindrical, or lamellar morphology, depending on  $f_{\text{PS:PI}}$ ,  $\chi$ , and  $P_n$ . The molecular parameters were analyzed by SEC and DSC, the isoprenes' microstructure via  $^1\text{H-NMR}$ , and structural information using SAXS, see the Appendix Chapter B and C.1. Table 5.1 summarizes the composition, molecular parameters, and morphology of the samples. More information can be found in the literature.<sup>162</sup> The samples are named as follows: S and I represent the used polymers in the corresponding block order, i.e., SI stands for PS-*b*-PI diblock copolymer; the first number represents  $M_w$ , and the second value  $\phi_{\text{PI}}$ .

Table 5.1. Molecular characteristics of the PS and PI blends, di- and triblock copolymers.<sup>162</sup>

Sample	$M_w$ [kg mol <sup>-1</sup> ]	$\bar{D}$	$\phi_{\text{PI}}$ [mol%]	$f_{\text{PS:PI}}$ [vol%]	Morph- ology <sup>a</sup>	$L_0$ [nm] <sup>b</sup>	$d_0$ [nm] <sup>b</sup>	$B_0$ [nm] <sup>b</sup>
PS/PI blends (PS/PI)								
PS/PI10%	PS:400	PS:1.10	10	93:7	-	-	-	-
	PI:170	PI:1.07						
PS/PI20%	PS:400	PS:1.10	20	85:15	-	-	-	-
	PI:170	PI:1.07						
PS/PI40%	PS:400	PS:1.10	40	66:33	-	-	-	-
	PI:170	PI:1.07						
PS- <i>b</i> -PI diblock copolymers (SI)								
SI400k10%	445	1.13	10	93:7	S	68.8	39.5	97.4
SI400k20%	413	1.15	20	85:15	C	139.8	56.9	121.1
SI400k30%	381	1.13	30	76:24	C	124.2	61.9	107.6
SI400k40%	374	1.12	40	66:33	L	- <sup>c</sup>	- <sup>c</sup>	- <sup>c</sup>
PS- <i>b</i> -PI- <i>b</i> -PS triblock copolymers (SIS)								
SIS200k10%	240	1.08	10	93:7	S	29.3	16.8	41.4
SIS400k10%	466	1.13	10	93:7	S	41.4	25.6	58.5
SIS400k20%	395	1.17	20	85:15	C	82.8	33.7	71.7
SIS400k30%	378	1.13	30	76:24	C	71.7	35.7	62.1

Table 5.1 continued.

Sample	$M_w$ [kg mol <sup>-1</sup> ]	$\bar{D}$	$\phi_{PI}$ [mol%]	$f_{PS:PI}$ [vol%]	Morph- ology	$L_0$ [nm] <sup>b</sup>	$d_0$ [nm] <sup>b</sup>	$B_0$ [nm] <sup>b</sup>
SIS400k40%	380	1.12	40	66:33	L	77.5	31.0	77.5
SIS1000k10%	1025	1.16	10	93:7	S	74.6	42.8	105.5
PI- <i>b</i> -PS- <i>b</i> -PI triblock copolymer (ISI)								
ISI400k10%	469	1.06	10	93:7	S	47.6	27.0	66.5
ISI400k20%	494	1.06	20	85:15	C	58.8	23.9	50.9
ISI400k30%	413	1.05	30	76:24	C	67.8	33.8	58.7
ISI400k40%	479	1.08	40	66:33	L	89.0	35.6	89.0

<sup>a</sup>Microdomain morphology as implicit from the PI-content (vol%) and the corresponding phase diagrams. <sup>b</sup>Calculated from the scattering vector  $q_0$  of the first-order maximum. <sup>c</sup>Failure of the determination of the long-distance order as the  $L_0$  value exceeds the limit of the instrument.

Figure 5.3 a) gives an example of a typical SAXS pattern for lamellar block copolymers, b) visualizes  $d_0$  as a function of  $M_w$  for di- and triblock copolymers forming spheres, while c) displays  $d_0$  as a function of  $\phi_{PI}$  for  $M_w \approx 400$  kg mol<sup>-1</sup>.

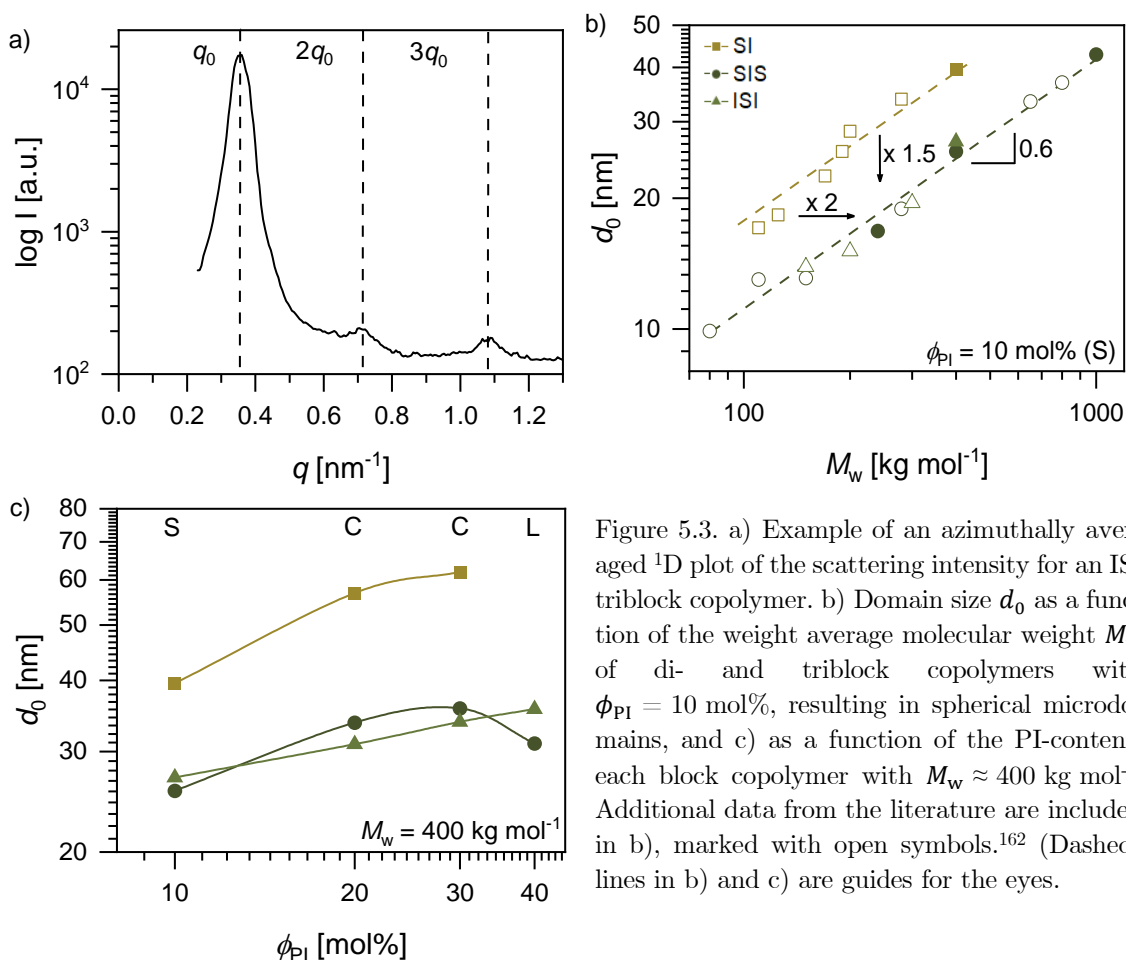


Figure 5.3. a) Example of an azimuthally averaged 1D plot of the scattering intensity for an ISI triblock copolymer. b) Domain size  $d_0$  as a function of the weight average molecular weight  $M_w$  of di- and triblock copolymers with  $\phi_{PI} = 10$  mol%, resulting in spherical microdomains, and c) as a function of the PI-content, each block copolymer with  $M_w \approx 400$  kg mol<sup>-1</sup>. Additional data from the literature are included in b), marked with open symbols.<sup>162</sup> (Dashed lines in b) and c) are guides for the eyes.

The di- and triblock copolymers (**S**) show that  $d_0$  increases with increasing  $M_w$ . Moreover,  $d_0$  follows a power-law relation with a scaling exponent of 0.6. The exponent can be expected from the literature, as  $d_0 \propto L_0 \propto P_n^{0.68} \chi^{0.19}$ , calculated from self-field theories for lamellar morphologies.<sup>162,200</sup> The exponent was estimated in the literature to be between 0.5 and 0.68 based on the end-to-end radius and the Flory-Huggins mixing parameter  $\chi$ .<sup>162</sup> Since the end-to-end radius scales with the square root of the degree of polymerization<sup>114</sup>, a simple estimate for the exponent would be 0.5. Meaning that if  $P_n$  ( $\propto M_w$ ) doubles, the end-to-end distance of a polymer ( $\propto L_0$ ) should only increase by the square root of 2. Consequently, a slope of 0.5 would appear in a double-logarithmic plot. Since the PS- and PI-block copolymers within this study have a fixed  $\chi$ , the domain size of the lamellar microstructure is predicted to scale with an exponent of 0.68. When comparing the simple assumption from the end-to-end distance of the polymer and the phase field calculations for the lamellar microstructure, the exponent of 0.6 determined empirically for the spherical microstructure meets the values. Furthermore,  $d_0$  of the diblock is a factor of 1.54 larger than the one for the respective triblock copolymers, while the triblock copolymers have similar  $d_0$  values for  $\phi_{PI} = 10$  mol%.

The total ratio of isoprene monomers governs the volume of the sphere and hence, the length and number of PI-blocks. Moreover, the number of PI-blocks in a PI-sphere relies on its surfaces' PS-block attachment space. For instance, SIS and ISI have twice as many PS-blocks on the surface of each PI-microdomain than SI, therefore  $d_{0,SIS} = d_{0,ISI} < d_{0,SI}$  at a comparable molecular weight. The difference in  $d_0$  for di- and triblock copolymers as a function of  $M_w$  indicates that the triblock copolymers have identical  $L_0$  values at approximately two times  $M_{w,SI}$ . Assuming that  $M_{w,SIS,ISI} \approx 2 M_{w,SI}$ , the domain size would increase by  $d_0 = 2^{0.6} = 1.51$ , which is close to the experimentally found value of  $d_0 \propto L_0 = 1.54$ , as discussed in more detail in the corresponding publication.<sup>162</sup>

Graphical representation of  $d_0$  as a function of  $\phi_{PI}$  for samples with similar  $M_w$  demonstrates an analogous trend of SIS, ISI, and SI with increasing PI fraction, namely  $d_0$  grows with  $\phi_{PI}$ . An increase in both,  $d_0$  and  $L_0$ , ultimately leads to an increase of  $B_0$ , meaning an increasing distance between the individual PI domains. As the surface area reduces from spheres to cylinders and the  $\phi_{PI}$  increases, it is reasonable to anticipate an increase in  $d_0$ .<sup>162</sup>

The number of PI-spheres within 1 cm<sup>3</sup> sample can be calculated according to the volume of the spheres ( $V_{\text{sphere}} = \frac{4}{3}r^3\pi$ ), the volume of the cuboid and the number of spheres within one cuboid or repeating unit, with equals two for BCC morphology. Assuming that one sphere leads to the formation of one cell in the final foam, the maximum cell density  $N_{\text{max}}$  can be calculated and varies between  $N_{\text{max}} = 1.70 \times 10^{15} - 2.82 \times 10^{16}$  cells cm<sup>-3</sup> for all investigated PS- and PI-based block copolymers with  $\phi_{PI} = 10$  mol%.

PHYSICAL FOAMING – DOMAIN SIZE. The impact of the microdomains' morphology on the nucleation stage, and hence, the cell density, is investigated using SI, SIS, and ISI block copolymers. Blends of both polymers (PS/PI) with the same PI-content as the block copolymers, i.e.,  $\phi_{\text{PI}} = 10 \text{ mol}\%$ ,  $20 \text{ mol}\%$ , and  $40 \text{ mol}\%$ , serve as reference. Here, PS serves as a matrix, as the higher viscosity ensures distinct cell stabilization during the foaming process compared to low viscous polymers, such as PI.<sup>196</sup> The SEM images of selected foams foamed at  $T_f = 80 \text{ }^\circ\text{C}$ , are illustrated in Figure 5.4, while  $T_{g,\text{PI}} < T_f (80 \text{ }^\circ\text{C}) < T_{g,\text{PS}}$ .

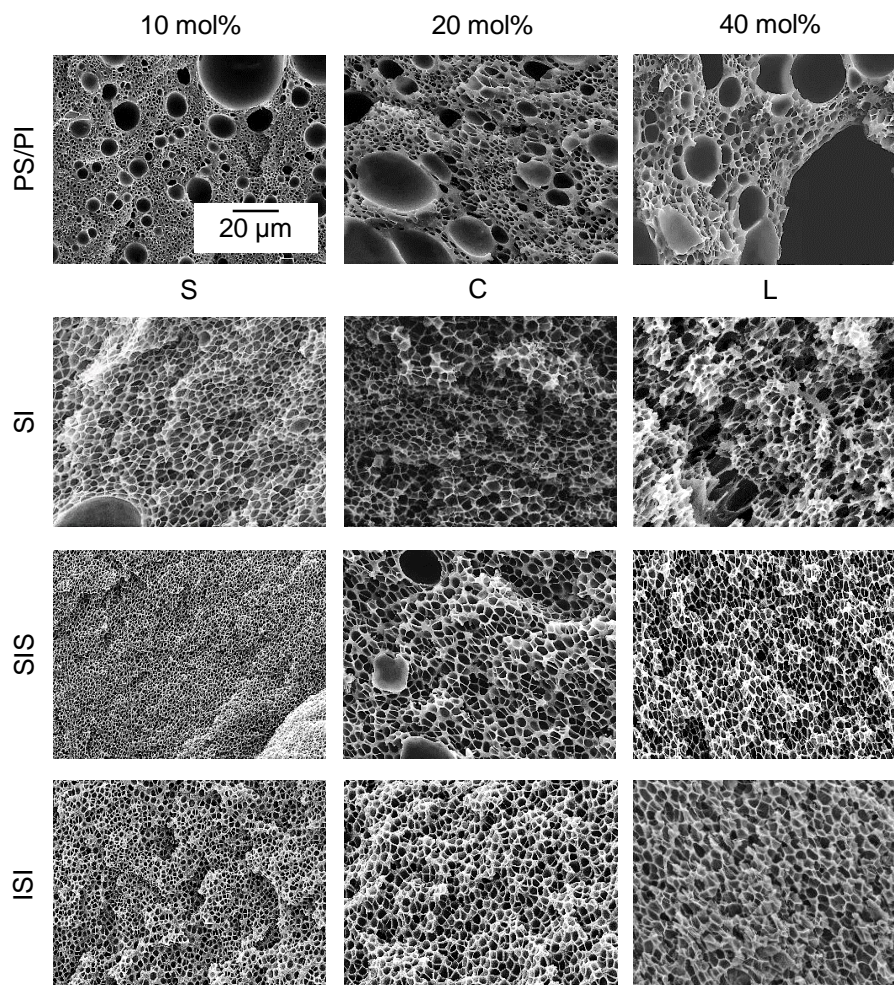


Figure 5.4. SEM images of PS- and PI-based di- and triblock copolymer foams. The PI-content increases from  $\phi_{\text{PI}} = 10 \text{ mol}\%$  to  $40 \text{ mol}\%$ , resulting in spherical (S), cylindrical (C), and lamellar (L) morphologies of the microdomains. Blends based on PS and PI with similar comonomer content (top row) serve as reference samples. The scaling bar is valid for each image within this figure. Foaming conditions:  $T_f = 80 \text{ }^\circ\text{C}$ ,  $p = 500 \text{ bar}$ ,  $t_{\text{sat}} = 8 \text{ h}$ , and  $dp/dt \approx 200 \text{ bar s}^{-1}$ .

Comparing the foams based on PS/PI blends with foamed block copolymers reveals considerable differences in cell morphology and foam heterogeneity. While the blends display macroscopic defects, chemically linking the two polymer phases tremendously reduces cell size and homogenizes the overall cell morphology.

The macroscopic defects can be attributed to the low  $T_g$  of the PI with  $T_{g,PI} \approx -70$  °C, leading to a lower shear viscosity and lower melt strength of the PI-phase. Consequently, the cell growth rate and the tendency to coalesce increase within the relatively soft PI-phase in the PS/PI blends. Investigations in the literature confirm this assumption, as the appearance of macroscopic defects in foams from polymer blends was also reported by studying blends based on PS/PEG or PPE/SAN.<sup>188,196</sup> In both studies, smaller cells were observed in the more viscous polymer phase and larger cells in the less viscous one. Simultaneously, the diffusivity of the blowing agent is higher in the low viscous phase, leading to an earlier cell coalescence and, consequently, the formation of larger cells. Copolymerizing PI with a stiffer and more viscous polymer under the environmental conditions, such as PS ( $T_{g,PS} \approx 100$  °C), introduces chemical bonds into the polymer chain, constraining the chain mobility. This implemented growth restriction contributes to a relatively homogeneous cell size distribution by inhibiting pronounced cell growth within the soft PI-phase and minimizing cell coalescence.

Further improvement of the foam morphology, i.e., decreasing cell size and increasing foam homogeneity, is observed for the SIS and ISI triblock copolymers with 10 mol% PI (S), which have a particular smaller  $D$  compared to the samples with  $\phi_{PI} = 20$  mol% or 40 mol% or the corresponding SI diblock copolymers. A smaller cell size usually corresponds to a higher cell density if an equal amount of blowing agent is dissolved in the overall sample. Hence, fewer CO<sub>2</sub> molecules are available in the polymer matrix for cell growth. Nevertheless, the SEM images show that the formation of phase boundaries within a polymer matrix leads to a substantial change in cell density, demonstrating that the phase boundaries and the overall microdomain morphology strongly control cell nucleation.

As introduced before, the domain size, and thus, the surface area of phase boundaries, which support heterogeneous nucleation, change with an increasing PI fraction. To investigate whether the morphology and the size of the microdomains influence the resulting cell density, Figure 5.5 displays  $N$  as a function of the foaming temperature of SIS triblock copolymers with  $M_w \approx 400$  kg mol<sup>-1</sup> and  $\phi_{PI} = 10$  mol%, to 40 mol%. The SIS triblock series were used to monitor the impact of  $\phi_{PI}$ , i.e., phase morphology, while  $M_w$ , as the diameter of the spheres is reduced compared to SI diblock copolymers, as already shown in Figure 5.3. As first approximation, it is assumed that smaller sphere diameters should lead to an increased cell density. This is due to the fact that spheres with a smaller diameter lead to a higher surface area at the same PI fraction. Thus, more phase boundaries are formed between the PI-spheres and the PS, which in turn reduce  $\Delta G_{het}$  and facilitate heterogeneous nucleation. The domain size of the investigated SIS triblock copolymers varies between  $d_0 = 25.6$  nm – 33.7 nm and hence, exceeds the critical radius for nucleation under the used foaming conditions of  $p = 500$  bar,  $T_f = 60$  °C – 120 °C.



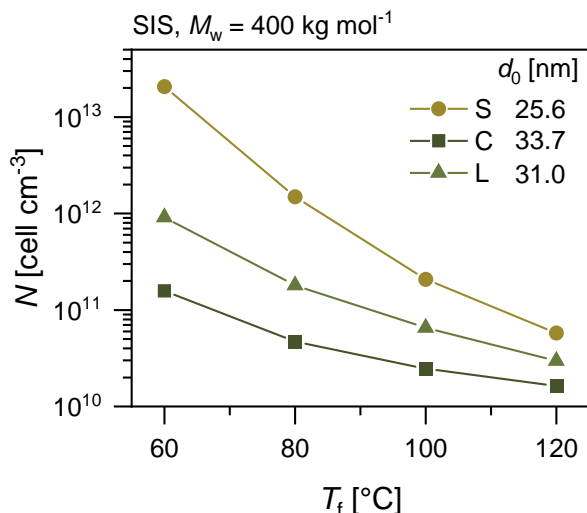


Figure 5.5. Cell density  $N$  as a function of the foaming temperature  $T_f$  for SIS triblock copolymers with  $\phi_{\text{PI}} = 10 \text{ mol}\% - 40 \text{ mol}\%$  of PI, resulting in spherical (S), cylindrical (C), and lamellar (L) microdomains, respectively. Each sample has a weight average molecular weight of around  $M_w \approx 400 \text{ kg mol}^{-1}$ . The domain sizes vary between 25.6 nm and 33.7 nm. Foaming conditions:  $T_f = 60 \text{ }^\circ\text{C} - 120 \text{ }^\circ\text{C}$ ,  $p = 500 \text{ bar}$ ,  $t_{\text{sat}} = 8 \text{ h}$ , and  $dp/dt \approx 200 \text{ bar s}^{-1}$ .

The cell density decreases with increasing temperature, as higher  $T$  leads to a longer period for cell expansion, which reduces  $N$  by cell coalescence. The amount of dissolved  $\text{CO}_2$  inside the polymer decreases with increasing  $T$ , as introduced in Chapter 2.2. Furthermore, the highest  $N$  value was reached by SIS400k10% (S) with  $N = 2.07 \times 10^{13} \text{ cell cm}^{-3}$ . Additionally, its cell size is remarkably small, with only  $D \approx 0.39 \text{ }\mu\text{m}$ . All statistical cellular parameters of the block copolymer based foams are summarized in the Appendix, see Table C.1. The low cell size can be attributed to the following: First, spheres exhibit the smallest domain size and the largest content of phase boundaries. Second, the copolymer consists of the lowest PI fraction, so the possibility of coalescence is lower than at higher PI concentrations, i.e., larger PI domains. In addition, it has to be considered that PI has a higher  $\text{CO}_2$ -solubility than PS<sup>53</sup>, and thus, the  $T_{g,\text{eff}}$  decreases with increasing PI-content. Detailed information about the blowing agent solubility in PS and PI is given in Chapter 5.2. Consequently, the higher foaming temperatures soften the PI-phase, yielding a higher tendency for cell coalescence. This is favored by an increased  $\text{CO}_2$ -solubility, even if the overall  $\text{CO}_2$ -solubility in polymeric materials decreases slightly with increasing temperatures.<sup>33</sup> Moreover, as the temperature increases, the phase separation within the block copolymers declines, according to Equation (4.8). Interestingly, even though the SIS copolymer with  $\phi_{\text{PI}} = 40 \text{ mol}\%$  has the highest concentration of soft PI-phase,  $N$  is higher compared to the samples with  $\phi_{\text{PI}} = 20 \text{ mol}\%$  PI. This phenomenon is in accordance with the domain size, as  $d_0 = 31.0 \text{ nm}$  and  $33.7 \text{ nm}$  for SIS400k40% and SIS400k20%, respectively. The found trend that small  $d_0$ , or conversely a high surface area at phase boundaries, is accompanied by an increased  $N$  and occurs not only using SIS triblock copolymers but also within the series of the triblock copolymer with an inverse block order (ISI) and the SI diblock copolymer, both series with similar molecular composition, as summarized in Table C.1.

Further investigation regarding the nucleation via PI-spheres, and especially their domain size, is based on the following two molecular parameters: Molecular weight and the block number. First, the total molecular weight was systematically varied between  $M_w = 200 - 1,000 \text{ kg mol}^{-1}$ , by maintaining  $\phi_{PI} = 10 \text{ mol}\%$ , which results in the formation of PI-spheres with  $d_0 = 16.8 \text{ nm} - 42.8 \text{ nm}$ . Figure 5.6 a) shows the cell density as a function of the foaming temperature and b) summarizes the resulting cell size as a function of the foam density.

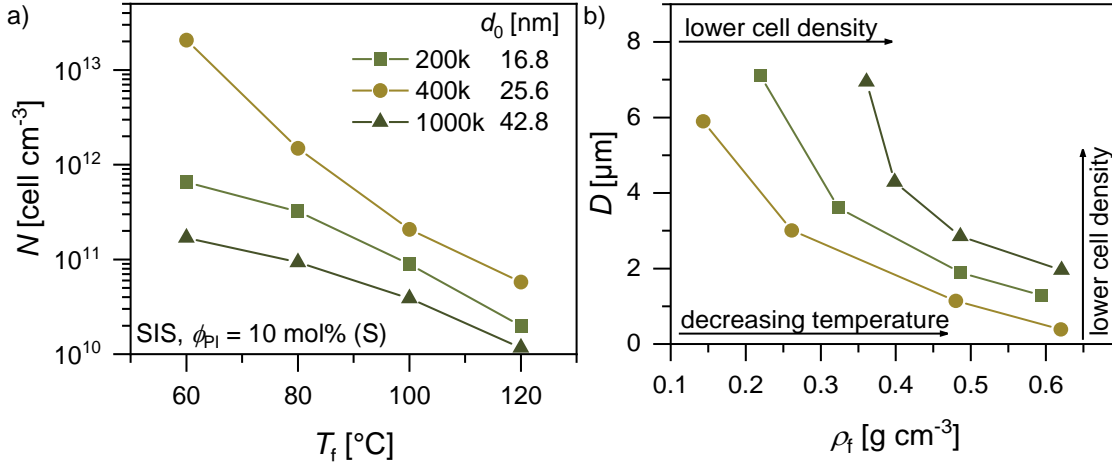


Figure 5.6. Cell density  $N$  as a function of the foaming temperature  $T_f$  (a) and cell size  $D$  as a function of the foam density  $\rho_f$  (b) for SIS triblock copolymers with  $M_w = 200 \text{ kg mol}^{-1}$  to  $1,000 \text{ kg mol}^{-1}$  and a spherical morphology of the microdomains ( $\phi_{PI} = 10 \text{ mol}\%$  PI). The domain sizes vary between  $16.8 \text{ nm}$  to  $42.8 \text{ nm}$ . Foaming conditions:  $T_f = 60 \text{ }^\circ\text{C} - 120 \text{ }^\circ\text{C}$ ,  $p = 500 \text{ bar}$ ,  $t_{\text{sat}} = 8 \text{ h}$ , and  $dp/dt \approx 200 \text{ bar s}^{-1}$ .

Investigating SIS triblock copolymers with  $M_w = 200 - 1,000 \text{ kg mol}^{-1}$  and  $\phi_{PI} = 10 \text{ mol}\%$  (S),  $N$  increases with increasing  $T_f$ . Moreover, the temperature influence is less pronounced for the sample with  $M_w = 1,000 \text{ kg mol}^{-1}$ , due to its high molecular weight, consequently leading to increased viscosity and melt strength over the investigated temperature range of  $T_f = 60 \text{ }^\circ\text{C} - 120 \text{ }^\circ\text{C}$ . The impact of the soft PI-phase also decreases with increasing  $M_w$  as the corresponding entanglement number increases from  $Z_{PS} \approx 14$  for the PS-blocks of SIS200k10% to  $Z_{PS} \approx 61$  for the PS-blocks of SIS1000k10%, with  $M_{e,PS} = 16.8 \text{ kg mol}^{-1}$  and  $M_{e,PI} = 4.5 \text{ kg mol}^{-1}$ .<sup>201</sup> Although SIS200k10% forms smaller domains ( $d_0 = 16.8 \text{ nm}$ ) than SIS400k10% ( $d_0 = 25.6 \text{ nm}$ ), the cell density is more than one order of magnitude lower at  $T_f = 60 \text{ }^\circ\text{C}$ . The difference in  $N$  between both materials decreases as a function of  $T_f$ .

A lower  $M_w$  typically facilitates expansion due to lower entanglements and a decreased viscosity of linear polymer chains. As a result, the pressure inside the cell can deform the polymer matrix more easily. Though, the viscosity of the samples investigated in this chapter could not be determined by shear rheology as the high molecular weight samples require high measurement temperatures of over  $200 \text{ }^\circ\text{C}$ , leading to the formation of crosslinks between the PI-blocks.

A disadvantage of the polymer melts' lower viscosity is the resulting CO<sub>2</sub>-loss, as it diffuses out of the matrix before the vitrification takes place. This phenomenon should result in decreased  $N$  values with similar  $D$  but lower  $\rho_f$ . Figure 5.6 b) links  $D$  with resulting  $\rho_f$  for SIS triblock copolymers with 10 mol% PI (spheres) and an increasing  $M_w$ . At  $T_f = 120$  °C, the samples reach cell sizes in the range of  $D = 4.3 - 7.9$   $\mu\text{m}$ , while the foam density varies strongly between  $\rho_f = 0.14 - 0.36$   $\text{g cm}^{-3}$ , and the cell density in the final foam is around  $N = 1.17 \times 10^{10} - 5.78 \times 10^{10}$   $\text{cell cm}^{-3}$ . These results support the assumption that SIS200k10% loses CO<sub>2</sub> during the foaming procedure, as similar  $D$  but an increased  $\rho_f$  associated with a lower  $N$  can only occur at a lower overall CO<sub>2</sub>-concentration in the sample. As the CO<sub>2</sub>-solubility remains the same under the same foaming conditions, CO<sub>2</sub> has to diffuse out of the polymer matrix. This effect does not occur at lower  $T_f$ , as here, similar  $\rho_f$  are reached in combination with lower  $N$  but higher  $D$  values. The finding can be attributed to the increased viscosity at lower temperatures. Hence, CO<sub>2</sub>-loss is minimized, but cell coalescence still takes place, leading to increased  $D$ . In contrast, cell expansion is tremendously decelerated by very high  $M_w$ , the resulting high number of entanglements of around  $Z \approx 75$  of SIS1000k10% and increased viscosity, hindering cell formation. Therefore, a molecular weight of around  $M_w = 400$   $\text{kg mol}^{-1}$  represents a compromise, also reflected in the significantly increased  $N$ .

Another possibility to adjust the domain size is increasing the block number or changing the block order. The corresponding SI, SIS, and ISI block copolymers are based on the following molecular parameters:  $M_w = 400$   $\text{kg mol}^{-1}$  with  $\phi_{\text{PI}} = 10$  mol% (S), leading to the formation of PI-spheres with  $d_0 = 25.6$   $\text{nm} - 39.5$   $\text{nm}$ . The resulting  $N$  is shown as a function of  $T_f$  in Figure 5.7.

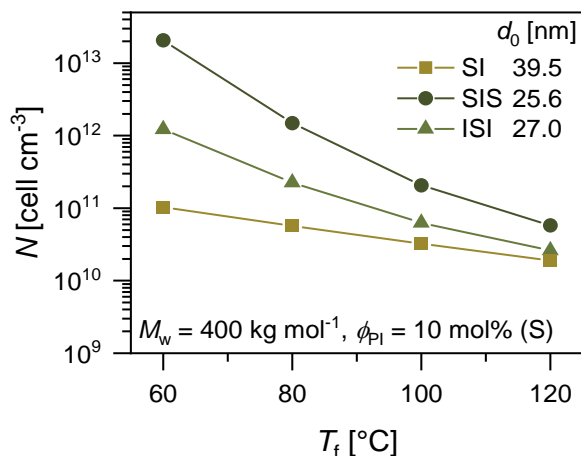


Figure 5.7. Comparison of the resulting cell density  $N$  of foamed PS- and PI-based di- and triblock copolymers with a spherical microdomain morphology ( $\phi_{\text{PI}} = 10$  mol%) at temperatures between 60 °C and 120 °C. Each block copolymer has a molecular weight of around  $M_w \approx 400$   $\text{kg mol}^{-1}$ . Foaming conditions:  $T_f = 60$  °C – 120 °C,  $p = 500$  bar,  $t_{\text{sat}} = 8$  h, and  $dp/dt \approx 200$  bar s<sup>-1</sup>.

As expected from CNT theory<sup>4,61,72-76</sup>,  $N$  decreases with increasing  $T_f$ . Additionally, the temperature influence is more pronounced for the SIS triblock copolymer, which also has the smallest domain size of  $d_0 = 25.6$  nm.

A substantial difference in  $N$  with more than two orders of magnitude is found for the SIS triblock and SI diblock copolymer at  $T_f = 60$  °C, while its difference at  $T_f = 120$  °C is less pronounced. This effect correlates with the domain sizes, as these two block copolymers show the largest size difference of  $d_0 = 25.6$  nm and 39.5 nm for the SIS400k10% and SI400k10% tri- and diblock copolymer, respectively.

The difference in  $N$  between SIS and its inverse counterpart ISI can be attributed to the block arrangement. The soft block is located in the center and covalently connected to both chain ends with PS-blocks, restricting the PI-blocks' movement and cell coalescence due to minimized chain mobility and, therefore, failure within the PI-phase. This explains why the cell density of the SIS triblock copolymer foam is higher than that of the ISI triblock copolymer, despite an equal PI-content and similar domain size. Furthermore, the effect is minimized at higher temperatures, as the PS-phase is softened by the higher  $T_f$ , and the difference between PS and PI decreases.

In contrast to our findings, it was found in the literature that the cell size decreased with increasing domain size by studying PMMA/MMT nanocomposites within a PS matrix.<sup>189</sup> This phenomenon was attributed to both the increased CO<sub>2</sub>-solubility in the PMMA-phase, serving as a CO<sub>2</sub>-reservoir, and the diffusion of CO<sub>2</sub> across these domains to the phase boundaries. Nevertheless, the PS and PI blends and block copolymers show a clear trend toward an increasing  $D$  with increasing  $d_0$ , and thus, a decreasing  $N$ . The fact that the CO<sub>2</sub>-solubility in PI is similar to the one in PMMA<sup>53</sup> leads to the hypothesis that a difference in chain mobility between the PMMA- and PI-phase within the PS-matrix might be the reason for the different trend.

Within the study, three distinct regimes are of particular interest, depending on the relation of  $T_g$  of the pure polymer and the foaming temperature  $T_f$ : (I)  $T_f < T_g$ : Low expansion due to the plastification effect of the blowing agent, (II)  $T_f = T_g$ : Comparable expansion for all samples, and (III)  $T_f > T_g$ : A higher tendency for cell coalescence or collapse of cells within the blends' PI-phase. Furthermore, the copolymerization of PS and PI and the associated covalent bonds stabilizes the foam morphology due to restrictions of chain mobility, especially with PS-based end blocks. Therefore, SIS400k10% is the most promising candidate, as  $N$  exceeds  $10^{13}$  cell cm<sup>-3</sup>, leading to average cell sizes down to  $D = 390$  nm at  $T_f = 60$  °C. However, the experiments reveal that the cell coalescence within the here investigated di- and triblock copolymers is still a challenge, as the theoretically maximum cell density  $N_{\max}$  is around two to three orders of magnitudes higher than the maximum achieved  $N$  of SIS400k10%. A strategy for future work should be to combine phase separated block copolymers with polymers showing an increased melt strength, as a high melt strength would reduce the tendency of cell coalescence. This could be done, for example, by introducing sidearms to a linear backbone, which is discussed in more detail in Chapter 6.

Before discussing the influence of sidearms on the foamability of amorphous polymers, the next chapter first addresses the impact of copolymers with similar chain mobility but heterogeneous CO<sub>2</sub>-solubility on their foamability based on PS-*b*-PMMA diblock copolymers to investigate the interaction between the  $T_g$  of the copolymer, or more precisely, its difference between the used copolymers.

## 5.2 HETEROGENEOUS GAS SOLUBILITY VS. CHAIN MOBILITY

Besides the domain size, copolymers can differ by gas solubility or chain mobility for each polymer part. Using self-assembled block copolymers or blends in the foaming process of polymers allows the investigation of the relationship between intrinsic molecular polymer properties and cell nucleation to a certain extent, but it still reveals some severe drawbacks. For instance, each polymer has a specific processing window depending on its molecular parameters and dynamics, i.e., viscosity and  $T_g$ . The overall foamability of a copolymer can strongly deteriorate if the foaming windows of the homopolymers are too different, reflected in a decreased foam homogeneity. Heterogeneous cell morphology and cell collapse became especially obvious between the PS/PI blends with a difference in glass transition temperature of  $\Delta T_g \approx 170$  °C, as discussed in Chapter 5.1. Here, the limitations of foamability were particularly overcome by covalently bonding both polymers. Based on these findings, the question derived whether heterogeneity of CO<sub>2</sub>-solubility or mobility differences within the copolymer blocks exerts a more significant influence on the cell structure, especially cell density, as schematically represented in Figure 5.8.

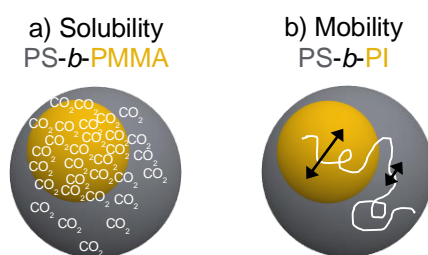


Figure 5.8. The illustration of heterogeneous CO<sub>2</sub>-solubility (a) and heterogeneous chain mobility (b) are both exemplarily shown in spherical microdomains. For instance, PS-*b*-PMMA and PS-*b*-PI can be used as polymeric model systems to investigate the impact of solubility and mobility, respectively.

Poly(methyl methacrylate) is a well-suited counterpart for PI for comparing chain mobilities while keeping a similar CO<sub>2</sub>-solubility due to the difference between their glass transition temperatures of  $\Delta T_g = 170$  °C, as  $T_{g,PI} \approx -70$  °C and  $T_{g,PMMA} \approx 100$  °C, but similar affinity to CO<sub>2</sub>.<sup>53,202</sup> The solubility of CO<sub>2</sub> in PMMA and PI is about 22 to 25 g per 100 g polymer at around  $T = 35$  °C and  $p \approx 100$  bar, respectively. In comparison, the solubility of CO<sub>2</sub> is significantly lower and only around 5 g per 100 g in PS under the same conditions.<sup>53</sup> These characteristics make block copolymers based on PS and PI or PMMA ideal candidates to investigate the impact of heterogeneity in chain mobility and CO<sub>2</sub>-solubility.

SEQUENTIAL LIVING ANIONIC POLYMERIZATION. Symmetrical and well-defined PS-*b*-PMMA (SMMA) diblock copolymers with  $M_w \approx 400 \text{ kg mol}^{-1}$  and  $\phi_{\text{PMMA}} = 10 \text{ mol}\%$ ,  $20 \text{ mol}\%$ , and  $40 \text{ mol}\%$  were synthesized by sequential living anionic polymerization in THF, see Figure 5.9, and compared to SI diblock copolymers with a similar molecular composition. To minimize the nucleophilic attack at the carbonyl group, the reactivity of the formed PS macro-anions was reduced by adding 1,1-Diphenylethylene (DPE) to the reaction solution.

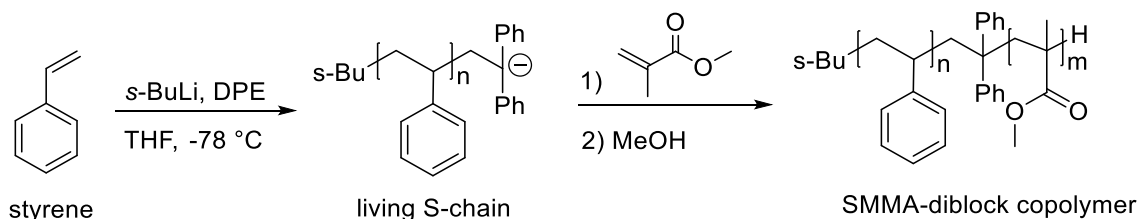


Figure 5.9. Sequential living anionic polymerization of styrene (S) and methyl methacrylate (MMA) to a PS-*b*-PMMA (SMMA) diblock copolymer.

The molecular parameters of the resulting SMMA diblock copolymers were characterized by SEC and  $^1\text{H-NMR}$ . The morphology of the microdomains was assumed from the volume percentage of PMMA when compared to the corresponding phase diagram. The resulting samples and their composition, molecular parameters, and morphology are summarized in Table 5.2.

Table 5.2. Molecular characteristics of the investigated PS-*b*-PI<sup>162</sup> and PS-*b*-PMMA diblock copolymers.

Sample	$M_w$ [ $\text{kg mol}^{-1}$ ]	$\bar{D}$	$\phi_{\text{PI}}$ [mol%]	Morphology
PS- <i>b</i> -PI diblock copolymers (SI)				
SI400k10%	445	1.13	10	<b>S</b>
SI400k20%	413	1.15	20	<b>C</b>
SI400k40%	374	1.12	40	<b>L</b>
Sample	$M_w$ [ $\text{kg mol}^{-1}$ ]	$\bar{D}$	$\phi_{\text{PMMA}}$ [mol%]	Morphology
PS- <i>b</i> -PMMA diblock copolymers (SMMA)				
SMMA400k10%	431	1.16	10	<b>S</b>
SMMA400k20%	394	1.20	20	<b>C</b>
SMMA400k40%	413	1.14	40	<b>L</b>

PHYSICAL FOAMING – SOLUBILITY VS. MOBILITY. In the synthesized SI and SMMA diblock copolymers, either the chain mobility (SI) or the  $\text{CO}_2$ -solubility (SMMA) is varied, affecting the resulting diblock copolymers' foaming behavior and enabling an independent investigation of their influence. Figure 5.10 illustrates the SEM images of SI and SMMA-based foams foamed at  $T_f = 120 \text{ }^\circ\text{C}$ .

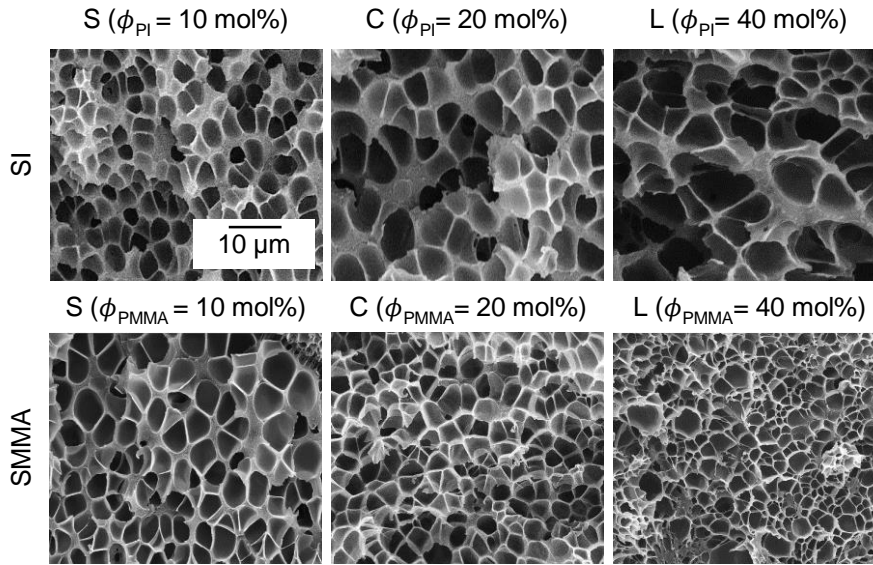


Figure 5.10. SEM images of SI and SMMA diblock copolymers with spherical (S), cylindrical (C), and lamellar (L) morphology. The scaling bar is valid for each image within this figure. Foaming conditions:  $T_f = 120 \text{ }^\circ\text{C}$ ,  $p = 500 \text{ bar}$ ,  $t_{\text{sat}} = 8 \text{ h}$ , and  $dp/dt \approx 200 \text{ bar s}^{-1}$ .

The SEM images imply an inverse behavior of  $D$  with increasing fractions of PI or PMMA. The cell size increases with increasing comonomer amount ( $\phi_{\text{PI,PMMA}} = 10 \% - 40 \%$ ) using SI diblock copolymers, whereas  $D$  of SMMA-based foams decreases.

One crucial factor in the foaming of block copolymers is the processing window of the individual polymers.<sup>196</sup> The  $T_f$  was adjusted as follows:  $T_f = 60 \text{ }^\circ\text{C} - 120 \text{ }^\circ\text{C}$  (SI) and  $T_f = 100 \text{ }^\circ\text{C} - 140 \text{ }^\circ\text{C}$  (SMMA), as SI-based foams collapsed already at  $T_f > 120 \text{ }^\circ\text{C}$  due to  $\text{CO}_2$ -loss. In contrast, foamed SMMA resulted in a pronounced heterogeneous cell morphology at  $T_f < 100 \text{ }^\circ\text{C}$ . Figure 5.11 depicts  $N$  as a function of  $T_f$  for foamed SI (a) and SMMA (b) with  $M_w \approx 400 \text{ kg mol}^{-1}$  and  $\phi_{\text{PI,PMMA}} = 10 \text{ mol}\% - 40 \text{ mol}\%$ .

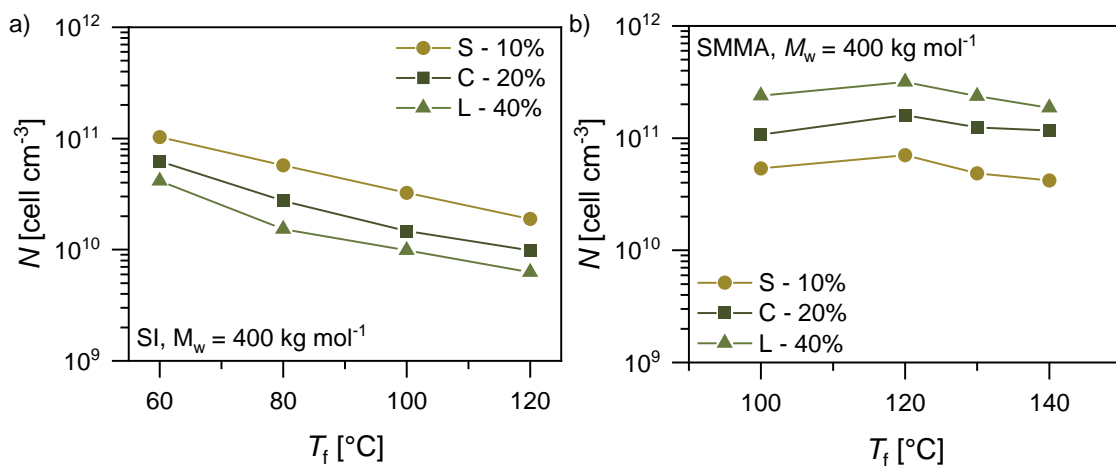


Figure 5.11. Cell density  $N$  as a function of the foaming temperature  $T_f$  for SI (a) and SMMA (b) diblock copolymers with  $M_w \approx 400 \text{ kg mol}^{-1}$  and  $\phi_{\text{PI,PMMA}} = 10 \text{ mol}\% - 40 \text{ mol}\%$ , resulting in spheres (S), cylinders (C), or lamellas (L), respectively.

Foaming conditions:  $T_f = 60 \text{ }^\circ\text{C} - 140 \text{ }^\circ\text{C}$ ,  $p = 500 \text{ bar}$ ,  $t_{\text{sat}} = 8 \text{ h}$ , and  $dp/dt \approx 200 \text{ bar s}^{-1}$ .

The trends of the SI diblock copolymers have been thoroughly discussed in Chapter 5.1. In summary, higher nucleation densities are obtained with lower foaming temperatures and a spherical microdomain morphology. The cell density varies between  $N = 6.30 \times 10^9$  and  $1.03 \times 10^{11}$  cell  $\text{cm}^{-3}$  for  $\phi_{\text{PI}} = 10$  mol% to 40 mol% at  $T_f = 60$  °C – 120 °C. In contrast, cell densities between  $N = 4.19 \times 10^{10}$  and  $3.16 \times 10^{11}$  cell  $\text{cm}^{-3}$  were found within foamed SMMA diblock copolymers within  $T_f = 100$  °C – 140 °C. The following trends become apparent: First, only minor differences can be detected compared to the temperature influence in SI-based diblock copolymer foams. Second, with higher PMMA-content, the  $\text{CO}_2$ -solubility increases, which ultimately favors nucleation, leading to  $N = 3.16 \times 10^{11}$  cell  $\text{cm}^{-3}$  for SMMA400k40% at  $T_f = 120$  °C. Figure 5.12 compares the achieved  $N$  of SI and SMMA, influenced by heterogeneous chain mobility or  $\text{CO}_2$ -solubility at  $T_f = 100$  °C (a) and 120 °C (b). Foaming temperatures of  $T_f = 100$  °C – 120 °C were chosen to compare the resulting cell morphology under the same foaming conditions.

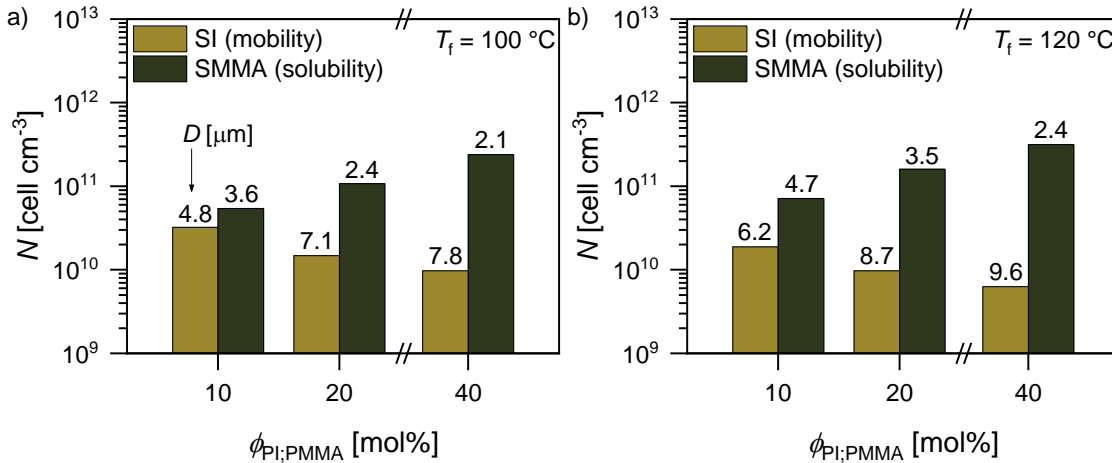


Figure 5.12. Cell density  $N$  as a function of the comonomer content  $\phi_{\text{PI;PMMA}}$  of SI- and SMMA-based foams. Foaming conditions:  $T_f = 100$  °C (a) and 120 °C (b),  $p = 500$  bar,  $t_{\text{sat}} = 8$  h, and  $dp/dt \approx 200$  bar  $\text{s}^{-1}$ . The number above the bars correspond to the average cell size in  $\mu\text{m}$ .

At both foaming temperatures,  $N$  increases with increasing  $\phi_{\text{PMMA}}$ , whereas it decreases with increasing  $\phi_{\text{PI}}$ . A higher  $\text{CO}_2$ -solubility with similar chain mobility of both polymer blocks (SMMA) favors higher  $N$  values than mobility differences (SI). This can be attributed to the higher cell growth rate and the significantly more pronounced tendency for cell coalescence in the soft PI-phase. Moreover, with decreasing  $N$  (SI), the cell size increases from  $D = 4.8 - 7.8$   $\mu\text{m}$ , whereas increasing  $N$  values (SMMA) results in reduced average cell sizes from  $D = 3.6 - 2.1$   $\mu\text{m}$  at  $T_f = 100$  °C, as expected from CNT.

However, it should be noted that a foaming temperature of  $T = 100$  °C or 120 °C is still not ideal for the SI samples due to the already low viscosity of the PI-phase. However, a direct comparison under the same foaming conditions at lower  $T$  is not possible due to the resulting heterogeneous cell morphology within the SMMA samples.



Nevertheless, comparing foams produced using different foaming conditions is challenging because the CO<sub>2</sub>-solubility depends on the temperature, as introduced in Chapter 2.2, see Figure 2.4 and Equation (2.3). Thus, the PS-blocks' characteristics, i.e., solubility and mobility, would also vary. Comparable characteristics of both copolymers are often advantageous for promoting simultaneous nucleation and cell growth in both copolymer phases.<sup>196</sup>

Similar observations have been made in immiscible blends of amorphous PS and a semi-crystalline PEG, where the amorphous fraction within the PEG-phase exhibits a significantly higher solubility towards CO<sub>2</sub>.<sup>28,188</sup> Foaming resulted in a heterogeneous cell size distribution, while larger cells were formed within the PEG-phase. The authors postulated the behavior of the inherent mobility and solubility differences between the two polymer phases. Furthermore, the authors suggested a morphological evolution mechanism, where cell nucleation and growth start in the low viscous PEG-phase. Once the cell growth spreads to the more viscous PS-phase, the cells within the PEG-phase already begin to collapse, forming larger cells until the matrix is solidified.

The results of studying the heterogeneity of blowing agent solubility and chain mobility reveal that a positive influence on the cellular morphology in terms of higher  $N$  and lower  $D$  values strongly depends on the corresponding foaming temperature. While the cell density at higher  $T_f$  is more likely to be increased using a higher blowing agent solubility (SMMA), a softer polymer phase, i.e., lower  $T_g$  (SI), with a spherical microdomain morphology, is advantageous to support nucleation and achieve higher  $N$  at lower  $T_f$ . Therefore, it is necessary to distinguish between both effects concerning the desired process conditions.

### 5.3 INTRINSIC AND EXTRINSIC HETEROGENEOUS NUCLEATION

Disclaimer. The nucleation particles were provided by Prof. Dr. Claus Feldmann (Institute of Inorganic Chemistry, Karlsruhe Institute of Technology (KIT)). Synthesis and characterization of the particles were carried out by Mark Rutschmann.

---

The standard procedure to impact nucleation and, therefore, cell density of a polymer foam is adding nucleation particles to the polymer melt. To compare the intrinsic nucleation of phase boundaries in block copolymers with extrinsic nucleation caused by the addition of nucleation particles, an increasing weight percentage  $w$  of SiO<sub>2</sub>-nanocarrier particles with  $w_{\text{SiO}_2} = 0.25 - 1.00$  wt% and an average diameter of  $d_{\text{SiO}_2} \approx 80$  nm were added to a linear PS with  $M_w = 310$  kg mol<sup>-1</sup> (PS310k). The nanoparticles were melt blended with linear PS for 5 min at 180 °C using a minilab extruder. A homogeneous distribution was evaluated by SEM analysis. Details about the synthesis procedure and characterization of these nanoparticles can be found in the literature.

Moreover, SI, SIS, and ISI block copolymers were used as comparative. For each block copolymer type, the sample that maintained the highest  $N$  values after foaming was used for the comparison, i.e., SIS with  $M_w = 400 \text{ kg mol}^{-1}$ ,  $\phi_{\text{PI}} = 10 \text{ mol}\%$ . Figure 5.13 displays the SEM images of the corresponding foams at  $T_f = 80 \text{ }^\circ\text{C}$ .

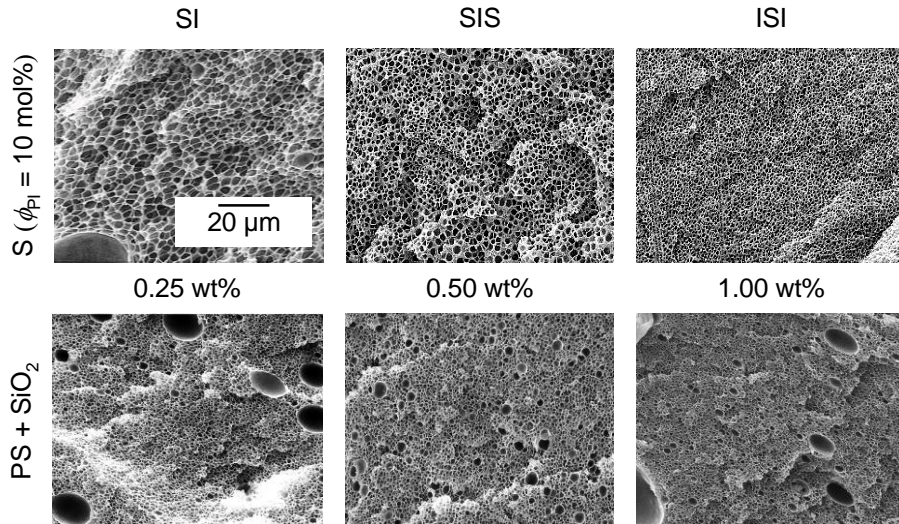


Figure 5.13. SEM images of PS- and PI-based di- and triblock copolymers with  $M_w = 400 \text{ kg mol}^{-1}$  and  $\phi_{\text{PI}} = 10 \text{ mol}\%$  with a spherical (S) morphology and PS301k with added  $\text{SiO}_2$ -based nanoparticles with  $d_{\text{SiO}_2} \approx 80 \text{ nm}$  and  $w_{\text{SiO}_2} = 0.25 - 1.00 \text{ wt}\%$ . The scaling bar is valid for each image within this figure. Foaming conditions:  $T_f = 80 \text{ }^\circ\text{C}$ ,  $p = 500 \text{ bar}$ ,  $t_{\text{sat}} = 8 \text{ h}$ , and  $dp/dt \approx 200 \text{ bar s}^{-1}$ .

As indicated by the SEM images and discussed in Chapter 5.1, all foams based on block copolymers exhibit a relatively homogeneous cell structure. However, the samples with added  $\text{SiO}_2$  nanoparticles show macroscopic defects. The  $N$  as a function of  $T_f$  of the resulting foams based on either the block copolymers or the linear PS with added  $\text{SiO}_2$ -particles is represented in Figure 5.14 a) and b), respectively.

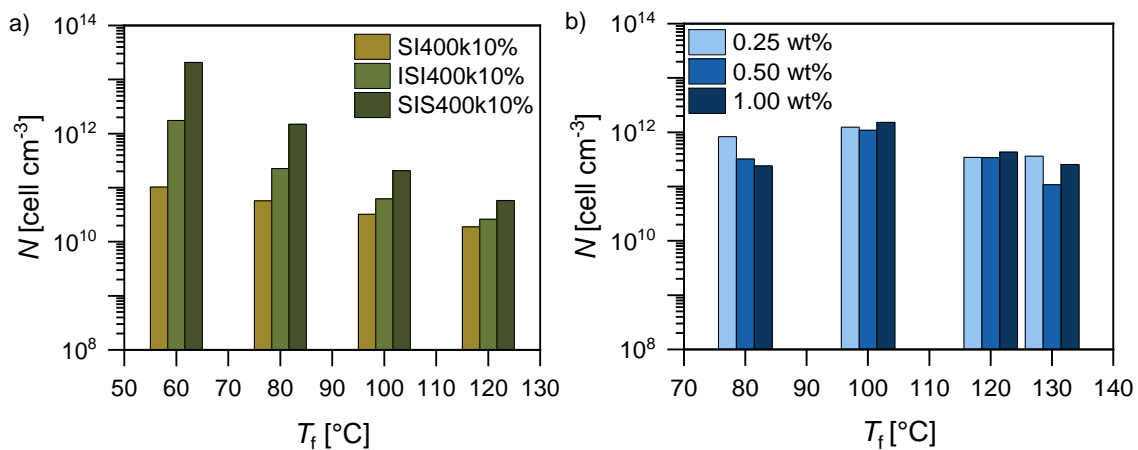


Figure 5.14. Cell density  $N$  as a function of the foaming temperature  $T_f$  for PS-, PI- and PMMA-based block copolymers (a) and PS with an increasing weight percentage from  $w = 0.25 - 1 \text{ wt}\%$  of nucleation particles (b). The samples listed were selected according to their maximum achieved  $N$ . Foaming conditions:  $T_f = 60 \text{ }^\circ\text{C} - 130 \text{ }^\circ\text{C}$ ,  $p = 500 \text{ bar}$ ,  $t_{\text{sat}} = 8 \text{ h}$ , and  $dp/dt \approx 200 \text{ bar s}^{-1}$ .

Cell density decreases with increasing foaming temperature for both the block copolymers based on PS and PI and the PS+SiO<sub>2</sub>-based systems. While the influence of phase boundaries on cell nucleation has already been discussed in the previous sections of Chapter 5, the focus here is on its comparison with the usage of particles and its comparison with the block copolymers. In general,  $N$  increases slightly with increasing weight percentage of SiO<sub>2</sub>-particles, except for a foaming temperature of  $T_f = 80$  °C. However, especially at a foaming temperature of  $T_f = 120$  °C,  $N$  values show no clear trend. Agglomerates may have formed here, which have a negative effect on cell nucleation as they reduce the overall particle concentration. Also, their size is greater, and it is known that increased nucleation particles are less efficient in nucleation.

Within the investigated temperature window of  $T_f = 60$  °C – 120 °C, SIS400k10% with PI-spheres achieved similar  $N$  values as the PS+SiO<sub>2</sub> systems. It should be mentioned that the foams based on PS+SiO<sub>2</sub> led to an inhomogeneous cell distribution, as mentioned before, for pure PS matrices. The soft PI-phase of the block copolymers allows foaming at lower temperatures due to its high chain mobility and low  $T_g$ . Simultaneously, the matrix undergoes greater plasticization due to the increased CO<sub>2</sub>-solubility. While the high mobility of the PI chains also ensures that the cells in SI and ISI block copolymers tend to coalesce since the PI-blocks are only covalently linked to PS at one chain end and, thus, have a free, moving chain end enhancing coalescence. Overall, it can be stated that SIS400k10% with PI-spheres behaves similarly to the extrinsic nucleation particles studied. The statistical cellular parameters exhibit similar trends, even though the size distribution of the particles is more heterogeneous. The more heterogeneous particle size distribution might be the reason for the macroscopic cells within the foams observed in the SEM images shown in Figure 5.13.

Compared to block copolymers and polymer/particle systems in the literature, the achieved cell densities for nanocellular foams are considered to be relatively low and the cell size is rather large. Ideal values are up to  $N \approx 10^{15} - 10^{16}$  cell cm<sup>-3</sup> and cell sizes smaller than 100 nm. Foams with this combination are expected to achieve a significantly reduced thermal conductivity, attributed to the frequent collision of gas molecules with the cell walls than other gas molecules. This diffusive phenomenon is known as Knudsen-effect<sup>38,39</sup> and occurs if the cell sizes are only around the mean free path of gas molecules (approximately 70 nm). The high cell density, i.e., high porosity and thin cell walls, ensure no heat transfer through the solid polymer.

However, this basic investigation that only gave some initial insights into cell nucleation should be further deepened based on the first promising findings of intrinsic cell nucleation within SIS400k10%. Moreover, also the particles can be optimized regarding higher nucleation efficiencies, for instance, by chemically modifying the particle surface with low surface energy polymers combined with a high CO<sub>2</sub>-affinity, like PDMS.



---

## 6 CELL GROWTH

Topology determines polymers' melt shear and extensional rheological properties and, thus, the expansion process. This chapter defines critical topological parameters of branched architectures and uses their rheological characteristics to explain the origins of foamability. Notably, foamability is frequently associated with high foam homogeneity, relatively small cell size, and low foam density.<sup>196</sup> By systematically varying the topology regarding backbone and sidearm length, number of sidearms and stars, the influence of shear and elongational viscosity, and the corresponding strain hardening behavior are discussed. The correlation of melt rheological properties with the resulting cellular structure of the foams reveals maximized volume expansion ratios and average cell sizes through maximum stretchability and low viscosity. Additionally, architectural suggestions regarding a particular cellular morphology are listed, like combining high volume expansion and small cells.

Disclaimer. The content of this chapter has been published in *Macromolecules* (ACS) and *Macromolecular Chemistry and Physics* (Wiley-VCH GmbH).<sup>107,203,204</sup> Parts of this chapter and the corresponding parts in the experimental section were adapted with permission from Röpert, M.-C.; Schußmann, M. G.; Esfahani, M. K.; Wilhelm, M.; Hirschberg, V. Effect of Side Chain Length in Polystyrene POM-POMs on Melt Rheology and Solid Mechanical Fatigue. *Macromolecules* 2022. DOI: 10.1021/acs.macromol.2c00199. Copyright 2022 American Chemical Society; Röpert, M.-C.; Goecke, A.; Wilhelm, M.; Hirschberg, V. Threading Polystyrene Stars: Impact of Star to POM-POM and Barbwire Topology on Melt Rheological and Foaming Properties. *Macromol. Chem. Phys.* 2022, 2200288. DOI: 10.1002/macp.202200288. Copyright 2022 Wiley-VCH GmbH; and Röpert, M.-C.; M.; Hirschberg; Schußmann, M. G.; Wilhelm, M. Impact of Topological Parameters on Melt Rheological Properties and Foamability of PS POM-POMs. *Macromolecules* 2023. DOI: 10.1021/acs.macromol.2c02051. Copyright 2022 American Chemical Society. All publications are written by the author (Marie-Christin Röpert). Parts of the experimental work result from supervising the master thesis or advanced work ("Vertiefearbeit") of Max Schußmann and Anika Goecke, respectively, in collaboration with Dr. Valerian Hirschberg.

---

Foaming of polymers and particularly the foam expansion, i.e., cell growth, requires specific polymer characteristics such as a sufficiently low melt shear viscosity  $\eta(\dot{\gamma})$  in combination with a high melt strength to enhance the elongation behavior of the polymer melt.<sup>1,3-6,33</sup> Consequently, both zero-shear viscosity  $\eta_0$  and elongational melt strength are essential rheological parameters for understanding and controlling the flows' respective processing behavior in polymer foaming. Polymers combining these two key rheological parameters are ideally suited for foaming since they enhance foamability by minimizing cell coalescence and rupture. Accordingly, the viscoelastic behavior of the melt is rather the origin of a homogeneous foam morphology, combined with a small average cell size  $D$  and a high volume expansion ratio  $VER$ , i.e., low foam density  $\rho_f$ .<sup>9,10,57,62,205,206</sup>

Modifying the architecture of a polymer through the introduction of undefined long-chain branches is a common procedure in both academic and industry. Insufficiently controllable synthesis routes frequently lead to rather unknown and undefined topologies regarding arm length, location, and number of branches. The most prominent example of a long-chain branched polymer with industrial relevance might be LDPE.

Despite the substantial industrial importance of undefined long-chain branched polymers like LDPE, only a limited number of low-disperse polymers with a defined topology have been examined. Therefore, the correlation of specific topological parameters with the melt rheological properties and the foam morphology remains challenging. The majority of studies that utilize defined polymers with a specified structure are based on predominantly semi-crystalline polymers.<sup>9–14,206,207</sup> For instance, a series based on isotactic polypropylene (*i*-PP) and poly(ethylene-co-1-butene) was synthesized, yielding combs with a crystalline backbone and amorphous sidearms.<sup>12</sup> The branching density varied from 1.17 – 11.9 branches per  $10^4$  carbon of the *i*-PP backbone, and arm lengths ranged between 1.45 – 37.8 kg mol<sup>-1</sup>. The complexity of separating the effects of viscoelasticity and crystallinity on foam morphology has been reported due to the continuously altered ratio of crystalline backbone and amorphous arms. Additionally, the copolymerization of a semi-crystalline and an amorphous polymer typically leads to localized phase separation, impacting the nucleation behavior due to forming phase boundaries.<sup>12,208</sup> However, it was determined that the arm length had a more significant impact on the melt rheological properties in contrast to the branching density. To avoid this overlap, it is crucial to investigate amorphous, well-defined polymer architectures to determine the underlying structure-property relationship of topology and cellular morphology.

In one of the few studies examining the effect of rheological properties of solely amorphous polymers on foam morphology, atactic LCB-PS was modified by free radical polymerization resulting in branching levels ranging from 0.15 to 1.6 branching points per  $10^4$  carbon atoms.<sup>62</sup> By extending the backbone length, the materials' viscosity and elasticity were increased, leading to reduced  $D$ . Moreover, the influence of branching became more pronounced at higher foaming temperatures, ranging from 60 °C to 110 °C. In the preliminary work of our group, melt rheological properties were investigated and correlated to the cellular morphology based on well-defined, monodisperse PS combs with increasing branching density. The samples were foamed at  $p = 180$  bar and  $T_f = 125$  °C – 145 °C.<sup>57,209</sup> The synthesized combs had the same backbone length with  $M_{w,b} = 290$  kg mol<sup>-1</sup>, the same sidearm length with  $M_{w,b} = 44$  kg mol<sup>-1</sup> and an overall arm number of  $q = 3 - 190$ . It was found that  $q \approx 120$  is the optimal number of arms per backbone to achieve the highest foam expansion with  $VER = 40$  for polymer combs. The combination of these topological parameters in PS combs coupled a maximum strain hardening factor of  $SHF = 200$  with a rather low zero-shear viscosity of  $\eta_0 = 1.68 \times 10^5$  Pa s at  $T_{ref} = 180$  °C.

In another approach, a second generation of short sidearms with  $M_w = 14 \text{ kg mol}^{-1}$  was grafted onto a comb polymer, leading to dendritic (branch-on-branch, bob) structures. With  $SHF_{\max} > 1,700$  ( $\dot{\epsilon} = 0.005 \text{ s}^{-1}$ ,  $T = 180 \text{ }^\circ\text{C}$ ), the impact of the bob topology was extraordinarily pronounced. However, the influence on the cellular structure was negligible, as the relevant shear rates during foaming are between  $1 \text{ s}^{-1}$  and  $10 \text{ s}^{-1}$ .<sup>210</sup>

The experiments using defined architectures demonstrate the enormous relevance of controlled topologies to evaluate the structure-property relationship. Besides H-polymers, the pom-pom topology is considered to be the simplest yet defined molecular architecture, combining strain hardening in elongational flow and strain softening in shear. However, a comprehensive understanding of the interrelationship between the topology of branched amorphous structures and the resulting foam morphology remains elusive. Consequently, it is still unknown how to select defined polymer topological parameters like backbone length, arm length, and number to incorporate the necessary rheological behavior for tuning the cellular structure of polymer foams in terms of  $VER$  and  $D$  concerning desired applications.

## 6.1 THE POM-POM TOPOLOGY

Polymers with a pom-pom topology consist of two star-shaped polymers covalently connected with a linear polymer chain, as visualized in Figure 6.1. The topology can be described by three main structural parameters, (I) the weight average molecular weight of sidearms  $M_{w,a}$ , (II) the number of sidearms per star  $q$ , and (III) the weight average molecular weight of the backbone  $M_{w,b}$ . Different approaches have been investigated to synthesize pom-pom-shaped polymers, either by covalently linking two stars or coupling a dianion with an excessive amount of tetra- or hexa-functional linkers, such as tetrachlorosilane.<sup>211-213</sup> However, the nature of this reaction type restricts the number of sidearms to typically three to five, as one functionality per star is required to connect the backbone.

**ANIONIC POLYMERIZATION AND GRAFTING-ONTO.** Well-defined and low-dispersed PS pom-pom-shaped polymers were polymerized by combining LAP and a grafting-onto methodology. First, a PI-*b*-PS-*b*-PI triblock copolymer (ISI) is synthesized by sequential LAP in cyclohexane, later serving as the backbone. Cyclohexane was chosen as an unpolar solvent to increase the content of the 1,4-*cis* configuration of the double bonds of the PI-blocks<sup>147-149</sup>, as only this configuration can be epoxidized.<sup>214</sup> The double bonds within the PI-blocks were subsequently epoxidized by a Prileschajew reaction<sup>214</sup>, yielding approximately 50 % conversion of double bonds to epoxides. The synthesis procedure was followed by freeze-drying of the samples. Previously synthesized living anionic PS chains were grafted onto the epoxidized ISI-precursor resulting in the characteristic pom-pom architecture. The synthetic procedure is shown in Figure 6.1.

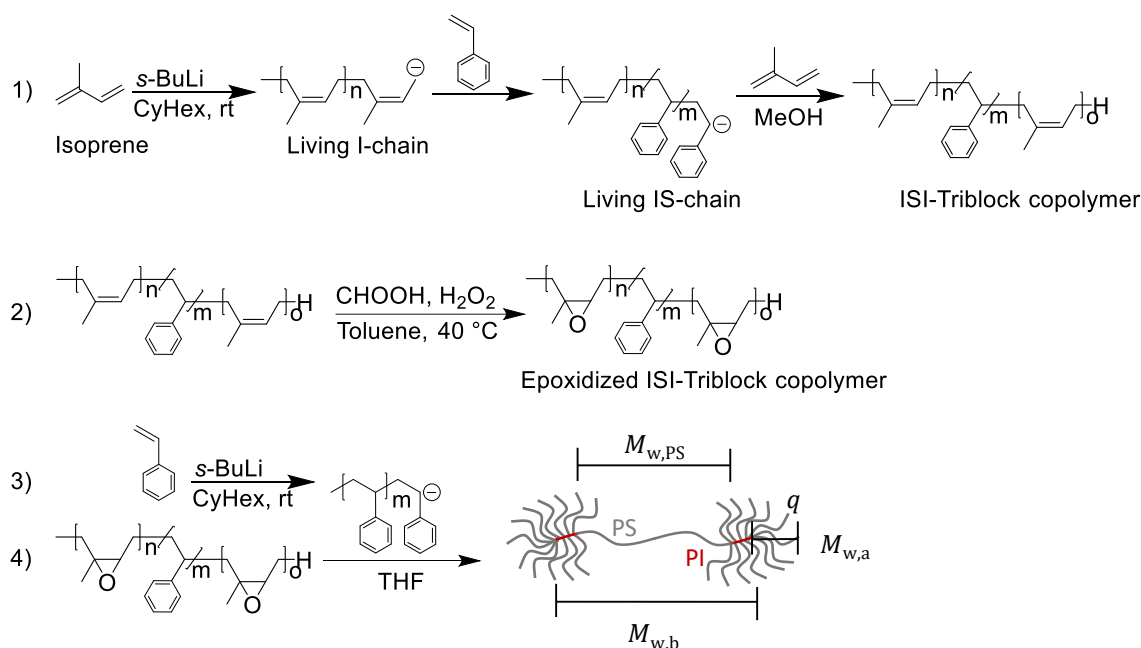


Figure 6.1. The synthesis procedure of low-disperse PS pom-poms is exemplary outlined using the following molecular parameters:  $M_{w,b} = 100 \text{ kg mol}^{-1}$ ,  $M_{w,a} = 50 \text{ kg mol}^{-1}$  and  $q \approx 2 \times 14$ . 1) Living anionic polymerization of an ISI triblock copolymer as backbone, 2) epoxidation of the double bonds within the PI-blocks via Prileschajew reaction, 3) Living anionic polymerization of PS sidearms, 4) grafting of living sidearms onto the epoxidized ISI-precursor.

This synthetic approach enables high control over the molecular parameters and allows the grafting of a small or large number of sidearms. According to  $^1\text{H-NMR}$  measurements, the PI-blocks of the backbone have a fixed length of each  $M_{w,PI} = 5 \text{ kg mol}^{-1}$ , corresponding to approximately 70 isoprene units on each side. The topological parameters were systematically adjusted within the following range:  $M_{w,b} = 100 - 400 \text{ kg mol}^{-1}$ , with  $q \approx 2 \times 5 - 2 \times 30$  of  $M_{w,a} = 7 - 300 \text{ kg mol}^{-1}$ . Typically, two to three fractionation steps were necessary to purify the mixture of pom-pom and non-grafted linear PS-sidearms. The detailed polymerization procedure and characterization methods are listed in the Appendix, Chapters A.3 and B, respectively. For instance, the pom-poms with sidearms of around  $q \approx 12$  chains per star result in materials with a high branching density of about one sidearm at roughly every sixth isoprene unit. A pom-pom topology with a star branching density  $Z_s$  of about  $Z_s = Z_{b,PI}/(q + 1) \approx 0.083$  entanglements between each branching point can be considered as two connected loosely grafted bottlebrushes. A loosely grafted bottlebrush is defined by  $0.021 \leq Z_s \leq 0.14$ .<sup>209</sup> In this regard, the materials are not classical pom-poms, where the sidearms emanate only from both endpoints of the backbone.

The molecular weight of the backbone, the sidearms, and the resulting pom-pom were determined by size exclusion chromatography (SEC) with either a differential refractometer (DRI) or multiangle laser light scattering (MALLS) detector. Two approaches were used to identify the number of sidearms  $q$  based on SEC.<sup>209</sup>



First,  $M_{w,t}$  of the pom-pom was used to calculate  $q$  based on the known molecular weight of both the sidearms and the backbone itself, yielding

$$q_c = \frac{(M_{w,t} - M_{w,b})}{M_{w,a}}. \quad (6.1)$$

However, the molecular weight of the ISI-precursor and the PS sidearms were individually determined via DRI detection before grafting. The second possibility to investigate the mixture of pom-pom and linear sidearms is via SEC-MALLS with

$$q_n = \left(\frac{m_t}{m_r}\right) \times \left(\frac{n_a}{2n_b}\right), \quad (6.2)$$

where  $m_t$  is the known total mass of the pom-pom,  $m_r$  is the total mass of the raw product,  $n_a$  is the total number of added sidearms,  $n_b$  is the number of backbones. More details about the measurements can be found in the Appendix, see Chapter B.1. The molecular details of all synthesized PS pom-poms, ISI-precursor, and linear PS references ( $M_w \approx M_{w,b}$ ) are summarized in Table 6.1. The samples are abbreviated as  $M_{w,b}-2 \times q - M_{w,a}$ .

Table 6.1. Molecular characteristics of the PS pom-poms, linear ISI-precursor, and PS references.

Sample	Series	<sup>a</sup> $M_{w,t}$ [kg mol <sup>-1</sup> ]	<sup>a</sup> $\mathcal{D}_t$	<sup>b</sup> $q_c$	$M_{w,a}$ [kg mol <sup>-1</sup> ]	$\mathcal{D}_a$	<sup>d</sup> $Z_a$
PS100k	-	100	1.01	-	-	-	<sup>c</sup> 5.95
PS310k	-	310	1.10	-	-	-	<sup>c</sup> 17.26
ISI(PS90k-2×5k(PI))	-	100	1.05	-	-	-	<sup>c</sup> 7.50
ISI(PS210k-2×5k(PI))	-	220	1.06	-	-	-	<sup>c</sup> 14.72
ISI(PS390k-2×5k(PI))	-	400	1.11	-	-	-	<sup>c</sup> 25.44
100k-2×5-25k	Q <sub>a,s</sub>	350	1.12	2×5	25	1.05	1.43
100k-2×9-25k	Q <sub>a,s</sub> , B	550	1.15	2×9	25	1.11	1.43
100k-2×9-110k	Q <sub>a,l</sub>	2,080	1.29	2×9	110	1.16	6.54
100k-2×11-9k	A	298	1.13	2×11	9	1.02	0.53
100k-2×12-24k	Q <sub>a,s</sub> , A	600	1.18	2×12	24	1.05	1.43
100k-2×12-40k	A	1,060	1.16	2×12	40	1.08	2.38
100k-2×12-120k	Q <sub>a,l</sub> , A	2,980	1.56	2×12	120	1.12	7.14
100k-2×14-50k	A	1,500	1.27	2×14	50	1.20	2.97
100k-2×14-300k	A	8,220	1.27	2×14	300	1.14	18.45
100k-2×22-25k	Q <sub>a,s</sub>	1,200	1.15	2×22	25	1.14	1.43
100k-2×22-110k	Q <sub>a,l</sub>	4,940	1.06	2×22	110	1.04	6.54
220k-2×9-25k	B	670	1.16	2×9	25	1.05	1.49
400k-2×9-23k	B	814	1.24	2×9	23	1.04	1.37

<sup>a</sup>Dispersities were determined from the SEC-DRI signal, whereas absolute weight average molecular weights were obtained using MALLS detections. <sup>b</sup>The number of sidearms per star is calculated by Equation (6.2). <sup>c</sup>Entanglement number of the total linear polymer. <sup>d</sup> $M_{e,PS} = 16.8 \text{ kg mol}^{-1}$ ,  $M_{e,PI} = 4.5 \text{ kg mol}^{-1}$ .<sup>201</sup>

First, the rheological properties of the individual series are examined, followed by the influence of the respective topological parameters on the cell morphology. The overall topological impact is then correlated with underlying rheological properties and foamability.

**MELT RHEOLOGICAL PROPERTIES.** During cell growth, the polymer melt experiences both shear and biaxial elongational deformation.<sup>59,60</sup> As discussed in detail in Chapter 3.2, cell growth is primarily influenced by shear and elongational deformations within the linear viscoelastic regime. As the cell wall becomes thinner during cell expansion, non-linear biaxial elongational viscosity governs cell growth. Consequently, exploring the polymer melts' shear viscosity (shear flow) and strain hardening behavior (elongational flow) is particularly relevant when examining polymers' foamability.

The viscoelastic behavior was analyzed through SAOS measurements, focusing on the impact of the topological parameter. The results were referenced to  $T_{\text{ref}} = 160 \text{ }^\circ\text{C}$ , yielding to the master curves of  $G'$  and  $G''$  shown in Figure 6.2.

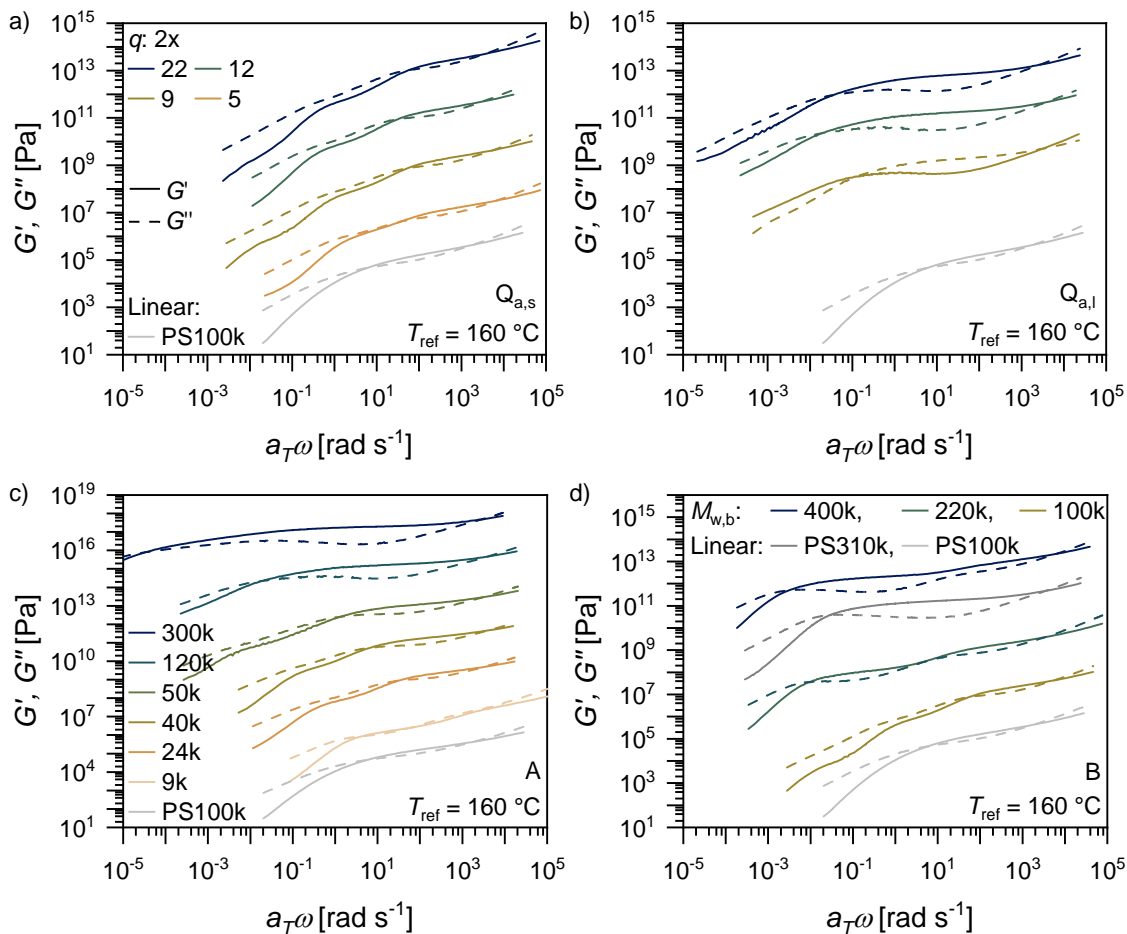


Figure 6.2. Pom-pom master curves; series:  $Q_{a,s}$  (a),  $Q_{a,l}$  (b), A (c), and B (d) at  $T_{\text{ref}} = 160 \text{ }^\circ\text{C}$ . The rheological response shows three characteristic regimes with increasing angular frequency: the flow behavior of the whole molecule in the terminal regime ( $G' \propto \omega^2$ ,  $G'' \propto \omega^1$ ), the backbones' relaxation process, and the rheological influence of the sidearms at  $a_T\omega < 10^3 \text{ rad s}^{-1}$ . The master curves were vertically shifted by a factor of  $10^2$ , for instance, in a)  $10^2$ ,  $10^4$ ,  $10^6$ , and  $10^8$ .

All pom-pom-shaped samples exhibit the expected scaling behavior of  $G' \propto \omega^2$  and  $G'' \propto \omega^1$  at low frequencies, i.e., in the terminal regime. For the sample with unentangled sidearms, 100k-2×11-9k ( $M_{w,a} < M_e$ ), only a rubber plateau is found in the low-frequency regime at  $G'$  values between  $10^5 - 10^6$  Pa, which can be attributed to the entangled backbone. Analogous rheological behavior is described in the literature for a densely grafted comb.<sup>209,215,216</sup> It was postulated that the combs' sidearms dilute the entanglements of the entire molecule, leading to solvent-free super-soft materials.<sup>215</sup> Moreover, pom-pom topologies with an entangled backbone but unentangled sidearms respond similarly as blends of high and low molecular weight linear chains, where the molecular weight of the short chains is equivalent to  $M_{w,a}$ , and one of the long chains corresponds to two times  $M_{w,a}$  plus  $M_{w,b}$ .<sup>217</sup>

All samples with  $M_{w,a} \leq 50$  kg mol<sup>-1</sup> show one rubber plateau caused by the sidearms at high  $a_T\omega$  and a regime, where  $G'$  and  $G''$  are parallel with a scaling exponent of 0.6 in a double-logarithmic plot at low  $a_T\omega$ . A slope of 0.6 indicates that the backbone exhibits constraint release Rouse-like behavior instead of a reptation mechanism.<sup>209,215,218-220</sup> This phenomenon may be attributed to the entangled sidearms, which entangle with the backbone and prevent the backbone from becoming entangled with itself, resulting in the absence of the backbones' rubber plateau.<sup>107</sup> Hence, these samples fall out of the scope and assumptions of the pom-pom model.<sup>218</sup> A similar trend has been observed in comb polymers with similar molecular characteristics.<sup>209,215,220</sup> By lengthening the backbone to  $M_{w,b} = 220 - 400$  kg mol<sup>-1</sup>, the backbones entangle with each other.

The entangled sidearms lead to a rubber plateau in the high-frequency regime. With increasing  $M_{w,a}$ , the rubber plateau extends to lower frequencies, resulting in a shift of the cross over to lower frequencies and an increase in the relaxation time. For instance, the rubber regime of the pom-pom with  $M_{w,a} = 300$  kg mol<sup>-1</sup> extends over eight decades, and the cross over point is barely reached even at  $T = 290$  °C. Notably, no degradation has occurred during the measurements up to  $T = 290$  °C under N<sub>2</sub>-atmosphere ( $\geq 99.5$  %), as analyzed via SEC measurements. Additionally, thermogravimetric analysis (TGA) experiments were exemplarily performed to investigate the temperature-dependent decomposition of the polymer under N<sub>2</sub>-atmosphere, see Figure B.2. The cross over occurs at very low angular frequencies of  $3.2 \times 10^{-5}$  rad s<sup>-1</sup>, which corresponds to a very long sidearm relaxation time of  $\tau_a \approx 196,500$  s (= 54.6 h) at  $T_{\text{ref}} = 160$  °C. The relaxation time of complex architectures follows a topology-defined order, also known as relaxation hierarchy.<sup>221,222</sup> Figure 6.3 illustrates  $\tau_a$  as a function of  $M_{w,a}$ , while  $\tau_a$  was either determined by the local maximum ( $M_{w,a} = 9 - 50$  kg mol<sup>-1</sup>), the inflection point ( $M_{w,a} = 120$  kg mol<sup>-1</sup>) or the value at  $\tan(\beta) = 1$  ( $M_{w,a} = 300$  kg mol<sup>-1</sup>), depending on the relaxation mechanism of the samples.

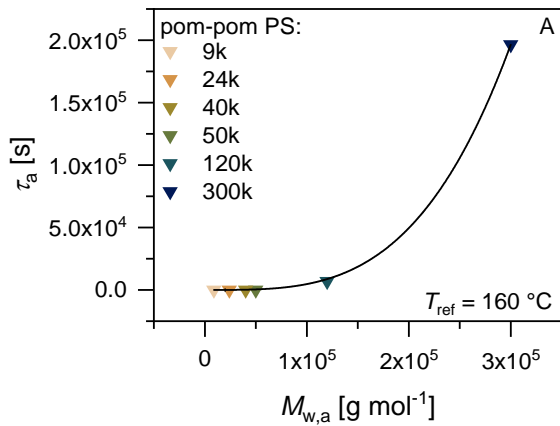


Figure 6.3. Sidearm relaxation time  $\tau_a$  is presented as a function of the weight average molecular weight of the side arms  $M_{w,a}$  at a reference temperature of  $T_{\text{ref}} = 160$  °C. The black solid line represents a non-linear least-square fit according to a simple power-law, where  $M_{w,a}$  is given in  $\text{g mol}^{-1}$  (prefactor =  $4.7 \times 10^{-14}$ , scaling exponent = 3.4).

Series A:  $M_{w,b} = 100 \text{ kg mol}^{-1}$ ,  $q \approx 2 \times 12$   
 $M_{w,a} = 7 - 300 \text{ kg mol}^{-1}$ .

The dominant sidearm relaxation time increases exponentially as expected with increasing  $M_{w,a}$ , which is attributable to the increasing  $Z_a$ .<sup>89</sup> Consequently, pinning the sidearms densely at one end to the backbone drastically slows down the relaxation process. Moreover, relaxed sidearms of branched polymers can act as an internal plasticizer, thereby accelerating the relaxation of long polymer chains and reducing  $\eta_0$ .<sup>221,222</sup>

The relaxation process of the sidearms is also reflected in the absolute value of the complex viscosity  $|\eta^*(\omega)|$ , since a second plateau at intermediate to high frequencies occurs in a  $|\eta^*|$  vs.  $a_T\omega$  plot, as exemplarily shown for series A in Figure 6.4.

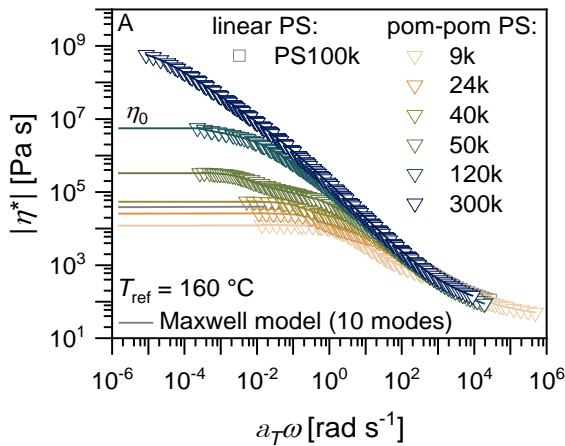


Figure 6.4. The absolute complex viscosity  $|\eta^*|$  as a function of the angular frequency  $a_T\omega$  at a reference temperature of  $T_{\text{ref}} = 160$  °C. The solid lines represent the fitting with the multi-mode Maxwell model (10 modes).

Series A:  $M_{w,b} = 100 \text{ kg mol}^{-1}$ ,  $q \approx 2 \times 12$   
 $M_{w,a} = 7 - 300 \text{ kg mol}^{-1}$ .

By fitting  $|\eta^*(\omega)|$  with the multi-mode Maxwell model,  $\eta_0$  can be obtained, which is a crucial parameter for the processing and foaming of polymers. In Figure 6.5,  $\eta_0$  values are displayed as a function of  $M_{w,t}$ . The materials' rheological parameters, like Maxwell modes and  $\eta_0$  values are provided in the Appendix, Table C.2.

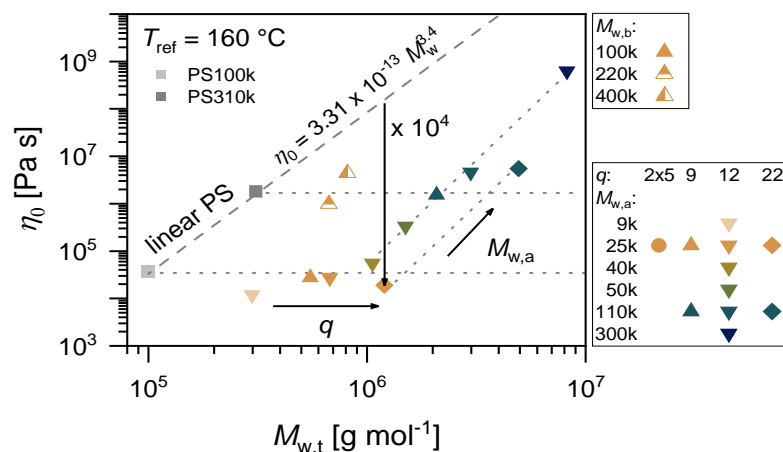


Figure 6.5. The zero-shear viscosity  $\eta_0$  as a function of the total weight average molecular weight  $M_{w,t}$  of pom-pom PS at  $T_{\text{ref}} = 160$  °C. Samples with the same symbol have the same  $q$  and the same color represents similar  $M_{w,a}$ . The closed symbols represent pom-poms with  $M_{w,b} = 100$  kg mol $^{-1}$ , and the half-open symbols pom-poms with  $M_{w,b} = 220$  kg mol $^{-1}$  and 400 kg mol $^{-1}$ . The grey squares are associated with linear PS references with  $M_{w,b} = 100$  kg mol $^{-1}$  and 310 kg mol $^{-1}$ . The dashed grey line corresponds to the predicted  $\eta_0$  of linear PS with increasing molecular weights in g mol $^{-1}$  and scales with  $\eta_0 \sim M_w^{3.4}$  (prefactor =  $3.31 \times 10^{-13}$ ). The dotted gray lines are guides for the eyes.

Since grafted sidearms plasticize the backbone,  $\eta_0$  of the pom-poms is reduced compared to linear PS with the same  $M_{w,t}$ , irrespective of their compositions. Comparing the pom-pom topology to its linear PS counterpart reveals a maximum viscosity reduction of a factor of  $10^4$ . In general, the following trends can be observed: As  $q$  increases (for  $M_{w,a} < 3 \times M_e$ ),  $\eta_0$  decreases slightly with  $M_{w,t}$  for same  $M_{w,a}$ , as the dilution effect is amplified by numerous sidearms. Furthermore,  $\eta_0$  increases with increasing  $M_{w,a}$  or  $M_{w,b}$  when  $q$  is held constant due to less dilution and higher entanglements of the sidearms or backbone.

Non-linear, uniaxial elongation measurements of all samples are conducted at 160 °C and strain rates between  $\dot{\epsilon} = 0.01$  s $^{-1}$  – 10 s $^{-1}$ . All branched samples exhibit strain hardening over a broad range of elongation rates, depending on their topological composition. The calculated  $SHF$  are summarized in the Appendix, see Table C.3. On the contrary, the linear PS reference having  $M_w = 100$  kg mol $^{-1}$  does not exhibit strain hardening during the selected measurement conditions. To establish a correlation between the  $SHF$  and the foaming potential of polymers, the maximum achieved strain hardening factor  $SHF_{\text{max}}$  measured at  $\dot{\epsilon} = 1$  s $^{-1}$  to 10 s $^{-1}$  was used. This particular range was deemed relevant in the context of polymer foaming processes.<sup>223</sup> The  $SHF_{\text{max}}$  of all samples are summarized in Figure 6.6 as a function of the respective topological parameter, i.e.,  $q$  (a),  $M_{w,a}$  (b), or  $M_{w,b}$  (c).

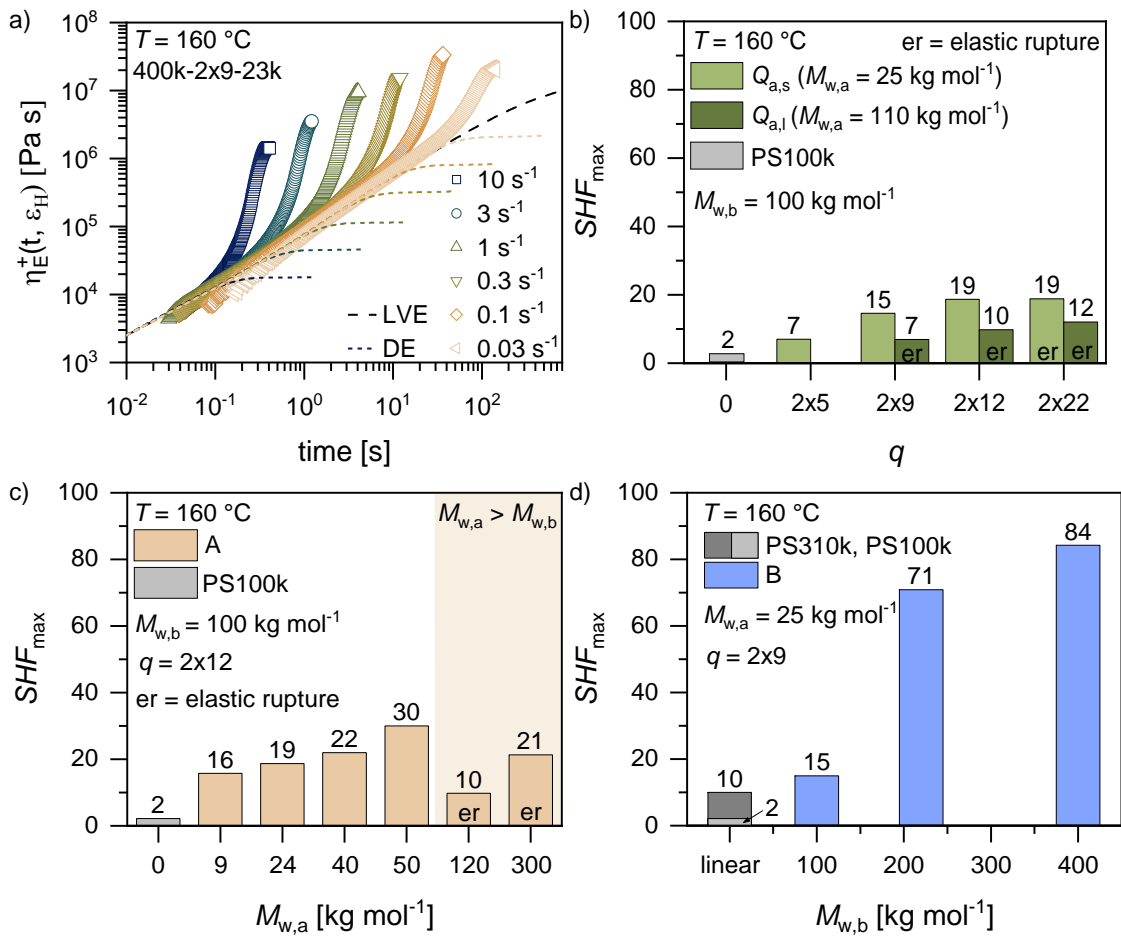


Figure 6.6. a) Viscosity growth curves of 400k-2x9-23k measured at elongation strain rates  $\dot{\epsilon} = 0.03\text{ s}^{-1} - 10\text{ s}^{-1}$  at  $T_{\text{ref}} = 160\text{ °C}$ . Dashed and dotted lines represent the linear viscoelastic (LVE) regime and the Doi-Edwards (DE) model, respectively.<sup>114,119,120</sup> Maximum strain hardening factor  $SHF_{\max} = \eta_{E,\max}^+(t, \dot{\epsilon}_H) / \eta_{E,DE}^+(\dot{\epsilon}_H)$  in the strain rate range of  $\dot{\epsilon} = 1\text{ s}^{-1}$  to  $10\text{ s}^{-1}$  as a function of the respective topological parameter measured at  $160\text{ °C}$ . The influence of  $q$  (series Q),  $M_{w,a}$  (series A), and  $M_{w,b}$  (series B) on the  $SHF_{\max}$  are shown in b) – d), respectively. The grey square represents the linear PS reference. All samples displaying elastic rupture are marked with “er”.

The linear PS reference PS100k has neither significant strain hardening nor softening between the imposed elongation rates at  $T = 160\text{ °C}$ . The Rouse time  $\tau_r$  for the linear PS reference is determined by the cross over of a vertical line with the value of  $G_N^0$  and fit in the high-frequency data of  $G'$  with a slope of 0.5, as described in the literature.<sup>209,219</sup> The Rouse relaxation time<sup>219</sup> can be estimated as  $\tau_{R,\text{lin}} = \tau_e Z^2$  at  $160\text{ °C}$ , where  $\tau_e = 7.87 \times 10^{-3}\text{ s}$  and  $Z = 5.95$  for the linear PS reference. Thus, strain hardening is anticipated to occur for strain rates larger than  $\tau_r^{-1} = 3.25\text{ s}^{-1}$ . Strain hardening can be observed at elongation rates higher than the inverse Rouse time, regardless of the materials' topology. However, monodisperse linear entangled polymers do not strain harden if  $\tau < 1/\tau_r$ . In contrast, branched polymers like the pom-pom-shaped PS will also strain harden at lower rates due to the presence of additional entanglements.

Series  $Q_{a,s}$  ( $M_{w,b} = 100 \text{ kg mol}^{-1}$ ,  $M_{w,a} = 25 \text{ kg mol}^{-1}$ , and  $q \approx 2 \times 5 - 2 \times 22$ ) and  $Q_{a,l}$  ( $M_{w,b} = 100 \text{ kg mol}^{-1}$ ,  $M_{w,a} = 110 \text{ kg mol}^{-1}$ , and  $q \approx 2 \times 5 - 2 \times 22$ ) show both an increase in strain hardening with increasing  $q$ , until a plateau is reached in  $Q_{a,s}$ . The  $SHF_{\max}$  of series  $Q_{a,s}$  increases from  $SHF_{\max} = 7$  to 19, whereas in series  $Q_{a,l}$ ,  $SHF_{\max} \approx 12$ . Nonetheless, the sample with  $q \approx 2 \times 22$  of series  $Q_{a,s}$  and all samples of series  $Q_{a,l}$  ruptured elastically<sup>224</sup> (er, elastic rupture) during elongation, as the flow regime for materials with densely packed sidearms or with  $M_{w,a} > M_{w,b}$  shifts to lower strain rates/higher temperatures as more arms increase the resistance of the branch point, until it is pulled inside the tube. The phenomenon of elastic rupture was observed by visually inspecting the sample behavior with a camera, during its elongational deformation. Under the investigated elongation conditions, the materials labeled as “er” are more likely to fracture than to flow due to the high number of entanglements present in the samples. The observed phenomenon can be attributed to a change in the failure mechanism from chain disentanglement to chain scission, which has been previously documented in the context of PS solutions and melts, as well as polystyrene-polybutadiene copolymers.<sup>224–227</sup> To delineate the distinct elongation behavior caused by the topologies, it is necessary to adjust the temperature and elongation rates according to the relaxation behavior of the respective polymer, ascertained by SAOS measurements. This has already been demonstrated with linear polypropylene and polyoctadecene.<sup>228</sup> To establish a correlation between the rheological behavior and the cellular structure of the foams, the respective  $SHF_{\max}$  appearing within  $\dot{\epsilon} = 0.1 \text{ s}^{-1} - 10 \text{ s}^{-1}$  at  $T = 160 \text{ }^\circ\text{C}$  was utilized.

Strain hardening is observed for the pom-poms with  $M_{w,a} = 24 - 50 \text{ kg mol}^{-1}$  of series A ( $M_{w,b} = 100 \text{ kg mol}^{-1}$ ,  $M_{w,a} = 9 - 300 \text{ kg mol}^{-1}$ , and  $q \approx 2 \times 12$ ). Here,  $\dot{\epsilon} < \tau_R$  (Appendix, Table C.2), but the samples still show significant strain hardening behavior, which means that the backbone dominates the viscosity, as suggested by the pom-pom theory. The samples undergo strain hardening, which increases with increasing  $M_{w,a}$  until the strain rate is lower than the relaxation time of the sample. The  $SHF_{\max}$  increases from 2 for the linear PS reference up to  $SHF_{\max} = 30$  for the sample with  $M_{w,a} = 50 \text{ kg mol}^{-1}$ . However, elastic rupture occurs during the experiment for  $M_{w,a} > M_{w,b}$ . At this stage, the  $SHF_{\max}$  decreases significantly to  $SHF_{\max} = 10$  (100k-2×12-120k) and increases again with a tripled arm length  $M_{w,a} > 3M_{w,b}$  to 21 (100k-2×14-300k). According to the pom-pom model<sup>94,118,123,124</sup> and multi-chain slip-link simulations<sup>118,229–231</sup>, two different stages are distinguished: a dominant influence of (I) the sidearms or (II) the backbone. The alteration in the rheological characteristics of the pom-poms leads to the following discontinuity of the elongation behavior: first, the  $SHF$  increases with increasing arm length ( $2M_{w,a} < M_{w,b}$ ), then initially decreases, followed by a recurrent increase with increasing arm length ( $2M_{w,a} \geq M_{w,b}$ ).

Series B ( $M_{w,b} = 100 - 400 \text{ kg mol}^{-1}$ ,  $M_{w,a} = 25 \text{ kg mol}^{-1}$ , and  $q \approx 2 \times 9$ ) shows an immense increase in the strain hardening factor up to  $SHF_{\max} = 84$ . While the highest  $SHF_{\max}$  was achieved at  $\dot{\epsilon} = 1 \text{ s}^{-1}$  by elongating the sample 400k-2×9-23k. All samples have a similar dilution effect of the sidearms, as they are composed of similar  $q$  and  $M_{w,a}$ . The observed rise in  $SHF_{\max}$  shows that the backbone lengths' influence on elongation is more significant than the arm length or number. Moreover, the high impact of  $M_{w,b}$  can be attributed to its entanglements, as specified by SAOS measurements (Figure 6.2 d)). A rubber plateau of the backbone occurs, whereas  $G'$  and  $G''$  of 100k-2×9-25k are parallel with a slope of about 0.6 in a double-logarithmic plot at low  $a_T\omega$ , indicating constraint release Rouse-like relaxation.<sup>219</sup> Consequently, especially the backbone stretch contributes to  $SHF$  as predicted by the pom-pom constitutive equations.<sup>118</sup> If the  $SHF$  shall be maximized by the variation of the polymer topology, the combination of a long and entangled backbone with an arm length of  $M_{w,a} \approx M_c$  and a moderate to high number of arms of  $q \approx 2 \times 9 - 2 \times 22$  should be considered as a starting point for further investigations. Moreover, high  $q$  values are in accordance with the assumptions of the pom-pom constitutive equation.<sup>118,231</sup>

PHYSICAL FOAMING – NUMBER OF SIDEARMS ( $Q$ ). The influence of the number of arms ( $q \approx 2 \times 5 - 2 \times 22$ ) is analyzed using short and long sidearms of around  $M_{w,a} = 25 \text{ kg mol}^{-1}$  ( $Q_{a,s}$ ) and  $110 \text{ kg mol}^{-1}$  ( $Q_{a,l}$ ). The backbone length was kept constant at  $M_{w,b} = 100 \text{ kg mol}^{-1}$ , since polymers with seven to eight entanglements already show sufficient good rheological properties.<sup>232</sup> The combination leads to the following relationship between arms and backbone within this dissertation:  $M_{w,a}(Q_{a,s}) < M_{w,b} < M_{w,a}(Q_{a,l})$ . The SEM images of selected foams foamed at  $T_f = 140 \text{ }^\circ\text{C}$  are illustrated in Figure 6.7.

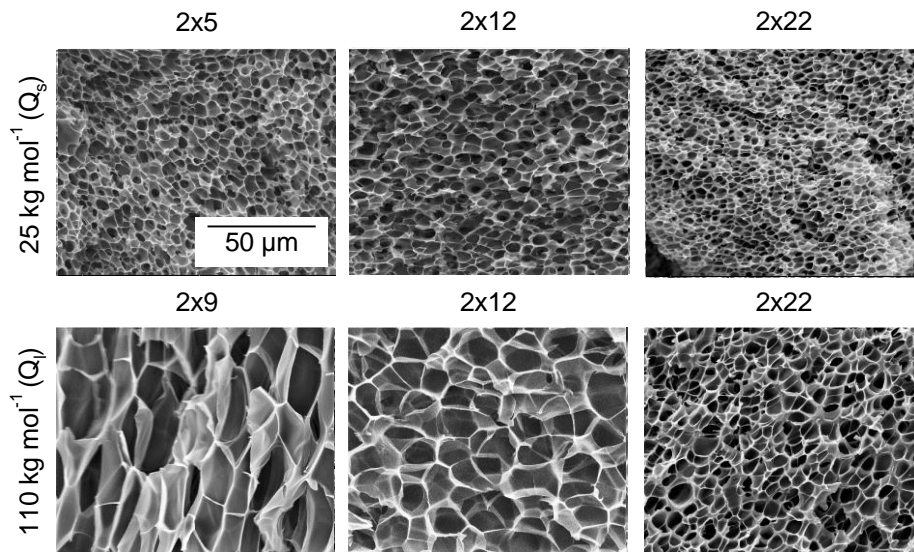


Figure 6.7. SEM images of PS pom-pom foams with  $M_{w,a} = 25 \text{ kg mol}^{-1}$  ( $Q_{a,s}$ ), or  $M_{w,a} = 110 \text{ kg mol}^{-1}$  ( $Q_{a,l}$ ),  $q \approx 2 \times 5 - 2 \times 22$ , and  $M_{w,b} = 100 \text{ kg mol}^{-1}$ . The scaling bar is valid for each image within this figure. Foaming conditions:  $T_f = 140 \text{ }^\circ\text{C}$ ,  $p = 500 \text{ bar}$ ,  $t_{\text{sat}} = 8 \text{ h}$ , and  $dp/dt \approx 200 \text{ bar s}^{-1}$ .



The SEM images show that the cells exhibit larger radii in series  $Q_{a,l}$  than in  $Q_{a,s}$ . In both series, the sample with  $q \approx 2 \times 22$  demonstrates the smallest cells. To analyze the cellular structure of the foams more in detail,  $VER$  and  $D$  are shown as a function of  $q$  in Figure 6.8 a), b)  $M_{w,a} = 25 \text{ kg mol}^{-1}$  ( $Q_{a,s}$ ) and c), d)  $M_{w,a} = 110 \text{ kg mol}^{-1}$  ( $Q_{a,l}$ ).

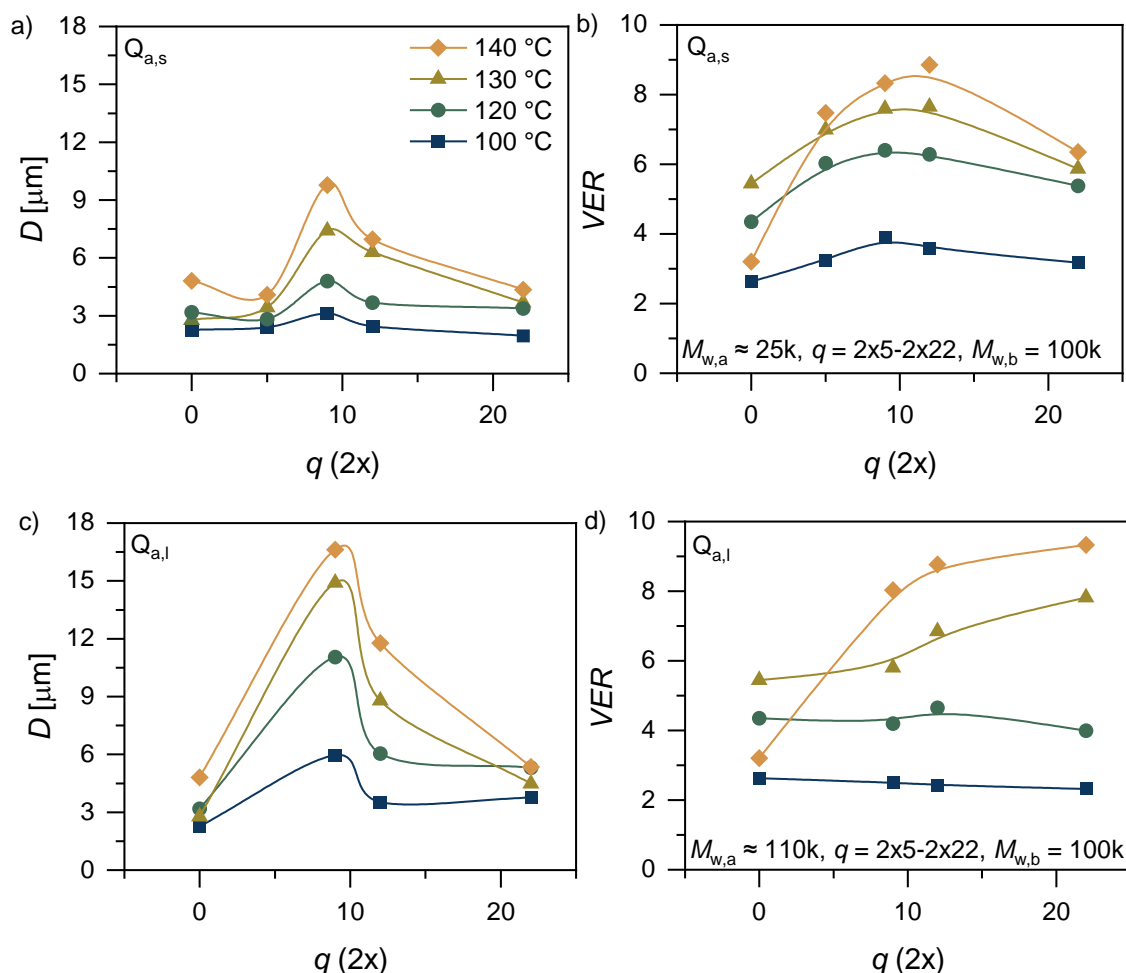


Figure 6.8. Average cell size  $D$  and volume expansion ratio  $VER$  as a function of the number of sidearms  $q$  of  $Q_{a,s}$  a), b),  $M_{w,a} = 25 \text{ kg mol}^{-1}$ ) and  $Q_{a,l}$  c), d),  $M_{w,a} = 110 \text{ kg mol}^{-1}$ ). The molecular weight of the backbone was constant at  $M_{w,b} = 100 \text{ kg mol}^{-1}$  and  $q$  increases continuously from  $q \approx 2 \times 5 - 2 \times 22$ . Lines are guides for the eyes.

Foaming conditions:  $T_f = 100^\circ\text{C} - 140^\circ\text{C}$ ,  $p = 500 \text{ bar}$ ,  $t_{\text{sat}} = 8 \text{ h}$ , and  $dp/dt \approx 200 \text{ bar s}^{-1}$ .

Both linear PS foams collapsed at  $130^\circ\text{C}$ . Conversely, the foamability of the pom-poms extends up to  $140^\circ\text{C}$ . The higher  $T_f$  indicate that the pom-pom topology supports the melt strength, thereby improving cell growth and stability, despite the comparatively lower zero-shear viscosity of the pom-poms in relation to the linear PS310k. Moreover, for both series,  $D$  increases with increasing  $T_f$  and  $q$ . Series  $Q_{a,s}$  exhibits an average cell size ranging from  $D = 4 - 7 \mu\text{m}$ , whereas series  $Q_{a,l}$  reached  $D = 4 - 15 \mu\text{m}$  at  $T_f = 140^\circ\text{C}$ . Moreover, the maximum  $D$  is obtained at  $q = 2 \times 9$  for both series. However,  $q$  has a minor impact on  $D$  for  $M_{w,a} < M_{w,b}$ , but the effect becomes more pronounced for  $M_{w,a} > M_{w,b}$ .

The  $VER$  increases with increasing  $T_f$  and  $q$ , while the sample with  $q \approx 2 \times 22$  ( $Q_{a,s}$ ) has a reduced  $VER$  than the residual samples of its respective series. The alteration in foamability can be ascribed to the elastic rupture behavior during elongational flow along with low shear viscosity. During cell expansion, the internal cell pressure is insufficient to counteract the elastic behavior and restoring forces of the polymer melt until cell growth stops by reaching  $T_g$  of the polymer matrix. Consequently, the kinetic of cell growth is reduced, leading to decreased  $VER$  and  $D$  values in contrast to the samples possessing a lower number of arms in series  $Q_{a,s}$ . The elongational rheological behavior of series  $Q_{a,l}$  remains consistent, as evidenced by their uniform tendency towards elastic rupture. These aforementioned results indicate that the effect of branching towards foaming properties is contingent upon the ratio of  $M_{w,a}$  to  $M_{w,b}$ , and  $q$ .

PHYSICAL FOAMING – SIDEARM LENGTH (A). Within sample series A, the sidearm length is systematically increased between  $M_{w,a} = 9 - 300 \text{ kg mol}^{-1}$ , which is equivalent to 0.5 – 18 entanglements, using  $M_{e,PS} = 16.8 \text{ kg mol}^{-1}$ ,  $M_{e,PI} = 4.5 \text{ kg mol}^{-1}$ .<sup>201</sup> The number of sidearms varies between  $q \approx 11 - 14$  per star. In the literature, the focus is mainly on pom-poms with only a low amount of unentangled sidearms ( $2 \times 5$ ) or dumbbell polymers with an extremely high amount of sidearms ( $2 \times 32$ ).<sup>217,233</sup> To analyze the influence of  $M_{w,a}$  on the  $VER$  and  $D$ ,  $M_{w,b}$  was kept constant  $100 \text{ kg mol}^{-1}$ . A number of arms of  $q \approx 2 \times 12$  were grafted onto the backbone since this amount already supported expandability, compared to fewer arms. The arms are not as crowded as  $q \approx 2 \times 22$ , and thus, neither minimize cell expansion nor show elastic rupture during elongation. Corresponding SEM images of selected foams foamed at  $T_f = 100 \text{ }^\circ\text{C}$  and  $140 \text{ }^\circ\text{C}$  are shown in Figure 6.9.

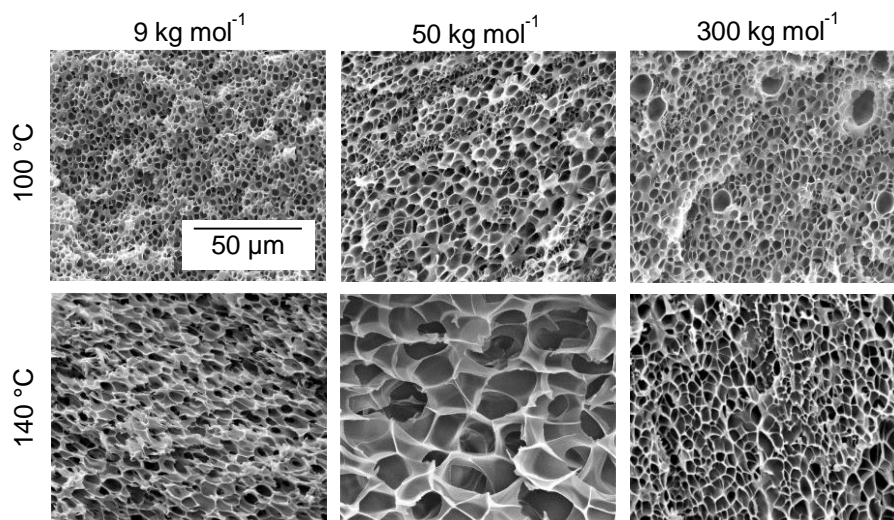


Figure 6.9. SEM images of PS pom-pom foams of series A with  $M_{w,b} = 100 \text{ kg mol}^{-1}$ ,  $q \approx 2 \times 12$ , and  $M_{w,a} = 9 \text{ kg mol}^{-1}$ ,  $50 \text{ kg mol}^{-1}$ , and  $300 \text{ kg mol}^{-1}$ . The scaling bar is valid for each image within this figure.

Foaming conditions:  $T_f = 100 \text{ }^\circ\text{C}$  and  $140 \text{ }^\circ\text{C}$ ,  $p = 500 \text{ bar}$ ,  $t_{\text{sat}} = 8 \text{ h}$ , and  $dp/dt \approx 200 \text{ bar s}^{-1}$ .

The average cell diameter  $D$  increases as a function of  $M_{w,a}$  with increasing temperature, as indicated by the SEM images, where  $D$  reaches a maximum within the investigated range of  $M_{w,a} = 9 - 300 \text{ kg mol}^{-1}$ . The resulting values of  $VER$  and  $D$  as a function of  $M_{w,a}$  are depicted in Figure 6.10.

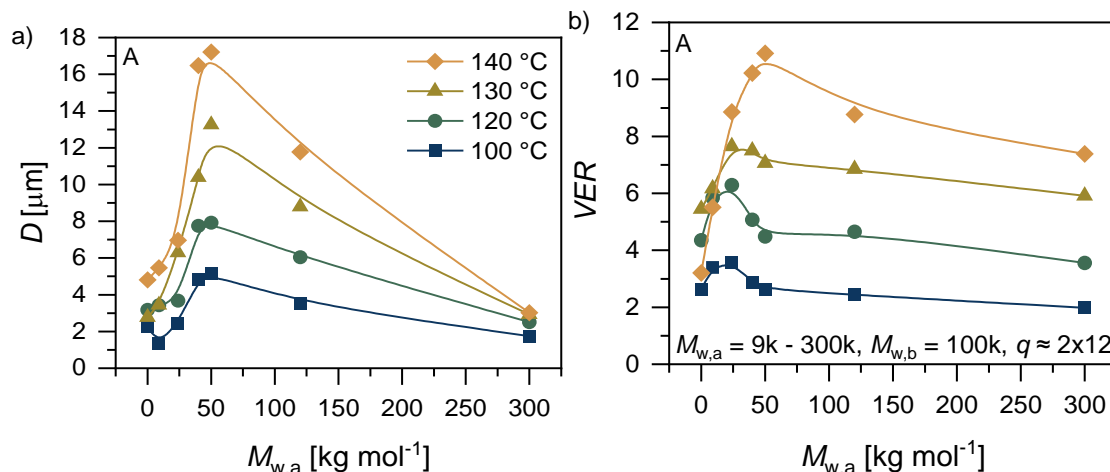


Figure 6.10. Average cell diameter  $D$  (a) and volume expansion ratio  $VER$  (b) of series A ( $M_{w,b} = 100 \text{ kg mol}^{-1}$ ,  $q \approx 2 \times 12$ , and  $M_{w,a} = 9 - 300 \text{ kg mol}^{-1}$ ). Lines are guides for the eyes. Foaming conditions:  $T_f = 100 \text{ }^\circ\text{C} - 140 \text{ }^\circ\text{C}$ ,  $p = 500 \text{ bar}$ ,  $t_{\text{sat}} = 8 \text{ h}$ , and  $dp/dt \approx 200 \text{ bar s}^{-1}$ .

Generally, the potential for cell expansion, i.e.,  $VER$ , rises as the viscosity of the polymer matrix is reduced with increasing temperatures. The maximum volume expansion is temperature-dependent and shifts with increasing  $T$  from  $M_{w,a} = 24 \text{ kg mol}^{-1}$  to  $50 \text{ kg mol}^{-1}$  and the influence of  $M_{w,a}$  is found to be most pronounced at  $140 \text{ }^\circ\text{C}$ . For instance, while  $D$  differs from  $3.03 \mu\text{m}$  up to  $17.21 \mu\text{m}$  at  $T_f = 140 \text{ }^\circ\text{C}$ , the difference at  $100 \text{ }^\circ\text{C}$  is only  $3.8 \mu\text{m}$ , increasing from  $D = 1.33$  to  $5.13 \mu\text{m}$ .

The sample with  $M_{w,a} = 50 \text{ kg mol}^{-1}$  (equals  $M_{c,PS}$ ) achieved the highest volume expansion with  $VER = 11$ , resulting in the largest average cell size of  $D = 17.2 \mu\text{m}$  at  $T_f = 140 \text{ }^\circ\text{C}$ . The high expandability is caused by the combination of low shear melt viscosity of  $\eta_0 \approx 3.35 \times 10^5 \text{ Pa s}^{-1}$  with the highest  $SHF_{\text{max}}$  of up to 30 ( $T = 160 \text{ }^\circ\text{C}$ ). The data indicate that cell expansion of polymers is favored, if  $M_{w,a} \approx M_{c,PS}$ . An increase beyond  $M_{c,PS}$  and hence, a higher number of entanglements and increasing viscosity limits cell growth and expansion for the investigated samples with  $M_{w,b} = 100 \text{ kg mol}^{-1}$ .

The sample with  $M_{w,a} = 300 \text{ kg mol}^{-1}$  has no significant change in  $D$  with increasing temperature, but the  $VER$  almost quadruples from 1.9 to 7.4. This can be related to the high melt stability and the elastic behavior, indicated by melt rheological properties (Figure 6.2 c)), as the combination of both prevent cells from coalescence and results in higher  $N$ . The overall cell density of the sample with  $M_{w,a} = 300 \text{ kg mol}^{-1}$  is  $N = 4.4 \times 10^{11} \text{ cells cm}^{-3}$ , which is one or two orders of magnitudes higher than the other pom-pom-shaped or linear samples, where  $N$  ranges from  $3.7 \times 10^9 - 6 \times 10^{10} \text{ cells cm}^{-3}$ .

Therefore, this finding confirms the assumption that arms with  $M_{w,a} \approx M_c$  supports cell growth by minimizing cell coalescence and rupture. Additionally, a relationship of  $M_{w,a} \gg M_{w,b}$ , where the polymer topology resembles a star, enables the combination of a relatively high  $VER$  of 7.4 with a small  $D$  of  $3.03 \mu\text{m}$  ( $T_f = 140 \text{ }^\circ\text{C}$ ).

PHYSICAL FOAMING – BACKBONE LENGTH (B). The backbone length is the third and last parameter of the pom-pom topology. Samples with backbone length between  $M_{w,b} = 100 - 400 \text{ kg mol}^{-1}$ , and  $M_{w,a} \approx 25 \text{ kg mol}^{-1}$  and  $q \approx 2 \times 9$ , are summarized as sample series B. A detailed insight into the resulting cellular morphology at  $T_f = 140 \text{ }^\circ\text{C}$  is provided via SEM images in Figure 6.11, using two magnifications.

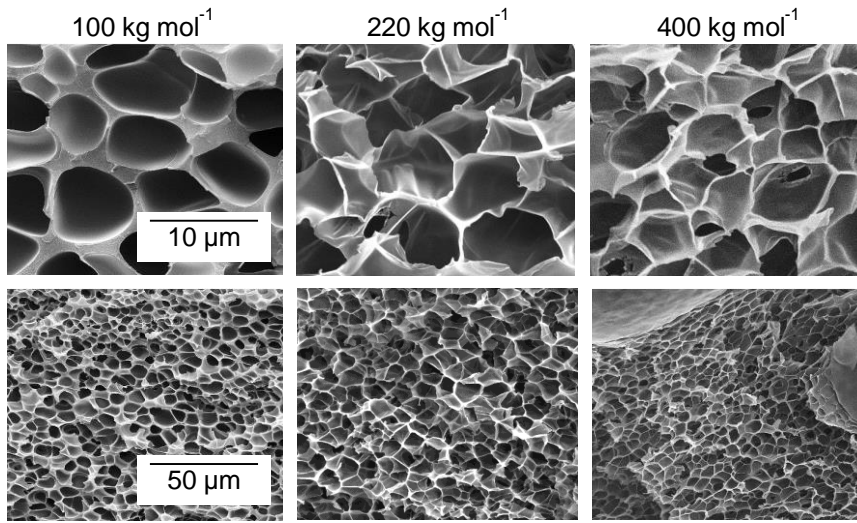


Figure 6.11. Two magnifications of SEM images based on foamed pom-poms with a backbone length of  $M_{w,b} = 100 \text{ kg mol}^{-1}$ ,  $220 \text{ kg mol}^{-1}$  and  $400 \text{ kg mol}^{-1}$ . Each sample with  $q \approx 2 \times 9$  and  $M_{w,a} = 25 \text{ kg mol}^{-1}$ . The scaling bars are valid for each image within this figure. Foaming conditions:  $T_f = 140 \text{ }^\circ\text{C}$ ,  $p = 500 \text{ bar}$ ,  $t_{\text{sat}} = 8 \text{ h}$ , and  $dp/dt \approx 200 \text{ bar s}^{-1}$ .

The SEM images indicate similar  $D$  over the whole sample set. However, the cell wall thickness  $d$  becomes much finer with increasing  $M_{w,b}$ ; especially the one of sample 100k-2 $\times$ 9-25k shows significant coarsening. Besides the impact of  $M_{w,b}$  on  $d$  (c), Figure 6.12 depicts its impact on  $VER$  (a) and  $D$  (b).

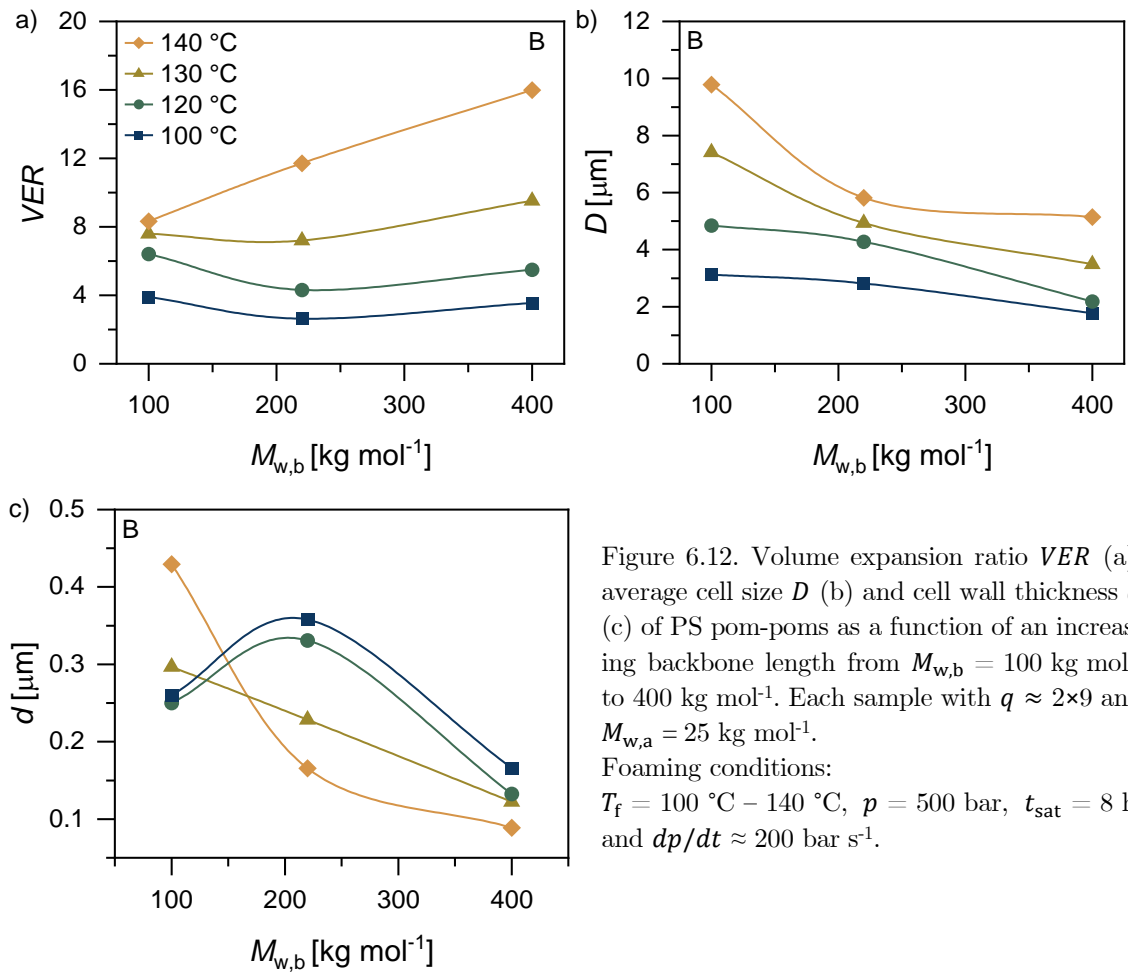


Figure 6.12. Volume expansion ratio  $VER$  (a), average cell size  $D$  (b) and cell wall thickness  $d$  (c) of PS pom-poms as a function of an increasing backbone length from  $M_{w,b} = 100$   $\text{kg mol}^{-1}$  to 400  $\text{kg mol}^{-1}$ . Each sample with  $q \approx 2 \times 9$  and  $M_{w,a} = 25$   $\text{kg mol}^{-1}$ . Foaming conditions:  $T_f = 100$  °C – 140 °C,  $p = 500$  bar,  $t_{\text{sat}} = 8$  h, and  $dp/dt \approx 200$  bar  $\text{s}^{-1}$ .

As already observed for the series with increasing  $q$  and  $M_{w,a}$ , the  $VER$  and  $D$  increase with increasing foaming temperature. Furthermore, cell wall thickness increases from  $d = 0.36 - 0.09$   $\mu\text{m}$  with increasing foaming temperature for  $M_{w,b} = 220$   $\text{kg mol}^{-1}$  and 400  $\text{kg mol}^{-1}$ , while it increases from  $d = 0.26 - 0.43$   $\mu\text{m}$  for  $M_{w,b} = 100$   $\text{kg mol}^{-1}$ . The coarsening reveals the beginning of cell coalescence at  $T_f = 130$  °C, as the melt viscosity is only  $\eta_0 = 2.77 \times 10^4$  Pa s approximately 160 times lower compared to the other two samples at  $T_{\text{ref}} = 160$  °C.

The volume expansion ratio increases with increasing  $M_{w,b}$  up to  $VER \approx 16$ , while  $D$  shows a reverse trend. Since the sample with  $M_{w,b} = 400$   $\text{kg mol}^{-1}$  combines a high stretchability on the one hand ( $SHF_{\text{max}} = 84$ ,  $T = 160$  °C), but a relatively high  $\eta_0$  on the other hand ( $\eta_0 = 4.44 \times 10^6$  Pa s,  $T_{\text{ref}} = 160$  °C), the cell walls can be highly stretched without cell coalescence, as also confirmed by the SEM images in Figure 6.11. Thus, a higher  $N$  is maintained in combination with minimized  $D$  and a reduced  $d$ .

CORRELATION OF TOPOLOGY, MELT RHEOLOGY AND FOAMABILITY. The cellular foam morphology depends on the polymer topology and its relationship to their melt rheological properties. To guide the design and control of foamability by using topological features like  $M_{w,b}$ ,  $M_{w,a}$ , and  $q$ , its impact was investigated and summarized as  $VER$  vs.  $D$ , depending on the corresponding foaming temperature, in Figure 6.13.

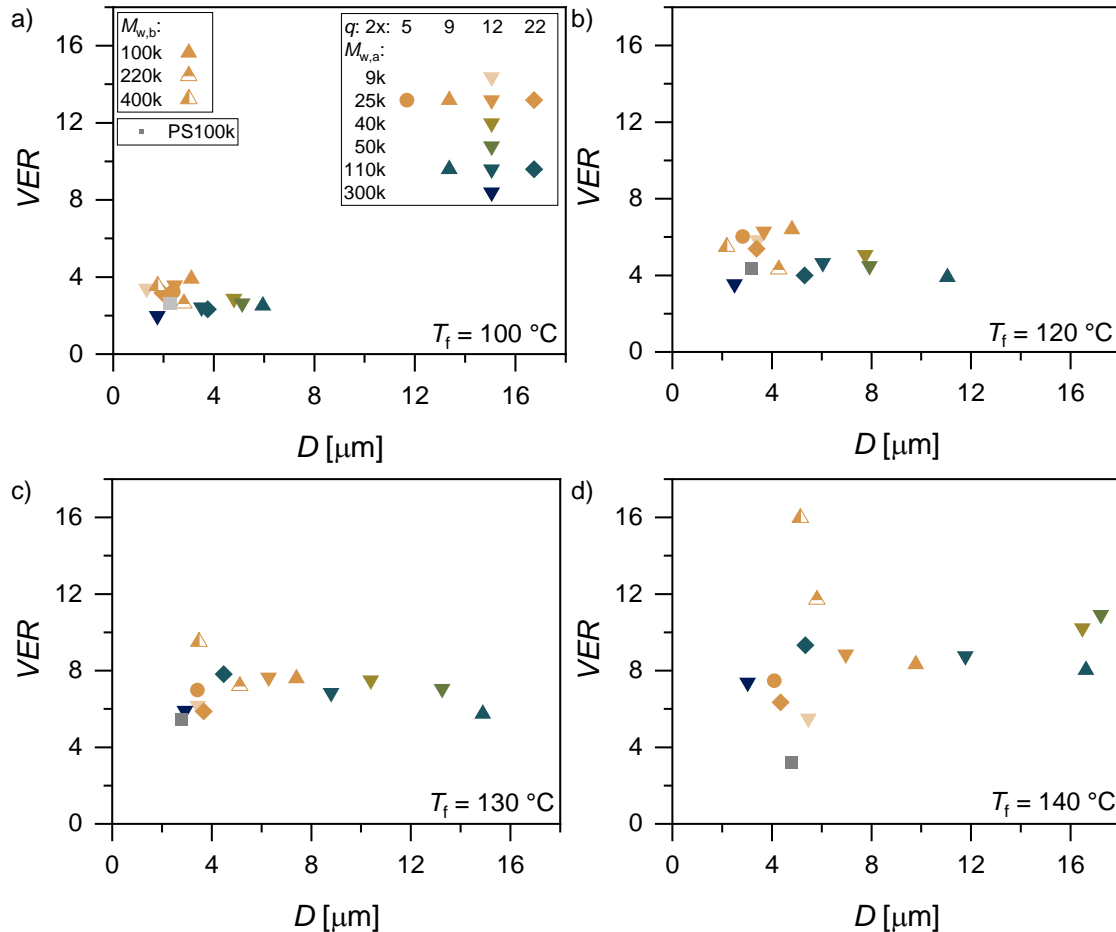


Figure 6.13. Volume expansion ratio  $VER$  vs. average cell size  $D$  foamed at a)  $100\text{ }^\circ\text{C}$ , b)  $120\text{ }^\circ\text{C}$ , c)  $130\text{ }^\circ\text{C}$ , and d)  $140\text{ }^\circ\text{C}$ . Foaming conditions:  $p = 500\text{ bar}$ ,  $t_{\text{sat}} = 8\text{ h}$ , and  $dp/dt \approx 200\text{ bar s}^{-1}$ .

The findings indicate that the impact of the topological changes implied in the model systems on  $D$  and  $VER$  is more pronounced at a higher foaming temperature as the growth period extended with rising temperatures. Thus, the dissimilarity in melt rheological properties, i.e., melt strength and strain hardening in elongational flow, can exert a more decisive influence. For instance, a more substantial effect of the polymer topology on  $D$  at higher foaming temperatures was also reported for chemically modified PS with an increasing LCB level in the literature.<sup>62</sup> The pom-poms with  $M_{w,a} < M_c$  maintain their average cell size with increasing  $T_f$  but increase significantly in  $VER$  exhibit a higher cell density  $N$  due to less cell coalescence. Materials with  $M_{w,a} \approx M_{w,b}$  show an increase in  $D$  and  $VER$  without a pronounced increase in  $N$ , as presented in Table C.4 located in the Appendix.

The rise of  $D$  can be attributed to the reduction in viscosity of the polymer melt at elevated temperatures, which also enhances the diffusion rate of  $\text{CO}_2$ . Both effects accelerate cell growth, leading to larger cells until the polymer matrix stabilizes by reaching  $T_g$  although the overall  $\text{CO}_2$ -solubility decreases. The impact of the temperature on the viscosity of pom-poms with  $M_{w,a} < M_c$  is negligible, as the plasticization of the sidearms already lowers the viscosity compared to the samples with  $M_{w,a} \approx M_{w,b}$ .

The samples 100k-2×14-300k and 100k-2×22-110k show comparable relations of  $VER$  to  $D$  as the samples with  $M_{w,a} < M_e$  over the entire investigated temperature range (Figure 6.13). Both samples achieved the highest  $\eta_0$  values with  $\eta_0 = 6.3 \times 10^8$  Pa s and  $5.5 \times 10^6$  Pa s, respectively. The observed increase of  $\eta_0$  can be ascribed to higher amounts of entanglements, which resulted in a decelerated cellular growth rate, presumably due to the comparable stress exerted by the  $\text{CO}_2$  toward the cell walls. Moreover, the cell growth dynamics are severely hindered under the same foaming conditions regardless of whether the higher  $\eta_0$  results from relatively long arms ( $M_{w,a} = 300$  kg mol<sup>-1</sup>) or a high number of grafted arms ( $q \approx 2 \times 22$ ). This finding aligns with the outcomes reported in the literature regarding LCB PS.<sup>62</sup> Nevertheless, both samples combine a high volume expansion ratio of  $VER = 7.38$  and  $9.33$  with  $D = 3.03$   $\mu\text{m}$  and  $5.34$   $\mu\text{m}$  at  $T_f = 140$  °C, respectively, as shown in Figure 6.13 d). The combination of a low  $D$  but high  $VER$  is often a desired combination for foam applications, where good solid mechanical or insulation properties are required.

In contrast, the samples with longer backbones (B) show an enormous increase in  $VER$ , especially at  $T_f = 140$  °C (Figure 6.13 d)). While  $D$  grows only moderately, which is also comparably low within the overall foaming window compared to samples with  $M_{w,a} = 100$  kg mol<sup>-1</sup>. For instance, the  $VER$  of sample 400k-2×9-23k increases from 3.5 (100 °C) to 16.0 (140 °C), whereas  $D$  increases from 1.8  $\mu\text{m}$  (100 °C) to 5.1  $\mu\text{m}$  (140 °C). This can be attributed to the high tremendously increased melt strength and the corresponding reducing cell coalescence, as evidenced by the increased stretchability based on the significantly increased  $SHF_{\text{max}}$  and the decreased  $d$ . As a result, higher  $N$  are maintained during the cell growth phase over the investigated temperature range, as summarized in the Appendix, see Table C.4. As evidenced by the maintenance of the significantly higher  $N$  values after cell stabilization, the study suggests that longer backbone with consequently a higher number of entanglements along the backbone minimizes cell coalescence. Moreover, our findings point towards a more significant influence of  $M_{w,a}$  on  $D$ , whereas  $M_{w,b}$  has a substantial impact on  $VER$ .

Throughout the foaming procedure, the polymer chains undergo various deformations and stress at different locations within the final foam structure. As evidenced by three-point bending, it has been observed that the magnitude of acting stresses is greater at the surfaces of cells in comparison to the center of the cell walls. Similarly, the connection points of cells, known as struts, also undergo high levels of stress.

Consequently, the actual stress and strain distribution across the foam vary greatly. Strain rates of approximately  $0.1 \text{ s}^{-1}$  were determined during an in situ observation of cell growth, utilizing PP at  $\text{CO}_2$  saturation pressures of around 110 bar.<sup>2</sup> Nonetheless, the experiments conducted within this study employ a saturation pressure that is nearly five times greater, leading to a depressurization rate of  $200 \text{ bar s}^{-1}$ . Thus, a simplified approach was employed to estimate the overall stretch ratio by  $VER^{1/3}$ . The synthesized pom-pom-shaped samples exhibit a maximum  $VER$  of approximately 10, resulting in an overall stretch ratio of 2.15. Consequently, the used depressurization rate of  $dp/dt \approx 200 \text{ bar s}^{-1}$  leads to an elongation rate of around  $\dot{\epsilon} = 0.86 \text{ s}^{-1}$  during cell expansion within the polymer melt. This rate falls within the range of applied strain rates of  $\dot{\epsilon} = 0.01 \text{ s}^{-1}$  to  $10 \text{ s}^{-1}$  utilized during the elongation experiments. However, this simplified estimation holds validity solely as an initial approximation for the whole set of globally occurring stresses and strains within the polymer melt, as it does not consider the different local stress and strain. Therefore, the highest strain and stress are of utmost importance for forming a homogeneous cell structure.

Additionally, the temperature fluctuations during foaming are ascribed to the pressure release, as the so-called Joule-Thomson-effect occurs. Thus, the rheological properties of the melt undergo alterations as the Weissenberg number increases continuously. For the formation of homogeneous cell morphology, strain hardening prevents the rupture of cells, especially in the areas of the cell walls, where the greatest strain and stress are present; thus, it is of utmost importance for foaming. Hence, to establish a correlation between the melt rheological behavior and the foamability of the polymer melt, it is crucial to consider the measurement conditions, particularly the temperature. As the  $T_g$  of the  $\text{CO}_2$ -saturated polymer decreases to approximately  $45 \text{ }^\circ\text{C}$  under the used foaming conditions, the difference between foaming temperature and  $T_g$  is at least  $55 \text{ }^\circ\text{C}$ . Table 6.2 depicts the influence of the topological parameter of the pom-pom topology on the melt rheological properties measured at  $T = 160 \text{ }^\circ\text{C}$  and the resulting cellular structure of the foams foamed at  $T_f = 140 \text{ }^\circ\text{C}$ . The morphological structure of the foams is representatively shown as maximizing  $VER$  and minimizing  $D$  at  $T_f = 140 \text{ }^\circ\text{C}$ . In addition, the sample for each series with the maximized ratio of a high  $VER$  and small  $D$  are highlighted, as the combination represents a frequently sought-after relationship between the two characteristics in foam applications, particularly for developing lightweight materials.

Table 6.2. Overview of the impact of the topological parameter of the pom-pom topology, i.e.,  $M_{w,b}$ ,  $M_{w,a}$  and  $q$  on the melt rheological properties ( $\eta_0$ ,  $SHF$ ) at  $T = 160 \text{ }^\circ\text{C}$  and the cellular structure of the foams at  $T_f = 140 \text{ }^\circ\text{C}$ .

Parameter	$T \text{ [}^\circ\text{C]}$	$Q_{a,s}$	$Q_{a,l}$	A	B
$M_{w,b} \text{ [kg mol}^{-1}\text{]}$	-	100	100	100	100–400
$M_{w,a} \text{ [kg mol}^{-1}\text{]}$	-	25	110	9–300	25
$q$	-	$2 \times 5$ – $2 \times 22$	$2 \times 9$ – $2 \times 22$	$2 \times 12$	$2 \times 9$



Table 6.2 continued.

Parameter	$T$ [°C]	$Q_{a,s}$	$Q_{a,l}$	A	B
Lowest $\eta_0$	160	2×22	2×9	9k	100k
Highest $SHF$	160	2×12, 2×22	2×22	50k	400k
Highest $VER$	140	2×12	2×22	50k	400k
Lowest $D$	140	2×5	2×22	300k	100k
Combination: high $VER$ to low $D$	140	2×5	2×22	300k	400k

The rheological properties, i.e.,  $SHF_{\max}$  (a) and  $\eta_0$  (b), at  $T = 160$  °C are linked with the resulting  $VER$  of the foams at  $T_f = 140$  °C in Figure 6.14. Thereby, a foaming temperature of  $T_f = 140$  °C represents the temperature, where the maximum  $VER$  is achieved for the majority of the synthesized samples.

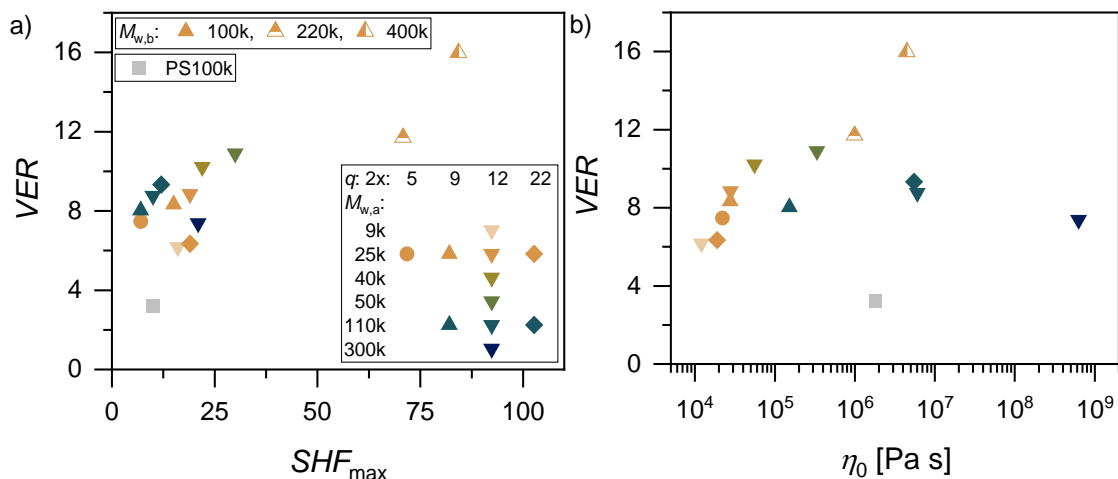


Figure 6.14. Overview of the foam expansion, i.e.,  $VER$ , at  $T_f = 140$  °C as a function of the rheological parameter, i.e.,  $SHF_{\max}$  (a) and  $\eta_0$  (b), at  $T = 160$  °C for the whole sample set. Foaming conditions:  $p = 500$  bar,  $t_{\text{sat}} = 8$  h, and  $dp/dt \approx 200$  bar  $s^{-1}$ .

Considering the rheological differences, like the occurrence of elastic rupture during elongation, the results indicate that the  $VER$  is affected by the strain hardening and the zero-shear viscosity of the polymer melt. More specifically, the  $VER$  increases with increasing  $SHF_{\max}$  and appears to reach a plateau, while it seems that the  $VER$  reached a maximum under viscosity influence within the investigated samples at values between  $\eta_0 \approx 10^5 - 10^6$  Pa s. However, it is important to consider the comparatively reduced quantity of samples featuring an elongated backbone. Further research should therefore be conducted to thoroughly examine the impact of the backbone length in pom-pom polymers.

Finally, the overall resulting rheological properties were correlated with the foaming behavior in Figure 6.15, which represents  $D$ ,  $VER$ ,  $SHF$ , and  $\eta_0$  as a function of  $M_{w,t}$ . The rheological parameters were measured at 160 °C, while the foaming behavior was analyzed at  $T_f = 140$  °C. The rheological behavior is significantly impacted by changes in  $M_{w,b}$ , therefore the following analysis will solely focus on samples with  $M_{w,b} = 100$  kg  $\text{mol}^{-1}$ .

Moreover, a distinction is made between the samples that experienced elastic rupture during elongation (grey area and open symbols) and those that did not (closed symbols).

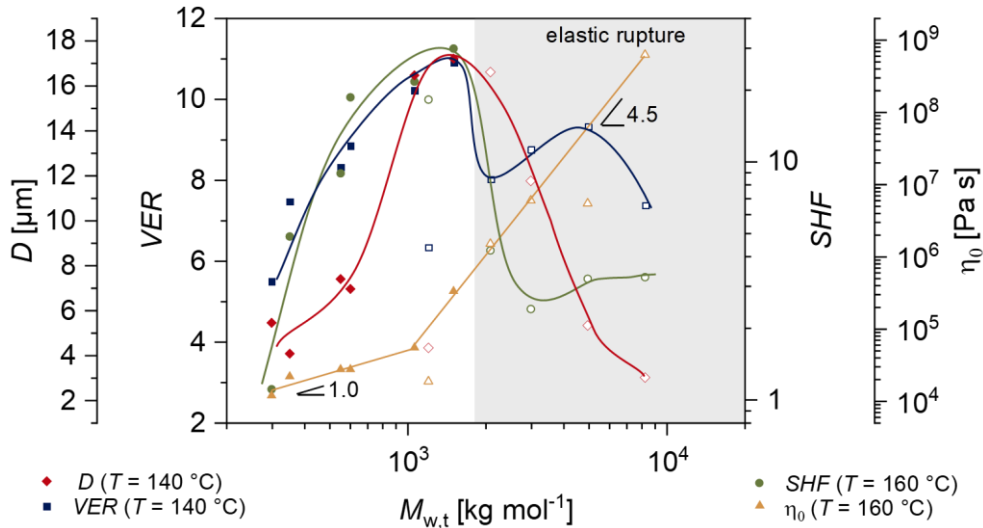


Figure 6.15. Correlation of the rheological parameter, i.e.,  $SHF$  and  $\eta_0$ , and the foaming behavior, i.e.,  $D$  and  $VER$ , as function of the total molecular weight  $M_{w,t}$  for samples with  $M_{w,b} = 100 \text{ kg mol}^{-1}$ ,  $M_{w,a} = 7 - 300 \text{ kg mol}^{-1}$  and  $q \approx 2 \times 5 - 2 \times 22$ . Rheological properties were measured or referenced to  $T = 160 \text{ }^\circ\text{C}$  and correlated to the foaming behavior at  $T_f = 140 \text{ }^\circ\text{C}$ ; the  $SHF$  was quantified at  $\dot{\epsilon} = 1 \text{ s}^{-1}$ . Solid lines are to guide the eye. All samples in the grey area marked with half-open symbols undergo elastic rupture during elongational flow. Foaming conditions:  $p = 500 \text{ bar}$ ,  $t_{\text{sat}} = 8 \text{ h}$ , and  $dp/dt \approx 200 \text{ bar s}^{-1}$ .

With increasing  $M_{w,t}$ , the  $D$ ,  $VER$ , and  $SHF$  reach all a maximum value with  $D = 17.2 \text{ } \mu\text{m}$ ,  $VER = 11$ , and  $SHF = 30$ , whereas the  $\eta_0$  increases linearly with a slope of 1 and 4.5 in a double-logarithmic plot. The maxima of  $D$ ,  $VER$ , and  $SHF$  occur around  $M_{w,t} \approx 1,500 \text{ kg mol}^{-1}$ , i.e.,  $Z_t \approx 89$ , which is also nearly the same area, where the slope of  $\eta_0$  changed. In previous investigations of our research group, we discovered a maximization of  $VER = 40$  ( $T_f = 125 \text{ }^\circ\text{C} - 140 \text{ }^\circ\text{C}$ ,  $p = 180 \text{ bar}$ ) accompanied with  $SHF_{\text{max}} = 200$  and a minimum  $\eta_0 = 1.68 \times 10^5 \text{ Pa s}$  ( $T = 180 \text{ }^\circ\text{C}$ ) using PS combs. For more details, the reader is referred to the corresponding literature.<sup>57</sup> However, it should be noted that a higher pressure was utilized for foaming, and a marginally reduced temperature was chosen for the rheological measurements. Thereby rendering solely the general trend comparable.

The experiments revealed that blending the pom-pom-shaped samples with linear polymers and studying their rheological behavior and foamability would be a compelling area of research. This is particularly relevant in the context of maintaining low viscosities while simultaneously enhancing strain hardening, as compared to the use of linear polymers. The cellular structure of foams can be adjusted by considering the topology of the polymers and the relationship with its melt rheological properties. However, another influencing parameter is the number of interconnected stars, which will be examined in the subsequent chapter.

## 6.2 THREADING POLYSTYRENE STARS ALONG A CHAIN

Despite the high number of publications on polymer stars and related like pom-poms (equivalent to a two-star system), no study on multiple, chemically bonded stars, i.e., barbwire type architectures, and the influence of the inherent topological parameters on the melt rheological properties and foaming behavior have been conducted.

**ANIONIC POLYMERIZATION AND GRAFTING-ONTO.** The samples with increasing covalently connected stars  $s$  were synthesized using a combination of living anionic polymerization and grafting-onto procedure, like the synthesis method of pom-pom-shaped polymers. The main difference compared to the pom-pom architectures ( $s = 2$ ), however, lies in preparing the required backbone of the barbwire topologies with  $s = 3, 4$ . The 3- and 4-star samples are based on a penta- and heptablock copolymer as backbones, respectively. To generate the ISISI- and ISISISI-precursor, first, asymmetric ISI' and ISIS' triblock and quadroblock copolymers with  $I = 2 \times I'$  and  $S = 2 \times S'$  were synthesized by sequential living anionic polymerization. The PS-block (S) length corresponds to  $90 \text{ kg mol}^{-1}$ , while the PI-block (I) length corresponds to  $5 \text{ kg mol}^{-1}$ , where  $S'$  and  $I'$  are half of S and I, respectively. After the complete conversion of the monomers for the ISI' and ISIS' blocks, the blocks were linked using a bifunctional linker,  $\alpha, \alpha'$ -dibromo-*p*-xylene, resulting in the penta- and heptablock copolymers.

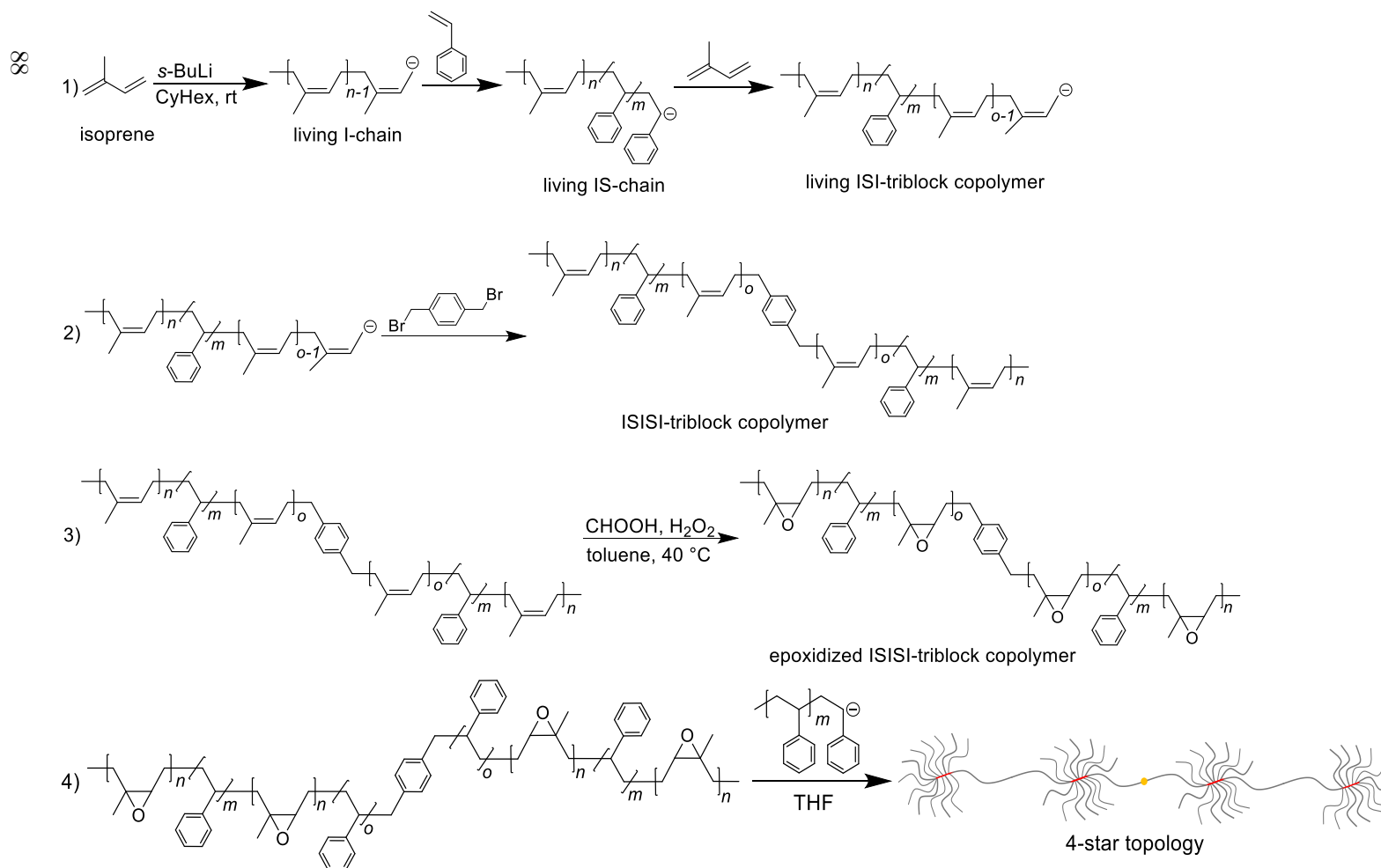


Figure 6.16. Synthesis of barbwire with four connected stars ( $s = 4$ ) by combining living anionic polymerization, epoxidation, and grafting-onto methodology. The exemplarily shown sample has a backbone length of  $M_{w,b} = 382 \text{ kg mol}^{-1}$ , sidearm length of  $M_{w,a} = 27 \text{ kg mol}^{-1}$ , and the number of sidearms is around  $q \approx 12$  per star. Depending on  $s$ , the number of PS- and PI-blocks increases from only one PI-block for the star ( $s = 1$ ) up to ISISI for the barbwire structure with  $s = 4$ . The yellow marked area represents the linking spot with the bifunctional linker  $\alpha, \alpha'$ -dibromo-*p*-xylene.

Within the sample series,  $s$  increases systematically from one single star (star,  $s = 1$ ) to four connected stars (4-star,  $s = 4$ ) with a linear PS chain of  $M_{w,PS} \approx 90 \text{ kg mol}^{-1}$ . The resulting samples are schematically visualized in Figure 6.17 and will be called barbwire in the course of the dissertation. Therefore, the length of the backbone was increased from  $M_{w,b} = 7 - 382 \text{ kg mol}^{-1}$ , depending on  $s$ . The molecular weight of the sidearms is approximately  $M_{w,a} = 25 \text{ kg mol}^{-1}$ , with an average number of sidearms per star of  $q \approx 12$ , as investigations on the pom-pom-shaped polymers revealed that this combination is appropriate for studying the shear and elongational rheological properties. A pom-pom with a backbone length of  $M_{w,b} = 280 \text{ kg mol}^{-1}$  served as a reference to determine if the impact of topology is a result of increasing  $s$  or  $M_{w,b}$ .

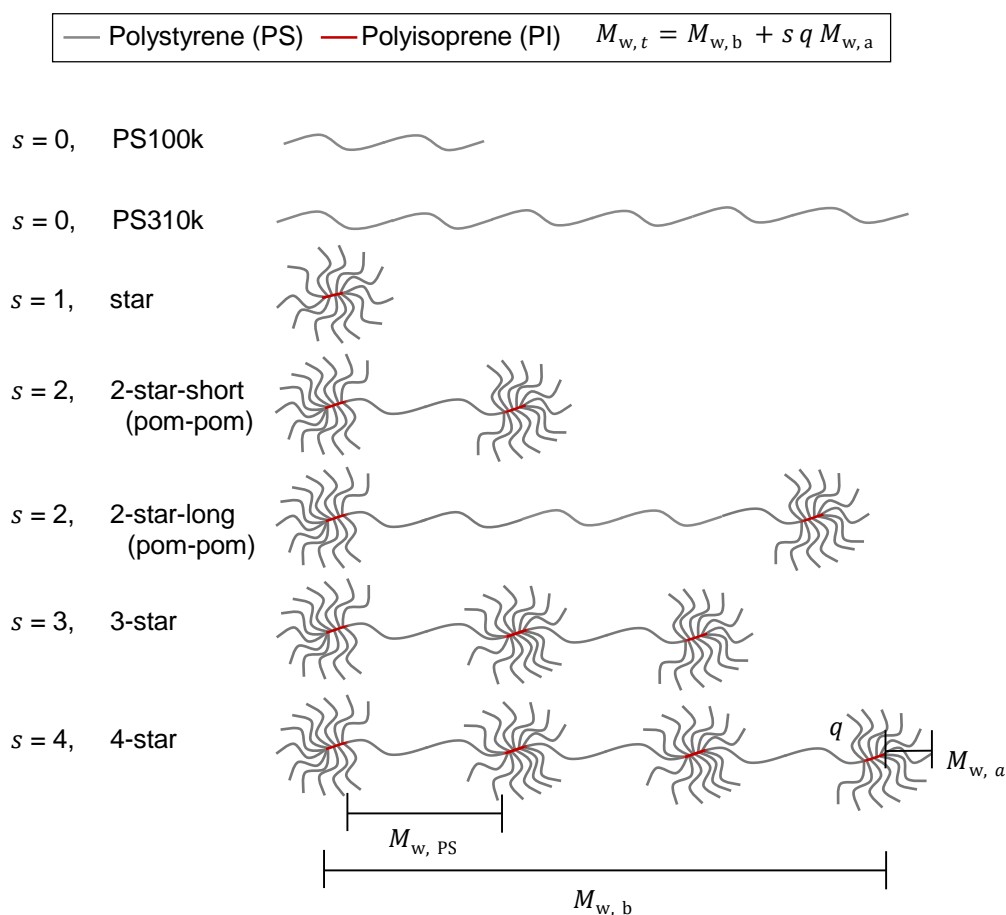


Figure 6.17. Two linear PS references with a molecular weight of  $100 \text{ kg mol}^{-1}$  and  $310 \text{ kg mol}^{-1}$  ( $s = 0$ ), one star ( $s = 1$ ), two pom-poms ( $s = 2$ , 2-star-short with  $M_{w,b} = 100 \text{ kg mol}^{-1}$  and 2-star-long with  $M_{w,b} = 280 \text{ kg mol}^{-1}$ ), and barbwire topologies ( $s = 3, 4$ ) with increasing amount of covalently connected stars  $s$  with a linear PS chain with  $M_{w,PS} \approx 90 \text{ kg mol}^{-1}$ . Grey and red lines correspond to PS and PI, respectively.

The characterization procedure is performed equivalently to the pom-pom materials, as introduced in Chapter 6.1. The resulting molecular details of the synthesized samples, the precursors, and the linear PS references are summarized in Table 6.3.

Table 6.3. Molecular characteristics of the PS pom-poms and barbwires, linear ISI-precursor, and PS references.

Sample	$s$	${}^aM_{w,t}$ [kg mol $^{-1}$ ]	${}^a\mathcal{D}_t$	${}^bq$	$M_{w,a}$ [kg mol $^{-1}$ ]	$\mathcal{D}_a$	${}^cZ_t$
PS100k	-	100	1.01	-	-	-	5.95
PS310k	-	310	1.10	-	-	-	17.26
PI (precursor for $s = 1$ )	-	7	1.10	-	-	-	1.56
ISI (precursor for $s = 2$ , short)	-	100	1.05	-	-	-	7.50
ISI (precursor for $s = 2$ , long)	-	280	1.08	-	-	-	12.30
ISISI (precursor for $s = 3$ )	-	213	1.16	-	-	-	14.05
ISISISI (precursor for $s = 4$ )	-	382	1.35	-	-	-	20.51
Star (8k-11-27k)	1	305	1.09	11	27	1.07	19.46
2-star-short (100k-2×12-24k)	2	600	1.18	2×12	24	1.05	42.46
2-star-long (280k-2×13-22k)	2	852	1.17	2×13	22	1.08	52.94
3-star (213k-3×11-25k)	3	1,038	1.10	3×11	25	1.09	65.08
4-star (382k-4×11-27k)	4	1,570	1.14	4×11	27	1.12	95.67

<sup>a</sup>Dispersities were determined using SEC-DRI signal, whereas absolute  $M_w$  values were obtained using MALLS detection. <sup>b</sup>Number of sidearms per star is calculated by Equation (6.2). <sup>c</sup> $M_{e,PS} = 16.8$  kg mol $^{-1}$ ,  $M_{e,PI} = 4.5$  kg mol $^{-1}$  were used to calculate the total number of entanglements  $Z_t$ .<sup>201</sup>

MELT RHEOLOGICAL PROPERTIES. The influence of an increasing  $s$  on the viscoelastic behavior was studied by small-amplitude oscillatory shear measurements at  $T = 130$  °C – 180 °C. Figure 6.18 a) and b) display that  $s$  distinctly affects  $G'$  and  $G''$ , and thus, the relaxation behavior of the samples.

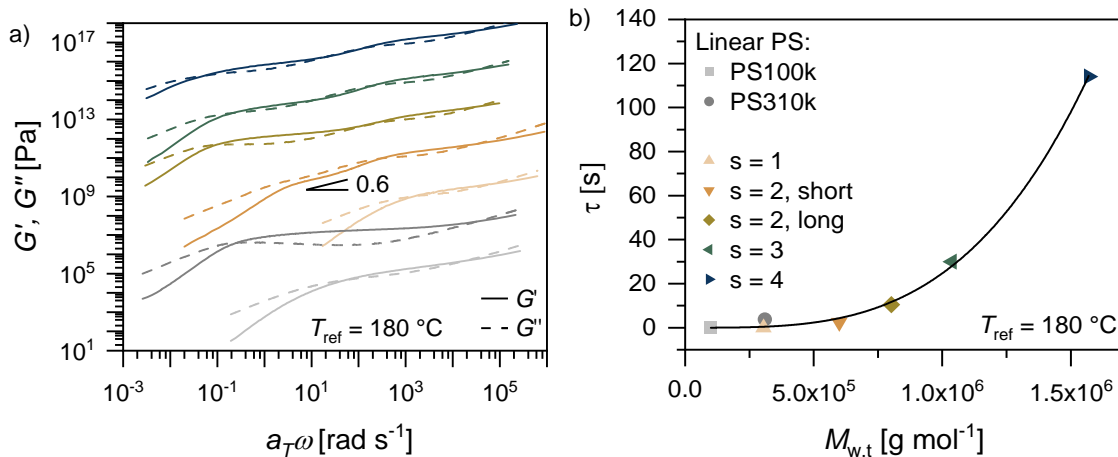


Figure 6.18. In a) master curves of the linear PS references and branched samples are shown at a reference temperature of  $T_{ref} = 180$  °C, indicating an asymptotic behavior in the flow region according to the Maxwell model. The master curves are vertically shifted by  $10^2$ ,  $10^4$ , and  $10^6$ . In b) is the average longest relaxation time  $\tau_1$  plotted against the total weight average molecular weight  $M_{w,t}$  at  $T_{ref} = 180$  °C. The black solid line represents a non-linear least-square fit according to a simple power-law, where  $M_{w,t}$  is given in g mol $^{-1}$  (prefactor =  $1 \times 10^{-20}$ , scaling exponent = 3.4).

The cross over in the high-frequency area ( $\omega = 10^4 - 10^5 \text{ rad s}^{-1}$ , for  $T_{\text{ref}} = 180 \text{ }^\circ\text{C}$ ) of the master curves in Figure 6.18 a) can be attributed to the local segmental relaxation of the styrene units.<sup>89</sup> The relaxation process of branched structures follows a hierarchical order.<sup>221,222</sup> Hence, the sidearms relax first at lower temperatures, i.e., higher frequencies. Therefore, the adjacent rubber plateau ( $\omega = 10^2 - 10^5 \text{ rad s}^{-1}$ ) is caused by entangled sidearms, while the cross over at around  $\omega = 210 \text{ rad s}^{-1}$  can be attributed to the sidearm relaxation time  $\tau_a$ . As all branched materials have similar  $M_{w,t}$ ,  $\tau_a$  for all branched materials is around  $\tau_a \approx 0.03 \text{ s}$ ; except for the single star, where  $\tau_a \approx 0.004 \text{ s}$ .

The 2-star-short shows only one rubber plateau caused by the sidearms and a regime, where  $G'$  and  $G''$  are parallel with a scaling exponent of 0.6 in a double-logarithmic plot. A slope of 0.6 indicates that the backbone exhibits constraint release Rouse-like behavior instead of the reptation mechanism, as introduced within Chapter 6.1.<sup>209,215,218,219,234</sup> This phenomenon can be attributed to the entangled sidearms, which entangle with the backbone and prevent the backbone from becoming entangled with itself, resulting in the absence of the backbones' rubber plateau. By lengthening the backbone to  $M_{w,b} \approx 280 \text{ kg mol}^{-1}$ , the backbone entangles with each other. For the samples with  $s = 3, 4$ , two rubber plateaus occur, indicating that sidearms and backbones are entangled. Moreover, the cross over in the low-frequency regime can be attributed to  $\tau_l$ , which increases exponentially from  $4 \times 10^3 \text{ s}$  to  $114 \text{ s}$  ( $T_{\text{ref}} = 180 \text{ }^\circ\text{C}$ ) with increasing  $M_{w,t}$ , as shown in Figure 6.18 b). The scaling of  $\tau_l$  with  $\tau_l \sim M_{w,t}^{3.4}$  is regardless of whether the increased  $M_{w,t}$  is due to the backbones' extension or to an additional linked star. Figure 6.19 displays the van Gorp-Palmen plot. This way to display the viscoelastic shear response under oscillatory excitation is, at first approximation, independent of the molecular weight for a linear topology, as only the  $\delta$  value of the minimum decreases with increasing molecular weight.<sup>235,236</sup> Consequently, the effect of topologies is amplified, allowing to compare the viscoelastic behavior of polymers with varying topologies like an increasing  $s$ .

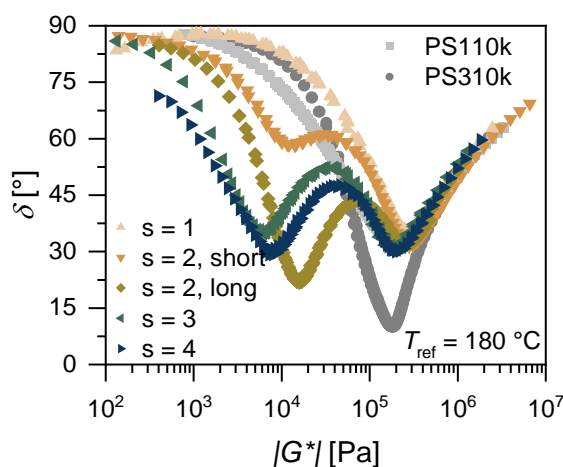


Figure 6.19. The van Gorp-Palmen (vGP) plot of the branched samples with  $s = 1 - 4$ ,  $M_{w,a} = 25 \text{ kg mol}^{-1}$  and  $q \approx s \times 11$ , and the two linear PS references at  $T_{\text{ref}} = 180 \text{ }^\circ\text{C}$ .

The observed local minima in the vGP plot at  $|G^*| = 6.0 \times 10^3 - 1.5 \times 10^4$  Pa for the branched topologies are related to the backbone as it is diluted by the sidearms. The second minimum in  $\delta$  at  $|G^*| \approx 2.0 \times 10^5$  Pa, a typical value for PS, is related to the entangled sidearms corresponding to the rubber plateau.<sup>235,236</sup> The phase angle at the local minimum caused by the backbone ( $|G^*| = 6.0 \times 10^3 - 1.5 \times 10^4$  Pa) decreases continuously with increasing  $s$  from  $\delta = 58^\circ$  (2-star-short) to  $\delta = 29^\circ$  (4-star), if the distance between the two covalently connected stars remains the same. By exceeding the distance, the minimum of  $\delta$  occurs at lower values with  $\delta = 22^\circ$  (2-star-long). The phase angle of the sidearms' minimum is about  $\delta \approx 32^\circ$ , confirming similar  $M_{w,a}$  for the branched structures investigated. Additionally,  $\delta$  of the linear topology decreases from  $\delta = 32^\circ$  to  $10^\circ$  with increasing  $M_{w,t}$ , as expected.<sup>235,236</sup>

It is well-known that branching highly impacts the viscosity of polymers, as short sidearms act as a plasticizer, reducing  $\eta_0$  of the polymer melt.<sup>221,222</sup> The  $\eta_0$  was determined by applying the multi-mode Maxwell model to  $G'$  and  $G''$ , considering the relaxation process of both the sidearms and the backbone to determine the LVE regime. Figure 6.20 a) illustrates  $|\eta^*(\omega)|$  as a function of  $a_T \omega$  while b) summarizes  $\eta_0$  as a function of  $M_{w,t}$ .

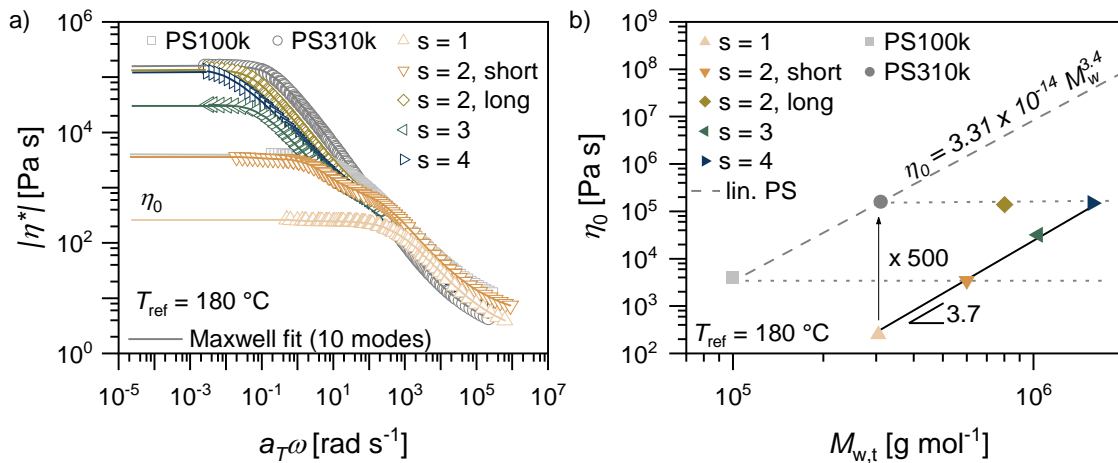


Figure 6.20. a) The absolute complex viscosity  $|\eta^*|$  as a function of the angular frequency  $a_T \omega$  at a reference temperature of  $T_{\text{ref}} = 180$  °C. The solid lines represent the fitting with the multi-mode Maxwell model (10 modes). b) The zero-shear viscosity  $\eta_0$  as a function of the total weight average molecular weight  $M_{w,t}$ . The grey dashed line represents the prediction for linear PS from literature and scales with  $\eta_0 \approx M_w^{3.4}$  (prefactor =  $3.31 \times 10^{-14}$ ).<sup>237</sup> The solid black line represents a non-linear least-square fit according to a simple power-law, where  $M_{w,t}$  is given in  $\text{g mol}^{-1}$  (prefactor =  $1 \times 10^{-19}$ , and scaling exponent = 3.7). The grey-dotted horizontal lines are to guide the eyes.

The sidearms dramatically reduce  $\eta_0$  compared to linear PS with the same  $M_{w,t}$ . For instance, the star has 500 times lower  $\eta_0$  compared to linear PS310k, even though their molecular weight is quite similar. Moreover, 2-star-short has a similar  $\eta_0$  as the linear PS100k, which corresponds to the  $M_{w,b}$ , although  $M_{w,t}$  is six times higher. The zero-shear viscosity of linear homopolymer melts follows a power-law dependency with increasing molecular weight with  $\eta_0 \sim M_w^{3.4}$ , as known from reptation theory for  $M_w > M_c$ .<sup>234</sup>



The sample series with increasing  $s$  show a scaling behavior of  $\eta_0 \sim M_w^{3.7}$ , which is nearly the same as for linear polymers with increasing molecular weights, but with an overall viscosity reduction by a factor of 500. Moreover, the  $\eta_0$  of the 2-star-long does not follow the trend compared to the other branched materials with a shorter backbone.

Elongation measurements were performed to investigate the melt properties under uniaxial stretching. The experiments were conducted at 180 °C between strain rates of  $\dot{\epsilon} = 0.003 - 10 \text{ s}^{-1}$ . A parameter to evaluate the elongation capability is the strain hardening factor  $SHF$ , which is described by the ratio of the maximum measured tensile stress growth coefficient  $\eta_{E,\max}^+(t, \dot{\epsilon}_H)$  to the theoretical viscoelastic linear response predicted using the Doi-Edwards model (DE)  $\eta_{E,DE}^+(\dot{\epsilon}_H)$ .<sup>114</sup> Figure 6.21 a) exemplarily shows the viscosity growth curves of the 4-star at  $T = 180 \text{ °C}$ . Figure 6.21 b) provides the resulting  $SHF$  as function of  $\dot{\epsilon}$  and the reached values are summarized in the Appendix, Table C.6.

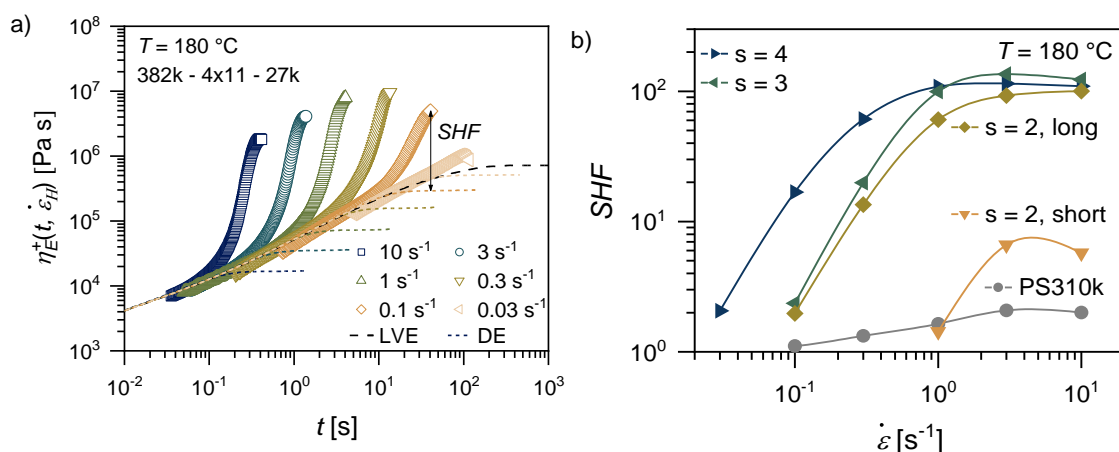


Figure 6.21. a) Viscosity growth curves of the 4-star measured at elongation strain rates  $\dot{\epsilon}$  ranging from  $0.03 \text{ s}^{-1}$  to  $10 \text{ s}^{-1}$  at  $T_{\text{ref}} = 180 \text{ °C}$ . Dashed and dotted lines represent the linear viscoelastic (LVE) regime and the Doi-Edwards (DE) model, respectively.<sup>114,119,120</sup> b) Strain hardening factors  $SHF$  of all samples as a function of the elongation strain rate  $\dot{\epsilon}$ . As the elongational viscosity of both, the star ( $s = 1$ ) and the short linear PS100k reference, was too low, and therefore, the elongational viscosity could not be measured; no data are included in the graph. The lines are guides to the eyes.

No elongation measurement could be performed with PS100k and the single star as the viscosities were too low at  $T = 180 \text{ °C}$ . However, no strain hardening is expected for a star-like topology, as it has only one branching point. At least two spatially separated branching points are required to generate strain hardening in elongational flow, e.g., H-shaped or pom-pom topology.<sup>118,231</sup> The linear PS310k exhibit a minor  $SHF$  of  $SHF = 2$  at  $\dot{\epsilon} = 10$ .

By increasing  $M_{w,b}$  from  $M_{w,b} = 100 - 280 \text{ kg mol}^{-1}$ , but keeping  $s = 2$ , the maximum  $SHF$  massively increases from  $SHF_{\text{max}} = 7$  to  $\sim 100$ , respectively. The distinct difference between these two samples is justified in the backbones' entanglement number. For  $s = 2$ , only the backbone of the sample with  $M_{w,b} \approx 280 \text{ kg mol}^{-1}$  is entangled with other backbones, confirmed by the rubber plateau in the low-frequency regime, see Figure 6.18.

Thus, the entanglement of both the backbone and the sidearms contributes to the SHF, resulting in a significant increase, while for the sample with  $M_{w,b} \approx 100 \text{ kg mol}^{-1}$  and  $s = 2$ , only the entanglement with the sidearms contributes to the SHF. The addition of even more stars along the backbone has a minor influence, as  $SHF = 135$  and  $114$  for  $s = 3$  and  $4$ , respectively. Therefore, minimum a single backbone with several entanglements between two branching points seems to be the critical parameter for extreme strain hardening in branched topologies. Furthermore, the SHF decreases with decreasing  $\dot{\epsilon}$  for all materials, and the minimum  $\dot{\epsilon}$ , where strain hardening still occurs decreases with increasing  $s$ .

PHYSICAL FOAMING – NUMBER OF STARS (S). Materials combining strain hardening in elongational flow at  $\dot{\epsilon} = 1 - 10 \text{ s}^{-1}$  with a low  $\eta_0$  in shear are highly suitable for foaming polymers, as they support foamability by reducing cell coalescence and rupture.<sup>9,10,57,62,205,206</sup> As the presented series meets both criteria, the samples are ideal for investigating their foaming behavior. Hence, the samples were foamed and the corresponding SEM images of the foams conducted at  $T_f = 100 \text{ }^\circ\text{C}$  and  $140 \text{ }^\circ\text{C}$  are exemplarily shown in Figure 6.22.

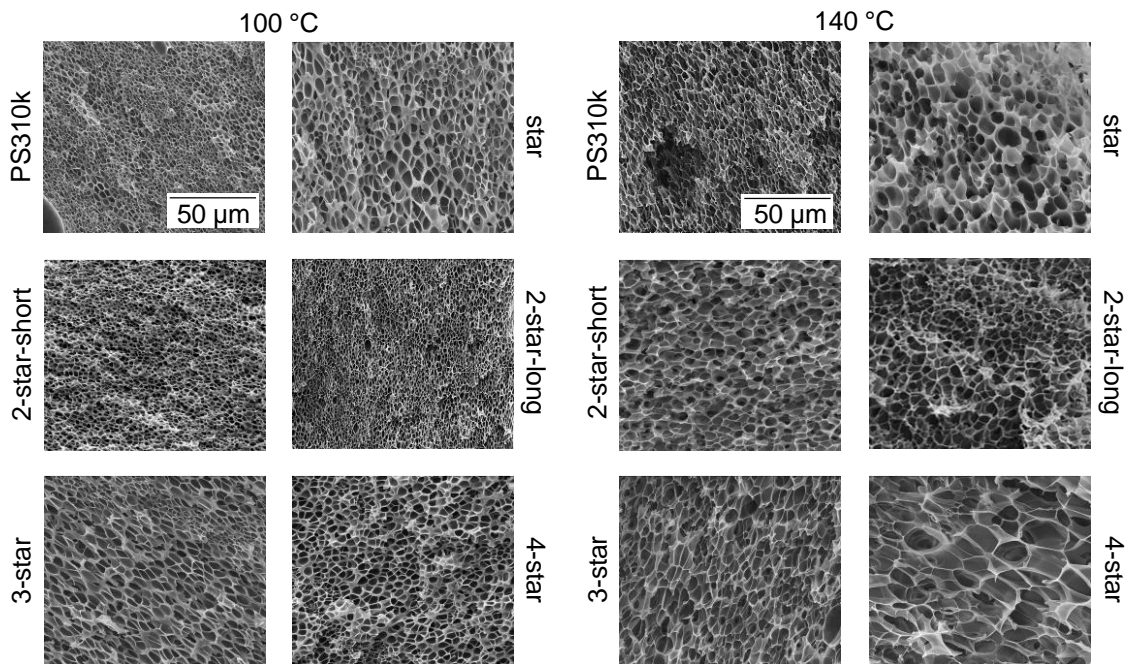


Figure 6.22. SEM images of the linear PS reference PS310k and the branches samples with  $s = 1 - 4$ ,  $M_{w,a} = 25 \text{ kg mol}^{-1}$  and  $q \approx s \times 11$ . The scaling bar is valid for each image within this figure. Foaming conditions:  $T_f = 100 \text{ }^\circ\text{C}$  and  $140 \text{ }^\circ\text{C}$ ,  $p = 500 \text{ bar}$ ,  $t_{\text{sat}} = 8 \text{ h}$ , and  $dp/dt \approx 200 \text{ bar s}^{-1}$ .

The SEM images indicate a relatively homogeneous cellular structure within all investigated samples, ranging from linear PS to a star and multiple covalently bonded stars of up to  $s = 4$ . Additionally, the effect of branching on the cell size becomes more pronounced at higher foaming temperatures, as visualized within the SEM images. For instance, the average cell size increases significantly with increasing  $s$ , especially at  $T_f = 140 \text{ }^\circ\text{C}$ .

A selective part of the complete statistical data is depicted in Figure 6.23, displaying the  $VER$  (a) and  $D$  (b) as a function of  $s$ , foamed at  $T_f = 100\text{ }^\circ\text{C} - 140\text{ }^\circ\text{C}$ . At higher temperatures, i.e.,  $T_f = 150\text{ }^\circ\text{C}$ , the foams collapsed. The complete statistical results of the foam density  $\rho_f$ , volume expansion ratio  $VER$ , average cell size  $D$ , and cell density  $N$  are summarized in the Appendix, Table C.7.

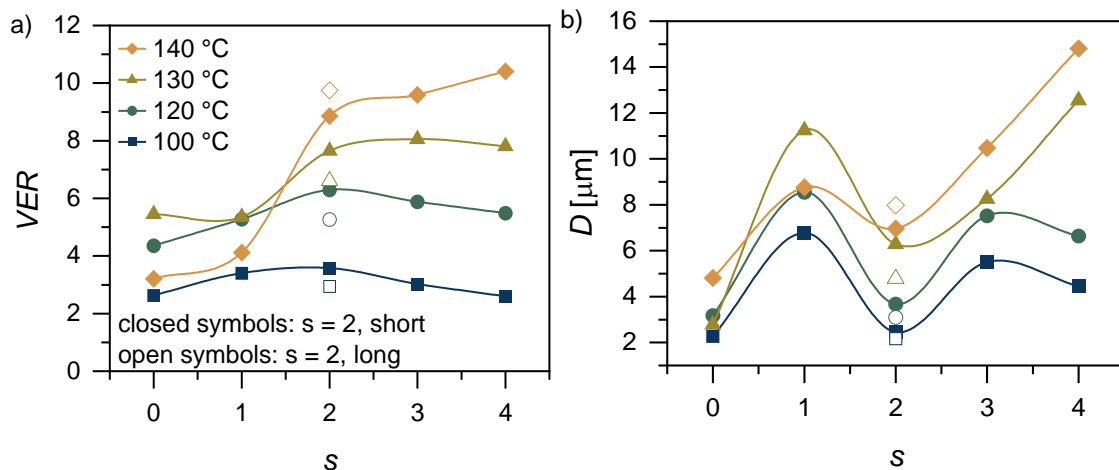


Figure 6.23. Volume expansion ratio  $VER$  (a) and average cell diameter  $D$  (b) as a function of the number of connected stars  $s$ .

Foaming conditions:  $T_f = 100\text{ }^\circ\text{C} - 140\text{ }^\circ\text{C}$ ,  $p = 500\text{ bar}$ ,  $t_{\text{sat}} = 8\text{ h}$ , and  $dp/dt \approx 200\text{ bar s}^{-1}$ .

The  $VER$  and  $D$  increase with increasing foaming temperature until the foams collapse. The foams based on the linear PS310k and single star collapsed at  $T_f = 130\text{ }^\circ\text{C}$ . In contrast, the barbwires were foamable up to  $T_f = 150\text{ }^\circ\text{C}$ , underlining the importance of topology and the requirement of at least two branching points, resulting in high melt strength, i.e., strain hardening. The single star ( $s = 1$ ) exhibits  $VER$  of  $VER = 2.63 - 5.35$  within  $T_f = 100\text{ }^\circ\text{C} - 130\text{ }^\circ\text{C}$ . In combination with the formation of relatively large cells with  $D = 6.8 - 11.2\text{ }\mu\text{m}$ , compared to the other branched samples, the experiments revealed that the significantly lower  $\eta_0$  and the low melt strength of the star leads to an increased tendency for cell coalescence.

At lower temperatures, no significant difference of  $VER$  occurs over the entire samples. As soon as the foaming temperature rises, the foams based on the barbwires ( $s = 2 - 4$ ) expand significantly more than the linear PS and the star. The maximum reached  $VER$  of the linear PS, and the star is  $VER = 5.45$  and  $5.35$  at  $T_f = 130\text{ }^\circ\text{C}$ , respectively, while the barbwires reached  $VER = 8.85 - 10.41$  at  $T_f = 140\text{ }^\circ\text{C}$ . However, an increasing  $s$  has a tremendous impact on  $D$ , which is also more pronounced at higher temperatures. At lower foaming temperatures, the resulting  $D$  of the 4-star is smaller than  $D$  of the 3-star, as it combines the highest  $\eta_0$  of  $\eta_0 \approx 1.48 \times 10^5\text{ Pa s}$  ( $s = 4$ ) compared to  $\eta_0 \approx 3.1 \times 10^4\text{ Pa s}$  ( $s = 3$ ) and the highest overall amount of entanglements of  $Z_t \approx 95$ , suppressing the cell growth rate and resulting in smaller cell sizes.<sup>62,238</sup>

Nevertheless, the effect is minimized at  $T_f = 140$  °C, and thus,  $D$  increases significantly with increasing  $s$  from  $6.3\ \mu\text{m}$  ( $s = 2$ , short) to  $14.8\ \mu\text{m}$  ( $s = 4$ ), revealing that lower viscosities promote higher  $VER$  and the formation of larger cells, due to the reduced viscosity-driven resistance to cell growth. These findings are in agreement with the literature. For instance, it was shown by numerical analysis that the cell growth rate is strongly affected by the viscosity variation during the initial step of cell growth.<sup>238</sup>

These findings highlight the importance of controlling the polymers' topology and the associated rheological melt properties in shear and elongational flow to achieve a desired cellular structure of the resulting polymer foams.

---

## 7 CELL STABILIZATION

Abstract: Stabilization of the cellular morphology of the foam occurs as soon as the polymer matrix vitrifies. This chapter elucidates the influence of the polymers' dynamic, specifically its glass transition temperature, on the solidification of the foam. Polystyrene derivatives with the same molecular weight were synthesized and compared to the foaming behavior of PS. Solubility measurements indicate similar CO<sub>2</sub>-solubilities for the materials, and consequently, the cellular morphology depends strongly on the foaming temperature. Higher cell densities and smaller average cell sizes were found with increasing glass transition temperatures due to earlier vitrification of the polymer matrix. The findings imply that the adaption of the glass transition temperature is a powerful tool to change the polymer property and the associated control of the structure of polymer foams.

---

The foaming temperature substantially impacts the foams' microstructure during the foaming process. The following explains the relationship between  $T_g$  of the polymer matrix and  $T_f$  and gives insights into the associated influence on the foaming process:<sup>55</sup>

1.  $T_f < T_g$ : Dissolved CO<sub>2</sub> lowers the  $T_g$  of the polymer melt and its shear viscosity; both promoting foamability. Due to the consumption of CO<sub>2</sub> during cell growth,  $T_{g,eff}$  returns to its initial value  $T_g$ , and the polymer respective foam vitrifies.
2.  $T_f = T_g$ : If the pressure difference between the cells inside and the reactor environment vanishes, cell growth stops as the polymer melt can only be deformed at a sufficiently high-pressure difference combined with a low viscosity.
3.  $T_f > T_g$ : High temperatures reduce the CO<sub>2</sub>-solubility inside the polymer, hence, decreasing the number of nuclei. The viscosity reduction associated with high  $T$  enhances cell growth, leading to increased average cell sizes and, ultimately, cell coalescence, as cell growth stops only by reaching the initial  $T_g$ .

However, the viscosity reduction caused by a high temperature extends the cell growth period and accelerates CO<sub>2</sub>-diffusivity. As a result, CO<sub>2</sub> can diffuse out of the polymer matrix, leading to a loss of blowing agent and an overall reduction of cell density.<sup>36,55,64</sup> Consequently, the polymers'  $T_g$  significantly affects the foamability of polymers.

LIVING ANIONIC POLYMERIZATION. PS and its derivatives poly(2-vinyl naphthalene) (P2VN), 4-Polyvinylbiphenyl (PVBP), and Poly( $\alpha$ -methyl styrene) (P $\alpha$ MS) were polymerized via LAP, leading to linear polymers with  $T_g$  ranging between 100 °C and 170 °C, see Figure 7.1. Depending on the polymers' solubility, the syntheses were performed in either toluene, THF, or benzene. All LAPs were carried out at room temperature (rt) except for P $\alpha$ MS, as the ceiling temperature is only about  $T \approx 61$  °C.

To avoid exceeding the ceiling temperature of P $\alpha$ MS despite the heat of the reaction generated due to the exothermal character and allow obtaining a monodisperse polymer, the polymerization was performed in THF at  $T = -78\text{ }^{\circ}\text{C}$ .

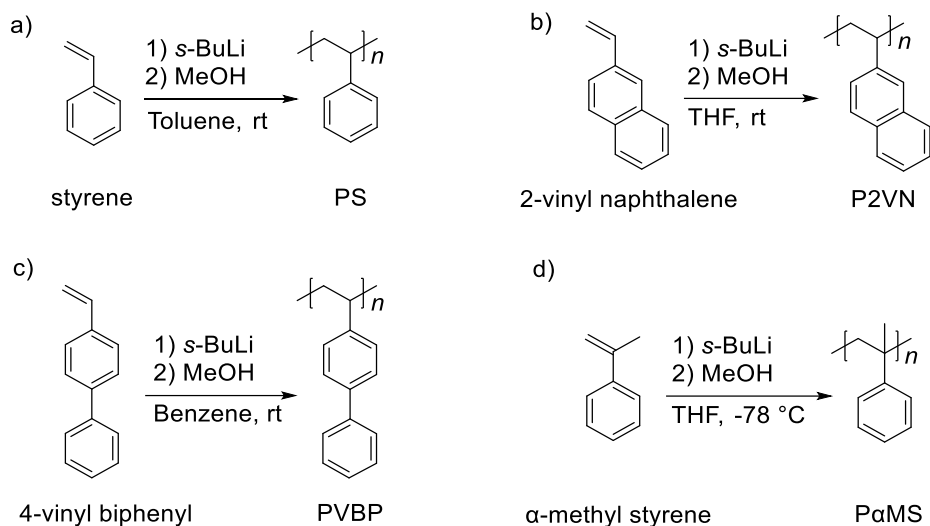


Figure 7.1. Living anionic polymerization of styrene and styrene derivatives resulting in PS (a), P2VN (b), PVBP (c), and P $\alpha$ MS (d).

The molecular information and dynamics of resulting linear polymers were analyzed by SEC and DSC. The resulting values like  $M_w$ ,  $\mathfrak{D}$ , and  $T_g$  are summarized in Table 7.1.

Table 7.1. Molecular characteristics of the linear PS and its derivatives P2VN, PVBP, and P $\alpha$ MS.

Sample	$M_w$ [kg mol <sup>-1</sup> ]	$\mathfrak{D}$	$T_g$ [°C]
PS	220	1.04	109
P2VN	170	1.17	139
PVBP	190	1.11	156
P $\alpha$ MS	200	1.01	176

PHYSICAL FOAMING – MOLECULAR DYNAMICS. Solubility is generally defined as the equilibrium blowing agent concentration for specific saturation conditions. The CO<sub>2</sub>-solubility in PS and P $\alpha$ MS was analyzed by the sorption method<sup>239</sup> at a saturation temperature of  $T_{\text{sat}} = 23\text{ }^{\circ}\text{C}$  and a pressure of  $p = 500\text{ bar}$ . The corresponding desorption curves are shown in Figure 7.2, while the sorption method is introduced in the Appendix, see Chapter B.

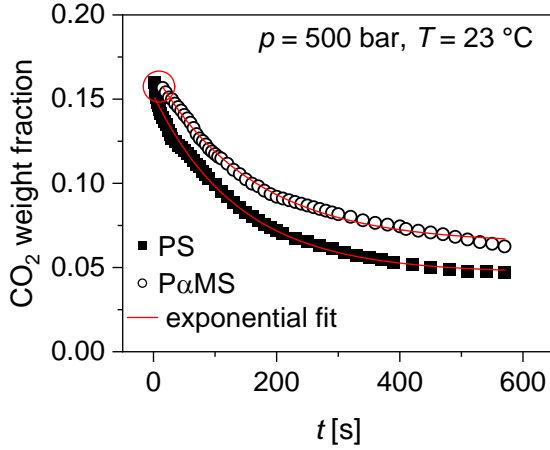


Figure 7.2. Desorption curves of CO<sub>2</sub> out of PS and PαMS at  $T_{\text{sat}} = 23 \text{ }^\circ\text{C}$  and  $p = 500 \text{ bar}$ , to measure the mass uptake of blowing agent. Samples were saturated with the blowing agent for 24 h. The maximum amount of dissolved CO<sub>2</sub> within the polymer matrices is marked in red.

The extrapolation of the desorption curves to a desorption time of  $t = 0 \text{ s}$  shows that the solubility of CO<sub>2</sub> in PS and PαMS is around 16 wt% at  $T_{\text{sat}} = 23 \text{ }^\circ\text{C}$  and  $p = 500 \text{ bar}$ . Similar results of the CO<sub>2</sub>-solubility in PS were found in the literature.<sup>56</sup> By comparing all polymers within this series, identical foaming conditions and molecular parameters like molecular weight should lead to comparable foaming behavior. The viscosity of the samples was determined experimentally via oscillatory rheological measurements to prove if the present viscosities of the pure polymers are sufficiently similar. The resulting  $|\eta^*|$  values are displayed as a function of  $a_T\omega$  in Figure 7.3.

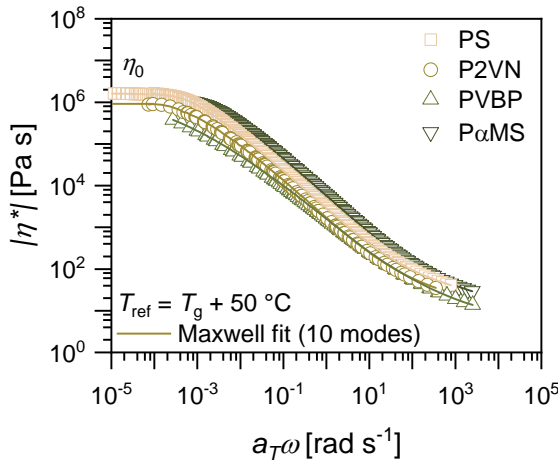


Figure 7.3. The absolute complex viscosity  $|\eta^*|$  as a function of the angular frequency  $a_T\omega$  at a reference temperature of  $T_{\text{ref}} = T_g + 50 \text{ }^\circ\text{C}$ . The solid lines represent the fitting with the multi-mode Maxwell model (10 modes).

All samples exhibit similar  $\eta_0$  of around  $10^6 \text{ Pa s}$  at  $T_{\text{ref}} = T_g + 50 \text{ }^\circ\text{C}$ . Accordingly, the impact of  $T_g$  on the stabilization of the cellular morphology is evident, as parameters like the viscosity or the blowing agent solubility match each other. Nevertheless, the question arises whether the polymers exhibit differences in cellular morphologies or not at different foaming temperatures but with an equal difference to the respective  $T_g$ . The samples were therefore foamed within a temperature range of  $-40 \text{ }^\circ\text{C} \leq T_g \leq 40 \text{ }^\circ\text{C}$  concerning  $T_g$ . Notably, the CO<sub>2</sub>-solubility decreases with increasing foaming temperature. Hence, a continuous decrease in the overall CO<sub>2</sub>-concentration from PS to PαMS occurs. Figure 7.4 displays the SEM images of foamed PS and its derivatives at  $T_f \approx T_g$ .

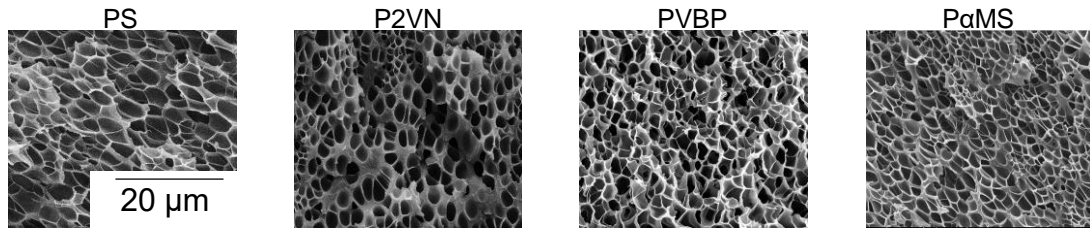


Figure 7.4. SEM images of foams based on linear PS, P2VN, PVBP, and P $\alpha$ MS. The scaling bar is valid for each image within this figure.

Foaming conditions:  $T_f \approx T_g$ ,  $p = 500$  bar,  $t_{\text{sat}} = 8$  h, and  $dp/dt \approx 200$  bar  $s^{-1}$ .

An uniform cellular morphology was observed in all foams, and  $D$  decreases slightly with increasing  $T_g$  of the polymer. However, the cell wall thickness of the P2VN-based foam is comparably thicker than the other samples, indicating higher cell coalescence. The cellular parameters such as  $VER$ ,  $N$ , and  $D$  are plotted as a function of  $T_f - T_g$  in Figure 7.5.

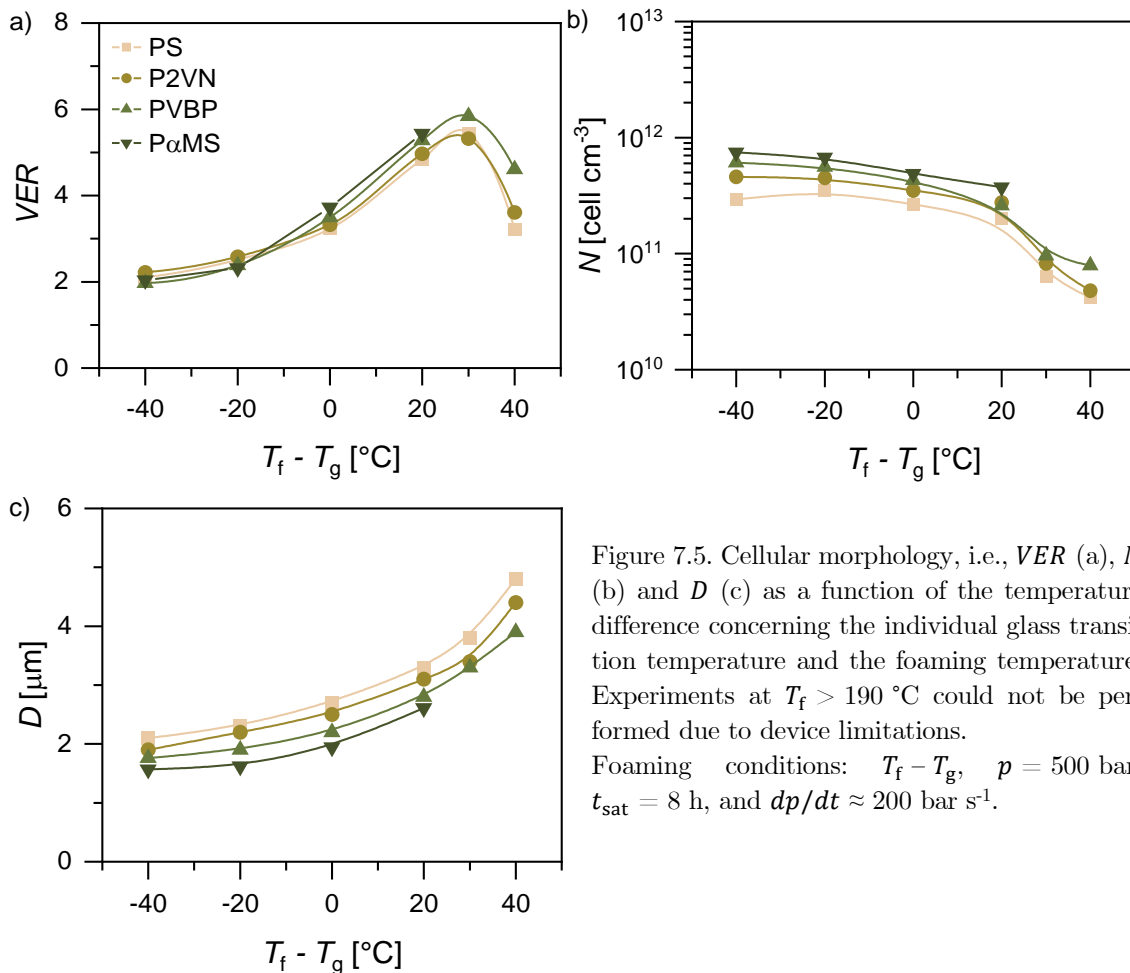


Figure 7.5. Cellular morphology, i.e.,  $VER$  (a),  $N$  (b) and  $D$  (c) as a function of the temperature difference concerning the individual glass transition temperature and the foaming temperature. Experiments at  $T_f > 190$  °C could not be performed due to device limitations.

Foaming conditions:  $T_f - T_g$ ,  $p = 500$  bar,  $t_{\text{sat}} = 8$  h, and  $dp/dt \approx 200$  bar  $s^{-1}$ .

The  $VER$  increases from 1.82 to 5.84 with increasing  $T_f$ , and the maximum occurs for all samples at  $T_f - T_g = 30$  °C. P $\alpha$ MS could not be foamed at  $T_f > T_g + 20$  °C due to instrumentation limits, but it shows the highest  $VER$  over the investigated temperature range compared to PS, P2VN, and PVBP. However, the difference in the maximum  $VER$  is only around a factor of 1.1. Foams based on PS, P2VN, and PVBP collapsed at  $\Delta T = 40$  °C.



The  $N$  decreases with increasing  $T_f$  due to a lower viscosity, higher diffusivity, cell growth rate, and span, as introduced in Chapter 2.2. Despite the lower overall  $\text{CO}_2$ -solubility of  $\text{CO}_2$  in  $\text{P}\alpha\text{MS}$  according to the higher foaming temperatures, the highest  $N$  is observed for  $\text{P}\alpha\text{MS}$  and its maximum value is around  $N \approx 7.45 \times 10^{11}$  cells  $\text{cm}^{-3}$  at  $T_f = 130$  °C, which corresponds to  $T_f - T_g = -40$  °C. Under the investigated experimental conditions, it was found that  $D$  is much smaller at lower  $T_f$  for all samples. This trend can be expected, as not only the polymers' viscosity is higher, but the period for cell growth is much shorter until the polymer matrix stabilizes. As  $T_f$  increases, the viscosity decreases, supporting expansion. The foam characteristics are summarized in the Appendix, see Table C.8.

Similar trends have been established in the literature by investigating the influence of glass transition temperature using cyclic olefin copolymers (COC). Cyclic olefin copolymers represent an umbrella term for amorphous copolymers of ethylene and norbornene.<sup>66</sup> The investigated COCs had glass transition temperatures of  $T_g = 78$  °C and 158 °C. It was found that both the blowing agents' solubility and its diffusivity up to  $T_f = 50$  °C were around 20 % – 50 % or around 15 % higher for the high  $T_g$  COC, respectively. For temperatures beyond 50 °C, the diffusivity within the low  $T_g$  COC increased much faster, as it was already in the rubbery state. Also, a higher minimum  $T_f$  was needed for the high  $T_g$  COC to ensure a proper cell expansion at similar blowing agent concentrations. Within the investigated temperature range of  $T_f = 50$  °C – 110 °C and  $T_f = 110$  °C – 170 °C for the low and high  $T_g$  COC, respectively, the high  $T_g$  COC exhibits lower average cell sizes of around  $D = 2 - 10$   $\mu\text{m}$  and cell densities between  $N = 2 \times 10^9 - 7 \times 10^9$  cells  $\text{cm}^{-3}$ .

To decouple the effect of gas concentration and  $T_g$ , the linear PS and its derivatives were foamed at  $T_f = 130$  °C and the relationships between  $N$  and  $D$  were analyzed as a function of  $T_g$ , as shown in Figure 7.6.

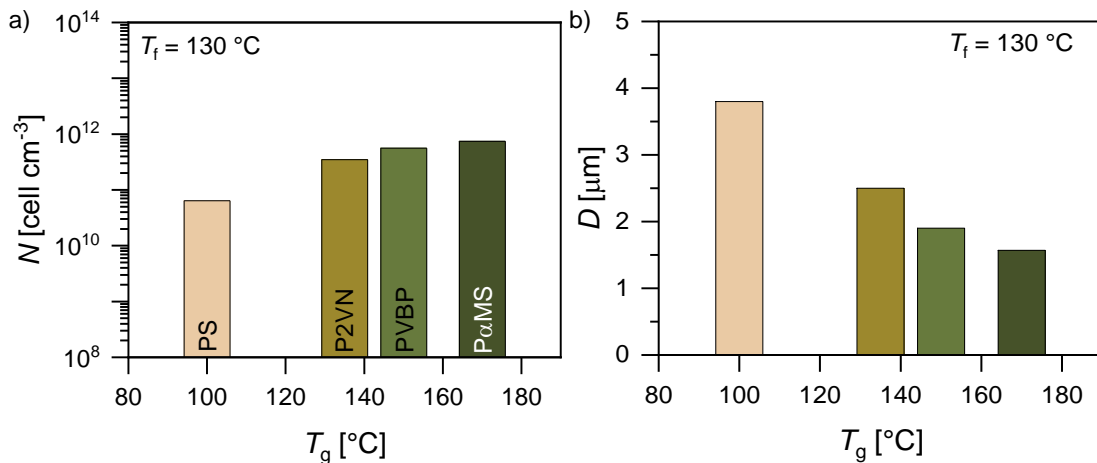


Figure 7.6. Effect of glass transition temperature  $T_g$  on the cell density  $N$  (a) and the average cell size  $D$  (b) using PS, P2VN, PVBP, and  $\text{P}\alpha\text{MS}$ .

Foaming conditions:  $T_f = 130$  °C,  $p = 500$  bar,  $t_{\text{sat}} = 8$  h, and  $dp/dt \approx 200$  bar  $\text{s}^{-1}$ .

The cell density increases from  $N = 6.4 \times 10^{10}$  cell  $\text{cm}^{-3}$  to  $7.45 \times 10^{11}$  cell  $\text{cm}^{-3}$  with increasing  $T_g$  while the average cell size decreases from  $D = 3.8 \mu\text{m}$  to  $0.97 \text{ nm}$  at a foaming temperature of  $T_f = 130 \text{ }^\circ\text{C}$ . The trends can be justified by the fact that an increasing  $T_g$  shortens the cell growth phase by earlier occurring vitrification of the polymer matrix. Subsequently, the intracellular pressure fails to attain the required threshold for inducing further cell deformation. Cell expansion is also restricted by the accompanying viscosity-difference of the samples, as polymers with a higher  $T_g$  exhibit higher viscosities compared to low  $T_g$  polymers with the same molecular weight under the same temperature influence. Consequently, cell coalescence is further minimized, leading to higher  $N$  and smaller  $D$ .

The investigation implies that the glass transition temperature exhibits a pronounced influence on the resulting cellular morphology, as it influences the growing span of the cells. By adapting the local polymer dynamics, i.e., an increase in  $T_g$ , the cell density could be increased by simultaneously reducing the average cell size. Based on these insights, further investigations should be based on high  $T_g$  polymers as the matrix, like P $\alpha$ Ms, in combination with branches. This combination would reduce viscosity and incorporate strain hardening to minimize cell coalescence and control cell stabilization simultaneously. Ideally, leading to high expandable foams with a high cell density and small cell sizes but thin cell walls, which is an often-desired morphology in thermal insulations or lightweight constructions applications.

---

## 8 CONCLUSION AND OUTLOOK

This dissertation aimed to synthesize model polymers with defined molecular parameters, including molecular weight, block order or branching, and low dispersity. The resulting polymer properties, such as mobility, solubility, branching, or molecular dynamics, significantly impact one of the three main stages of the physical foaming process: cell nucleation, growth, and stabilization of the foam. The polymer model architectures, which are of utmost importance for the dissertation, were synthesized using living anionic polymerization, primarily utilizing amorphous polystyrene. Thereby, the subsequent polymer parameters turned out to be particularly suitable:

1. The morphology of block copolymers exerts a strong influence on cell nucleation, as phase boundaries can decrease the free energy barrier of nucleation.
2. Polymers with a branched topology support foam expansion. The added sidearms decrease the overall viscosity due to plasticization and improve melt strength by incorporating strain hardening; cell coalescence and rupture are thereby minimized.
3. The molecular dynamics, i.e., glass transition temperature, determine foam stabilization, as the cells' expansion period shortens due to faster vitrification of the polymer matrix.

For evaluating the impact of polymer properties on the foaming behavior, batch foaming was chosen as a straightforward, controllable, and well-established technique. The polymers were foamed using the following conditions:  $p = 500$  bar,  $dp/dt \approx 200$  bar  $s^{-1}$ ,  $t_{\text{sat}} = 8$  h, and  $T_f = 60$  °C – 150 °C. Below 60 °C, all samples exhibited heterogeneous cell distribution, whereas, above 150 °C, all foams collapsed.

CELL NUCLEATION. Two main influence parameters were differentiated by investigating the impact of polymer properties on the resulting cellular morphology, especially the cell density: chain mobility and CO<sub>2</sub>-solubility. Therefore, linear di- and triblock copolymers were synthesized by sequential living anionic polymerization based on PS and PI or PS and PMMA. The average molecular weight varied between  $M_w = 200$  kg  $\text{mol}^{-1}$  and 1,000 kg  $\text{mol}^{-1}$ , while the PI- or PMMA-content systematically increased from  $\phi = 10$  mol% to 40 mol%, resulting in a spherical, cylindrical, or lamellar morphology of the PI-phase. Samples were named according to their chemical composition and molecular properties. For instance, a PS-*b*-PI-*b*-PS triblock copolymer with a  $M_w = 400$  kg  $\text{mol}^{-1}$  and a PI-content of  $\phi_{\text{PI}} = 10$  mol% was abbreviated as: SIS400k10%. Inorganic SiO<sub>2</sub>-particles with a diameter of  $d = 80$  nm were extrusion blended into a linear PS matrix with a weight content of  $w_{\text{particle}} = 0.25, 0.50, \text{ and } 1.00$  wt%, serving as a reference systems.

The investigation of the chain mobility was studied using PI-blocks, as the mobility of the PI is much higher due to its low glass transition temperature with  $T_{g,PI} \approx -70$  °C, whereas  $T_{g,PS} \approx 100$  °C. Moreover, different molecular weights, block lengths, and orders resulted in different morphologies, i.e., spherical, cylindrical, and lamellar microdomains, with domain sizes between  $d_0 = 16.8 - 61.9$  nm, while  $d_0$  could be correlated with the cell density  $N$  and average cell size  $D$ . The results indicate that spheres especially support heterogeneous nucleation. For instance, SIS400k10% with  $d_0 = 25.6$  nm leading to the highest cell density of  $N = 2.07 \times 10^{13}$  cell cm<sup>-3</sup> and the smallest average cell size of  $D \approx 0.39$  μm at a foaming temperature of  $T_f = 60$  °C, while the volume expansion ratio was  $VER = 1.66$ . The theoretical maximum cell density, which can be achieved using the here investigated samples with a spherical morphology, varies between  $N_{max} = 1.70 \times 10^{15} - 2.82 \times 10^{16}$  cells cm<sup>-3</sup>, depending on the molecular composition and foaming conditions.

Diblock copolymers with equal chain mobility, like PS-*b*-PMMA, were synthesized to study the influence of heterogeneous CO<sub>2</sub>-solubility. The following results could be achieved: The cell density increased with an increasing amount of PMMA within the diblock copolymer up to  $N = 3.16 \times 10^{11}$  cell cm<sup>-3</sup> ( $T_f = 120$  °C) for SMMA400k40%. In contrast,  $N$  of the analog SI diblock copolymer (SI400k40%) reference is around two orders of magnitudes lower at similar foaming conditions due to cell coalescence within the soft PI-phase. In future work, a block copolymer with the same CO<sub>2</sub>-solubility but different  $T_g$  could be used to prove and confirm the assumption based on the differences in chain mobility and CO<sub>2</sub>-solubility. Moreover, the comparison with the addition of nucleation particles to promote heterogeneous nucleation should be further developed.

In future work, the suitability of the synthesized block copolymers as compatibilization agents in corresponding blends of the same polymers could be investigated to enhance the blends' poor foam homogeneity and foamability. Moreover, the blending of block copolymers should refine the cellular morphology by improving the interfacial adhesion between the blend phases, as the block is selectively miscible in either blend component.<sup>196,240-243</sup> Consequently, adding block copolymers leads to increased interfacial strength, and minimized coalescence and interfacial tension among the blend phases.

CELL GROWTH. The topological relationship to cell expansion was investigated by polymers with pom-pom- or barbwire-shaped model architectures that affect the melt strength and viscosity, both known to reduce cell coalescence and rupture. The polymer backbone length, sidearm length, number of sidearms, and stars were systematically varied between:  $M_{w,b} = 100 - 400$  kg mol<sup>-1</sup>,  $M_{w,a} = 7 - 300$  kg mol<sup>-1</sup>,  $q \approx 2 \times 5 - 2 \times 22$ , and  $s = 1 - 4$ , respectively. Thereby, the volume expansion ratio and average cell size reached values between  $VER = 2.0 - 16.0$  and  $D = 1.3 - 17.2$  μm at  $T_f = 100$  °C - 150 °C. Additionally, the data indicate that  $M_{w,a}$  has a more significant impact on  $D$ , while the  $VER$  is substantially influenced by  $M_{w,b}$ .

---

Moreover, the resulting cellular morphology was associated with the rheological properties, i.e., strain hardening factor  $SHF$  and zero-shear viscosity  $\eta_0$ . The study revealed a maximization of  $VER$  and  $D$  by incorporating high  $SHF$  and low  $\eta_0$  within the polymer models. Since the combination of both improves cell growth with simultaneous minimization of cell coalescence or rupture.

An ideal structure-property relationship to maximize  $VER$  should be provided by pom-poms with the following molecular parameters: long, high entangled backbone and short sidearms to achieve high  $D$ , or long sidearms to achieve small  $D$ . Additionally, moderate to as high as possible sidearms, resulting in  $M_{w,b} \geq 400 \text{ kg mol}^{-1}$ ,  $M_{w,a} \approx 25 \text{ kg mol}^{-1}$  or  $M_{w,a} \approx 300 \text{ kg mol}^{-1}$  and  $q \geq 9$ . Moreover, Table 6.2 of Chapter 6.1 provides an overview of the influence of each topological parameter.

The findings regarding the correlation of rheological properties and cellular morphology in dependence on the polymer topology could be transferred to polymers with industrial relevance that are easy to manufacture to exploit the insights based on complex but well-defined, elaborately synthesized polymer model architectures. One approach for future work could be blending commonly available polymers to adjust viscosity and strain hardening behavior and study foamability. Moreover, the pom-pom and barbwire polymer topologies can be used as additives in linear polymers to increase melt strength, minimize coalescence and maximize cell expansion.

**CELL STABILIZATION.** The impact of the molecular dynamics as the glass transition temperature on the stabilization of the polymer matrix was investigated by linear PS and its derivatives, namely P2VN, PVBP, and P $\alpha$ MS with the same molecular weight of  $M_w \approx 200 \text{ kg mol}^{-1}$  and  $T_g \approx 100 \text{ }^\circ\text{C} - 170 \text{ }^\circ\text{C}$ . Under the same foaming conditions ( $T_f = 130 \text{ }^\circ\text{C}$ ), the cell density increased from  $N = 6.4 \times 10^{10} \text{ cell cm}^{-3}$  to  $7.5 \times 10^{11} \text{ cell cm}^{-3}$  with increasing  $T_g$ . Additionally, the average cell size decreased from  $D = 3.8 \text{ }\mu\text{m}$  to  $1.6 \text{ }\mu\text{m}$ . The findings indicate a possible control of foamability by taking the  $T_g$  of the polymer matrix into account for constant foaming conditions.

In future work, high  $T_g$ -polymers can be used as main component, e.g., in block copolymers or branched polymers, to shorten the cell expansion period and improve cell density by maximizing cell coalescence and minimizing average cell size. The structure-property relationship of these parameters is crucial for applications, where the lowest possible density combined with maximized  $N$  and minimized  $D$  is essential. These properties are especially important for lightweight materials in construction applications or automotive parts.

**SUMMARY.** The comprehensive study of the individual and independently investigated parameters can serve as a guideline to design and achieve the intended cellular morphology of polymer foams by considering the polymer properties, including mobility, solubility, branching, and molecular dynamics, as well as the underlying rheological properties.

The achieved cell morphologies are summarized as  $D$  vs.  $VER$  in Figure 8.1. For an exact assignment of the samples, the reader is referred to the respective Chapters 5 (block copolymers), 6 (pom-poms, stars and barbwires), and 7 (PS and derivatives).

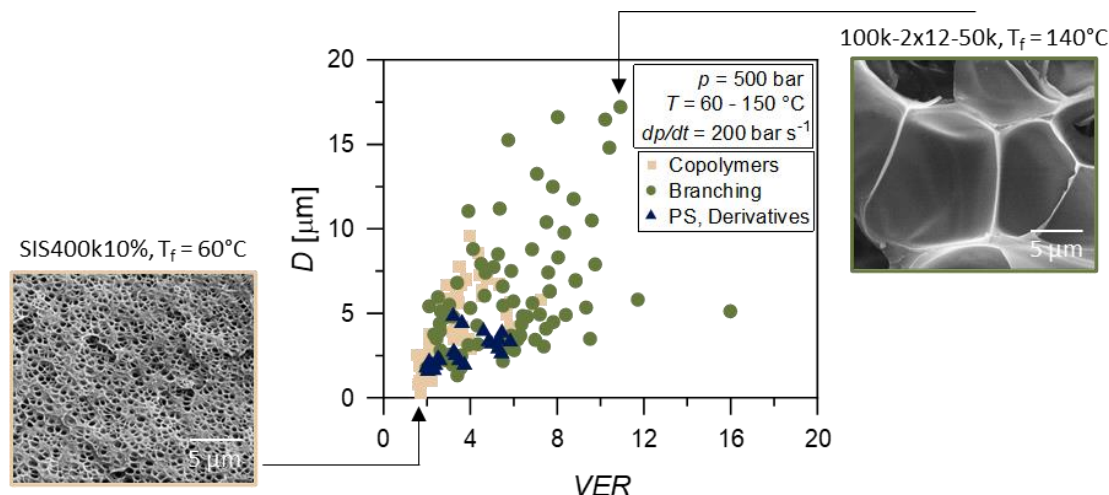


Figure 8.1. Summary of the resulting cell morphologies obtained using PS-based model systems studied within this dissertation. Cell size  $D$  as a function of volume expansion ratio  $VER$ ; Foaming conditions:  $p = 500$  bar,  $t_{\text{sat}} = 8$  h,  $dp/dt \approx 200$  bar  $s^{-1}$ , and  $T_f = 60$  °C – 150 °C.

Based on the results obtained during this dissertation, a polymer combining the following molecular feature should be promising to achieve high  $VER$  and  $N$ : A high  $T_g$ , such as  $P\alpha MS$  with as many sidearms as possible, a sidearm length of around the critical molecular weight for a maximize  $D$  and long sidearms around  $M_{w,a} = 300$  kg  $mol^{-1}$  to minimize  $D$ . Additionally, the backbone length should be as long as possible (around  $M_{w,b} = 400$  kg  $mol^{-1}$  was the maximum within this dissertation). Simultaneously, a polymer with a higher  $CO_2$ -affinity could be used as a copolymer component, such as PI or PMMA. The choice of copolymer depends to a decisive extent on its  $T_g$  and the desired foaming temperature. All details are summarized in Table 8.1.

Table 8.1. Summary of the investigated influencing parameters and the combination of these towards an optimized structure-property relationship regarding the resulting cellular morphology.

Parameter	Interest	Promising polymer property	Ideal combination
Solubility	High $N$ , low $D$	Spherical morphology with low sphere diameter	High solubility, low mobility, and as many as possible phase boundaries or addition of particles
Mobility	High $N$ , low $D$	Similar mobility but high solubility	

Table 8.1 continued.

Parameter	Interest	Promising polymer property	Ideal combination
Branching	Low $\eta_0$	Short and/or many sidearms	Long backbone combined with a moderate number of sidearms around the critical molecular weight (Combination of high $SHF$ and low $\eta_0$ )
	High $SHF$	Long, entangled backbone, moderate sidearm lengths, and number	
	High $VER$	Long, entangled backbone, moderate sidearm lengths, and number	
	Low $D$	Long, entangled backbone, moderate sidearm lengths, and number	
Glass transition temperature	High $N$ , low $D$	Polymer with high $T_g$	High $T_g$

In future work, the molecular findings should be extended and strengthened by including the analysis of the mechanical properties of foams. Afterward, the obtained knowledge can be incorporated again into the molecular properties of the model systems in a circular process until the best possible understanding between intrinsic molecular properties and application properties is achieved, as outlined in Figure 8.2.

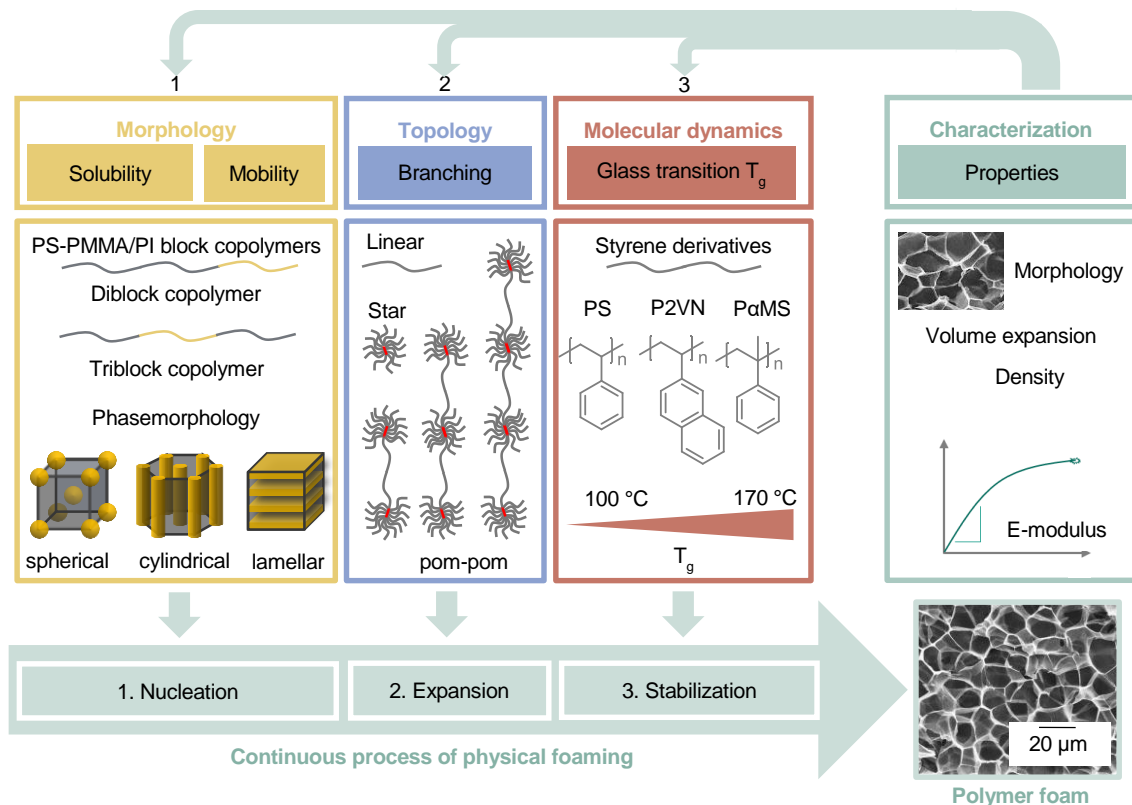


Figure 8.2. Outlook: The knowledge gained within the individual studies should be used to modify the model systems further and verify their influence on the mechanical stability of the foams.

The knowledge gained in the application should make it possible to directly determine the best possible polymer morphology respective topology for a planned specific application for the foam, thus greatly simplifying the application-specific adaptation of the manufacturing process.



---

PART III

APPENDIX



---

## A SYNTHESIS AND PURIFICATION

### A.1 PURIFICATION METHODS

MONOMERS. Stabilized styrene (99 %, extra pure, Sigma-Aldrich), methyl methacrylate (> 99.0 %, VWR), and  $\alpha$ -methyl styrene (> 99.0 %, Sigma-Aldrich) were purified by distillation after stirring one night over calcium hydride ( $\text{CaH}_2$ , 92 %, Fisher Scientific). Then, the monomers were distilled from di-*n*-butyl-magnesium (0.5 M, Fisher Scientific) into ampoules and degassed by three successive freezing-evacuation-thawing cycles. The monomers 2-vinyl naphthalene (97 %, Fisher Scientific) and 4-vinyl biphenyl (> 97.5 %, Sigma-Aldrich) were purified by sublimation under argon atmosphere at a continuously reduced pressure at 70 °C or 90 °C, respectively. Stabilized isoprene (98 %, VWR) was purified by cooling the monomer in an ice bath and adding *n*-butyllithium (2.5 M in cyclohexane, Sigma-Aldrich). The monomer was distilled into an ampoule when the solution turned yellowish. The purified monomers were stored under argon atmosphere at -18 °C until needed.

SOLVENTS. Toluene (> 99.0 %, Roth), cyclohexane (99 %, Fisher Scientific), and benzene (99.7 %, Sigma-Aldrich) were stored over living PS and distilled before use. Tetrahydrofuran (THF, 99.5 %, Roth) was distilled from  $\text{CaH}_2$ , stored over sodium/benzophenone, and distilled before synthesis. 1,4-Dioxane ( $\geq$  99.8 %, Fisher Scientific) was distilled to remove the stabilizer.

OTHER CHEMICALS. Methanol (> 99 %, Fisher Scientific) was degassed by three successive freezing-evacuation-thawing cycles. Hydrogen peroxide ( $\text{H}_2\text{O}_2$ , 30 wt%, Acros), formic acid (98 %, Roth), di-*n*-butyl-magnesium (0.5 M, Fisher Scientific), as well as *sec*-butyllithium (*s*-BuLi, 1.4 M in cyclohexane, Aldrich) were used as received. Butylated hydroxytoluene (BHT, VWR) was used as an antioxidant. For SEC measurements, SEC-grade THF was used (0.025 % BHT, Fisher Scientific). Deuterated chloroform ( $\text{CDCl}_3$ , > 99.8 %, Sigma-Aldrich) was used for  $^1\text{H}$ -NMR measurements. 1,1-Diphenylethylene (DPE, 97 %, Sigma-Aldrich) was used to reduce the reactivity of the formed macro-anions.

### A.2 PHASE SEPARATING BLOCK COPOLYMERS

The PS- and PI-based block copolymers were synthesized using LAP in dry cyclohexane (200 mL) at rt using high-vacuum techniques (approximately  $10^{-3}$  mbar) under argon atmosphere. The comonomers were added sequentially to the reaction flask after the complete conversion of the previous block, using *s*-BuLi as the initiator. The amount of added styrene, isoprene, and *s*-BuLi depends on the overall  $M_w$  of the block copolymer and the volume percentage of the PI-phase.

Subsequently, the living chains of the block copolymers were terminated with degassed methanol, and the polymer was precipitated in a large excess of methanol.

The PS- and PMMA-based diblock copolymers were synthesized using the same procedure introduced for the PS- and PI-based copolymers. However, the reactivity of the PS anions had to be reduced to minimize the reaction with the carbonyl of MMA using DPE. Therefore, styrene was polymerized in THF at -78 °C with *s*-BuLi as initiator. Then, DPE with the same concentration as the initiator was added, followed by MMA. The living anionic chains were terminated using degassed MeOH, and the resulting polymer was precipitated in a large excess of methanol.

### A.3 COMPLEX TOPOLOGICAL MODEL SYSTEMS

The synthesis procedure of all investigated branched materials is based on the following three steps: (I) living anionic polymerization, (II) epoxidation, and (III) grafting-onto. Each step is explained in detail for synthesizing the pom-pom topology, followed by a brief summary of the synthesis of stars and barbwires, considering the main synthesis differences.

**SYNTHESIS PROCEDURE – POM-POM / LIVING ANIONIC POLYMERIZATION.** An ISI triblock copolymer was synthesized using LAP in dry cyclohexane (200 mL) at rt using high-vacuum techniques (approximately  $10^{-3}$  mbar) under argon atmosphere. Thereafter, the comonomers were added sequentially to the reaction flask after the complete conversion of the previous block ( $V_{\text{PS}} = 9.9$  mL,  $V_{\text{PI}} = 0.74$  mL for each block). For further details, the reader is referenced to Chapter A.2. Subsequently, the living anionic chains of the triblock were terminated with degassed methanol, and the resulting polymer was precipitated in a large excess of methanol. The resulting ISI triblock is used as the backbone for the pom-poms and has a molecular weight of  $M_{\text{w,b}} = 100$  kg mol<sup>-1</sup> (degree of polymerization  $P_{\text{n,ISI}} = 938$ , obtained by SEC measurements based on a PS calibration). The PI-blocks in each ISI backbone had  $M_{\text{w,PI}} = 5$  kg mol<sup>-1</sup>, corresponding to approximately 70 isoprene units on each side as quantified via <sup>1</sup>H-NMR. Volumes of styrene and isoprene, as well as the initiator concentration, were adjusted accordingly to the desired backbone length, i.e., weight average molecular weight of the backbone.

The PS sidearms that would later be grafted onto the backbone were polymerized by LAP, following the same procedure, except that only styrene was used as a monomer. Moreover, the sidearms were left unterminated to ensure a reaction of the living anionic chains with the epoxidized backbone, see the epoxidation procedure below.

**EPOXIDATION.** The ISI triblock previously prepared was subjected to an epoxidation reaction to convert some of the double bonds of the isoprene units into epoxides. Note only the double bonds within the 1,4-*cis* configuration of the PI-blocks can be epoxidized.<sup>214</sup>

---

Epoxidation of the synthesized ISI backbone (10 g) was performed for 2 h in toluene (200 mL) at 40 °C with H<sub>2</sub>O<sub>2</sub> (1.77 g, 52.1 mmol) and formic acid (0.75 g, 16.3 mmol) as a catalyst, as described in the literature.<sup>214</sup> Afterward, the resulting epoxidized ISI backbone was freeze-dried out of destabilized dioxane to remove residual amounts of protonic compounds, like water. The epoxidation level was determined using <sup>1</sup>H-NMR analysis from the relative intensities of the C=C-H resonance in 1,4-*cis* PI at a chemical shift of 5.10 ppm and the corresponding proton resonance in epoxidized 1,4-units at 2.70 ppm, which yields in average to 50 % of epoxides.

GRAFTING-ONTO. The previously synthesized living anionic PS sidearms were grafted onto the epoxidized backbone under argon atmosphere at room temperature leading to the pom-pom topology, as demonstrated in Figure 6.1. The resulting PS pom-poms were purified by two to three fractionation steps in a THF/methanol mixture at room temperature. The entire synthesis of the pom-poms, including backbone polymerization and functionalization, freeze-drying, grafting-onto, and multiple purifications, required two weeks.

SYNTHESIS PROCEDURE – STAR. The star was synthesized in three steps. First, a linear PI backbone (10 mL isoprene, 99.8 mmol) was synthesized via living anionic polymerization in cyclohexane (150 mL) at room temperature with *s*-BuLi (0.97 mL, 1.36 mmol) as the initiator. Cyclohexane was used as a solvent to control the microstructure of the PI, as only 1,4-*cis*-PI are epoxidizable with the conditions used.<sup>214</sup> The synthesis of the PI backbone was followed by epoxidation of the double bonds with formic acid (3.75 g, 81.5 mmol) and H<sub>2</sub>O<sub>2</sub> (8.85 g, 260.3 mmol) at 40 °C in toluene (150 mL) to functionalize the backbone for the following grafting-onto of living PS chains.

SYNTHESIS PROCEDURE – BARBWIRE. The samples with  $s = 3, 4$  (3-star, 4-star) are based on a penta- and heptablock copolymer as a backbone, respectively. To synthesize the penta- and heptablock copolymers based on PI and PS, asymmetric ISI' triblock and ISIS' quadrobloc copolymers with  $I = 2 \times I'$  and  $S = 2 \times S'$  were synthesized in cyclohexane (200 mL) with *s*-BuLi (0.133 mL, 0.186 mmol; 0.089 mL, 0.125 mmol) as initiator at room temperature. The length of the polystyrene (S) blocks corresponds to 90 kg mol<sup>-1</sup> (18.4 mL, 161 mmol), and the length of polyisoprene (I) blocks to 5 kg mol<sup>-1</sup> (1.34 mL, 13.38 mmol), while S' and I' are each half of S and I, respectively. After complete conversion of the ISI' and ISIS' blocks, the blocks were subsequently linked with a bifunctional linker,  $\alpha, \alpha'$ -dibromo-*p*-xylene (4.3 mL, 0.094 mmol; 2.9 mL, 0.063 mmol), to obtain the penta- (ISISI) and heptablock (ISISISI) copolymer, respectively. The PI-parts of the backbones were functionalized by epoxidation<sup>214</sup>, followed by grafting of living PS sidearms onto the backbones, resulting in the 3-star and 4-star topology. The resulting polymers were purified by three fractionation steps in a THF/methanol mixture until a purity of > 93 % was reached.

## A.4 STYRENE DERIVATIVES

Linear PS, P2VN, PVBP, and P $\alpha$ MS (approximately 10 g) were synthesized using LAP with *s*-BuLi (0.036 mL, 0.051 mmol) as initiator. PS and P2VN were synthesized in toluene (200 mL) at rt. Due to its comparatively low solubility in solvents, PVBP was synthesized using benzene (200 mL) as solvent at rt, and P $\alpha$ MS was synthesized at -78 °C in THF (200 mL) due to its low ceiling temperature. The living anionic chains were terminated in all syntheses using degassed MeOH, and the resulting polymers were precipitated in a large excess of methanol.

---

## B CHARACTERIZATION AND METHODS

### B.1 SIZE-EXCLUSION CHROMATOGRAPHY (SEC)

The used SEC instrument has a 4-detector configuration, with UV, followed by MALLS detection; after a flow split, the eluent passes through a viscometer and DRI detector (Polymer Standards Service, PSS, Germany). The SEC device was from the Agilent 1200 series, and the MALLS unit was the SLD7000/BI-MwA (PSS, Brookhaven Instruments). The columns (SDV-Lux 5  $\mu\text{m}$  (guard column), SDV-Lux-1,000  $\text{\AA}$ , SDV-Lux 100,000  $\text{\AA}$ , PSS) were calibrated using monodisperse linear PS standards with average molecular weights between 476  $\text{g mol}^{-1}$  to  $2.5 \times 10^6 \text{ g mol}^{-1}$ . Tetrahydrofuran was used as the eluent with a flow rate of 1  $\text{mL min}^{-1}$  at an operating temperature of 23  $^\circ\text{C}$ . Typically, 100  $\mu\text{L}$  of the filtered sample solution with a concentration of around 1  $\text{mg mL}^{-1}$  was injected onto the columns, using an autosampler. All linear polymers are characterized by a differential refractometer (DRI). The mass-weighted molecular weight of the branched samples was determined by MALLS using the  $\text{dn/dc}$  value of linear PS as the concentration of the PI-parts in the final pom-poms is  $< 2 \text{ wt}\%$ . Moreover, it was experimentally found that the  $\text{dn/dc}$  value of 0.1095 in THF is valid for linear PS and PS combs.

### B.2 NUCLEAR MAGNETIC RESONANCE SPECTROSCOPY ( $^1\text{H-NMR}$ )

All  $^1\text{H-NMR}$  spectra were measured with a Bruker Ascend III 400 MHz spectrometer with a frequency of 400 MHz at room temperature with 1024 scans. All samples were dissolved in deuterated chloroform  $\text{CDCl}_3$ .

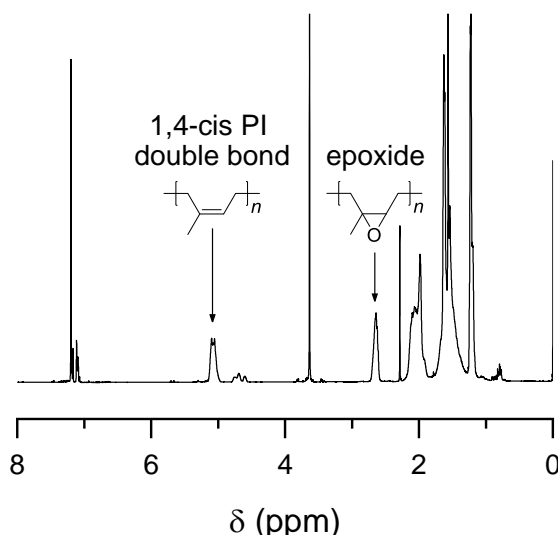


Figure B.1.  $^1\text{H-NMR}$  spectra of an epoxidized ISI backbone precursor. The chemical shift of the double bond peak is around 5.13 ppm, and the one of the epoxide is around 2.71 ppm.

### B.3 DIFFERENTIAL SCANNING CALORIMETRY (DSC)

Non-isothermal measurements to investigate the glass transition temperature  $T_g$  were conducted under  $N_2$ -atmosphere ( $50 \text{ mL min}^{-1}$ ) by differential scanning calorimetry (DSC, Q200, TA Instruments) equipped with an RSC 90 cooler. The weight of the sample was kept around 15 mg. First, samples were heated to  $200 \text{ }^\circ\text{C}$  and held for 5 min to erase the thermal history. Second, samples were cooled well below their specific  $T_g$  with a cooling rate of  $10 \text{ }^\circ\text{C min}^{-1}$  and held for 5 min. Subsequently, the samples were heated again over the  $T_g$ . The signal of the second heating curve was used to determine the  $T_g$ .

### B.4 THERMOGRAVIMETRIC ANALYSIS (TGA)

Thermogravimetric experiments (TGA 5500, TA Instruments) were performed by analyzing the percentage weight loss under  $N_2$ -atmosphere. In each experiment, a total mass of 5 mg was used, and the heating rate was constant at  $10 \text{ K min}^{-1}$ .

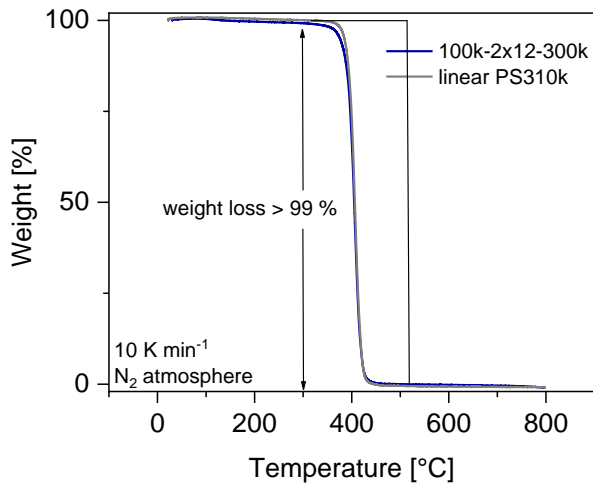


Figure B.2. Thermogravimetric curve of the linear reference PS310k and the pom-pom-shaped PS 100k-2×12-300k of series A under  $N_2$ -atmosphere. The heating rate was  $10 \text{ K min}^{-1}$ .

### B.5 SMALL-ANGLE X-RAY SCATTERING (SAXS)

The long-distance orders  $L_0$  of the block copolymers were investigated via small-angle X-ray scattering (SAXS) measurements with an S3-Micro, Hecus X-ray system. The measurements were used to calculate the periodicity  $L_0$  from the scattering wave vector  $q_0$  of the first-order maximum according to Bragg's law, with

$$L_0 = 2\pi/q_0. \quad (\text{B.1})$$

If phase separating systems provide periodicity, the scattering reflections that arise convey information about the spatial distribution of the scattering objects. Each morphology exhibits a distinct series of scattering reflections observed in the scattering pattern.

Classification of the different morphologies is based on the presence of higher-order reflections concerning the scattering vector  $\vec{q}$ , which are summarized in Table B.1.



Table B.1. Characteristic reflections of different microphase symmetries.<sup>150</sup>

Morphology	High order reflections							
BCC (spheres)	$q_0$	$\sqrt{2}q_0$	$\sqrt{3}q_0$	$\sqrt{4}q_0$	$\sqrt{5}q_0$	$\sqrt{6}q_0$	$\sqrt{7}q_0$	...
Hexagonal (cylinders)	$q_0$	$\sqrt{3}q_0$	$\sqrt{4}q_0$	$\sqrt{7}q_0$	$\sqrt{9}q_0$	$\sqrt{11}q_0$	$\sqrt{13}q_0$	...
Gyroid (bicontinuous)	$q_0$	$\sqrt{3}q_0$	$\sqrt{4}q_0$	$\sqrt{7}q_0$	$\sqrt{8}q_0$	$\sqrt{10}q_0$	$\sqrt{11}q_0$	...
Symmetric lamellar	$q_0$	$3q_0$	$5q_0$	$7q_0$	...			
Lamellar	$q_0$	$2q_0$	$3q_0$	$4q_0$	$5q_0$	$6q_0$	...	

## B.6 SHEAR RHEOLOGY

Small-amplitude oscillatory shear (SAOS) measurements were performed on a strain-controlled ARES-G2 rheometer (TA Instruments). Oscillatory shear and uniaxial elongation experiments were conducted under N<sub>2</sub>-atmosphere (N<sub>2</sub> > 99.5 vol%) to minimize polymer degradation at high temperatures. Samples were prepared as follows: disc-shaped samples (thickness: 1 mm, diameter: 13 mm) were press-molded under vacuum at 180 °C for 15 min using a Weber press. For SAOS measurements, parallel plates with a diameter of 13 mm were used. Oscillatory strain sweeps ( $\gamma_0 = 0.1 - 100$  %) at a constant angular frequency of  $\omega = 100$  rad s<sup>-1</sup> were conducted to determine the linear viscoelastic regime (LVE), followed by oscillatory frequency sweeps. Strain amplitudes between  $\gamma_0 = 1 - 7$  % were chosen in a temperature range of 120 °C – 290 °C, depending on the LVE of each polymer. The master curves were referenced to  $T_{\text{ref}} = 160$  °C, using the TTS principle.

## B.7 ELONGATIONAL RHEOLOGY

The elongation measurements were performed on a strain-controlled ARES-G2 rheometer (TA Instruments) using an extensional viscosity fixture (EVF) with a maximum possible Hencky strain of  $\epsilon_{\text{H}} = 4$ . The elongational rates were varied between  $\dot{\epsilon} = 0.001$  s<sup>-1</sup> – 10 s<sup>-1</sup>, and the experiments were repeated thrice to ensure reproducibility. Rectangular-shaped samples (thickness: 0.7 mm, width: 10 mm, and length: 18 mm) were press-molded under vacuum at 180 °C for 15 min using a Weber press. Linear viscoelastic predictions based on the Maxwell model were fitted to the SAOS data using relaxation spectra  $g_i$  and  $\tau_i$ . The software IRIS Rheo-Hub of Mours and Winter<sup>244,245</sup>, enabling to extent linear and non-linear rheological measurements by predicting theories, was used to calculate the Doi-Edwards model.

## B.8 PHYSICAL FOAMING

Physical foaming experiments were performed in a 100 mL autoclave (Supercritical Fluid Technologies, HPR-Series) using supercritical carbon dioxide (scCO<sub>2</sub>, critical point:  $T_c = 30.98$  °C,  $p_c = 73.75$  bar<sup>246</sup>) as the foaming agent.

The autoclave is equipped with an on-off ball valve to ensure fast pressure release and is connected to a supercritical fluid pump (SFT-10, Supercritical Fluid Technologies). The samples were saturated at  $p = 500$  bar for  $t_{\text{sat}} = 8$  h to enable a complete saturation with the foaming agent. Foaming took place at  $T_f = 100$  °C – 150 °C with approximately  $dp/dt \approx 200$  bar s<sup>-1</sup>, resulting in a closed cell structure. The solubility of scCO<sub>2</sub> under these conditions is about 11 g CO<sub>2</sub>/100 g PS<sup>56,247,248</sup>, which results in a reduction of the glass transition temperature of around 55 °C leading to a  $T_g$  of about 45 °C before foaming.<sup>56,58</sup>

Foam densities  $\rho_f$  were measured based on the water-displacement method, which is based on Archimedes' principle using a density kit (YDK-01, Sartorius AG). First, the foams were weighted on a balance  $m_{\text{air}}$  and followed by submerging them in distilled water to measure its apparent mass  $m_{\text{water}}$ , which is reduced by buoyant forces.

$$\rho_f = \frac{m_{\text{air}}}{m_{\text{air}} - m_{\text{water}}} \rho_{\text{water}}. \quad (\text{B.2})$$

The resulting volume expansion ratio was calculated according to

$$VER = \frac{\rho_p}{\rho_f}, \quad (\text{B.3})$$

where  $\rho_p$  is the density of the neat polymer. Scanning electron microscopy (SEM, Quanta 250 ESEM FEG, FEI) was used to analyze the average cell size  $D$ , the cell density  $N$ . The latter is defined as

$$N = VER \left( \frac{n}{A} \right)^{\frac{3}{2}}, \quad (\text{B.4})$$

where  $N$  is the cell density in cell cm<sup>-3</sup>, and  $n$  is the number of cells in an observed area  $A$  in  $\mu\text{m}^2$ . The average cell size is given by the diameter  $D$  in  $\mu\text{m}$  and can be calculated by

$$D = 10^4 \left[ \frac{(VER - 1)}{\left( \frac{N\pi}{6} \right)} \right]^{1/3}. \quad (\text{B.5})$$

The cell wall thickness  $d$  was estimated by<sup>249</sup>

$$d = D \left( \frac{1}{\sqrt{1 - \frac{\rho_f}{\rho_p}}} - 1 \right). \quad (\text{B.6})$$

Moreover, the software ImageJ was used for the graphical evaluation of  $D$ ,  $N$ , and  $d$ .

---

## B.9 SORPTION EXPERIMENTS

Sorption experiments were conducted by placing a polymer disc (1 cm in width, 1 mm in high) in a pressure vessel at  $p = 500$  bar and a saturation temperature of  $T_{\text{sat}} = 23$  °C for  $t = 24$  h. The samples were taken from the pressure vessel and weighed on a Mettler AE240 analytical scale. A short-time interval between the pressure release and weight measurement occurred in the sorption experiment. Therefore, the solubility of CO<sub>2</sub> in the samples was obtained by extrapolating the desorption curve to zero desorption time, according to the literature.<sup>239</sup>

## B.10 SCANNING ELECTRON MICROSCOPY (SEM)

Investigation of the cellular morphology of the foams was performed by Scanning Electron Microscopy (SEM, S5-70, Hitachi and Quanta 250 ESEM FEG, FEI). Therefore, the foams were cooled in liquid nitrogen, cool-fractured, and sputtered with a gold layer of around 5 nm (SCD040, Bulzers Union). The resulting SEM images were analyzed using ImageJ.



## C SUPPORTING INFORMATION

### C.1. PHASE SEPARATING BLOCK COPOLYMERS

#### DYNAMIC SCANNING CALORIMETRY:

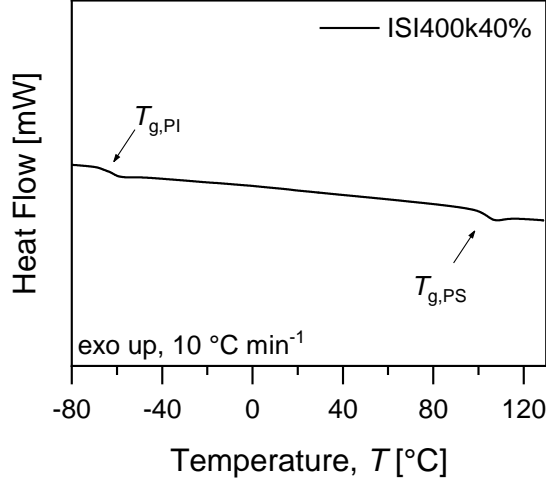


Figure C.1. Example of an on-isothermal measurement of a phase separated ISI triblock copolymer with a heating rate of 10 °C min<sup>-1</sup> (exo up). The glass transition temperature of PI is around  $T_{g,PI} \approx -70$  °C and the one of PS around  $T_{g,PS} \approx 100$  °C.

#### FOAMING PARAMETERS:

Table C.1. Statistical cellular parameters, i.e., foam density  $\rho_f$ , volume expansion ratio  $VER$ , average cell size  $D$ , cell density  $N$  of block copolymer and PS+SiO<sub>2</sub>-based foams. Physical foaming experiments were performed at  $p = 500$  bar,  $\Delta p/\Delta t \approx 200$  bar s<sup>-1</sup>, and  $T_f = 60$  °C – 140 °C.

Sample	$T_f$ [°C]	$\rho_f$ [g cm <sup>-3</sup> ]	$VER$	$D$ [μm]	$N$ [cell cm <sup>-3</sup> ]
PS/PI10%	60	0.55	1.89	- <sup>a</sup>	- <sup>a</sup>
	80	0.53	1.97	- <sup>a</sup>	- <sup>a</sup>
	100	0.43	2.43	- <sup>a</sup>	- <sup>a</sup>
	120	0.21	4.82	- <sup>a</sup>	- <sup>a</sup>
PS/PI20%	60	0.63	1.63	- <sup>a</sup>	- <sup>a</sup>
	80	0.55	1.86	- <sup>a</sup>	- <sup>a</sup>
	100	0.33	3.11	- <sup>a</sup>	- <sup>a</sup>
	120	0.20	5.22	- <sup>a</sup>	- <sup>a</sup>
PS/PI40%	60	0.59	1.67	- <sup>a</sup>	- <sup>a</sup>
	80	0.40	2.47	- <sup>a</sup>	- <sup>a</sup>
	100	0.35	2.81	- <sup>a</sup>	- <sup>a</sup>
	120	0.19	4.96	- <sup>a</sup>	- <sup>a</sup>
SI400k10%	60	0.55	1.88	2.54	$1.03 \times 10^{11}$
	80	0.42	2.46	3.65	$5.72 \times 10^{10}$
	100	0.36	2.90	4.82	$3.24 \times 10^{10}$
	120	0.31	3.34	6.19	$1.90 \times 10^{10}$

Table C.1 continued.

Sample	$T_f$ [°C]	$p_f$ [g cm <sup>-3</sup> ]	$VER$	$D$ [μm]	$N$ [cell cm <sup>-3</sup> ]
SI400k20%	60	0.49	2.10	3.23	$6.24 \times 10^{10}$
	80	0.35	2.94	5.12	$2.76 \times 10^{10}$
	100	0.27	3.75	7.08	$1.48 \times 10^{10}$
	120	0.24	4.32	8.65	$9.79 \times 10^9$
SI400k40%	60	0.46	2.15	3.77	$4.12 \times 10^{10}$
	80	0.36	2.73	5.91	$1.60 \times 10^{10}$
	100	0.29	3.45	7.83	$9.77 \times 10^9$
	120	0.25	3.95	9.64	$6.30 \times 10^9$
SIS200k10%	60	0.59	1.74	1.29	$6.53 \times 10^{11}$
	80	0.49	2.13	1.88	$3.22 \times 10^{11}$
	100	0.32	3.20	3.61	$8.92 \times 10^{10}$
	120	0.22	4.72	7.11	$1.98 \times 10^{10}$
SIS400k10%	60	0.62	1.66	0.39	$2.07 \times 10^{13}$
	80	0.48	2.17	1.14	$1.49 \times 10^{12}$
	100	0.26	3.96	3.01	$2.07 \times 10^{11}$
	120	0.14	7.22	5.90	$5.78 \times 10^{10}$
SIS400k20%	60	0.62	1.64	1.98	$1.58 \times 10^{11}$
	80	0.44	2.29	3.74	$4.72 \times 10^{10}$
	100	0.30	3.40	5.70	$2.47 \times 10^{10}$
	120	0.23	4.39	7.35	$1.63 \times 10^{10}$
SIS400k40%	60	0.62	1.61	1.08	$9.12 \times 10^{11}$
	80	0.46	2.17	2.32	$1.80 \times 10^{11}$
	100	0.31	3.17	3.99	$6.52 \times 10^{10}$
	120	0.22	4.53	6.10	$2.96 \times 10^{10}$
SIS1000k10%	60	0.62	1.67	1.96	$1.70 \times 10^{11}$
	80	0.48	2.13	2.85	$9.30 \times 10^{10}$
	100	0.40	2.59	4.29	$3.87 \times 10^{10}$
	120	0.36	2.87	6.73	$1.17 \times 10^{10}$
ISI400k10%	60	0.65	1.59	0.89	$1.76 \times 10^{12}$
	80	0.42	2.45	2.11	$2.25 \times 10^{11}$
	100	0.29	3.57	4.28	$6.25 \times 10^{10}$
	120	0.19	5.28	6.79	$2.61 \times 10^{10}$
ISI400k20%	60	0.62	1.64	0.97	$1.22 \times 10^{12}$
	80	0.48	2.13	2.77	$1.62 \times 10^{11}$
	100	0.28	3.60	3.56	$1.10 \times 10^{11}$

Table C.1 continued.

Sample	$T_f$ [°C]	$p_f$ [g cm <sup>-3</sup> ]	$VER$	$D$ [μm]	$N$ [cell cm <sup>-3</sup> ]
	120	0.23	4.49	6.48	$2.45 \times 10^{10}$
ISI400k40%	60	0.64	1.53	2.61	$5.75 \times 10^{10}$
	80	0.48	2.06	3.82	$1.81 \times 10^{10}$
	100	0.39	2.56	5.34	$1.17 \times 10^{10}$
	120	0.28	3.54	6.76	$1.04 \times 10^{10}$
SMMA400k10%	100	0.46	2.26	3.55	$5.38 \times 10^{10}$
	120	0.32	3.25	4.68	$7.06 \times 10^{10}$
	130	0.19	5.63	5.01	$4.85 \times 10^{10}$
	140	0.18	5.80	5.74	$4.19 \times 10^{10}$
SMMA400k20%	100	0.50	2.10	2.36	$1.18 \times 10^{11}$
	120	0.29	3.67	3.51	$1.61 \times 10^{11}$
	130	0.27	3.86	3.52	$1.25 \times 10^{11}$
	140	0.18	5.79	4.28	$1.17 \times 10^{11}$
SMMA400k40%	100	0.50	2.11	2.07	$2.39 \times 10^{11}$
	120	0.33	3.16	2.35	$3.16 \times 10^{11}$
	130	0.19	5.46	3.30	$2.37 \times 10^{11}$
	140	0.19	5.47	3.58	$1.87 \times 10^{11a}$
PS+SiO <sub>2</sub> 0.25%	80	0.56	1.89	1.27	$8.29 \times 10^{11}$
	100	0.36	2.93	1.44	$1.25 \times 10^{12}$
	120	0.22	4.78	2.75	$3.46 \times 10^{11}$
	130	0.20	5.34	2.83	$3.64 \times 10^{11}$
PS+SiO <sub>2</sub> 0.5%	80	0.57	1.85	1.72	$3.22 \times 10^{11}$
	100	0.38	2.78	1.46	$1.09 \times 10^{12}$
	120	0.21	4.95	2.80	$3.42 \times 10^{11}$
	130	0.19	5.63	4.33	$1.09 \times 10^{11}$
PS+SiO <sub>2</sub> 1.0%	80	0.57	1.84	1.88	$2.39 \times 10^{11}$
	100	0.37	2.83	1.32	$1.52 \times 10^{12}$
	120	0.23	4.50	2.49	$4.32 \times 10^{11}$
	130	0.20	5.32	3.18	$2.57 \times 10^{11}$

<sup>a</sup>Heterogeneous cell size distribution results in a failure of calculations of  $D$  and  $N$ .

## C.2. POM-POM TOPOLOGY

## SIZE-EXCLUSION CHROMATOGRAPHY:

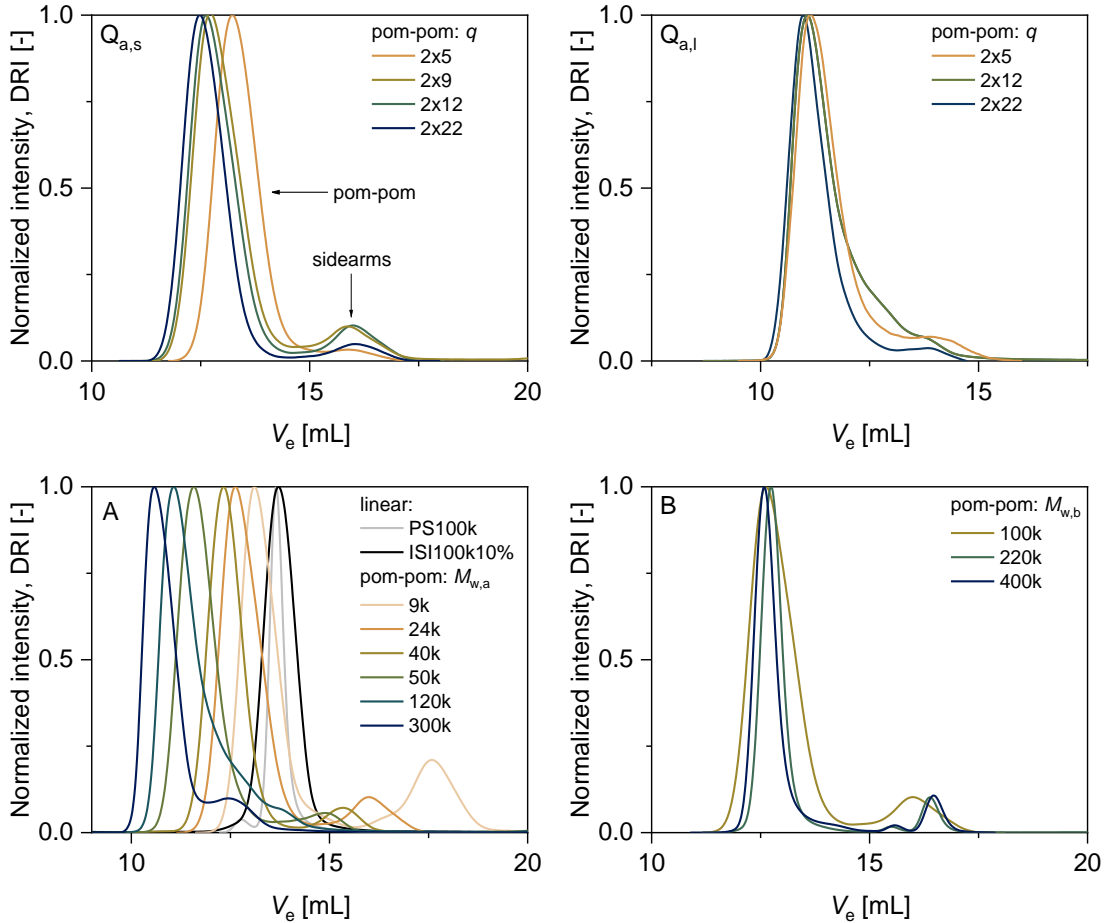


Figure C.2. Elution chromatograms of the purified pom-poms, the linear ISI-precursor, and the linear PS references detected by SEC-DRI. After three purification steps, the amount of residual sidearms varies from 2 – 13 % over the entire set of PS pom-poms.

## OSCILLATORY SHEAR RHEOLOGY:

Table C.2. WLF parameter and zero-shear viscosity  $\eta_0$  of the PS pom-poms and the linear PS references at  $T_{\text{ref}} = 160$  °C.

Sample	C <sub>1</sub>	C <sub>2</sub> [K]	$\eta_0$ [Pa s]	$\tau_R$ [s <sup>-1</sup> ] <sup>a</sup>	$\tau_R$ [s <sup>-1</sup> ] <sup>b</sup>
PS100k	6.16	105.86	36,500	3.25	-
PS310k	5.87	137.92	1,810,000	0.55	-
100k-2x5-25k	5.98	123.98	22,100	13.23	6.97
100k-2x9-25k	6.06	114.77	27,700	10.86	5.73
100k-2x9-110k	5.86	103.90	152,000	3.92	0.54
100k-2x11-9k	5.25	112.02	12,100	22.63	17.41
100k-2x12-24k	6.22	113.80	27,900	4.44	2.34



Table C.2 continued.

Sample	$C_1$	$C_2$ [K]	$\eta_0$ [Pa s]	$\tau_R$ [s <sup>-1</sup> ] <sup>a</sup>	$\tau_R$ [s <sup>-1</sup> ] <sup>b</sup>
100k-2×12-40k	6.16	114.35	55,500	3.76	1.42
100k-2×12-120k	5.67	103.66	6,030,000	3.38	0.41
100k-2×14-50k	6.11	108.90	335,000	3.10	0.97
100k-2×14-300k	6.36	110.49	628,000,000	2.56	0.08
100k-2×22-25k	6.26	112.24	18,900	7.97	4.20
100k-2×22-110k	6.36	110.33	5,490,000	4.04	0.55
220k-2×9-25k	6.08	109.12	992,000	1.63	1.14
400k-2×9-23k	5.71	112.40	4,440,000	0.68	0.55

<sup>a</sup> $\tau_R = \tau_e \times Z_b$  and <sup>b</sup> $\tau_R = \tau_e \times Z_{b+(2 \times a)}$ .

#### ELONGATIONAL RHEOLOGY:

Table C.3. Overview of the reached strain hardening factors *SHF* measured at  $T = 160$  °C at strain rates ranging from  $\dot{\epsilon} = 0.01 - 10$  s<sup>-1</sup>.

Strain rates	10 [s <sup>-1</sup> ]	3 [s <sup>-1</sup> ]	1 [s <sup>-1</sup> ]	0.3 [s <sup>-1</sup> ]	0.1 [s <sup>-1</sup> ]	0.03 [s <sup>-1</sup> ]	0.01 [s <sup>-1</sup> ]
Samples							
PS100k	2.17	1.09	0.77	0.56	-	-	-
PS310k	9.83	6.02	2.36	1.18	-	-	-
100k-2×5-25k	6.64	6.80	4.86	1.46	-	-	-
100k-2×9-25k	12.33	14.61	8.95	1.18	-	-	-
100k-2×9-110k	6.92	4.55	4.25	-	-	-	-
100k-2×11-9k	15.79	4.99	1.11	-	-	-	-
100k-2×12-24k	14.02	16.10	18.68	5.85	-	-	-
100k-2×12-40k	11.71	18.21	21.73	13.98	2.73	-	-
100k-2×12-120k	9.83	3.38	2.41	-	-	-	-
100k-2×14-50k	17.32	25.48	29.90	41.72	49.23	57.18	17.25
100k-2×14-300k	21.29	7.87	3.28	-	-	-	-
100k-2×22-25k	14.28	18.86	18.26	4.29	-	-	-
100k-2×22-110k	12.05	5.46	3.23	-	-	-	-
220k-2×9-25k	49.26	55.20	69.70	70.86	47.80	20.68	4.80
400k-2×9-23k	81.67	78.32	84.24	48.50	14.78	10.37	-

## FOAMING PARAMETERS:

Table C.4. Statistical cellular parameters, i.e., foam density  $p_f$ , volume expansion ratio  $VER$ , average cell size  $D$ , cell density  $N$ , and cell wall thickness  $d$  of the samples. Physical foaming experiments were performed at  $p = 500$  bar,  $\Delta p/\Delta t \approx 200$  bar  $s^{-1}$ , and  $T_f = 100$  °C – 150 °C.

Sample	$T_f$ [°C]	$p_f$ [g $cm^{-3}$ ]	$VER$	$D$ [ $\mu m$ ]	$N$ [cell $cm^{-3}$ ]	$d$ [ $\mu m$ ]
PS310k	100	0.40	2.63	2.27	$2.67 \times 10^{11}$	0.29
	120	0.24	4.35	3.17	$2.00 \times 10^{11}$	0.24
	130	0.19	5.45	2.77	$3.98 \times 10^{11}$	0.17
	140	0.33	3.21	4.81	$3.79 \times 10^{10}$	0.50
	150	-	-	-	-	-
100k-2×5-25k	100	0.33	3.25	2.39	$3.15 \times 10^{11}$	0.24
	120	0.17	6.02	2.82	$4.28 \times 10^{11}$	0.16
	130	0.15	6.99	3.43	$2.84 \times 10^{11}$	0.16
	140	0.14	7.48	4.09	$1.81 \times 10^{11}$	0.18
	150	-	-	-	-	-
100k-2×9-25k	100	0.27	3.90	3.12	$1.83 \times 10^{11}$	0.26
	120	0.16	6.41	4.84	$9.16 \times 10^{10}$	0.25
	130	0.13	7.59	7.41	$3.44 \times 10^{10}$	0.30
	140	0.14	8.33	9.78	$1.34 \times 10^{10}$	0.43
	150	-	-	-	-	-
100k-2×9-110k	100	0.42	2.51	5.95	$1.36 \times 10^{10}$	0.79
	120	0.25	3.90	11.05	$1.17 \times 10^{10}$	0.63
	130	0.18	5.74	15.25	$4.06 \times 10^9$	0.96
	140	0.13	8.03	16.62	$1.97 \times 10^9$	0.62
	150	0.50	2.10	5.41	$1.31 \times 10^{10}$	0.86
100k-2×11-9k	100	0.31	3.40	1.33	$1.92 \times 10^{12}$	0.13
	120	0.18	5.85	3.43	$2.29 \times 10^{11}$	0.19
	130	0.17	6.17	3.44	$2.42 \times 10^{11}$	0.19
	140	0.19	5.51	5.46	$5.28 \times 10^{10}$	0.33
	150	-	-	-	-	-
100k-2×12-24k	100	0.29	3.57	2.45	$3.35 \times 10^{11}$	0.23
	120	0.17	6.29	3.68	$2.03 \times 10^{11}$	0.19
	130	0.14	7.65	6.29	$3.75 \times 10^{10}$	0.30
	140	0.12	8.85	6.97	$6.04 \times 10^{10}$	0.24
	150	-	-	-	-	-
100k-2×12-40k	100	0.36	2.88	4.80	$3.24 \times 10^{10}$	0.56
	120	0.21	5.07	7.74	$1.67 \times 10^{10}$	0.51
	130	0.14	7.50	10.39	$1.11 \times 10^{10}$	0.46
	140	0.10	10.22	16.47	$3.94 \times 10^9$	0.54

Table C.4 continued.

Sample	$T_f$ [°C]	$p_f$ [g cm <sup>-3</sup> ]	$VER$	$D$ [μm]	$N$ [cell cm <sup>-3</sup> ]	$d$ [μm]
100k-2×12-120k	100	0.43	2.43	3.52	$6.29 \times 10^{10}$	0.48
	120	0.23	4.65	6.04	$3.16 \times 10^{10}$	0.43
	130	0.15	6.84	8.79	$1.64 \times 10^{10}$	0.43
	140	0.12	8.76	11.77	$9.09 \times 10^9$	0.45
	150	0.40	2.60	3.94	$5.00 \times 10^{10}$	0.50
100k-2×14-50k	100	0.40	2.64	5.13	$2.32 \times 10^{10}$	0.65
	120	0.23	4.49	7.92	$1.34 \times 10^{10}$	0.59
	130	0.15	7.06	13.25	$4.97 \times 10^9$	0.63
	140	0.09	10.91	17.21	$3.71 \times 10^9$	0.52
	150	0.18	5.98	5.71	$5.12 \times 10^{10}$	0.32
100k-2×14-300k	100	0.53	1.98	1.75	$3.47 \times 10^{11}$	0.29
	120	0.30	3.55	2.50	$3.10 \times 10^{11}$	0.23
	130	0.18	5.91	2.93	$3.75 \times 10^{11}$	0.16
	140	0.14	7.38	3.03	$4.40 \times 10^{11}$	0.14
	150	0.35	3.04	2.55	$2.35 \times 10^{11}$	0.28
100k-2×22-25k	100	0.33	3.17	1.96	$5.52 \times 10^{11}$	0.21
	120	0.19	5.38	3.38	$2.17 \times 10^{11}$	0.21
	130	0.18	5.87	3.68	$1.87 \times 10^{11}$	0.21
	140	0.16	6.35	4.35	$1.24 \times 10^{11}$	0.23
	150	-	-	-	-	-
100k-2×22-110k	100	0.45	2.32	3.75	$4.77 \times 10^{10}$	0.54
	120	0.26	3.99	5.31	$3.81 \times 10^{10}$	0.44
	130	0.13	7.82	4.48	$1.45 \times 10^{11}$	0.19
	140	0.11	9.33	5.34	$1.04 \times 10^{11}$	0.19
	150	0.66	1.60	-	-	-
220k-2×9-25k	100	0.40	2.62	2.81	$1.39 \times 10^{11}$	0.36
	120	0.24	4.31	4.28	$8.08 \times 10^{10}$	0.33
	130	0.14	7.20	4.93	$9.88 \times 10^{10}$	0.23
	140	0.09	11.71	5.81	$1.04 \times 10^{11}$	0.17
400k-2×9-23k	100	0.29	3.55	1.77	$8.79 \times 10^{11}$	0.17
	120	0.19	5.50	2.18	$8.25 \times 10^{11}$	0.13
	130	0.11	9.51	3.49	$3.84 \times 10^{11}$	0.12
	140	0.06	15.98	5.12	$2.13 \times 10^{11}$	0.10

## C.3. STAR AND BARBWIRE STRUCTURES

## SIZE-EXCLUSION CHROMATOGRAPHY:

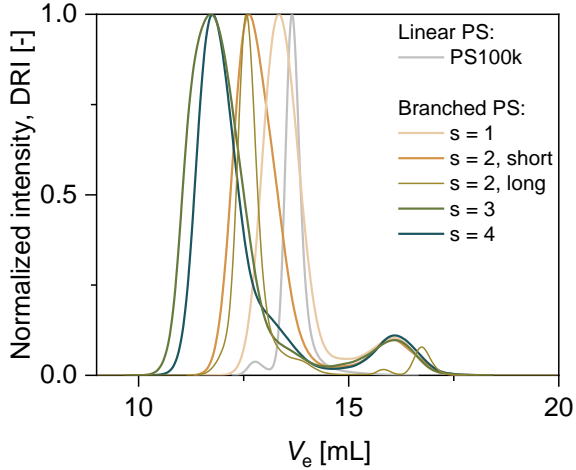


Figure C.3. Elution chromatograms of the purified barbwires with increasing  $s$  from one to four, and the linear PS reference detected by SEC-DRI. After three purification steps, the amount of residual arms is less than 7 % over the entire sample set.

## OSCILLATORY SHEAR RHEOLOGY:

Table C.5. WLF parameter, zero-shear viscosity  $\eta_0$ , and the glass transition temperature  $T_g$  of all the PS star, the PS barbwires, and the linear PS references at  $T_{\text{ref}} = 180$  °C.

Sample	$C_1$	$C_2$ [K]	$\eta_0$ [Pa s]	$T_g$ [°C]
PS100k	5.07	124.40	4,030	106
PS310k	5.24	128.10	159,700	108
Star (8k-11-27k)	5.97	154.99	250	86
2-star-short (100k-2×12-24k)	5.30	133.66	3,450	104
2-star-long (280k-2×13-23k)	4.97	131.60	138,020	104
3-star (213k-3×11-25k)	5.08	130.39	31,740	102
4-star (382k-4×11-27k)	5.06	124.76	148,540	103

## ELONGATIONAL RHEOLOGY:

Table C.6. Overview of the reached  $SHF$  measured at 180 °C at strain rates ranging from  $\dot{\epsilon} = 0.03$  s<sup>-1</sup> – 10 s<sup>-1</sup>.

Samples	Strain rates					
	10 [s <sup>-1</sup> ]	3 [s <sup>-1</sup> ]	1 [s <sup>-1</sup> ]	0.3 [s <sup>-1</sup> ]	0.1 [s <sup>-1</sup> ]	0.03 [s <sup>-1</sup> ]
PS100k	-	-	-	-	-	-
PS310k	2.01	2.08	1.64	1.33	1.11	1.08
Star (8k-11-27k)	-	-	-	-	-	-
2-star-short (100k-2×12-24k)	5.75	6.61	1.43	-	-	-
2-star-long (280k-2×13-22k)	100.34	92.88	60.75	13.49	1.97	-
3-star (213k-3×11-25k)	122.92	135.19	99.36	19.87	2.35	-
4-star (382k-4×11-27k)	109.52	114.80	108.80	61.11	16.86	2.06

---

FOAMING PARAMETERS:

Table C.7. Statistical cellular parameters, i.e., foam density  $p_f$ , volume expansion ratio  $VER$ , average cell size  $D$ , and cell density  $N$  of the resulting foams. Physical foaming experiments were performed at  $p = 500$  bar,  $\Delta p/\Delta t \approx 200$  bar s<sup>-1</sup>, and  $T_f = 100$  °C – 150 °C.

Sample	$T_f$ [°C]	$p_f$ [g cm <sup>-3</sup> ]	$VER$	$D$ [μm]	$N$ [cell cm <sup>-3</sup> ]
PS310k	100	0.40	2.63	2.3	$2.67 \times 10^{11}$
	120	0.24	4.35	3.3	$2.00 \times 10^{11}$
	130	0.19	5.45	2.8	$3.98 \times 10^{11}$
	140	0.33	3.21	4.8	$3.79 \times 10^{10}$
star	100	0.31	3.39	6.8	$1.47 \times 10^{10}$
8k-11-27k	120	0.20	5.27	8.5	$1.31 \times 10^{10}$
	130	0.20	5.35	11.2	$5.84 \times 10^9$
	140	0.25	4.12	8.8	$8.86 \times 10^9$
2-star-short	100	0.29	3.57	2.5	$3.35 \times 10^{11}$
100k-2×12-24k	120	0.17	6.29	3.7	$2.03 \times 10^{11}$
	130	0.14	7.65	6.3	$3.75 \times 10^{10}$
	140	0.12	8.85	6.9	$6.04 \times 10^{10}$
	150	0.22	4.69	7.4	$1.71 \times 10^{10}$
2-star-long	100	0.36	2.94	2.2	$3.60 \times 10^{11}$
100k-2×13-23k	120	0.20	5.27	3.1	$1.08 \times 10^{12}$
	130	0.16	6.61	4.8	$9.84 \times 10^{11}$
	140	0.11	9.75	7.9	$3.38 \times 10^{10}$
3-star	100	0.35	3.02	5.5	$2.32 \times 10^{10}$
213k-3×11-25k	120	0.18	5.88	7.5	$2.19 \times 10^{10}$
	130	0.13	8.05	8.3	$2.39 \times 10^{10}$
	140	0.11	9.59	10.5	$1.43 \times 10^{10}$
	150	0.12	8.40	4.9	$1.21 \times 10^{11}$
4-star	100	0.41	2.59	4.4	$3.47 \times 10^{10}$
382k-4×11-27k	120	0.19	5.48	6.6	$2.93 \times 10^{10}$
	130	0.13	7.80	12.5	$6.58 \times 10^9$
	140	0.10	10.41	14.8	$5.53 \times 10^9$
	150	0.15	6.86	5.6	$6.50 \times 10^{10}$

---

## C.4. STYRENE DERIVATIVES

## SIZE-EXCLUSION CHROMATOGRAPHY:

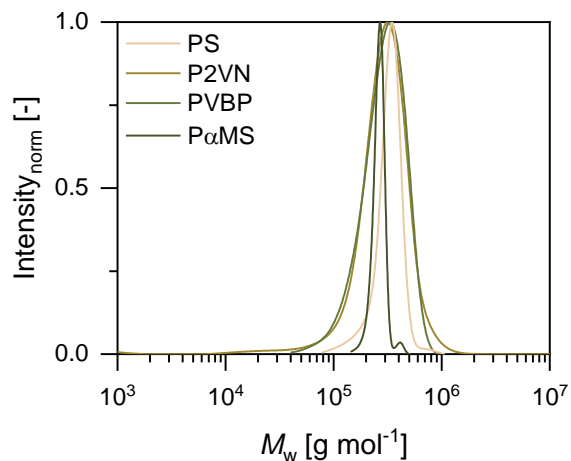


Figure C.4. Molecular weight distribution of linear PS, P2VN, PVBP and P $\alpha$ MS detected by SEC-DRI.

## DYNAMIC SCANNING CALORIMETRY:

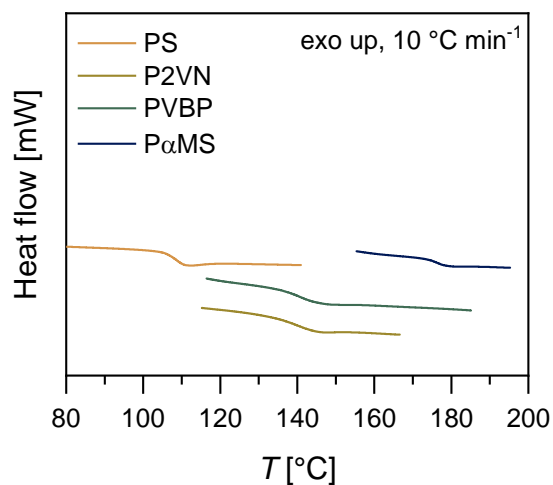


Figure C.5. Non-isothermal DSC-curves of the linear PS and PS derivatives P2VN, PVBP, and P $\alpha$ MS with  $M_w \approx 300$  kg mol<sup>-1</sup>, measured with a heating rate of 10 °C min<sup>-1</sup> under nitrogen flow within a temperature range of  $T = 80 - 200$  °C, depending on polymer dynamics.

---

FOAMING PARAMETERS:

Table C.8. Statistical cellular parameters, i.e., foam density  $\rho_f$ , volume expansion ratio  $VER$ , average cell size  $D$ , and cell density  $N$  of the resulting foams. Physical foaming experiments were performed at  $p = 500$  bar,  $\Delta p/\Delta t = 200$  bar  $s^{-1}$ , and  $\Delta T = T_g \pm 40$  °C.

Sample	$T$ [°C]	$\rho_f$ [g $cm^{-3}$ ]	$VER$	$D$ [ $\mu m$ ]	$N$ [cell $cm^{-3}$ ]
PS	60	0.52	2.10	2.13	$2.93 \times 10^{11}$
	80	0.43	2.51	2.31	$3.50 \times 10^{11}$
	100	0.37	3.23	2.72	$2.67 \times 10^{11}$
	120	0.23	4.84	3.33	$2.00 \times 10^{11}$
	130	0.20	5.45	3.84	$6.40 \times 10^{10}$
	140	0.34	3.21	4.82	$4.18 \times 10^{10}$
P2VN	90	0.48	2.22	1.90	$4.60 \times 10^{11}$
	110	0.41	2.58	2.21	$4.51 \times 10^{11}$
	130	0.32	3.32	2.52	$3.49 \times 10^{11}$
	150	0.21	4.97	3.18	$2.76 \times 10^{11}$
	160	0.20	5.32	3.42	$8.21 \times 10^{10}$
	170	0.29	3.61	4.41	$4.79 \times 10^{10}$
PVBP	110	0.54	1.97	1.76	$6.12 \times 10^{11}$
	130	0.45	2.38	1.91	$5.63 \times 10^{11}$
	150	0.31	3.49	2.20	$4.31 \times 10^{11}$
	170	0.21	5.28	2.89	$2.67 \times 10^{11}$
	180	0.18	5.84	3.31	$9.64 \times 10^{10}$
	190	0.23	4.61	3.92	$7.92 \times 10^{10}$
P $\alpha$ MS	130	0.53	2.04	1.57	$7.45 \times 10^{11}$
	150	0.46	2.32	1.62	$6.75 \times 10^{11}$
	170	0.29	3.72	1.94	$4.88 \times 10^{11}$
	190	0.19	5.43	2.61	$3.74 \times 10^{11}$





---

## 9 REFERENCES

- (1) Lee, S. T.; Ramesh, N. S.; Gendron, R., Eds. *Thermoplastic foam processing: Principles and development*; Polymeric foams series, Vol. 2; CRC Press, 2005.
- (2) Lee, S.-T.; Park, C. B., Eds. *Foam extrusion: Principles and practice*, Second Edition; Polymeric foams series; CRC Press, 2014.
- (3) Lee, S.-T.; Park, C. B.; Ramesh, N. S. *Polymeric foams: Science and technology*; Polymeric foams series, Vol. 3; CRC Press, 2007.
- (4) Lee, S.-T.; Ramesh, N. S., Eds. *Polymeric foams: Mechanisms and materials*; Polymeric foams series, Vol. 1; CRC Press, 2004.
- (5) Eaves, D., Ed. *Handbook of polymer foams*; Rapra Technology Limited, 2004.
- (6) Klemmner, D.; Sendijarević, V.; Aseeva, R. M., Eds. *Handbook of polymeric foams and foam technology*, 2. ed.; Hanser; Hanser Gardener, 2004.
- (7) Mills, N. *Polymer foams handbook: Engineering and biomechanics applications and design guide*, 1st ed.; ScienceDirect; Butterworth-Heinemann; ScienceDirect Online-Anbieter, 2007.
- (8) Khemani, K. C., Ed. *Polymeric Foams*; ACS Symposium Series; American Chemical Society, 1997. DOI: 10.1021/symposium.
- (9) Stange, J.; Münstedt, H. Effect of Long-chain Branching on the Foaming of Polypropylene with Azodicarbonamide. *J. Cell. Plast.* 2006, *42* (6), 445–467. DOI: 10.1177/0021955X06063520.
- (10) Stange, J.; Münstedt, H. Rheological properties and foaming behavior of polypropylenes with different molecular structures. *J. Rheol.* 2006, *50* (6), 907–923. DOI: 10.1122/1.2351880.
- (11) Weingart, N.; Raps, D.; Lu, M.; Endner, L.; Altstädt, V. Comparison of the Foamability of Linear and Long-Chain Branched Polypropylene-The Legend of Strain-Hardening as a Requirement for Good Foamability. *Polymers* 2020, *12* (3), 725. DOI: 10.3390/polym12030725.
- (12) Wang, L.; Wan, D.; Qiu, J.; Tang, T. Effects of long chain branches on the crystallization and foaming behaviors of polypropylene-g-poly(ethylene-co-1-butene) graft copolymers with well-defined molecular structures. *Polymer* 2012, *53* (21), 4737–4757. DOI: 10.1016/j.polymer.2012.08.036.
- (13) Spitael, P.; Macosko, C. W. Strain hardening in polypropylenes and its role in extrusion foaming. *Polym. Eng. Sci.* 2004, *44* (11), 2090–2100. DOI: 10.1002/pen.20214.
- (14) Jiang, R.; Yao, S.; Chen, Y.; Liu, T.; Xu, Z.; Park, C. B.; Zhao, L. Effect of chain topological structure on the crystallization, rheological behavior and foamability of TPEE using supercritical CO<sub>2</sub> as a blowing agent. *J. Supercrit. Fluids* 2019, *147*, 48–58. DOI: 10.1016/j.supflu.2019.02.006.
- (15) *Grand View Research*. <https://www.grandviewresearch.com/industry-analysis/polymer-foam-market> (accessed 2022-10-18).
- (16) Martini, J. E. The Production and Analysis of Microcellular Foam. M. Sc. Thesis, Massachusetts Institute of Technology, Cambridge, 1981.
- (17) Martini-Vvedensky, J. E.; Suh, N. P.; Waldmann, F. A. Microcellular closed cell foams and their method to manufacture: US Patent 4473665A.
- (18) Martini, J. E.; Waldmann, F. A.; Suh, N. P. *SPE ANTEC* 1982, *28*, 674–676.
- (19) Waldmann, F. A. The Processing of Microcellular Foam. M. Sc. Thesis, Massachusetts Institute of Technology, Cambridge, 1982.

- (20) Colton, J. S. The Nucleation of Microcellular Thermoplastic Foam. Ph.D. Thesis, Massachusetts Institute of Technology, Cambridge, 1985.
- (21) Baldwin, D. F. Microcellular Polymer Processing and the Design of a Continuous Sheet Processing Systems. Ph.D. Thesis, Massachusetts Institute of Technology, Cambridge, 1994.
- (22) Park, C. B. The Role of Polymer/Gas Solutions in Continuous Processing of Microcellular Polymers. Ph.D. Thesis, Massachusetts Institute of Technology, Cambridge, 1993.
- (23) Thomson, W. On the division of space with minimum partitional area. *Lond, Edinb. Dublin Philos. Mag. J. Sci.* 1887, *24* (151), 503–514. DOI: 10.1080/14786448708628135.
- (24) Weaire, D.; Phelan, R. A counter-example to Kelvin's conjecture on minimal surfaces. *Philosophical Magazine Letters* 1994, *69* (2), 107–110. DOI: 10.1080/09500839408241577.
- (25) Weaire, D.; Aste, T. *The Pursuit of Perfect Packing*; CRC Press, 2008. DOI: 10.1201/9781420068184.
- (26) Kusner, R.; Sullivan, J. M. Comparing the Weaire-Phelan equal-volume foam to Kelvin's foam. *Forma* 1996, *11*, 233–242.
- (27) Dabrowski, M. L.; Stubenrauch, C. Methacrylate-Based Polymer Foams with Controllable Pore Sizes and Controllable Polydispersities via Foamed Emulsion Templating. *Adv. Eng. Mater.* 2021, *23* (3), 2001013. DOI: 10.1002/adem.202001013.
- (28) Abetz, V., Ed. *Block Copolymers I*; Advances in Polymer Science; Springer-Verlag, 2005. DOI: 10.1007/b137234.
- (29) Llewelyn, G.; Rees, A.; Griffiths, C. A.; Jacobi, M. A Novel Hybrid Foaming Method for Low-Pressure Microcellular Foam Production of Unfilled and Talc-Filled Copolymer Polypropylenes. *Polymers* 2019, *11* (11). DOI: 10.3390/polym11111896.
- (30) Olson, D. A.; Chen, L.; Hillmyer, M. A. Templating Nanoporous Polymers with Ordered Block Copolymers. *Chem. Mater.* 2008, *20* (3), 869–890. DOI: 10.1021/cm702239k.
- (31) Notario, B.; Pinto, J.; Rodriguez-Perez, M. A. Nanoporous polymeric materials: A new class of materials with enhanced properties. *Progress in Materials Science* 2016, *78-79*, 93–139. DOI: 10.1016/j.pmatsci.2016.02.002.
- (32) Abbasi, M.; Faust, L.; Wilhelm, M. Molecular origin of the foam structure in model linear and comb polystyrenes: I. Cell density. *Polymer* 2020, *193*, 122351. DOI: 10.1016/j.polymer.2020.122351.
- (33) Gendron, R. *THERMOPLASTIC FOAM PROCESSING: Principles and development*; CRC Press, 2019.
- (34) Okolieocha, C.; Raps, D.; Subramaniam, K.; Altstädt, V. Microcellular to nanocellular polymer foams: Progress (2004–2015) and future directions – A review. *Eur. Poly. J.* 2015, *73*, 500–519. DOI: 10.1016/j.eurpolymj.2015.11.001.
- (35) Reverchon, E.; Cardea, S. Production of controlled polymeric foams by supercritical CO<sub>2</sub>. *J. Supercrit. Fluids* 2007, *40* (1), 144–152. DOI: 10.1016/j.supflu.2006.04.013.
- (36) Arora, K. A.; Lesser, A. J.; McCarthy, T. J. Preparation and Characterization of Microcellular Polystyrene Foams Processed in Supercritical Carbon Dioxide. *Macromolecules* 1998, *31* (14), 4614–4620. DOI: 10.1021/ma971811z.
- (37) Tammaro, D.; Astarita, A.; Di Maio, E.; Iannace, S. Polystyrene Foaming at High Pressure Drop Rates. *Ind. Eng. Chem. Res.* 2016, *55* (19), 5696–5701. DOI: 10.1021/acs.iecr.5b04911.

- 
- (38) Forest, C.; Chaumont, P.; Cassagnau, P.; Swoboda, B.; Sonntag, P. Polymer nano-foams for insulating applications prepared from CO<sub>2</sub> foaming. *Progress in Polymer Science* 2015, *41*, 122–145. DOI: 10.1016/j.progpolymsci.2014.07.001.
- (39) Notario, B.; Pinto, J.; Solorzano, E.; Saja, J. A. de; Dumon, M.; Rodríguez-Pérez, M. A. Experimental validation of the Knudsen effect in nanocellular polymeric foams. *Polymer* 2015, *56*, 57–67. DOI: 10.1016/j.polymer.2014.10.006.
- (40) Span, R.; Wagner, W. A New Equation of State for Carbon Dioxide Covering the Fluid Region from the Triple-Point Temperature to 1100 K at Pressures up to 800 MPa. *Journal of Physical and Chemical Reference Data* 1996, *25* (6), 1509–1596. DOI: 10.1063/1.555991.
- (41) Ozone Secreteriat. Handbook for the Montreal Protocol on Substances that Deplete the Ozone Layer 2019.
- (42) Tang, M.; Huang, Y.-C.; Chen, Y.-P. Sorption and diffusion of supercritical carbon dioxide into polysulfone. *J. Appl. Polym. Sci.* 2004, *94* (2), 474–482. DOI: 10.1002/app.20895.
- (43) Tuminello, W. H.; Dee, G. T.; McHugh, M. A. Dissolving Perfluoropolymers in Supercritical Carbon Dioxide. *Macromolecules* 1995, *28* (5), 1506–1510. DOI: 10.1021/ma00109a023.
- (44) Zhang, Z.; Handa, Y. P. An in situ study of plasticization of polymers by high-pressure gases. *J. Polym. Sci. B Polym. Phys.* 1998, *36* (6), 977–982. DOI: 10.1002/(SICI)1099-0488(19980430)36:6<977:AID-POLB5>3.0.CO;2-D.
- (45) Dong Hwang, Y.; Woon Cha, S. The relationship between gas absorption and the glass transition temperature in a batch microcellular foaming process. *Polym. Test.* 2002, *21* (3), 269–275. DOI: 10.1016/S0142-9418(01)00081-2.
- (46) Alessi, P.; Cortesi, A.; Kikic, I.; Vecchione, F. Plasticization of polymers with supercritical carbon dioxide: Experimental determination of glass-transition temperatures. *J. Appl. Polym. Sci.* 2003, *88* (9), 2189–2193. DOI: 10.1002/app.11881.
- (47) Yu, L.; Liu, H.; Dean, K. Thermal behaviour of poly(lactic acid) in contact with compressed carbon dioxide. *Polym. Int.* 2009, *58* (4), 368–372. DOI: 10.1002/pi.2540.
- (48) Nofar, M.; Park, C. B. Poly (lactic acid) foaming. *Progress in Polymer Science* 2014, *39* (10), 1721–1741. DOI: 10.1016/j.progpolymsci.2014.04.001.
- (49) Condo, P. D.; Sanchez, I. C.; Panayiotou, C. G.; Johnston, K. P. Glass transition behavior including retrograde vitrification of polymers with compressed fluid diluents. *Macromolecules* 1992, *25* (23), 6119–6127. DOI: 10.1021/ma00049a007.
- (50) Shieh, Y.-T.; Su, J.-H.; Manivannan, G.; Lee, P. H. C.; Sawan, S. P.; Spall, W. D. Interaction of supercritical carbon dioxide with polymers. I. Crystalline polymers. *J. Appl. Polym. Sci.* 1996, *59* (4), 695–705. DOI: 10.1002/(SICI)1097-4628(19960124)59:4<695:AID-APP15>3.0.CO;2-P.
- (51) Ma, Z.; Zhang, G.; Yang, Q.; Shi, X.; Shi, A. Fabrication of microcellular polycarbonate foams with unimodal or bimodal cell-size distributions using supercritical carbon dioxide as a blowing agent. *J. Cell. Plast.* 2014, *50* (1), 55–79. DOI: 10.1177/0021955X13503849.
- (52) Chiou, J. S.; Barlow, J. W.; Paul, D. R. Plasticization of glassy polymers by CO<sub>2</sub>. *J. Appl. Polym. Sci.* 1985, *30* (6), 2633–2642. DOI: 10.1002/app.1985.070300626.
- (53) Zhang, Y.; Gangwani, K. K.; Lemert, R. M. Sorption and swelling of block copolymers in the presence of supercritical fluid carbon dioxide. *J. Supercrit. Fluids* 1997, *11* (1-2), 115–134. DOI: 10.1016/S0896-8446(97)00031-4.

- (54) Wissinger, R. G.; Paulaitis, M. E. Molecular thermodynamic model for sorption and swelling in glassy polymer-carbon dioxide systems at elevated pressures. *Ind. Eng. Chem. Res.* 1991, *30* (5), 842–851. DOI: 10.1021/ie00053a006.
- (55) Li, R.; Zeng, D.; Liu, Q.; Jiang, Z.; Fang, T. Glass Transition Temperature in Microcellular Foaming Process with Supercritical Carbon Dioxide: A Review. *Polymer-Plastics Technology and Engineering* 2015, *54* (2), 119–127. DOI: 10.1080/03602559.2014.955203.
- (56) Iannace, S. *Biofoams: Science and Applications of Bio-Based Cellular and Porous Materials*; CRC Press, 2015.
- (57) Abbasi, M.; Faust, L.; Wilhelm, M. Molecular origin of the foam structure in model linear and comb polystyrenes: II. Volume expansion ratio. *Polymer* 2020, *193*, 122354. DOI: 10.1016/j.polymer.2020.122354.
- (58) Chow, T. S. Molecular Interpretation of the Glass Transition Temperature of Polymer-Diluent Systems. *Macromolecules* 1980, *13* (2), 362–364. DOI: 10.1021/ma60074a029.
- (59) Shafi, M. A.; Flumerfelt, R. W. Initial bubble growth in polymer foam processes. *Chem. Eng. Sci.* 1997, *52* (4), 627–633. DOI: 10.1016/S0009-2509(96)00434-4.
- (60) Shafi, M. A.; Lee, J. G.; Flumerfelt, R. W. Prediction of cellular structure in free expansion polymer foam processing. *Polym. Eng. Sci.* 1996, *36* (14), 1950–1959. DOI: 10.1002/pen.10591.
- (61) Leung, S. N.; Wong, A.; Guo, Q.; Park, C. B.; Zong, J. H. Change in the critical nucleation radius and its impact on cell stability during polymeric foaming processes. *Chem. Eng. Sci.* 2009, *64* (23), 4899–4907. DOI: 10.1016/j.ces.2009.07.025.
- (62) Liao, R.; Yu, W.; Zhou, C. Rheological control in foaming polymeric materials: I. Amorphous polymers. *Polymer* 2010, *51* (2), 568–580. DOI: 10.1016/j.polymer.2009.11.063.
- (63) Joule, J. P.; Thomson, W. On the thermal effects experienced by air in rushing through small apertures. *Lond. Edinb. Dublin Philos. Mag. J. Sci.* 1852, *4* (28), 481–492. DOI: 10.1080/14786445208647169.
- (64) Krause, B.; Mettinkhof, R.; van der Vegt, N. F. A.; Wessling, M. Microcellular Foaming of Amorphous High- Tg Polymers Using Carbon Dioxide. *Macromolecules* 2001, *34* (4), 874–884. DOI: 10.1021/ma001291z.
- (65) Costeux, S.; Khan, I.; Bunker, S. P.; Jeon, H. K. Experimental study and modeling of nanofoams formation from single phase acrylic copolymers. *J. Cell. Plast.* 2015, *51* (2), 197–221. DOI: 10.1177/0021955X14531972.
- (66) Guo, H.; Kumar, V. Effect of glass transition temperature and saturation temperature on the solid-state microcellular foaming of cyclic olefin copolymer. *J. Appl. Polym. Sci.* 2015, *132* (28), 42226. DOI: 10.1002/app.42226.
- (67) Leibler, L. Theory of Microphase Separation in Block Copolymers. *Macromolecules* 1980, *13* (6), 1602–1617. DOI: 10.1021/ma60078a047.
- (68) Henry, W. III. Experiments on the quantity of gases absorbed by water, at different temperatures, and under different pressures. *Phil. Trans. R. Soc.* 1803, *93*, 29–274. DOI: 10.1098/rstl.1803.0004.
- (69) Handge, U. A.; Altstädt, V. Viscoelastic properties of solutions of polystyrene melts and carbon dioxide: Analysis of a transient shear rheology approach. *J. Rheol.* 2012, *56* (4), 743–766. DOI: 10.1122/1.4708601.

- 
- (70) Fick, A. Ueber Diffusion. *Ann. Phys. Chem.* 1855, 170 (1), 59–86. DOI: 10.1002/andp.18551700105.
- (71) Fick, A. On liquid diffusion. *London, Edinb. Dublin Philos. Mag. J. Sci.* 1855, 10 (63), 30–39. DOI: 10.1080/14786445508641925.
- (72) Colton, J. S.; Suh, N. P. Nucleation of microcellular foam: Theory and practice. *Polym. Eng. Sci.* 1987, 27 (7), 500–503. DOI: 10.1002/pen.760270704.
- (73) Gibbs, J. W. *The scientific papers of J. Willard Gibbs: Thermodynamics*, Repr; Ox Bow Pr, 1970.
- (74) Leung, S. N.; Wong, A.; Wang, L. C.; Park, C. B. Mechanism of extensional stress-induced cell formation in polymeric foaming processes with the presence of nucleating agents. *J. Supercrit. Fluids* 2012, 63, 187–198. DOI: 10.1016/j.supflu.2011.12.018.
- (75) Leung, S. N.; Park, C. B.; Li, H. Numerical simulation of polymeric foaming processes using modified nucleation theory. *Plastics, Rubber and Composites* 2006, 35 (3), 93–100. DOI: 10.1179/174328906X103079.
- (76) Colton, J. S.; Suh, N. P. The nucleation of microcellular thermoplastic foam with additives: Part I: Theoretical considerations. *Polym. Eng. Sci.* 1987, 27 (7), 485–492. DOI: 10.1002/pen.760270702.
- (77) Butt, H. J.; Graf, K.; Kappl, M. *Physics and chemistry of interfaces*, Wiley-VCH, 2003.
- (78) Roebuck, J. R.; Osterberg, H. The Joule-Thomson Effect in Argon. *Phys. Rev.* 1934, 46 (9), 785–790. DOI: 10.1103/PhysRev.46.785.
- (79) Roebuck, J. R.; Osterberg, H. The Joule-Thomson Effect in Nitrogen. *Phys. Rev.* 1935, 48 (5), 450–457. DOI: 10.1103/PhysRev.48.450.
- (80) Barlow, E. J.; Langlois, W. E. Diffusion of Gas from a Liquid into an Expanding Bubble. *IBM J. Res. & Dev.* 1962, 6 (3), 329–337. DOI: 10.1147/rd.63.0329.
- (81) Street, J. R. The Rheology of Phase Growth in Elastic Liquids. *Transactions of the Society of Rheology* 1968, 12 (1), 103–131. DOI: 10.1122/1.549101.
- (82) Amon, M.; Denson, C. D. A study of the dynamics of foam growth: Analysis of the growth of closely spaced spherical bubbles. *Polym. Eng. Sci.* 1984, 24 (13), 1026–1034. DOI: 10.1002/pen.760241306.
- (83) Amon, M.; Denson, C. D. A study of the dynamics of foam growth: Simplified analysis and experimental results for bulk density in structural foam molding. *Polym. Eng. Sci.* 1986, 26 (3), 255–267. DOI: 10.1002/pen.760260311.
- (84) Guo, Q.; Wang, J.; Park, C. B.; Ohshima, M. A Microcellular Foaming Simulation System with a High Pressure-Drop Rate. *Ind. Eng. Chem. Res.* 2006, 45 (18), 6153–6161. DOI: 10.1021/ie060105w.
- (85) Leung, S. N.; Park, C. B.; Xu, D.; Li, H.; Fenton, R. G. Computer Simulation of Bubble-Growth Phenomena in Foaming. *Ind. Eng. Chem. Res.* 2006, 45 (23), 7823–7831. DOI: 10.1021/ie060295a.
- (86) Arefmanesh, A.; Advani, S. G.; Michaelides, E. E. An accurate numerical solution for mass diffusion-induced bubble growth in viscous liquids containing limited dissolved gas. *International Journal of Heat and Mass Transfer* 1992, 35 (7), 1711–1722. DOI: 10.1016/0017-9310(92)90141-E.

- (87) Yoon, J. D.; Cha, S. W. Change of glass transition temperature of polymers containing gas. *Polym. Test.* 2001, *20* (3), 287–293. DOI: 10.1016/S0142-9418(00)00034-9.
- (88) Osswald, T. A.; Rudolph, N. *Polymer rheology: Fundamentals and applications*, Hanser, 2015.
- (89) Dealy, J. M.; Read, D. J.; Larson, R. G. *Structure and Rheology of Molten Polymers*, 2nd ed.; Hanser eLibrary; Hanser, 2017. DOI: 10.3139/9781569906125.
- (90) Macosko, C. W. *Rheology: Principles, measurements, and applications*, Advances in interfacial engineering series; VCH, 1994.
- (91) Goodwin, J. W.; Hughes, R. W. *Rheology for chemists. An introduction*, 2. ed.; Royal Soc. of Chemistry, 2008.
- (92) Mezger, T. *The Rheology Handbook*; Vincentz Network, 2020. DOI: 10.1515/9783748603702.
- (93) Orbey, N.; Dealy, J. M. Determination of the relaxation spectrum from oscillatory shear data. *J. Rheol.* 1991, *35* (6), 1035–1049. DOI: 10.1122/1.550164.
- (94) Larson, R. G. *Constitutive Equations for Polymer Melts and Solutions. Butterworths Series in Chemical Engineering*; Elsevier Science, 1988.
- (95) Williams, M. L.; Landel, R. F.; Ferry, J. D. The Temperature Dependence of Relaxation Mechanisms in Amorphous Polymers and Other Glass-forming Liquids. *J. Am. Chem. Soc.* 1955, *77* (14), 3701–3707. DOI: 10.1021/ja01619a008.
- (96) Cox, W. P.; Merz, E. H. Correlation of dynamic and steady flow viscosities. *J. Polym. Sci.* 1958, *28* (118), 619–622. DOI: 10.1002/pol.1958.1202811812.
- (97) Münstedt, H.; Schwarzl, F. R. *Deformation and flow of polymeric materials*; Springer, 2014.
- (98) Fetters, L. J.; Lohse, D. J.; Richter, D.; Witten, T. A.; Zirkel, A. Connection between Polymer Molecular Weight, Density, Chain Dimensions, and Melt Viscoelastic Properties. *Macromolecules* 1994, *27* (17), 4639–4647. DOI: 10.1021/ma00095a001.
- (99) Graessley, W. W. Some phenomenological consequences of the Doi–Edwards theory of viscoelasticity. *J. Polym. Sci. Polym. Phys. Ed.* 1980, *18* (1), 27–34. DOI: 10.1002/pol.1980.180180103.
- (100) Trouton, F. T. On the coefficient of viscous traction and its relation to that of viscosity. *Proc. R. Soc. Lond. A* 1906, *77* (519), 426–440. DOI: 10.1098/rspa.1906.0038.
- (101) Luo, X.-L.; Tanner, R. I. Finite element simulation of long and short circular die extrusion experiments using integral models. *Int. J. Numer. Meth. Engng.* 1988, *25* (1), 9–22. DOI: 10.1002/nme.1620250104.
- (102) Khan, S. A.; Prud'homme, R. K.; Larson, R. G. Comparison of the rheology of polymer melts in shear, and biaxial and uniaxial extensions. *Rheol Acta* 1987, *26* (2), 144–151. DOI: 10.1007/BF01331972.
- (103) Nishioka, A.; Takahashi, T.; Masubuchi, Y.; Takimoto, J.-i.; Koyama, K. Description of uniaxial, biaxial, and planar elongational viscosities of polystyrene melt by the K-BKZ model. *J. Non-Newton. Fluid Mech.* 2000, *89* (3), 287–301. DOI: 10.1016/S0377-0257(99)00047-6.
- (104) Stadler, F. J.; Nishioka, A.; Stange, J.; Koyama, K.; Münstedt, H. Comparison of the elongational behavior of various polyolefins in uniaxial and equibiaxial flows. *Rheol Acta* 2007, *46* (7), 1003–1012. DOI: 10.1007/s00397-007-0190-y.
- (105) Röpert, M.-C.; Schußmann, M. G.; Esfahani, M. K.; Wilhelm, M.; Hirschberg, V. Effect of Side Chain Length in Polystyrene POM–POMs on Melt Rheology and Solid Mechanical Fatigue. *Macromolecules* 2022, *55* (13), 5485–5496. DOI: 10.1021/acs.macromol.2c00199.

- 
- (106) Doi, M.; Edwards, S. F. *The Theory of Polymer Dynamics*, Reprint; International series of monographs on physics, Vol. 73; Clarendon Press, 2013.
- (107) Gennes, P. G. de. Reptation of a Polymer Chain in the Presence of Fixed Obstacles. *J. Chem. Phys.* 1971, *55* (2), 572–579. DOI: 10.1063/1.1675789.
- (108) Edwards, S. F. The statistical mechanics of polymerized material. *Proc. Phys. Soc.* 1967, *92* (1), 9–16. DOI: 10.1088/0370-1328/92/1/303.
- (109) Doi, M.; Edwards, S. F. Dynamics of concentrated polymer systems. Part 1.—Brownian motion in the equilibrium state. *J. Chem. Soc., Faraday Trans. 2* 1978, *74* (0), 1789–1801. DOI: 10.1039/F29787401789.
- (110) Doi, M.; Edwards, S. F. Dynamics of concentrated polymer systems. Part 2.—Molecular motion under flow. *J. Chem. Soc., Faraday Trans. 2* 1978, *74* (0), 1802–1817. DOI: 10.1039/F29787401802.
- (111) Milner, S. T.; McLeish, T. C. B. Reptation and Contour-Length Fluctuations in Melts of Linear Polymers. *Phys. Rev. Lett.* 1998, *81* (3), 725–728. DOI: 10.1103/PhysRevLett.81.725.
- (112) Rubinstein, M.; Colby, R. H. *Polymer Physics*, repr; Oxford Univ. Press, 2014.
- (113) Wagner, M. H.; Ehrecke, P.; Hachmann, P.; Meissner, J. A constitutive analysis of uniaxial, equibiaxial and planar extension of a commercial linear high-density polyethylene melt. *J. Rheol.* 1998, *42* (3), 621–638. DOI: 10.1122/1.550939.
- (114) Rolón-Garrido, V. H.; Pivokonsky, R.; Filip, P.; Zatloukal, M.; Wagner, M. H. Modelling elongational and shear rheology of two LDPE melts. *Rheol. Acta* 2009, *48* (6), 691–697. DOI: 10.1007/s00397-009-0366-8.
- (115) Currie, P. K. Constitutive equations for polymer melts predicted by the Doi—Edwards and Curtiss—Bird kinetic theory models. *J. Non-Newton. Fluid Mech.* 1982, *11* (1-2), 53–68. DOI: 10.1016/0377-0257(82)85015-5.
- (116) McLeish, T. C. B.; Larson, R. G. Molecular constitutive equations for a class of branched polymers: The pom-pom polymer. *J. Rheol.* 1998, *42* (1), 81–110. DOI: 10.1122/1.550933.
- (117) Rolón-Garrido, V. H. The molecular stress function (MSF) model in rheology. *Rheol. Acta* 2014, *53* (9), 663–700. DOI: 10.1007/s00397-014-0787-x.
- (118) Wagner, M. H.; Yamaguchi, M.; Takahashi, M. Quantitative assessment of strain hardening of low-density polyethylene melts by the molecular stress function model. *J. Rheol.* 2003, *47* (3), 779–793. DOI: 10.1122/1.1562155.
- (119) Wagner, M. H.; Rubio, P.; Bastian, H. The molecular stress function model for polydisperse polymer melts with dissipative convective constraint release. *J. Rheol.* 2001, *45* (6), 1387–1412. DOI: 10.1122/1.1413503.
- (120) Kheirandish, S.; Stadlbauer, M. Molecular stress function theory and analysis of branching structure in industrial polyolefins. *J. Therm. Anal. Calorim.* 2009, *98* (3), 629–637. DOI: 10.1007/s10973-009-0507-4.
- (121) Lentzakis, H.; Das, C.; Vlassopoulos, D.; Read, D. J. Pom-pom-like constitutive equations for comb polymers. *J. Rheol.* 2014, *58* (6), 1855–1875. DOI: 10.1122/1.4895606.
- (122) Inkson, N. J.; McLeish, T. C. B.; Harlen, O. G.; Groves, D. J. Predicting low density polyethylene melt rheology in elongational and shear flows with “pom-pom” constitutive equations. *J. Rheol.* 1999, *43* (4), 873–896. DOI: 10.1122/1.551036.

- (123) Doi, M.; Kuzuu, N. Y. Rheology of star polymers in concentrated solutions and melts. *J. Polym. Sci. B Polym. Lett. Ed.* 1980, *18* (12), 775–780. DOI: 10.1002/pol.1980.130181205.
- (124) Staudinger, H. Über Polymerisation. *Ber. dtsh. Chem. Ges. A/B* 1920, *53* (6), 1073–1085. DOI: 10.1002/cber.19200530627.
- (125) Staudinger, H.; Fritsch, J. Über Isopren und Kautschuk. 5. Mitteilung. Über die Hydrierung des Kautschuks und über seine Konstitution. *HCA* 1922, *5* (5), 785–806. DOI: 10.1002/hlca.19220050517.
- (126) Szwarc, M.; Levy, M.; Milkovich, R. POLYMERIZATION INITIATED BY ELECTRON TRANSFER TO MONOMER. A NEW METHOD OF FORMATION OF BLOCK POLYMERS 1. *J. Am. Chem. Soc.* 1956, *78* (11), 2656–2657. DOI: 10.1021/ja01592a101.
- (127) Stavely, F. W.; Coworkers. Coral Rubber—A Cis -1,4-Polyisoprene. *Rubber Chemistry and Technology* 1956, *29* (3), 673–686. DOI: 10.5254/1.3542582.
- (128) Ionescu, M. *Chemistry and technology of polyols for polyurethanes*; Rapra Technology, 2005.
- (129) Hadjichristidis, N.; Hira, A., Eds. *Anionic polymerization: Principles, practice, strength, consequences and applications*; Springer Tokyo, 2015.
- (130) Elias, H.-G. *Makromoleküle: Chemische Struktur und Synthesen*, 6.th ed., Vol. 1; Wiley-VCH, 1999.
- (131) Young, R. J.; Lovell, P. A. *Introduction to polymers*, 3. ed.; CRC Press Taylor & Francis, 2011.
- (132) Wang, J.-S.; Jerome, R.; Teyssie, P. Anionic Polymerization of Acrylic Monomers. 19. Effect of Various Types of Ligands Other Than Lithium Chloride on the Stereochemistry of Anionic Polymerization of Methyl Methacrylate. *Macromolecules* 1994, *27* (18), 4902–4907. DOI: 10.1021/ma00096a009.
- (133) Wang, J. S.; Jerome, R.; Warin, R.; Teyssie, P. Anionic polymerization of (meth)acrylic monomers. 12. Effect of lithium chloride on the stereochemistry of the anionic polymerization of methyl methacrylate in THF and in a 9/1 toluene/THF mixture. *Macromolecules* 1993, *26* (22), 5984–5990. DOI: 10.1021/ma00074a021.
- (134) Tieke, B. *Makromolekulare Chemie: Eine Einführung*, Dritte Auflage; Wiley-VCH Verlag GmbH & Co. KGaA, 2014.
- (135) Koltzenburg, S.; Maskos, M.; Nuyken, O.; Müllhaupt, R.; Matyjaszewski, K. *Polymer chemistry*; Springer, 2017.
- (136) Lechner, M. D.; Nordmeier, E.; Gehrke, K. *Makromolekulare Chemie: Ein Lehrbuch für Chemiker, Physiker, Materialwissenschaftler und Verfahrenstechniker*, 4., überarb. und erw. Aufl.; Birkhäuser, 2010.
- (137) Kolmogorov, A. N. *Foundations of the theory of probability*, Second English edition; Martino Fine Books, 2013.
- (138) Ito, K. Derivation of distributions of the degree of polymerization by probability theory. *J. Polym. Sci. A-2 Polym. Phys.* 1969, *7* (1), 241–248. DOI: 10.1002/pol.1969.160070120.
- (139) Odian, G. G. *Principles of polymerization*, Fourth edition; Wiley, 2004. DOI: 10.1002/047147875X.
- (140) Quirk, R. P.; Chen, W.-C. Functionalization of polymeric organolithium compounds. Carbonation. *Makromol. Chem.* 1982, *183* (9), 2071–2076. DOI: 10.1002/macp.1982.021830905.



- 
- (141) Quirk, R. P.; Chen, W.-C. Functionalization of polymeric organolithium compounds. Oxidation. *J. Polym. Sci. Polym. Chem. Ed.* 1984, *22* (11), 2993–3000. DOI: 10.1002/pol.1984.170221122.
- (142) Quirk, R. P.; Ma, J.-J. Characterization of the functionalization reaction product of poly(styryl)lithium with ethylene oxide. *J. Polym. Sci. A Polym. Chem.* 1988, *26* (8), 2031–2037. DOI: 10.1002/pola.1988.080260804.
- (143) Hadjichristidis, N.; Pispas, S.; Floudas, G. *Block copolymers. Synthetic strategies, physical properties, and applications*; Wiley-Interscience, 2003.
- (144) Müller, A. H. E., Ed. *Controlled and living polymerizations. Methods and materials*; Wiley-VCH-Verl., 2009.
- (145) Ayano, S.; Yabe, S. Anionic Polymerization of Isoprene. II. Synthesis and Characterization of A–B–A-Type Block Copolymers by Oligomeric Dilithium Initiator. *Polym. J.* 1970, *1* (6), 706–715. DOI: 10.1295/polymj.1.706.
- (146) Bywater, S.; Worsfold, D. J. Charge distribution in substituted allyl-alkali metal compounds by <sup>13</sup>C NMR. *Journal of Organometallic Chemistry* 1978, *159* (3), 229–235. DOI: 10.1016/S0022-328X(00)93801-4.
- (147) Gebert, W.; Hinz, J.; Sinn, H. Umlagerungen bei der durch Lithiumbutyl initiierten Polymerisation der Diene Isopren und Butadien. *Makromol. Chem.* 1971, *144* (1), 97–115. DOI: 10.1002/macp.1971.021440109.
- (148) Hamley, I. W. *The physics of block copolymers*, Repr; Oxford science publications; Oxford University Press, 2003.
- (149) Flory, P. J. *Principles of polymer chemistry*, 10. print; Cornell Univ. Pr, 1978.
- (150) Flory, P. J. Thermodynamics of High Polymer Solutions. *J. Chem. Phys.* 1942, *10* (1), 51–61. DOI: 10.1063/1.1723621.
- (151) Matsen, M. W. The standard Gaussian model for block copolymer melts. *J. Phys. Condens. Matter* 2002, *14* (21), 21–47.
- (152) Thomas, E. L.; Anderson, D. M.; Henkee, C. S.; Hoffman, D. Periodic area-minimizing surfaces in block copolymers. *Nature* 1988, *334* (6183), 598–601. DOI: 10.1038/334598a0.
- (153) Bates, F. S.; Rosedale, J. H.; Fredrickson, G. H. Fluctuation effects in a symmetric diblock copolymer near the order–disorder transition. *J. Chem. Phys.* 1990, *92* (10), 6255–6270. DOI: 10.1063/1.458350.
- (154) Matsen, M. W.; Bates, F. S. Unifying Weak- and Strong-Segregation Block Copolymer Theories. *Macromolecules* 1996, *29* (4), 1091–1098. DOI: 10.1021/ma951138i.
- (155) Bates, F. S. Polymer-polymer phase behavior. *Science (New York, N.Y.)* 1991, *251* (4996), 898–905. DOI: 10.1126/science.251.4996.898.
- (156) Heck, M.; Schneider, L.; Müller, M.; Wilhelm, M. Diblock Copolymers with Similar Glass Transition Temperatures in Both Blocks for Comparing Shear Orientation Processes with DPD Computer Simulations. *Macromol. Chem. Phys.* 2018, *219* (9), 1700559. DOI: 10.1002/macp.201700559.
- (157) Langela, M.; Wiesner, U.; Spiess, H. W.; Wilhelm, M. Microphase Reorientation in Block Copolymer Melts As Detected via FT Rheology and 2D SAXS. *Macromolecules* 2002, *35* (8), 3198–3204. DOI: 10.1021/ma0115693.

- (158) Khandpur, A. K.; Foerster, S.; Bates, F. S.; Hamley, I. W.; Ryan, A. J.; Bras, W.; Almdal, K.; Mortensen, K. Polyisoprene-Polystyrene Diblock Copolymer Phase Diagram near the Order-Disorder Transition. *Macromolecules* 1995, *28* (26), 8796–8806. DOI: 10.1021/ma00130a012.
- (159) Abu-Sharkh, B.; AlSunaidi, A. Morphology and Conformation Analysis of Self-Assembled Triblock Copolymer Melts. *Macromol. Theory Simul.* 2006, *15* (6), 507–515. DOI: 10.1002/mats.200600014.
- (160) Hirschberg, V.; Faust, L.; Rodrigue, D.; Wilhelm, M. Effect of Topology and Molecular Properties on the Rheology and Fatigue Behavior of Solid Polystyrene/Polyisoprene Di- and Triblock Copolymers. *Macromolecules* 2020, *53* (13), 5572–5587. DOI: 10.1021/acs.macromol.0c00632.
- (161) Oelschlaeger, C.; Gutmann, J. S.; Wolkenhauer, M.; Spiess, H.-W.; Knoll, K.; Wilhelm, M. Kinetics of Shear Microphase Orientation and Reorientation in Lamellar Diblock and Triblock Copolymer Melts as Detected via FT-Rheology and 2D-SAXS. *Macromol. Chem. Phys.* 2007, *208* (16), 1719–1729. DOI: 10.1002/macp.200700150.
- (162) Matsen, M. W.; Bates, F. S. Origins of Complex Self-Assembly in Block Copolymers. *Macromolecules* 1996, *29* (23), 7641–7644. DOI: 10.1021/ma960744q.
- (163) Matsen, M. W.; Thompson, R. B. Equilibrium behavior of symmetric ABA triblock copolymer melts. *J. Chem. Phys.* 1999, *111* (15), 7139–7146. DOI: 10.1063/1.480006.
- (164) Owens, J. N.; Gancarz, I. S.; Koberstein, J. T.; Russell, T. P. Investigation of the microphase separation transition in low-molecular-weight diblock copolymers. *Macromolecules* 1989, *22* (8), 3380–3387. DOI: 10.1021/ma00198a032.
- (165) Hadjichristidis, N.; Pitsikalis, M.; Iatrou, H. Synthesis of Block Copolymers. In *Block Copolymers I*; Abetz, V., Ed.; Advances in Polymer Science; Springer-Verlag, 2005; pp 1–124. DOI: 10.1007/12\_005.
- (166) Pitsikalis, M.; Pispas, S.; Mays, J. W.; Hadjichristidis, N. Nonlinear Block Copolymer Architectures. In *Blockcopolymers - Polyelectrolytes - Biodegradation*; Bellon-Maurel, V., Calmon-Decriaud, A., Chandrasekhar, V., Hadjichristidis, N., Mays, J. W., Pispas, S., Pitsikalis, M., Silvestre, F., Eds.; Advances in Polymer Science; Springer Berlin Heidelberg, 1998; pp 1–137. DOI: 10.1007/3-540-69191-X\_1.
- (167) Guo, H.; Nicolae, A.; Kumar, V. Solid-state poly(methyl methacrylate) (PMMA) nanofoams. Part II: Low-temperature solid-state process space using CO<sub>2</sub> and the resulting morphologies. *Polymer* 2015, *70*, 231–241. DOI: 10.1016/j.polymer.2015.06.031.
- (168) Martín-de León, J.; Bernardo, V.; Rodríguez-Pérez, M. Á. Low Density Nanocellular Polymers Based on PMMA Produced by Gas Dissolution Foaming: Fabrication and Cellular Structure Characterization. *Polymers* 2016, *8* (7). DOI: 10.3390/polym8070265.
- (169) Pinto, J.; Dumon, M.; Rodríguez-Pérez, M. A.; Garcia, R.; Dietz, C. Block Copolymers Self-Assembly Allows Obtaining Tunable Micro or Nanoporous Membranes or Depth Filters Based on PMMA; Fabrication Method and Nanostructures. *J. Phys. Chem. C* 2014, *118* (9), 4656–4663. DOI: 10.1021/jp409803u.
- (170) Zhai, W.; Yu, J.; Wu, L.; Ma, W.; He, J. Heterogeneous nucleation uniformizing cell size distribution in microcellular nanocomposites foams. *Polymer* 2006, *47* (21), 7580–7589. DOI: 10.1016/j.polymer.2006.08.034.

- 
- (171) Siripurapu, S.; DeSimone, J. M.; Khan, S. A.; Spontak, R. J. Controlled Foaming of Polymer Films through Restricted Surface Diffusion and the Addition of Nanosilica Particles or CO<sub>2</sub>-philic Surfactants. *Macromolecules* 2005, *38* (6), 2271–2280. DOI: 10.1021/ma047991b.
- (172) Goren, K.; Chen, L.; Schadler, L. S.; Ozisik, R. Influence of nanoparticle surface chemistry and size on supercritical carbon dioxide processed nanocomposite foam morphology. *J. Supercrit. Fluids* 2010, *51* (3), 420–427. DOI: 10.1016/j.supflu.2009.09.007.
- (173) ZENG, C.; HAN, X.; LEE, L. J.; Koelling, K. W.; Tomasko, D. L. Polymer–Clay Nanocomposite Foams Prepared Using Carbon Dioxide. *Adv. Mater.* 2003, *15* (20), 1743–1747. DOI: 10.1002/adma.200305065.
- (174) Shen, J.; Zeng, C.; Lee, L. J. Synthesis of polystyrene–carbon nanofibers nanocomposite foams. *Polymer* 2005, *46* (14), 5218–5224. DOI: 10.1016/j.polymer.2005.04.010.
- (175) Doroudiani, S.; Park, C. B.; Kortschot, M. T. Processing and characterization of microcellular foamed high-density polyethylene/isotactic polypropylene blends. *Polym. Eng. Sci.* 1998, *38* (7), 1205–1215. DOI: 10.1002/pen.10289.
- (176) Huang, H.-X.; Wang, J.-K. Improving polypropylene microcellular foaming through blending and the addition of nano-calcium carbonate. *J. Appl. Polym. Sci.* 2007, *106* (1), 505–513. DOI: 10.1002/app.26483.
- (177) Rachtanapun, P.; Selke, S. E. M.; Matuana, L. M. Microcellular foam of polymer blends of HDPE/PP and their composites with wood fiber. *J. Appl. Polym. Sci.* 2003, *88* (12), 2842–2850. DOI: 10.1002/app.12170.
- (178) Zhang, P.; Zhou, N. Q.; Wu, Q. F.; Wang, M. Y.; Peng, X. F. Microcellular foaming of PE/PP blends. *J. Appl. Polym. Sci.* 2007, *104* (6), 4149–4159. DOI: 10.1002/app.26071.
- (179) Sahagún, C. Z.; González-Núñez, R.; Rodrigue, D. Morphology of Extruded PP/HDPE Foam Blends. *J. Cell. Plast.* 2006, *42* (6), 469–485. DOI: 10.1177/0021955X06063521.
- (180) Rogers, J.-V.; Kisner, R. D. Ultra low density polyolefin foam, foamable polyolefin compositions and process for making same: Patent US5225451A.
- (181) Reichelt, N.; Stadlbauer, M.; Folland, R.; Park, C. B.; Wang, J. PP-Blends with Tailored Foamability and Mechanical Properties. *Cell. Polym.* 2003, *22* (5), 315–327. DOI: 10.1177/026248930302200503.
- (182) Ruiz, J. A. R.; Pedros, M.; Tallon, J.-M.; Dumon, M. Micro and nano cellular amorphous polymers (PMMA, PS) in supercritical CO<sub>2</sub> assisted by nanostructured CO<sub>2</sub>-philic block copolymers – One step foaming process. *J. Supercrit. Fluids* 2011, *58* (1), 168–176. DOI: 10.1016/j.supflu.2011.04.022.
- (183) Pinto, J.; Reglero-Ruiz, J. A.; Dumon, M.; Rodriguez-Perez, M. A. Temperature influence and CO<sub>2</sub> transport in foaming processes of poly(methyl methacrylate)–block copolymer nanocellular and microcellular foams. *J. Supercrit. Fluids* 2014, *94*, 198–205. DOI: 10.1016/j.supflu.2014.07.021.
- (184) Pinto, J.; Dumon, M.; Pedros, M.; Reglero, J.; Rodriguez-Perez, M. A. Nanocellular CO<sub>2</sub> foaming of PMMA assisted by block copolymer nanostructuring. *Chem. Eng. J.* 2014, *243*, 428–435. DOI: 10.1016/j.cej.2014.01.021.
- (185) Siripurapu, S.; Gay, Y. J.; Royer, J. R.; DeSimone, J. M.; Spontak, R. J.; Khan, S. A. Generation of microcellular foams of PVDF and its blends using supercritical carbon dioxide in a continuous process. *Polymer* 2002, *43* (20), 5511–5520. DOI: 10.1016/S0032-3861(02)00407-X.

- (186) Taki, K.; Nitta, K.; Kihara, S.-I.; Ohshima, M. CO<sub>2</sub> foaming of poly(ethylene glycol)/polystyrene blends: Relationship of the blend morphology, CO<sub>2</sub> mass transfer, and cellular structure. *J. Appl. Polym. Sci.* 2005, *97* (5), 1899–1906. DOI: 10.1002/app.21930.
- (187) Han, X.; Lee, L. J.; Tomasko, D. L. CO<sub>2</sub> Foaming of Polymer Nanocomposite Blends. *Aust. J. Chem.* 2005, *58* (6), 492. DOI: 10.1071/CH05071.
- (188) Han, X.; Shen, J.; Huang, H.; Tomasko, D. L.; Lee, L. J. CO<sub>2</sub> foaming based on polystyrene/poly(methyl methacrylate) blend and nanoclay. *Polym. Eng. Sci.* 2007, *47* (2), 103–111. DOI: 10.1002/pen.20679.
- (189) Smith, P. J.; Cross, B. J. Foamed articles of styrenic and acrylic polymers blend: Patent: US6063485A.
- (190) Diaf, A.; Enick, R. M.; Beckman, E. J. Molecular redesign of expanded polystyrene to allow use of carbon dioxide as a foaming agent. I. Reversible binding of CO<sub>2</sub>. *J. Appl. Polym. Sci.* 1993, *50* (5), 835–844. DOI: 10.1002/app.1993.070500510.
- (191) Sarbu, T.; Styranec, T. J.; Beckman, E. J. Design and Synthesis of Low Cost, Sustainable CO<sub>2</sub>-philes. *Ind. Eng. Chem. Res.* 2000, *39* (12), 4678–4683. DOI: 10.1021/ie0003077.
- (192) Sun, H.; Mark, J. E.; Tan, S. C.; Venkatasubramanian, N.; Houtz, M. D.; Arnold, F. E.; Lee, C. Y.-C. Microcellular foams from some high-performance composites. *Polymer* 2005, *46* (17), 6623–6632. DOI: 10.1016/j.polymer.2005.05.016.
- (193) Vachon, C.; Tatibouët, J. Effect of Additives on the Solubility and Diffusivity of CO<sub>2</sub> in Polystyrene. *ANTEC SPE* 2004.
- (194) Ruckdäschel, H.; Gutmann, P.; Altstädt, V.; Schmalz, H.; Müller, A. H. E. Foaming of Microstructured and Nanostructured Polymer Blends. In *Complex Macromolecular Systems I*; Müller, A. H. E., Schmidt, H.-W., Eds.; Advances in Polymer Science; Springer Berlin Heidelberg, 2010; pp 199–252. DOI: 10.1007/12\_2009\_32.
- (195) Spitael, P.; Macosko, C. W.; McClurg, R. B. Block Copolymer Micelles for Nucleation of Microcellular Thermoplastic Foams. *Macromolecules* 2004, *37* (18), 6874–6882. DOI: 10.1021/ma049712q.
- (196) Shinkai, T.; Sugiyama, K.; Ito, K.; Yokoyama, H. Nanoporous fabrication of block copolymers via carbon dioxide swelling: Difference between CO<sub>2</sub>-swollen and nanoporous block copolymers. *Polymer* 2016, *100*, 19–27. DOI: 10.1016/j.polymer.2016.08.011.
- (197) Li, L.; Nemoto, T.; Sugiyama, K.; Yokoyama, H. CO<sub>2</sub> Foaming in Thin Films of Block Copolymer Containing Fluorinated Blocks. *Macromolecules* 2006, *39* (14), 4746–4755. DOI: 10.1021/ma060325l.
- (198) Matsen, M. W.; Schick, M. Lamellar phase of a symmetric triblock copolymer. *Macromolecules* 1994, *27* (1), 187–192. DOI: 10.1021/ma00079a027.
- (199) Cziep, M. A.; Abbasi, M.; Heck, M.; Arens, L.; Wilhelm, M. Effect of Molecular Weight, Polydispersity, and Monomer of Linear Homopolymer Melts on the Intrinsic Mechanical Nonlinearity  $3Q_0(\omega)$  in MAOS. *Macromolecules* 2016, *49* (9), 3566–3579. DOI: 10.1021/acs.macromol.5b02706.
- (200) Mark, J. E., Ed. *Polymer data handbook*, 2. ed.; Oxford Univ. Press, 2009.

- 
- (201) Röpert, M.-C.; Goecke, A.; Wilhelm, M.; Hirschberg, V. Threading Polystyrene Stars: Impact of Star to POM-POM and Barbwire Topology on Melt Rheological and Foaming Properties. *Macromol. Chem. Phys.* 2022, 2200288. DOI: 10.1002/macp.202200288.
- (202) Röpert, M.-C.; Hirschberg, V.; Schußmann, M. G.; Wilhelm, M. Impact of Topological Parameters on Melt Rheological Properties and Foamability of PS POM-POMs. *Macromolecules* 2023, 56 (5), 1921–1933. DOI: 10.1021/acs.macromol.2c02051.
- (203) Mahmud, M. B.; Anstey, A.; Shaayegan, V.; Lee, P. C.; Park, C. B. Enhancing the mechanical performance of PA6 based composites by altering their crystallization and rheological behavior via in-situ generated PPS nanofibrils. *Compos. B. Eng.* 2020, 195, 108067. DOI: 10.1016/j.compositesb.2020.108067.
- (204) Bahreini, E.; Aghamiri, S. F.; Wilhelm, M.; Abbasi, M. Influence of molecular structure on the foamability of polypropylene: Linear and extensional rheological fingerprint. *J. Cell. Plast.* 2018, 54 (3), 515–543. DOI: 10.1177/0021955X17700097.
- (205) Xu, M.; Lu, J.; Zhao, J.; Wei, L.; Liu, T.; Zhao, L.; Park, C. B. Rheological and foaming behaviors of long-chain branched polyamide 6 with controlled branch length. *Polymer* 2021, 224, 123730. DOI: 10.1016/j.polymer.2021.123730.
- (206) Müller, A. H. E.; Schmidt, H.-W., Eds. *Complex Macromolecular Systems I*; Advances in Polymer Science; Springer Berlin Heidelberg, 2010. DOI: 10.1007/978-3-642-12876-9.
- (207) Abbasi, M.; Faust, L.; Riazi, K.; Wilhelm, M. Linear and Extensional Rheology of Model Branched Polystyrenes: From Loosely Grafted Combs to Bottlebrushes. *Macromolecules* 2017, 50 (15), 5964–5977. DOI: 10.1021/acs.macromol.7b01034.
- (208) Faust, L.; Röpert, M.-C.; Esfahani, M. K.; Abbasi, M.; Hirschberg, V.; Wilhelm, M. Comb and Branch-on-Branch Model Polystyrenes with Exceptionally High Strain Hardening Factor SHF > 1000 and Their Impact on Physical Foaming. *Macromol. Chem. Phys.* 2022, 2200214. DOI: 10.1002/macp.202200214.
- (209) Archer, L. A.; Varshney, S. K. Synthesis and Relaxation Dynamics of Multiarm Polybutadiene Melts. *Macromolecules* 1998, 31 (18), 6348–6355. DOI: 10.1021/ma9802733.
- (210) Knauss, D. M.; Huang, T. Star -block -Linear -block -Star Triblock (Pom-Pom) Polystyrene by Convergent Living Anionic Polymerization. *Macromolecules* 2002, 35 (6), 2055–2062. DOI: 10.1021/ma010949l.
- (211) Lee, J. H.; Fetters, L. J.; Archer, L. A. Stress Relaxation of Branched Polymers. *Macromolecules* 2005, 38 (26), 10763–10771. DOI: 10.1021/ma051856x.
- (212) Yuan, Z.; Gauthier, M. Synthesis of Arborescent Isoprene Homopolymers. *Macromolecules* 2005, 38 (10), 4124–4132. DOI: 10.1021/ma0479565.
- (213) Daniel, W. F. M.; Burdyńska, J.; Vatankhah-Varnoosfaderani, M.; Matyjaszewski, K.; Paturej, J.; Rubinstein, M.; Dobrynin, A. V.; Sheiko, S. S. Solvent-free, supersoft and superelastic bottlebrush melts and networks. *Nat. Mater.* 2016, 15 (2), 183–189. DOI: 10.1038/nmat4508.
- (214) Simon, P. F. W.; Müller, A. H. E.; Pakula, T. Characterization of Highly Branched Poly(methyl methacrylate) by Solution Viscosity and Viscoelastic Spectroscopy. *Macromolecules* 2001, 34 (6), 1677–1684. DOI: 10.1021/ma0014766.

- (215) van Ruymbeke, E.; Kapnistos, M.; Vlassopoulos, D.; Huang, T.; Knauss, D. M. Linear Melt Rheology of Pom-Pom Polystyrenes with Unentangled Branches. *Macromolecules* 2007, *40* (5), 1713–1719. DOI: 10.1021/ma062487n.
- (216) Ferry, J. D. *Viscoelastic properties of polymers*, 3. ed.; Wiley, 1980.
- (217) Roland, C. M.; Archer, L. A.; Mott, P. H.; Sanchez-Reyes, J. Determining Rouse relaxation times from the dynamic modulus of entangled polymers. *J. Rheol.* 2004, *48* (2), 395–403. DOI: 10.1122/1.1645516.
- (218) Bailly, C.; Stephenne, V.; Muchtar, Z.; Schappacher, M.; Deffieux, A. Linear viscoelastic behavior of densely grafted poly(chloroethyl vinyl ether)-g-polystyrene combs in the melt. *J. Rheol.* 2003, *47* (4), 821–827. DOI: 10.1122/1.1579688.
- (219) McLeish, T. C. B. Hierarchical Relaxation in Tube Models of Branched Polymers. *EPL* 1988, *6* (6), 511–516. DOI: 10.1209/0295-5075/6/6/007.
- (220) McLeish, T. C. B. Tube theory of entangled polymer dynamics. *Adv. Phys.* 2002, *51* (6), 1379–1527. DOI: 10.1080/00018730210153216.
- (221) Ramesh, N. S.; Lee, S. T. Blowing Agent Effect on Extensional Viscosity Calculated from Fiber Spinning Method for Foam Processing. *J. Cell. Plast.* 2000, *36* (5), 374–385. DOI: 10.1106/W3LI-MTQY-PJA9-RNJB.
- (222) Wang, Y.; Wang, S.-Q. Rupture in rapid uniaxial extension of linear entangled melts. *Rheol. Acta* 2010, *49* (11-12), 1179–1185. DOI: 10.1007/s00397-010-0491-4.
- (223) Wang, Y.; Wang, S.-Q. Salient Features in Uniaxial Extension of Polymer Melts and Solutions: Progressive Loss of Entanglements, Yielding, Non-Gaussian Stretching, and Rupture. *Macromolecules* 2011, *44* (13), 5427–5435. DOI: 10.1021/ma200432q.
- (224) Wagner, M. H.; Narimissa, E.; Huang, Q. Scaling relations for brittle fracture of entangled polystyrene melts and solutions in elongational flow. *J. Rheol.* 2021, *65* (3), 311–324. DOI: 10.1122/8.0000184.
- (225) Wagner, M. H.; Narimissa, E.; Huang, Q. On the origin of brittle fracture of entangled polymer solutions and melts. *J. Rheol.* 2018, *62* (1), 221–233. DOI: 10.1122/1.4995497.
- (226) López-Barrón, C. R.; Shivokhin, M. E. Extensional Strain Hardening in Highly Entangled Molecular Bottlebrushes. *Phys. Rev. Lett.* 2019, *122* (3), 37801. DOI: 10.1103/PhysRevLett.122.037801.
- (227) Masubuchi, Y.; Matsumiya, Y.; Watanabe, H.; Marrucci, G.; Ianniruberto, G. Primitive Chain Network Simulations for Pom-Pom Polymers in Uniaxial Elongational Flows. *Macromolecules* 2014, *47* (10), 3511–3519. DOI: 10.1021/ma500357g.
- (228) Huang, Q.; Agostini, S.; Hengeller, L.; Shivokhin, M.; Alvarez, N. J.; Hutchings, L. R.; Hassager, O. Dynamics of Star Polymers in Fast Extensional Flow and Stress Relaxation. *Macromolecules* 2016, *49* (17), 6694–6699. DOI: 10.1021/acs.macromol.6b01348.
- (229) McLeish, T. C. B.; Allgaier, J.; Bick, D. K.; Bishko, G.; Biswas, P.; Blackwell, R.; Blottière, B.; Clarke, N.; Gibbs, B.; Groves, D. J.; Hakiki, A.; Heenan, R. K.; Johnson, J. M.; Kant, R.; Read, D. J.; Young, R. N. Dynamics of Entangled H-Polymers: Theory, Rheology, and Neutron-Scattering. *Macromolecules* 1999, *32* (20), 6734–6758. DOI: 10.1021/ma990323j.
- (230) Sperling, L. H. *Introduction to Physical Polymer Science*, 4th ed.; Wiley, 2006. DOI: 10.1002/0471757128.

- 
- (231) Houli, S.; Iatrou, H.; Hadjichristidis, N.; Vlassopoulos, D. Synthesis and Viscoelastic Properties of Model Dumbbell Copolymers Consisting of a Polystyrene Connector and Two 32-Arm Star Polybutadienes. *Macromolecules* 2002, *35* (17), 6592–6597. DOI: 10.1021/ma0204709.
- (232) Berry, G. C.; Fox, T.G. The viscosity of polymers and their concentrated solutions. *Adv. Polym. Sci.* 1968, *5*, 261–357. DOI: 10.1007/BFb0050985.
- (233) Trinkle, S.; Friedrich, C. Van Gorp-Palmen-plot: a way to characterize polydispersity of linear polymers. *Rheol. Acta* 2001, *40* (4), 322–328. DOI: 10.1007/s003970000137.
- (234) Trinkle, S.; Walter, P.; Friedrich, C. Van Gorp-Palmen Plot II - classification of long chain branched polymers by their topology. *Rheol. Acta* 2002, *41* (1-2), 103–113. DOI: 10.1007/s003970200010.
- (235) Hepperle, J.; Münstedt, H.; Haug, P. K.; Eisenbach, C. D. Rheological properties of branched polystyrenes: linear viscoelastic behavior. *Rheol. Acta* 2005, *45* (2), 151–163. DOI: 10.1007/s00397-005-0033-7.
- (236) Ataei, M.; Shaayegan, V.; Wang, C.; Costa, F.; Han, S.; Park, C. B.; Bussmann, M. Numerical analysis of the effect of the local variation of viscosity on bubble growth and deformation in polymer foaming. *J. Rheol.* 2019, *63* (6), 895–903. DOI: 10.1122/1.5113802.
- (237) Lee, J. K.; Yao, S. X.; Li, G.; Jun, M. B. G.; Lee, P. C. Measurement Methods for Solubility and Diffusivity of Gases and Supercritical Fluids in Polymers and Its Applications. *Polymer Reviews* 2017, *57* (4), 695–747. DOI: 10.1080/15583724.2017.1329209.
- (238) Utracki, L. A., Ed. *Polymer blends handbook*; Kluwer, 2002.
- (239) Paul, D. R.; Bucknall, C. B., Eds. *Polymer blends*; Wiley, 2000.
- (240) Sundararaj, U.; Macosko, C. W. Drop Breakup and Coalescence in Polymer Blends: The Effects of Concentration and Compatibilization. *Macromolecules* 1995, *28* (8), 2647–2657. DOI: 10.1021/ma00112a009.
- (241) Milner, S. T.; Xi, H. How copolymers promote mixing of immiscible homopolymers. *J. Rheol.* 1996, *40* (4), 663–687. DOI: 10.1122/1.550731.
- (242) Winter, H. H.; Mours, M. The cyber infrastructure initiative for rheology. *Rheol. Acta* 2006, *45* (4), 331–338. DOI: 10.1007/s00397-005-0041-7.
- (243) Poh, L.; Narimissa, E.; Wagner, M. H.; Winter, H. H. Interactive Shear and Extensional Rheology—25 years of IRIS Software. *Rheol. Acta* 2022, *61* (4-5), 259–269. DOI: 10.1007/s00397-022-01331-6.
- (244) Rumble, J. R.; Bruno, T. J.; Doa, M. J., Eds. *CRC handbook of chemistry and physics: A ready-reference book of chemical and physical data*, 101st edition, 2020-2021; CRC Press Taylor & Francis Group, 2020.
- (245) Tsivintzelis, I.; Angelopoulou, A. G.; Panayiotou, C. Foaming of polymers with supercritical CO<sub>2</sub>: An experimental and theoretical study. *Polymer* 2007, *48* (20), 5928–5939. DOI: 10.1016/j.polymer.2007.08.004.
- (246) Chen, X.; Feng, J. J.; Bertelo, C. A. Plasticization effects on bubble growth during polymer foaming. *Polym. Eng. Sci.* 2006, *46* (1), 97–107. DOI: 10.1002/pen.20434.
- (247) Wypych, G. *Handbook of foaming and blowing agents*, Second edition; ChemTec Publishing, 2022.





---

## LIST OF FIGURES

Figure 1.1. Dissertation outline: Investigation of the three stages of physical polymer foaming: (1) nucleation, (2) expansion, and (3) stabilization using well-defined, tailor-made polymer model systems synthesized by living anionic polymerization. ....	4
Figure 2.1. a) Tetrakaidekahedron structure of four cells of the Kelvin foam, resulting in a total of 14 neighboring cells. b) Eight cells, distorted dodecahedrons, and irregular tetradecahedrons form the Weaire-Phelan foam. This fundamental unit, on average, 13.5 neighboring cells, lowers the surface by 0.3 % (adapted and modified from literature <sup>26</sup> ). ....	8
Figure 2.2. Examples of the two basic foam structures: Open- (a) and closed-cell foam (b). Open-cell foams can be found in membranes, sponged, or cushions/mattresses. Closed-cell foams are used for lightweight constructions or insulations (adapted and updated from literature <sup>34</sup> ). ....	9
Figure 2.3. Scheme of the physical foaming process with its four stages, i.e., saturation, nucleation, growth, and stabilization. *To illustrate the process, the CO <sub>2</sub> -cells are shown oversized concerning the polymer matrix in the nucleation stage. ....	10
Figure 2.4. Comparison of the temperature-dependent solubility of carbon dioxide CO <sub>2</sub> and nitrogen N <sub>2</sub> in PS at a saturation pressure of about 120 bar. Adapted from literature. <sup>33</sup> ....	12
Figure 2.5. Dependency of cell nucleation and growth to Gibb's free energy barrier of homogeneous and heterogeneous nucleation ( $G_{hom}$ , $G_{het}$ ). By overcoming the corresponding free energy, stable cells with the radius $r$ are formed, which continue to growth via CO <sub>2</sub> -diffusion. Cells with $r < r^*$ collapse and the CO <sub>2</sub> lead to further growth of cells that have already exceeded $r^*$ . The red line describes the surface term and the blue line is the volume term.....	14
Figure 2.6. Heterogeneous nucleation occurs at the surface of a nucleating agent. ....	15
Figure 2.7. Illustration of the continuous increase of the elongation viscosity $\eta_E^+$ of a PS melt due to the time-dependent loss of the blowing agent CO <sub>2</sub> . The solid line represents the superposition effect of CO <sub>2</sub> -loss, i.e., phase separation and onset of strain hardening as a function of time $t$ . Adapted from literature. <sup>33</sup> ....	17
Figure 3.1. Graphical illustration of a simple shear experiment in a linear direction of motion. A material, e.g., a polymer melt, is placed between two parallel plates and deformed. <sup>91,92</sup> ....	19
Figure 3.2. Schematic representation of the Hookean spring model (a) for ideal elastic solids, where the periodic excitation and response are in the same phase with a phase difference of $\Delta\delta = 0^\circ$ (b). <sup>92</sup> ....	20
Figure 3.3. Schematic representation of the Newtonian dashpot model (a) for ideal viscous solids, where the periodic excitation and response exhibit a phase shift of $\delta = 90^\circ$ (b). <sup>92</sup> ....	20
Figure 3.4. Schematic representation of viscoelastic response by combining Hooke's and Newton's law, i.e., spring and dashpot model, in a parallel or serial alignment. (a) Kelvin-Voigt model for elastic solids with low viscous part and (b) Maxwell model for viscous fluids with low elastic part. <sup>89</sup> ....	21
Figure 3.5. Frequency dependence of the shear moduli ( $G'$ (green) and $G''$ (black)) of a linear monodisperse homopolymer melt and the four zones of the resulting master curve: (I) viscoelastic regime, (II) rubber plateau, (III) transition zone, and (IV) glass region. ....	24
Figure 3.6. Frequency-dependent moduli calculated by the Maxwell model. On the left side of the cross over $G' \propto \omega^2$ and $G'' \propto \omega^1$ . The cross over indicates the longest relaxation time $\tau_l$ . ....	25
Figure 3.7. Transient elongation experiment of a cylindrical sample. The sample is uniformly deformed in $x$ direction by $2 \times \Delta L$ with a constant force $F$ applied to both sample ends. <sup>90</sup> ....	27
Figure 3.8. Transient shear viscosity $\eta_S^+$ and elongation viscosity $\eta_E^+$ of a viscoelastic polymer melt at different shear $\gamma$ and elongation Hencky strain rates $\epsilon_H$ . The strain hardening factor is quantified	

by the ratio of the maximum measured $\eta_{E,max}^+(t, \varepsilon_H)$ (blue line) and the theoretical viscoelastic linear response predicted by the Doi-Edwards model $\eta_{E,DE}^+(\varepsilon_H)$ (red line), which is introduced in Chapter 3.3. ....	28
Figure 4.1. Examples of monomers suitable for living anionic polymerization. <sup>132</sup> .....	34
Figure 4.2. Impact of substituents (-R) on the reactivity of vinyl monomers according to a decreasing stabilization of the carbanions, i.e., -I/-M-effect. <sup>136</sup> .....	34
Figure 4.3. Character of ion pair interaction between polymer anions and metal counterions. ....	36
Figure 4.4. Initiation of styrene with sodium naphthalene (NaNp) by electron transfer. ....	36
Figure 4.5. Initiation of styrene with <i>s</i> -butyl lithium ( <i>s</i> -BuLi). ....	36
Figure 4.6. Chain propagation by monomer addition at the example of PS. ....	37
Figure 4.7. Induced termination of the living anionic PS chains by adding a protonic substance such as methanol (MeOH). ....	37
Figure 4.8. Examples of termination and functionalization of chain ends by reaction with oxygen via dimerization (a), carbon dioxide via nucleophilic addition (b), or ethylene oxide via ring-opening (c). ....	38
Figure 4.9. Microstructures of polyisoprene (PI). ....	39
Figure 4.10. a) Phase diagram of PS- <i>b</i> -PI diblock <sup>165</sup> and PS- <i>b</i> -PI- <i>b</i> -PS triblock <sup>161</sup> copolymers with BCC (spheres, <b>S</b> ), hexagonal (cylinders, <b>C</b> ), gyroid ( <b>G</b> ), or lamellar ( <b>L</b> ) microphase morphologies. Adapted with permission from literature. <sup>162</sup> b) Schematic representation of the resulting morphologies at $P_n \chi = 30$ ; dark zones correspond to the volume fraction of PS (A).....	40
Figure 4.11. Examples of different polymer architectures including a) ring, b) star, c) H-polymer, d) pom-pom, e) comb, f) dendritic, and g) barbwire structures. ....	41
Figure 5.1. Three-dimensional representation of ideal spheres (a), cylinders (b), and lamellar (c) microdomain morphology. Furthermore, the diameter $d_0$ of the dispersed phase, the periodicity $L_0$ and the crystallographic vector of the unit cell $B_0$ are labeled. ....	47
Figure 5.2. Sequential living anionic polymerization of styrene and isoprene to a PS- <i>b</i> -PI- <i>b</i> -PS (SIS) triblock copolymer. The monomers are added reverse order to synthesize the ISI triblock sequence. Diblock copolymers are obtained by terminating the anions after polymerization of the second block. ....	48
Figure 5.3. a) Example of an azimuthally averaged <sup>1</sup> D plot of the scattering intensity for an ISI triblock copolymer. b) Domain size $d_0$ as a function of the weight average molecular weight $M_w$ of di- and triblock copolymers with $\phi_{PI} = 10$ mol%, resulting in spherical microdomains, and c) as a function of the PI-content, each block copolymer with $M_w \approx 400$ kg mol <sup>-1</sup> . Additional data from the literature are included in b), marked with open symbols. <sup>162</sup> (Dashed) lines in b) and c) are guides for the eyes. ....	49
Figure 5.4. SEM images of PS- and PI-based di- and triblock copolymer foams. The PI-content increases from $\phi_{PI} = 10$ mol% to 40 mol%, resulting in spherical ( <b>S</b> ), cylindrical ( <b>C</b> ), and lamellar ( <b>L</b> ) morphologies of the microdomains. Blends based on PS and PI with similar comonomer content (top row) serve as reference samples. The scaling bar is valid for each image within this figure. Foaming conditions: $T_f = 80$ °C, $p = 500$ bar, $t_{sat} = 8$ h, and $dp/dt \approx 200$ bar s <sup>-1</sup> .....	51
Figure 5.5. Cell density $N$ as a function of the foaming temperature $T_f$ for SIS triblock copolymers with $\phi_{PI} = 10$ mol% – 40 mol% of PI, resulting in spherical ( <b>S</b> ), cylindrical ( <b>C</b> ), and lamellar ( <b>L</b> ) microdomains, respectively. Each sample has a weight average molecular weight of around $M_w \approx 400$ kg mol <sup>-1</sup> . The domain sizes vary between 25.6 nm and 33.7 nm. Foaming conditions: ..... $T_f = 60$ °C – 120 °C, $p = 500$ bar, $t_{sat} = 8$ h, and $dp/dt \approx 200$ bar s <sup>-1</sup> .....	53
Figure 5.6. Cell density $N$ as a function of the foaming temperature $T_f$ (a) and cell size $D$ as a function of the foam density $\rho_f$ (b) for SIS triblock copolymers with $M_w = 200$ kg mol <sup>-1</sup> to	

1,000 kg mol <sup>-1</sup> and a spherical morphology of the microdomains ( $\phi_{\text{PI}} = 10$ mol% PI). The domain sizes vary between 16.8 nm to 42.8 nm. Foaming conditions: $T_f = 60$ °C – 120 °C, $p = 500$ bar, $t_{\text{sat}} = 8$ h, and $dp/dt \approx 200$ bar s <sup>-1</sup> . .....	54
Figure 5.7. Comparison of the resulting cell density $N$ of foamed PS- and PI-based di- and triblock copolymers with a spherical microdomain morphology ( $\phi_{\text{PI}} = 10$ mol%) at temperatures between 60 °C and 120 °C. Each block copolymer has a molecular weight of around $M_w \approx 400$ kg mol <sup>-1</sup> . Foaming conditions: $T_f = 60$ °C – 120 °C, $p = 500$ bar, $t_{\text{sat}} = 8$ h, and $dp/dt \approx 200$ bar s <sup>-1</sup> . .....	55
Figure 5.8. The illustration of heterogeneous CO <sub>2</sub> -solubility (a) and heterogeneous chain mobility (b) are both exemplarily shown in spherical microdomains. For instance, PS- <i>b</i> -PMMA and PS- <i>b</i> -PI can be used as polymeric model systems to investigate the impact of solubility and mobility, respectively. ....	57
Figure 5.9. Sequential living anionic polymerization of styrene (S) and methyl methacrylate (MMA) to a PS- <i>b</i> -PMMA (SMMA) diblock copolymer.....	58
Figure 5.10. SEM images of SI and SMMA diblock copolymers with spherical (S), cylindrical (C), and lamellar (L) morphology. The scaling bar is valid for each image within this figure. Foaming conditions: $T_f = 120$ °C, $p = 500$ bar, $t_{\text{sat}} = 8$ h, and $dp/dt \approx 200$ bar s <sup>-1</sup> .....	59
Figure 5.11. Cell density $N$ as a function of the foaming temperature $T_f$ for SI (a) and SMMA (b) diblock copolymers with $M_w \approx 400$ kg mol <sup>-1</sup> and $\phi_{\text{PI,PMMA}} = 10$ mol% – 40 mol%, resulting in spheres (S), cylinders (C), or lamellas (L), respectively. Foaming conditions: $T_f = 60$ °C – 120 °C, $p = 500$ bar, $t_{\text{sat}} = 8$ h, and $dp/dt \approx 200$ bar s <sup>-1</sup> . .....	59
Figure 5.12. Cell density $N$ as a function of the comonomer content $\phi_{\text{PI,PMMA}}$ of SI- and SMMA-based foams. Foaming conditions: $T_f = 100$ °C (a) and 120 °C (b), $p = 500$ bar, $t_{\text{sat}} = 8$ h, and $dp/dt \approx 200$ bar s <sup>-1</sup> . The number above the bars correspond to the average cell size in $\mu\text{m}$ . .....	60
Figure 5.13. SEM images of PS- and PI-based di- and triblock copolymers with $M_w = 400$ kg mol <sup>-1</sup> and $\phi_{\text{PI}} = 10$ mol% with a spherical (S) morphology and PS301k with added SiO <sub>2</sub> -based nanoparticles with $d_{\text{SiO}_2} \approx 80$ nm and $w_{\text{SiO}_2} = 0.25 - 1.00$ wt%. The scaling bar is valid for each image within this figure. Foaming conditions: $T_f = 80$ °C, $p = 500$ bar, $t_{\text{sat}} = 8$ h, and $dp/dt \approx 200$ bar s <sup>-1</sup> .....	62
Figure 5.14. Cell density $N$ as a function of the foaming temperature $T_f$ for PS-, PI- and PMMA-based block copolymers (a) and PS with an increasing weight percentage from $w = 0.25 - 1$ wt% of nucleation particles (b). The samples listed were selected according to their maximum achieved $N$ . Foaming conditions: $T_f = 60$ °C – 130 °C, $p = 500$ bar, $t_{\text{sat}} = 8$ h, and $dp/dt \approx 200$ bar s <sup>-1</sup> . .....	62
Figure 6.1. The synthesis procedure of low-disperse PS pom-poms is exemplary outlined using the following molecular parameters: $M_{w,b} = 100$ kg mol <sup>-1</sup> , $M_{w,a} = 50$ kg mol <sup>-1</sup> and $q = 2 \times 14$ . 1) Living anionic polymerization of an ISI triblock copolymer as backbone, 2) epoxidation of the double bonds within the PI-blocks via Prileschajew reaction, 3) Living anionic polymerization of PS sidearms, 4) grafting of living sidearms onto the epoxidized ISI-precursor.....	68
Figure 6.2. Pom-pom master curves; series: Q <sub>scb</sub> (a), Q <sub>lcb</sub> (b), A (c), and B (d) at $T_{\text{ref}} = 160$ °C. The rheological response shows three characteristic regimes with increasing angular frequency: the flow behavior of the whole molecule in the terminal regime ( $G' \propto \omega^2$ , $G'' \propto \omega^1$ ), the backbones' relaxation process, and the rheological influence of the sidearms at $a_T \omega < 10^3$ rad s <sup>-1</sup> . The master curves were vertically shifted by a factor of 10 <sup>2</sup> , for instance, in a) 10 <sup>2</sup> , 10 <sup>4</sup> , 10 <sup>6</sup> , and 10 <sup>8</sup> . .....	70
Figure 6.3. Sidearm relaxation time $\tau_a$ is presented as a function of the weight average molecular weight of the side arms $M_{w,a}$ at a reference temperature of $T_{\text{ref}} = 160$ °C. The black solid line represents a non-linear least-square fit according to a simple power-law, where $M_{w,a}$ is given in g mol <sup>-1</sup> (prefactor = $4.7 \times 10^{-14}$ , scaling exponent = 3.4). .....	72

Figure 6.4. The absolute complex viscosity $ \eta^* $ as a function of the angular frequency $a_T\omega$ at a reference temperature of $T_{\text{ref}} = 160$ °C. The solid lines represent the fitting with the multi-mode Maxwell model (10 modes). .....	72
Figure 6.5. The zero-shear viscosity $\eta_0$ as a function of the total weight average molecular weight $M_{w,t}$ of pom-pom PS at $T_{\text{ref}} = 160$ °C. Samples with the same symbol have the same $q$ and the same color represents similar $M_{w,a}$ . The closed symbols represent pom-poms with $M_{w,b} = 100$ kg mol <sup>-1</sup> , and the half-open symbols pom-poms with $M_{w,b} = 220$ kg mol <sup>-1</sup> and 400 kg mol <sup>-1</sup> . The grey squares are associated with linear PS references with $M_{w,b} = 100$ kg mol <sup>-1</sup> and 310 kg mol <sup>-1</sup> . The dashed grey line corresponds to the predicted $\eta_0$ of linear PS with increasing molecular weights in g mol <sup>-1</sup> and scales with $\eta_0 \sim M_w^{3.4}$ (prefactor = $3.31 \times 10^{-13}$ ). The dotted gray lines are guides for the eyes. ....	73
Figure 6.6. a) Viscosity growth curves of 400k–2×9–23k measured at elongation strain rates $\varepsilon = 0.03$ s <sup>-1</sup> – 10 s <sup>-1</sup> at $T_{\text{ref}} = 160$ °C. Dashed and dotted lines represent the linear viscoelastic (LVE) regime and the Doi-Edwards (DE) model, respectively. <sup>114,119,120</sup> Maximum strain hardening factor $SHF_{\text{max}} = \eta E, \max + (t, \varepsilon H)/\eta E, \text{DE} + (\varepsilon H)$ in the strain rate range of $\varepsilon = 1$ s <sup>-1</sup> to 10 s <sup>-1</sup> as a function of the respective topological parameter measured at 160 °C. The influence of $q$ (series Q), $M_{w,a}$ (series A), and $M_{w,b}$ (series B) on the $SHF_{\text{max}}$ are shown in b) – d), respectively. The grey square represents the linear PS reference. All samples displaying elastic rupture are marked with “er”. .....	74
Figure 6.7. SEM images of PS pom-pom foams with $M_{w,a} \approx 25$ kg mol <sup>-1</sup> ( $Q_{a,s}$ ), or $M_{w,a} \approx 110$ kg mol <sup>-1</sup> ( $Q_{a,l}$ ), $q = 2 \times 5 - 2 \times 22$ , and $M_{w,b} = 100$ kg mol <sup>-1</sup> . The scaling bar is valid for each image within this figure. Foaming conditions: $T_f = 140$ °C, $p = 500$ bar, $t_{\text{sat}} = 8$ h, and $dp/dt \approx 200$ bar s <sup>-1</sup> . ....	76
Figure 6.8. Average cell size $D$ and volume expansion ratio $VER$ as a function of the number of sidearms $q$ of $Q_{a,s}$ (a), b), $M_{w,a} \approx 25$ kg mol <sup>-1</sup> ) and $Q_{a,l}$ (c), d), $M_{w,a} \approx 110$ kg mol <sup>-1</sup> ). The molecular weight of the backbone was constant at $M_{w,b} = 100$ kg mol <sup>-1</sup> and $q$ increases continuously from $q = 2 \times 5 - 2 \times 22$ . Lines are guides for the eyes. Foaming conditions: $T_f = 100$ °C – 140 °C, $p = 500$ bar, $t_{\text{sat}} = 8$ h, and $dp/dt \approx 200$ bar s <sup>-1</sup> . ....	77
Figure 6.9. SEM images of PS pom-pom foams of series A with $M_{w,b} = 100$ kg mol <sup>-1</sup> , $q \approx 2 \times 12$ , and $M_{w,a} = 9$ kg mol <sup>-1</sup> , 50 kg mol <sup>-1</sup> , and 300 kg mol <sup>-1</sup> . The scaling bar is valid for each image within this figure. Foaming conditions: $T_f = 100$ °C and 140 °C, $p = 500$ bar, $t_{\text{sat}} = 8$ h, and $dp/dt \approx 200$ bar s <sup>-1</sup> . ....	78
Figure 6.10. Average cell diameter $D$ (a) and volume expansion ratio $VER$ (b) of series A ( $M_{w,b} = 100$ kg mol <sup>-1</sup> , $q \approx 2 \times 12$ , and $M_{w,a} = 9 - 300$ kg mol <sup>-1</sup> ). Lines are guides for the eyes. Foaming conditions: $T_f = 100$ °C – 140 °C, $p = 500$ bar, $t_{\text{sat}} = 8$ h, and $dp/dt \approx 200$ bar s <sup>-1</sup> . ....	79
Figure 6.11. Two magnifications of SEM images based on foamed pom-poms with a backbone length of $M_{w,b} = 100$ kg mol <sup>-1</sup> , 220 kg mol <sup>-1</sup> and 400 kg mol <sup>-1</sup> . Each sample with $q = 2 \times 9$ and $M_{w,a} \approx 25$ kg mol <sup>-1</sup> . The scaling bars are valid for each image within this figure. Foaming conditions: $T_f = 140$ °C, $p = 500$ bar, $t_{\text{sat}} = 8$ h, and $dp/dt \approx 200$ bar s <sup>-1</sup> . ....	80
Figure 6.12. Volume expansion ratio $VER$ (a), average cell size $D$ (b) and cell wall thickness $d$ (c) of PS pom-poms as a function of an increasing backbone length from $M_{w,b} = 100$ kg mol <sup>-1</sup> to 400 kg mol <sup>-1</sup> . Each sample with $q = 2 \times 9$ and $M_{w,a} \approx 25$ kg mol <sup>-1</sup> . Foaming conditions: $T_f = 100$ °C – 140 °C, $p = 500$ bar, $t_{\text{sat}} = 8$ h, and $dp/dt \approx 200$ bar s <sup>-1</sup> . ....	81
Figure 6.13. Volume expansion ratio $VER$ vs. average cell size $D$ foamed at a) 100 °C, b) 120 °C, c) 130 °C, and d) 140 °C. Foaming conditions: $p = 500$ bar, $t_{\text{sat}} = 8$ h, and $dp/dt \approx 200$ bar s <sup>-1</sup> . ....	82
Figure 6.14. Overview of the foam expansion, i.e., $VER$ , at $T_f = 140$ °C as a function of the rheological parameter, i.e., $SHF_{\text{max}}$ (a) and $\eta_0$ (b), at $T = 160$ °C for the whole sample set. Foaming conditions: $p = 500$ bar, $t_{\text{sat}} = 8$ h, and $dp/dt \approx 200$ bar s <sup>-1</sup> . ....	85
Figure 6.15. Correlation of the rheological parameter, i.e., $SHF$ and $\eta_0$ , and the foaming behavior, i.e., $D$ and $VER$ , as function of the total molecular weight $M_{w,t}$ for samples with $M_{w,b} = 100$ kg mol <sup>-1</sup> ,	

$M_{w,a} = 7 - 300 \text{ kg mol}^{-1}$ and $q = 2 \times 5 - 2 \times 22$ . Rheological properties were measured or referenced to $T = 160 \text{ }^\circ\text{C}$ and correlated to the foaming behavior at $T_f = 140 \text{ }^\circ\text{C}$ ; the $SHF$ was quantified at $\varepsilon = 1 \text{ s}^{-1}$ . Solid lines are to guide the eye. All samples in the grey area marked with half-open symbols undergo elastic rupture during elongational flow. Foaming conditions: $p = 500 \text{ bar}$ , $t_{\text{sat}} = 8 \text{ h}$ , and $dp/dt \approx 200 \text{ bar s}^{-1}$ .....	86
Figure 6.16. Synthesis of barbwires with four connected stars ( $s = 4$ ) by combining living anionic polymerization, epoxidation, and grafting-onto methodology. The exemplarily shown sample has a backbone length of $M_{w,b} = 382 \text{ kg mol}^{-1}$ , sidearm length of $M_{w,a} = 27 \text{ kg mol}^{-1}$ , and the number of sidearms is around $q \approx 12$ per star. Depending on $s$ , the number of PS- and PI-blocks increases from only one PI-block for the star ( $s = 1$ ) up to ISISISI for the barbwire structure with $s = 4$ . The yellow marked area represents the linking spot with the bifunctional linker $\alpha, \alpha'$ -dibromo- <i>p</i> -xylene. ....	88
Figure 6.17. Two linear PS references with a molecular weight of $100 \text{ kg mol}^{-1}$ and $310 \text{ kg mol}^{-1}$ ( $s = 0$ ), one star ( $s = 1$ ), two pom-poms ( $s = 2$ , 2-star-short with $M_{w,b} = 100 \text{ kg mol}^{-1}$ and 2-star-long with $M_{w,b} = 280 \text{ kg mol}^{-1}$ ), and barbwire topologies ( $s = 3, 4$ ) with increasing amount of covalently connected stars $s$ with a linear PS chain with $M_{w,PS} \approx 90 \text{ kg mol}^{-1}$ . Grey and red lines correspond to PS and PI, respectively.....	89
Figure 6.18. In a) master curves of the linear PS references and branched samples are shown at a reference temperature of $T_{\text{ref}} = 180 \text{ }^\circ\text{C}$ , indicating an asymptotic behavior in the flow region according to the Maxwell model. The master curves are vertically shifted by $10^2$ , $10^4$ , and $10^6$ . In b) is the average longest relaxation time $\tau_l$ plotted against the total weight average molecular weight $M_{w,t}$ at $T_{\text{ref}} = 180 \text{ }^\circ\text{C}$ . The black solid line represents a non-linear least-square fit according to a simple power-law, where $M_{w,t}$ is given in $\text{g mol}^{-1}$ (prefactor = $1 \times 10^{-20}$ , scaling exponent = 3.4)....	90
Figure 6.19. The van Gurp-Palmen (vGP) plot of the branched samples with $s = 1 - 4$ , $M_{w,a} \approx 25 \text{ kg mol}^{-1}$ and $q \approx s \times 11$ . and the two linear PS references at $T_{\text{ref}} = 180 \text{ }^\circ\text{C}$ .....	91
Figure 6.20. a) The absolute complex viscosity $ \eta^* $ as a function of the angular frequency $a_T \omega$ at a reference temperature of $T_{\text{ref}} = 180 \text{ }^\circ\text{C}$ . The solid lines represent the fitting with the multi-mode Maxwell model (10 modes). b) The zero-shear viscosity $\eta_0$ as a function of the total weight average molecular weight $M_{w,t}$ . The grey dashed line represents the prediction for linear PS from literature and scales with $\eta_0 \approx M_w^{3.4}$ (prefactor = $3.31 \times 10^{-14}$ ). <sup>237</sup> The solid black line represents a non-linear least-square fit according to a simple power-law, where $M_{w,t}$ is given in $\text{g mol}^{-1}$ (prefactor = $1 \times 10^{-19}$ , and scaling exponent = 3.7). The grey-dotted horizontal lines are to guide the eyes. ....	92
Figure 6.21. a) Viscosity growth curves of the 4-star measured at elongation strain rates $\varepsilon$ ranging from $0.03 \text{ s}^{-1}$ to $10 \text{ s}^{-1}$ at $T_{\text{ref}} = 180 \text{ }^\circ\text{C}$ . Dashed and dotted lines represent the linear viscoelastic (LVE) regime and the Doi-Edwards (DE) model, respectively. <sup>114,119,120</sup> b) Strain hardening factors $SHF$ of all samples as a function of the elongation strain rate $\varepsilon$ . As the elongational viscosity of both, the star ( $s = 1$ ) and the short linear PS100k reference, was too low, and therefore, the elongation viscosity could not be measured; no data are included in the graph. The lines are guides to the eyes. ....	93
Figure 6.22. SEM images of the linear PS reference PS310k and the branches samples with $s = 1 - 4$ , $M_{w,a} \approx 25 \text{ kg mol}^{-1}$ and $q \approx s \times 11$ . The scaling bar is valid for each image within this figure. Foaming conditions: $T_f = 100 \text{ }^\circ\text{C}$ and $140 \text{ }^\circ\text{C}$ , $p = 500 \text{ bar}$ , $t_{\text{sat}} = 8 \text{ h}$ , and $dp/dt \approx 200 \text{ bar s}^{-1}$ .....	94
Figure 6.23. Volume expansion ratio $VER$ (a) and average cell diameter $D$ (b) as a function of the number of connected stars $s$ . Foaming conditions: $T_f = 100 \text{ }^\circ\text{C} - 140 \text{ }^\circ\text{C}$ , $p = 500 \text{ bar}$ , $t_{\text{sat}} = 8 \text{ h}$ , and $dp/dt \approx 200 \text{ bar s}^{-1}$ .....	95
Figure 7.1. Living anionic polymerization of styrene and styrene derivatives resulting in PS (a), P2VN (b), PVBP (c), and P $\alpha$ MS (d).....	98

Figure 7.2. Desorption curves of CO <sub>2</sub> out of PS and PαMS at $T_{\text{sat}} = 23$ °C and $p = 500$ bar, to measure the mass uptake of blowing agent. Samples were saturated with the blowing agent for 24 h. The maximum amount of dissolved CO <sub>2</sub> within the polymer matrices is marked in red. ....	99
Figure 7.3. The absolute complex viscosity $ \eta^* $ as a function of the angular frequency $a_T\omega$ at a reference temperature of $T_{\text{ref}} = T_g + 50$ °C. The solid lines represent the fitting with the multi-mode Maxwell model (10 modes). ....	99
Figure 7.4. SEM images of foams based on linear PS, P2VN, PVBP, and PαMS. The scaling bar is valid for each image within this figure. Foaming conditions: $T_f \approx T_g$ , $p = 500$ bar, $t_{\text{sat}} = 8$ h, and $dp/dt \approx 200$ bar s <sup>-1</sup> . ....	100
Figure 7.5. Cellular morphology, i.e., $VER$ (a), $N$ (b) and $D$ (c) as a function of the temperature difference concerning the individual glass transition temperature and the foaming temperature. Experiments at $T_f > 190$ °C could not be performed due to device limitations. Foaming conditions: $T_f - T_g$ , $p = 500$ bar, $t_{\text{sat}} = 8$ h, and $dp/dt \approx 200$ bar s <sup>-1</sup> . ....	100
Figure 7.6. Effect of glass transition temperature $T_g$ on the cell density $N$ (a) and the average cell size $D$ (b) using PS, P2VN, PVBP, and PαMS. Foaming conditions: $T_f = 130$ °C, $p = 500$ bar, $t_{\text{sat}} = 8$ h, and $dp/dt \approx 200$ bar s <sup>-1</sup> . ....	101
Figure 8.1. Summary of the resulting cell morphologies obtained using PS-based model systems studied within this dissertation. Cell size $D$ as a function of volume expansion ratio $VER$ ; Foaming conditions: $p = 500$ bar, $t_{\text{sat}} = 8$ h, $dp/dt \approx 200$ bar s <sup>-1</sup> , and $T_f = 60$ °C – 150 °C. ....	106
Figure 8.2. Outlook: The knowledge gained within the individual studies should be used to modify the model systems further and verify their influence on the mechanical stability of the foams. ...	107
Figure B.1. <sup>1</sup> H-NMR spectra of an epoxidized ISI backbone precursor. The chemical shift of the double bond peak is around 5.13 ppm, and the one of the epoxide is around 2.71 ppm. ....	115
Figure B.2. Thermogravimetric curve of the linear reference PS310k and the pom-pom-shaped PS 100k-2×12-300k of series A under N <sub>2</sub> atmosphere. The heating rate was 10 K min <sup>-1</sup> . ....	116
Figure C.1. Example of an on-isothermal measurement of a phase separated ISI triblock copolymer with a heating rate of 10 °C min <sup>-1</sup> (exo up). The glass transition temperature of PI is around $T_{g,PI} \approx -70$ °C and the one of PS around $T_{g,PS} \approx 100$ °C. ....	121
Figure C.2. Elution chromatograms of the purified pom-poms, the linear ISI-precursor, and the linear PS references detected by SEC-DRI. After three purification steps, the amount of residual sidearms varies from 2 – 13 % over the entire set of PS pom-poms. ....	124
Figure C.3. Elution chromatograms of the purified barbwires with increasing $s$ from one to four, and the linear PS reference detected by SEC-DRI. After three purification steps, the amount of residual arms is less than 7 % over the entire sample set. ....	128
Figure C.4. Molecular weight distribution of linear PS, P2VN, PVBP and PαMS detected by SEC-DRI. ....	130
Figure C.5. Non-isothermal DSC-curves of the linear PS and PS derivatives P2VN, PVBP, and PαMS with $M_w \approx 300$ kg mol <sup>-1</sup> , measured with a heating rate of 10 °C min <sup>-1</sup> under nitrogen flow within a temperature range of $T = 80 - 200$ °C, depending on polymer dynamics. ....	130

---

## LIST OF TABLES

Table 2.1. Characteristics of different foam types according to their cell morphology. <sup>2</sup> .....	9
Table 3.1. Scaling laws for the molecular weight dependence of the zero-shear viscosity $\eta_0$ and related relaxation modes of a polymer with a weight average molecular weight of $M_w$ . <sup>89,97</sup> .....	25
Table 5.1. Molecular characteristics of the PS and PI blends, di- and triblock copolymers. <sup>162</sup> .....	48
Table 5.2. Molecular characteristics of the investigated PS- <i>b</i> -PI <sup>162</sup> and PS- <i>b</i> -PMMA diblock copolymers. ....	58
Table 6.1. Molecular characteristics of the PS pom-poms, linear ISI-precursor, and PS references. ....	69
Table 6.2. Overview of the impact of the topological parameter of the pom-pom topology, i.e. $M_{w,b}$ , $M_{w,a}$ and $q$ on the melt rheological properties ( $\eta_0$ , SHF) at $T = 160$ °C and the cellular structure of the foams at $T_f = 140$ °C. ....	84
Table 6.3. Molecular characteristics of the PS pom-poms and barbwires, linear ISI-precursor, and PS references. ....	90
Table 7.1. Molecular characteristics of the linear PS and its derivatives P2VN, PVBP, and P $\alpha$ MS. ....	98
Table 8.1. Summary of the investigated influencing parameters and the combination of these towards an optimized structure-property relationship regarding the resulting cellular morphology.....	106
Table B.1. Characteristic reflections of different microphase symmetries. <sup>150</sup> .....	117
Table C.1. Statistical cellular parameters, i.e., foam density $\rho_f$ , volume expansion ratio $VER$ , average cell size $D$ , cell density $N$ of block copolymer and PS+SiO <sub>2</sub> -based foams. Physical foaming experiments were performed at $p = 500$ bar, $\Delta p/\Delta t \approx 200$ bar s <sup>-1</sup> , and $T_f = 60$ °C – 140 °C.....	121
Table C.2. WLF parameter and zero-shear viscosity $\eta_0$ of the PS pom-poms and the linear PS references at $T_{ref} = 160$ °C.....	124
Table C.3. Overview of the reached strain hardening factors $SHF$ measured at $T = 160$ °C at strain rates ranging from $\dot{\epsilon} = 0.01 - 10$ s <sup>-1</sup> . ....	125
Table C.4. Statistical cellular parameters, i.e., foam density $\rho_f$ , volume expansion ratio $VER$ , average cell size $D$ , cell density $N$ , and cell wall thickness $d$ of the samples. Physical foaming experiments were performed at $p = 500$ bar, $\Delta p/\Delta t \approx 200$ bar s <sup>-1</sup> , and $T_f = 100$ °C – 150 °C. ....	126
Table C.5. WLF parameter, zero-shear viscosity $\eta_0$ , and the glass transition temperature $T_g$ of all the PS star, the PS barbwires, and the linear PS references at $T_{ref} = 180$ °C. ....	128
Table C.6. Overview of the reached $SHF$ measured at 180 °C at strain rates ranging from $\dot{\epsilon} = 0.03$ s <sup>-1</sup> – 10 s <sup>-1</sup> .....	128
Table C.7. Statistical cellular parameters, i.e., foam density $\rho_f$ , volume expansion ratio $VER$ , average cell size $D$ , and cell density $N$ of the resulting foams. Physical foaming experiments were performed at $p = 500$ bar, $\Delta p/\Delta t \approx 200$ bar s <sup>-1</sup> , and $T_f = 100$ °C – 150 °C. ....	129
Table C.8. Statistical cellular parameters, i.e., foam density $\rho_f$ , volume expansion ratio $VER$ , average cell size $D$ , and cell density $N$ of the resulting foams. Physical foaming experiments were performed at $p = 500$ bar, $\Delta p/\Delta t = 200$ bar s <sup>-1</sup> , and $\Delta T = T_g \pm 40$ °C.....	131





---

## ACRONYMS AND ABBREVIATIONS

$\Delta E_D$	Activation energy of diffusion	$m'$	Mass of a gas molecule
$\Delta G$	Gibbs free energy	MAM	Poly(methyl methacrylate)-b-poly(butyl acrylate)-b-poly(methyl methacrylate)
$\Delta H_L$	Solution enthalpy		
$A_{\text{cell}}$	Cell surface	$M_c$	Critical molecular weight
$a_T$	Horizontal shifting factor	$M_n$	Number average molecular weight
ATRP	Atom transfer radical polymerization	MSF	Molecular stress function
$B_0$	Crystallographic vector of unit cell	$M_w$	Mass average molecular weight
$b_T$	Vertical shift factor	$N$	Cell density
C	Cylinders	$n$	Number of cells
CNT	Classical nucleation theory	N <sub>2</sub>	Nitrogen, Nitrogen
CO <sub>2</sub>	Carbon dioxide	NMP	Nitroxide-mediated polymerization
$D$	Cell size, Diffusion coefficient or diffusivity	O <sub>2</sub>	Oxygen
$d$	Cell wall thickness	$p$	Pressure
$\mathfrak{D}$	Dispersity	$p_c$	Critical pressure
$d_0$	Domain size	PC	Polycarbonate
$D_0$	Maximum diffusion coefficient at infinite temperature	$p_{\text{cell}}$	Cell pressure
DE	Doi-Edwards	PDMS	Poly(dimethyl siloxane)
$F$	Force	PE	Polyethylene
$f$	Volume fraction	PEG	Poly(ethylene glycol)
$F(\theta_c, \beta)$	Geometrical factor	PEP	Ethylene-propylene copolymer
$f_{\text{max}}$	MSF fitting parameter	PET	Poly(ethylene terephthalate)
$G$	Shear modulus	PFMA	Poly(perfluorooctylethyl methacrylate)
$G''$	Loss modulus	PI	Polyisoprene
$G'$	Storage modulus	PLA	Poly(lactic acid)
$g_i$	Partial moduli	$p_{\text{local}}$	Local pressure
$G_N^0$	Plateau modulus	PMMA	Poly(methyl methacrylate)
HDPE	High-density polyethylene	$P_n$	Polymerization degree
HMS-PP	High-melt-strength polypropylene	PP	Polypropylene
ISI	PI- <i>b</i> -PS- <i>b</i> -PI	PPE	Poly(p-phenylene oxide)
$J$	Diffusion flux	PS	Polystyrene
$J_{\text{het}}$	Heterogeneous nucleation rate	$p_{\text{sys}}$	Nucleating agents surface geometry
$J_{\text{hom}}$	Homogeneous nucleation rate	PU	Polyurethane
$k_b$	Boltzmann constant	PVC	Poly(vinyl chloride)
$K_H$	Henry's constant	$q$	Number of sidearms
$L$	Length, lamellar	$Q$	Ratio of the surface area of the heterogeneously nucleated cell to a spherical cell with the same radius of curvature
$L_0$	Periodicity, repeating unit		
LAP	Living anionic polymerization		
LCB	Long-chain branched		
LDPE	Low-density polyethylene		
LVE	Linear viscoelasticity	$r$	Radius

$R$	Universal gas constant	$\beta$	MSF fitting parameter
$r^*$	Critical radius	$\dot{\gamma}$	Shear rate
RAFT	Reversible addition fragmentation chain transfer	$\gamma$	Shear strain or deformation
ROMP	Ring-opening metathesis polymerization	$\gamma_{lg}$	Surface energy, interfacial tension
ROP	Ring-opening polymerization	$\gamma_0$	Deformation amplitude
$s$	Deformation	$\delta$	Phase angle
S	Spheres	$\epsilon_H$	Hencky strain
SAN	Styrene-acrylonitrile resin	$\dot{\epsilon}_H$	Hencky strain rate
SAXS	Small-angle X-ray scattering	$\eta$	Viscosity
SBM	Polystyrene- <i>b</i> -polybutadiene- <i>b</i> -poly(methyl methacrylate)	$\eta_0$	Zero-shear viscosity
scCO <sub>2</sub>	Supercritical carbon dioxide	$\eta_{E,DE}^+$	Transient elongational viscosity by DE prediction
SET-LRP	Single electron transfer living radical polymerization	$\eta_E^+$	Tensile stress growth coefficient, elongational viscosity
SI	PS- <i>b</i> -PI	$\eta_S^+$	Transient shear viscosity
SIS	PS- <i>b</i> -PI- <i>b</i> -PS	$\theta_c$	Contact angle
SMMA	PS- <i>b</i> -PMMA	$\rho_f$	Foam density
$T$	Temperature	$\rho_p$	Polymer density
$t$	Time	$\sigma$	Shear stress
$T_f$	Foaming temperature	$\sigma_{elong}$	Elongational stress, tensile stress
$T_{sat}$	Saturation temperature	$\tau$	Relaxation time
$\tan(\delta)$	Dissipation factor	$\tau_a$	Sidearm relaxation time
$T_c$	Critical temperature	$\tau_b$	Backbone relaxation time
$T_g$	Glass transition temperature	$\tau_i$	Relaxation times
$T_{g,eff}$	Effective glass transition temperature	$\tau_l$	Longest relaxation time
THF	Tetrahydrofuran	$v$	Velocity
$T_{ODT}$	Order-disorder-transition temperature	$\varphi$	Concentration of ideal mixtures
$T_{ref}$	Reference temperature	$\phi$	Molpercentage
TTS	Time-Temperature Superposition	$\Phi_b$	Volume fraction of the backbone segment
$V$	Volume	$\chi$	Flory-Huggins parameter
$V_{cell}$	Cell volume fraction	$\omega$	Excitation frequency
$VER$	Volume expansion ratio		
$W_{het}$	Energy barrier heterogeneous nucleation		
$W_{hom}$	Energy barrier homogeneous nucleation		
WLF	Williams-Landell-Ferry		
$x$	Position		
$Z_a$	Sidearm entanglement number		
$Z_b$	Backbone entanglement number		

---

## CURRICULUM VITAE

Marie-Christin Helena Röpert



### EDUCATION

- 12/2018 – 11/2022    Ph.D. Candidate  
Polymer Materials – Prof. Manfred Wilhelm  
Institute for Chemical Technology and Polymer Chemistry  
Karlsruhe Institute of Technology | Karlsruhe
- 05/2022 – 07/2022    Visiting Researcher  
Microcellular Plastics Manufacturing Laboratory – Prof. Chul B. Park  
Department of Mechanical & Industrial Engineering  
University of Toronto | Toronto
- 09/2016 – 08/2018    Polymer Chemistry | M.Sc  
Best graduate of the academic year, ECTS Grade: A  
Westphalian University of Applied Sciences | Recklinghausen  
University of Duisburg-Essen | Essen
- 09/2013 – 08/2016    Chemistry | B.Sc  
Best graduate of the academic year, ECTS Grade: A  
Westphalian University of Applied Sciences | Recklinghausen
- 09/2004 – 07/2013    General Qualification for University Entrance  
Priv. Gymnasium Schloss Wittgenstein | Bad Laasphe

## WORKING EXPERIENCES

- 12/2022 – today      Product Development Chemist – Adhesive Technologies  
Mobility and Electronics | Automotive Components  
Henkel AG & Co. KGaA | Düsseldorf
- 06/2018 – 08/2018      Research Assistant  
Technical and Macromolecular Chemistry  
Westphalian University of Applied Sciences | Recklinghausen
- 11/2016 – 07/2017      Research Assistant  
Organic Chemistry and Polymers  
Westphalian University of Applied Sciences | Recklinghausen
- 04/2016 – 09/2016      Internship, Bachelor-Thesis  
Chemical Catalysis  
Covestro Deutschland AG | Leverkusen
- 10/2015 – 01/2016      Mathematics Tutor  
Westphalian University of Applied Sciences | Recklinghausen
- 10/2015 – 01/2016      Student Assistant  
Analytical Chemistry and Plastics  
Westphalian University of Applied Sciences | Recklinghausen
- 08/2014 – 09/2014      Internship  
Robotchemie E. Weischenberg Nachf. GmbH & Co. KG | Gelsen-  
kirchen
- 04/2014 – 08/2015      Student Assistant  
Physics and Physical Chemistry  
Westphalian University of Applied Sciences | Recklinghausen
- 08/2013 – 08/2013      Internship  
W. Bosch GmbH + Co. KG, Papier- und Folienwerke | Wipper-  
fürth

---

## HONORS AND AWARDS

2022	Research Travel Grant Karlsruhe House of Young Scientists
2018	Best graduate of the academic year   M.Sc. Westphalian University of Applied Sciences
2017 – 2018	Deutschlandstipendium Federal Ministry of Education and Research
2018	Conference grant German Chemical Society
2016	Best graduate of the academic year   B.Sc. Westphalian University of Applied Sciences
2016	Award for outstanding achievements in studies German Chemical Society
2014 – 2016	Deutschlandstipendium Federal Ministry of Education and Research

## QUALIFICATIONS AND HONORARY

2022	Certified Project Manager in Business Chemistry German Chemical Society
11/2017 – 08/2018	Member of the Appointment Committee for Chemistry, esp. Chemical Processes Westphalian University of Applied Sciences
2016	Certificate of competence according to the Chemicals Prohibition Ordinance Westphalian University of Applied Sciences
01/2015 – 02/2016	Member of the Appointment Committee for Chemistry, esp. Technical Chemistry Westphalian University of Applied Sciences



---

## PUBLICATIONS

1. Hirschberg, V.; Schußmann, M. G.; Röpert, M.-C.; Wilhelm, M.; Super-tough thermoplastic elastomers of polystyrene and polyisoprene via the pom-pom topology. (in progress)
  2. Hirschberg, V.; Schußmann, M. G.; Röpert, M.-C.; Wilhelm, M.; Wagner, M. H.; Modeling elongational viscosity and brittle fracture of polystyrene Pom-Poms by the Hierarchical Molecular Stress Function model. *Rheol. Acta* 2023. DOI: 10.1007/s00397-023-01393-0.
  3. Röpert, M.-C.; Hirschberg, V.; Schußmann, M. G.; Wilhelm, M.; Impact of Topological Parameters on Melt Rheological Properties and Foamability of PS POM-POMs. *Macromolecules*, 2023, 1921-1933. DOI: 10.1021/acs.macromol.2c02051.
  4. Röpert, M.-C.; Goecke, A.; Wilhelm, M.; Hirschberg, V.; Threading Polystyrene Stars: Impact of Star to POM-POM and Barbwire Topology on Melt Rheological and Foaming Properties. *Macromol. Chem. Phys.* 2022, 2200288. DOI: 10.1002/macp.202200288.
  5. Faust, L.\*; Röpert, M.-C.\*; Esfahani, M. K.; Abbasi, M.; Hirschberg, V.; Wilhelm, M.; Comb and Branch-on-Branch Model Polystyrenes with Exceptionally High Strain Hardening Factor SHF > 1000 and Their Impact on Physical Foaming. *Macromol. Chem. Phys.* 2022, 2200214. DOI: 10.1002/macp.202200214.
- \*shared first authorship
6. Röpert, M.-C.; Schußmann, M. G.; Esfahani, M. K.; Wilhelm, M.; Hirschberg, V.; Effect of Side Chain Length in Polystyrene POM-POMs on Melt Rheology and Solid Mechanical Fatigue. *Macromolecules* 2022, 5485-5496. DOI: 10.1021/acs.macromol.2c00199.
  7. Kirchberg, A.; Esfahani, M. K.; Röpert, M.-C.; Wilhelm, M.; Meier, M. A. R.; Sustainable Synthesis of Non-Isocyanate Polyurethanes Based on Renewable 2,3-Butanediol. *Macromol. Chem. Phys.* 2022, 2200010. DOI: 10.1002/macp.202200010





---

## CONFERENCE CONTRIBUTIONS

### PRESENTATIONS:

1. Röpert, M.-C.; Hirschberg, V.; Wilhelm, M.; Importance of Mobility and Topology of Defined Polystyrene Model Architectures in the Physical Foaming Process, *2<sup>nd</sup> International Symposium on Plastics Technology*, Aachen, Germany, 2022.
2. Hirschberg, V.; Röpert, M.-C.; Schußmann, M. G.; Wilhelm, M.; Molecular origin of rheological properties of well-defined Polystyrene POM-POM model systems and comparison with well-defined PS combs and stars, *Joint Online Symposium on Rheology of the German Rheological Society (DRG)*, 2022.
3. Hirschberg, V.; Schußmann, M. G.; Röpert, M.-C.; Wilhelm, M.; Molecular origin of rheological properties of well-defined Polystyrene POM-POM model systems and comparison with well-defined PS combs and stars, *AERC*, Sevilla, Spain, 2022.
4. Röpert, M.-C.; Hirschberg, V.; Khabazian, M.; Wilhelm, M.; Rheological Studies of defined PS POM-POM Architectures, *Polymer Brushes*, online conference 2021.
5. Hirschberg, V.; Röpert, M.-C.; Faust, L.; Khabazian, M.; Wilhelm, M.; Molecular origin of rheological and mechanical properties of well-defined Polystyrene POM-POM model systems, *92<sup>th</sup> SoR*, hybrid conference 2021.
6. Röpert, M.-C.; Hirschberg, V.; Wilhelm, M.; Investigation of rheological and mechanical properties of tailor-made POM-POM model systems, *AERC 2021*, online conference 2021.
7. Röpert, M.-C.; Hirschberg, V.; Faust, L.; Wilhelm, M.; Monodisperse Block Copolymers: Influence of Morphology and Topology on Cell Size in Polymer Foams, *6<sup>th</sup> CellMAT*, online conference 2020.
8. Röpert, M.-C.; Weidmann, C.; Ostermann, R.; Hierarchical Porous Solvogel Monoliths - Synthesis and Application, *E-MRS*, Warschau, Polen 2018.

### POSTER:

1. Schußmann, M. G.; Hirschberg, V.; Röpert, M.-C.; Wilhelm, M.; High performance polystyrene/polyisoprene thermoplastic elastomers using PS/PI block copolymers and the POM-POM topology, *AERC*, Sevilla, Spain, 2022.
2. Hirschberg, V.; Schußmann, M. G.; Röpert, M.-C.; Wilhelm, M.; Influence of Topology on the Mechanical Solid State Performance of Polystyrene/Polyisoprene Block Copolymers for the Design of Sustainable Polymers, *Freiburg Macromolecular Colloquium*, online conference 2022.
3. Röpert, M.-C.; Abbasi, M.; Faust, L.; Wilhelm, M.; Model Comb Polystyrenes: Synthesis, Rheology and Correlated Foam Properties, *Polymer Brushes*, online conference 2021.

4. Röpert, M.-C.; Faust, L.; Hirschberg, V.; Abbasi, M.; Wilhelm, M.; Monodisperse Block Copolymers: Influence of Morphology and Topology on Cell Size in Polymer Foams, *EPF Summer School*, online conference 2021.
5. Röpert, M.-C.; Hirschberg, V.; Wilhelm, M.; Investigation of rheological and mechanical properties of tailor-made POM-POM model systems, *EPF Summer School*, online conference 2021.
6. Röpert, M.-C.; Weidmann, C.; Ostermann, R.; Hierarchical Porous Solvogel Monoliths: Synthesis and Application, *MRS*, Boston, Massachusetts, USA 2018.